Imperial College of Science, Technology and Medicine
Department of Mechanical Engineering

Uncertainty Quantification Of Performance And Stability Of High-Speed Axial Compressors

Venkatesh Suriyanarayanan

December 2020

Submitted in part fulfilment of the requirements for the degree of
Doctor of Philosophy in Mechanical Engineering of Imperial College London
and the Diploma of Imperial College London

Abstract

Geometrical uncertainties in a compressor (due to manufacturing tolerance and/or in-service degradation) often result in flow asymmetry around the annulus of a compressor that jeopardises compressor stability and performance. Usually, sensitivity of compressor stability and performance for any parametric variation is arrived at by considering all blades to have same dimension. In reality, an inherent blade-to-blade variation causes the blades to have a probability distribution. These blades can be redistributed circumferentially resulting in adjacent passage areas between different blades to be completely random and hence the performance variation. Surrogate model is preferred for quantifying the effects of parametric variation on compressor stability and performance given its quick turnaround time vis-a-vis CFD and experiments.

In this thesis, uncertainties for three test cases were considered: each representative of fans on military aircraft engines, fans on civil aircraft engines and a 1-stage transonic compressor used in industrial gas turbine. This research establishes a rule of thumb to arrange blades of differing dimensions around the compressor to eke out maximum performance and stability margin. The parameters tip gap and stagger angle represent manufacturing tolerance while in-service degradation was represented by leading edge damage. For both random tip gap variation (0.15% to 0.94% span) and random leading edge damage (4% to 18% chord), the compressor performance and stability boundaries were found to be best with a zigzag pattern of blade arrangement and worst with a sinusoidal pattern of arrangement. The converse was found to be true for blades having random stagger angle variation ($\pm$ 2.25% change in nominal stagger angle). The best/worst arrangement of blades with differing dimensions was ascertained using a mix of CFD and travelling salesman (TSP) analogy. The TSP analogy is handy for determining the best arrangement when two or more parameters vary simultaneously.

Generalised surrogate model was developed to accurately predict the performance of compressors undergoing random tip gap and stagger angle variation. Due to its robustness, the surrogate model was combined with Monte Carlo technique to gauge the impact of parametric variation on quantities of interest (QoI). The mean absolute percentage error between CFD and surrogate models of stagger angle and tip gap (for different QoI) were found to be less than 0.14% and 1.5% respectively. This *de novo* analysis considers only the aerodynamic effect from geometric variations while neglecting the associated aeroelastic effects. Detailed analyses based on past experience and physical reasoning were used to validate the numerical simulations.

Statement Of Originality

The thesis titled **"Uncertainty Quantification Of Performance And Stability Of High-Speed Axial Compressors"** is a bona fide work carried out by the candidate at Imperial College London for the award of degree of Doctor of Philosophy. No content of this work has been submitted, either in whole or in part, for the award of any degree or diploma at any other university or institution. References or quotations from other works have been fully acknowledged.

Venkatesh Suriyanarayanan

December 2020

Copyrights

The copyright of this thesis rests with the author. Unless otherwise indicated, its contents are licensed under a Creative Commons Attribution-NonCommercial 4.0 International Licence (CC BY-NC).

Under this licence, you may copy and redistribute the material in any medium or format. You may also create and distribute modified versions of the work. This is on the condition that: you credit the author and do not use it, or any derivative works, for a commercial purpose.

When reusing or sharing this work, ensure you make the licence terms clear to others by naming the licence and linking to the licence text. Where a work has been adapted, you should indicate that the work has been changed and describe those changes.

Please seek permission from the copyright holder for uses of this work that are not included in this licence or permitted under UK Copyright Law.

Acknowledgements

I would like to express my sincere gratitude to all the wonderful people without whose help and encouragement, this thesis would have been a distant dream.

First and foremost, I would like to thank my doctoral supervisors, Prof. Mehdi Vahdati and Dr. Loic Salles, for providing me with an opportunity to study at Imperial College London. The weekly meetings proved to be a great source of learning and provided an added impetus in carrying out the research work. I am grateful for their invaluable guidance throughout my PhD. They have given me the complete freedom to explore new ideas while apprising me of the merits and potential pitfalls. Their critiquing helped improve the overall quality of research work. Their immense support, especially during the last 6 months of my PhD is gratefully acknowledged. Thanks for organising the riverwalks and other fun social events.

I also take this opportunity to thank Dr. Quentin Rendu for all the help rendered during the last 3 years. His role in designing the wide-chord blade and co-development of the UQ code is much appreciated. Many thanks to Mr. Kentaro Suzuki for the collaborative work in damaged blade study. I am grateful to Dr. Minsuk Choi for all the help during the first year of my PhD. I would like to express my deep gratitude to Dr. Wenqiang Zhang, Dr. Fanzhou Zhao, Dr. Prathiban Sureshkumar, Dr. Sina Stapelfeldt, Dr. Yaozhi Lu, Mr. He Xiao and Mr. Jose Moreno for chipping in with their valuable help at different points in time. Word of thanks is also due to Daniel, Alfredo, Fadi, Mertol and Alessandra for making the PhD journey memorable.

Its a pleasure to have friends like Anjalus, Rajesh, Ramesh, Nikhil, Sandip and Swapnil who've always wished me well. I am deeply indebted to Reliance Industries Ltd (India) for sponsoring my PhD studies. A big thank you to Mr. Srinivasan Bodapati and his team at RIL (India) for ensuring timely disbursal of scholarship. My sincere thanks to Mr. Dilip Sharma and Mr. Raj Bedi for helping with stay arrangements in UK. Many thanks to Prof. Sunetra Sarkar and Prof. Sayan Gupta (my previous mentors at IIT-M) for always encouraging me to pursue PhD.

I owe a debt of gratitude to my parents, parents-in-law and other dear relatives for all the unconditional love and support they have showered on me. Finally, any words I could say would fall short in expressing my heartfelt gratitude to my beloved wife - Yogita, for being my best friend all these years. Your constant support kept me sane and allowed me to pursue my dreams. May you all be blessed with all the happiness in your life.

In the loving memory of my grandparents

You are missed beyond measure. Thanks for all the unconditional love.

ॐ असतो मा सद्गमय ।
तमसो मा ज्योतिर्गमय ।
मृत्योर्मा अमृतं गमय ।
ॐ शान्तिः शान्तिः शान्तिः ॥

Translation :

Lead us from illusion to reality
Lead us from darkness to light
Lead us from mortality to life-eternal
Om ! Let peace prevail forever

- The Upanishads

Notation

CFD	Computational Fluid Dynamics
DNS	Direct Numerical Simulation
LES	Large Eddy Simulation
$RANS$	Reynolds Averaged Navier-Stokes
UQ	Uncertainty Quantification
MCS	Monte Carlo Simulation
$gPCE$	Generalised Polynomial Chaos Expansion
TSP	Travelling Salesman Problem
FAA	Federal Aviation Administration
$WALE$	Wall-Adapting Local Eddy-Viscosity
SA	Spallart-Allmaras
SST	Shear Stress Transport
RSM	Reynolds stress model
CAD	Computer Aided Design
QoI	Quantities Of Interest
IGT	Industrial Gas Turbine
IGV	Inlet Guide Vane
$\dot{m}$	Mass Flow Rate Of Compressor
CMF	Corrected Mass Flow Of Compressor
$NCMF$	Normalised Corrected Mass Flow Of Compressor
PR	Pressure Ratio
η	Isentropic Efficiency Of Compressor
RE	Relative Efficiency Of Compressor
C_1, C_2	Parameters Used To Normalise CMF and η respectively
SM	Stall Margin
S_i	Stagger Angle Of 'i' th blade
$S_{ave.\ overall}$	Average Stagger Angle (Global)
$C\text{-}MIST$	Absolute Cumulative Mis-stagger (Global)
$LTO\text{-}STC$	Large Tip Gap With Stagger Open and Small Tip Gap With Stagger Closed
$STO\text{-}LTC$	Small Tip Gap With Stagger Open and Large Tip Gap With Stagger Closed
$S\text{-}mean_i$	Mean Stagger Angle (Local)
$S\text{-}abs.mist_i$	Absolute Mis-stagger (Local)

Contents

Abstract **i**

Statement Of Originality **iii**

Copyrights **v**

Acknowledgements **vii**

Notation **xiii**

1 Introduction **1**

1.1 Background 1

1.2 Motivation 4

1.3 Research Objectives 5

1.4 Dissertation Overview 6

1.5 Key Achievements 8

1.6 Publications 9

2 Literature Survey **10**

2.1 The Need For Uncertainty Quantification 10

2.2 Working Of An Axial Compressor 12

2.3 Geometric Uncertainties In Axial Compressors 16

2.3.1 Effect Of Tip Gap 16

2.3.2 Effect Of Leading Edge 19

2.3.3 Effect Of Stagger Angle 20

2.3.4 Effect Of Lean, Sweep And Fillet Radius 22

2.4 Classifying The Uncertainty : Aleatory or Epistemic? 23

2.5 Tools In Uncertainty Quantification 24

2.5.1 Monte Carlo Simulation 27

2.5.2 Surrogate Models 28

2.5.2.1 Generalised Polynomial Chaos Expansion (gPCE) 29

2.5.2.2 Sensitivity Method 31

2.5.2.3 Response Surface Models 31

2.5.2.4 Active Subspace Based Surrogate Model 32

2.6 Limitations Of CFD And Experiments 34

2.6.1 Limitations In CFD 35

2.6.1.1 Turbulence Modelling 36

2.6.1.2 Boundary Conditions 40

2.6.1.3 Exact Geometry 42

2.6.1.4 Mesh Dependency 43

2.6.1.5 Steady vs Unsteady 44

2.6.2 Limitations In Experiments 44

2.6.2.1 Limitations Of Measuring Equipments 46

2.6.2.2 Limitations Of Experimental Setup 46

2.7 Combinatorial Optimisation 47

2.8 Chapter Summary 48

3 Methods **49**

3.1 Numerical Methodology 49

3.2 Test Cases 51

3.3 Boundary Conditions 56

3.4 Mesh Generation 59

3.5 Scalability Test 61

3.6 Mesh Independence Study 65

3.7 Travelling Salesman Problem 74

3.8 Chapter Summary 76

4 Study Of Manufacturing Tolerance On Aircraft Engines **77**

4.1 Engineering Metrology And Quality Control 78

4.2 Compressor Stagger Angle 82

4.2.1 Single and Double Passage Simulation Of NASA Rotor 67 82

4.2.2 Single and Double Passage Simulation Of Wide Chord Blade 84

4.2.3 Full Annulus Simulation Of NASA Rotor 67 And Wide Chord Blade . . 87

4.3 Compressor Tip Gap 94

4.3.1 Single and Double Passage Simulation Of NASA Rotor 67 94

4.3.2 Single Passage Simulation Of Wide Chord Blade 99

4.3.3 Full Annulus NASA Rotor 67 . . . 101

4.4 Two Parameter Variation : Stagger And Tip Gap . . . 105

4.5 Chapter Summary . . . 115

5 Study of In-service Degradation In An Industrial Gas Turbine 117

5.1 Background To Damaged Blades In Compressors . . . 118

5.2 Maintenance, Repair And Overhaul (MRO) . . . 125

5.3 Behaviour Of Damaged Blades And Blades With Different Tip Gaps . . . 129

5.4 Optimised Arrangement Of Random Damaged Blades . . . 138

5.5 Future Work And Recent Advances . . . 144

5.6 Chapter Summary . . . 148

6 Development of Surrogate Model and Uncertainty Quantification 150

6.1 First Principles To Build The Surrogate Model . . . 152

6.2 Surrogate Model For Stagger Angle . . . 155

6.3 Surrogate Model For Tip Gap . . . 162

6.4 Limitations Of Surrogate Model . . . 169

6.5 Uncertainty Quantification . . . 172

6.5.1 UQ For Stagger Angle Variation . . . 172

6.5.1.1 Uncertainty In Maximum Efficiency . . . 173

6.5.1.2 Uncertainty In Stability Margin . . . 177

6.5.2 UQ for tip gap variation . . . 181

6.5.2.1 Uncertainty In Maximum Efficiency . . . 182

6.5.2.2 Uncertainty In Stall Margin . . . 184

6.6 Chapter Summary 186

7 Conclusions And Future Work **188**

7.1 Conclusions 188

7.2 Importance From Industrial Perspective 192

7.3 Future Work 193

7.3.1 Steady Simulation 193

7.3.2 Unsteady Simulation 194

Bibliography **195**

Appendix : Copy Rights Permission **209**

List of Tables

3.1 Blade Design Control Parameters 53

3.2 Comparison of Different Test Cases 56

3.3 Uncertainty In Nominal Tip Gap Of NASA Rotor 67 As Found In Literature . . 66

3.4 Mesh Convergence Study Of NASA Rotor 67 72

3.5 Example Of A Genetic Algorithm Used For Generating 3 Mutated Routes From The Shortest Route. Adapted from (Kirk, 2014) 75

4.1 Heuristic Method For Different Arrangement Of Stagger Angle (NASA Rotor 67) 90

List of Figures

1.1 Application Of Different Numerical Methods In Turbo-machinery 2

2.1 Images of (A) Space Shuttle Challenger (Credits : NASA) (B) Hubble Space Telescope (Credits : NASA) (C) Launch of Ariane 5 (Copyrights : ESA/CNES/Arianespace) (D) Launch of GSLV-F05 (Copyrights : ISRO, Reproduced With Kind Permission From ISRO) 11

2.2 Schematic Of An Axial Compressor (Hill and Peterson, 1992) 12

2.3 Velocity Triangle At Mean Radius Of A Compressor Stage (Hill and Peterson, 1992) 13

2.4 Design And Stalling Condition For An Axial Compressor (Hill and Peterson, 1992) 14

2.5 Schematic Of A Compressor Operating Map 15

2.6 Schematic Of Uncertainties In A Compressor Blade 17

2.7 Schematic Of Tip Leakage Flow - Adapted From Inoue and Kuroumaru (1989). [Reproduced With Kind Permission From ASME] 18

2.8 Subcritical Hopf Bifurcation As Seen In Desai (2011) 26

2.9 Sensitivities From Different Parameters on (A) Isentropic Efficiency (B) Loss Coefficient (C) Blade Turning. Figures Have Been Adapted From Lange et al. (2010) [Reproduced With Kind Permission From ASME] 27

2.10 Schematic Of Non-Intrusive Polynomial Chaos Expansion 30

2.11 3D Blade Parametrisation Showing 5 Degrees Of Freedom (Both Positive And Negative) From Seshadri et al. (2017) [Reproduced With Kind Permission From ASME] 34

2.12 Perturbations In Active Subspace Showing (A) Minimum Pressure Ratio Geometry (B) Maximum Pressure Ratio Geometry (C) Minimum Efficiency Geometry (D) Maximum Efficiency Geometry. Figures Adapted From Seshadri et al. (2017) [Reproduced With Kind Permission From ASME] 35

2.13 (A) Schematic Of The Experimental Setup Used By Gourdain (2015) [Reproduced With Kind Permission From Elsevier] (B) Schematic Of DGEN-380 Turbofan Used By Odier et al. (2017) 37

2.14 Comparison Of Experimental, RANS And LES Performance Curves (A) Pressure Ratio Vs. Mass Flow Rate From Gourdain (2015) [Reproduced With Kind Permission From Elsevier] (B) Efficiency Vs. Mass Flow Rate From Gourdain (2015) [Reproduced With Kind Permission From Elsevier] (C) Pressure Ratio Vs. Mass Flow Rate From Odier et al. (2017) (D) Efficiency Vs. Mass Flow Rate From Odier et al. (2017) 38

2.15 (A) Real Geometries In Turbomachinery (B) 3D Optical Scan Geometry. Adapted From Montomoli et al. (2015) [Reproduced With Kind Permission From Prof. F. Montomoli, Imperial College London, UK and Prof. M. Pinelli, University of Ferrara, Italy] 42

2.16 Bulls Eye Plot Showing Distinction Between Accuracy And Precision (A) Not Precise and Not Accurate (B) Not Precise But Accurate (C) Precise But Not Accurate (D) Precise and Accurate 45

3.1 Computational Domain Of NASA Rotor 67 52

3.2 Computational Domain Of 1-Stage Compressor Used In A Typical IGT 53

3.3 Computational Domain Of Wide Chord Blade 54

3.4 Functions Used In MULTALL (Denton, 2017) 54

3.5 Parameterisation Of Blade Section 55

3.6 Normalised Pressure ratio Of Different Blades At Respective Peak Efficiency . . 56

3.7 Schematic Showing (A) Computational Domain (B) Single Passage Rotor Domain (Left) And Double Passage Rotor Domain (Right) (C) Variable Area Nozzle 58

3.8 (A) Mesh Around The Blade Of NASA Rotor 67 (B) Radial Mesh Strategy In Case Of Blades With Different Tip Gaps 60

3.9 (A) Schematic Of Different Leading Edge Damages (B) Mesh Around Undamaged Rotor Blade Of 1-Stage IGT (C) Mesh Around Damaged Rotor Blade Of 1-Stage IGT 60

3.10 Time Required to Solve In AU3D For Different Meshes Sizes 63

3.11 Strong Scalability Test For Different Meshes In AU3D 63

3.12 Weak Scalability Test For 1 Million Mesh Points Per CPU In AU3D 64

3.13 Weak Scalability Test For 2 Million Mesh Points Per CPU In AU3D 64

3.14 Mesh Convergence For Different Single Passage Tip Gaps Of NASA Rotor 67 At 100% Speed 67

3.15 NASA Rotor 67 At 100% Speed (A) Mesh Convergence Of Double Passage Mixed Tip Gaps (B) Span-Wise Experimental Data (At Peak Efficiency, Stall) vs Simulation Results 67

3.16 Uncertainty In Experimental Data Of Performance Curve For NASA Rotor 67 . 68

3.17 Experiment vs. Computational (tip gap of 0.188% span and 0.376% span) Flow Field At Maximum Efficiency (A, B and C) And Stall (D, E and F) At 30% Span From The Hub 69

3.18 Experiment vs. Computational (tip gap of 0.188% span and 0.376% span) Flow Field At Maximum Efficiency (A, B and C) And Stall (D, E and F) At 70% Span From The Hub 70

3.19 Experiment vs. Computational (tip gap of 0.188% span and 0.376% span) Flow Field At Maximum Efficiency (A, B and C) And Stall (D, E and F) At 90% Span From The Hub 71

3.20 Mesh Convergence At 100% Speed (A) For Wide Chord Blade (B) Transonic Rotor In 1-stage IGT 72

3.21 (A) Flowchart Of Travelling Salesman Problem Using Genetic Algorithm Adapted from (Kirk, 2014) (B) Schematic of Travelling Salesman Problem With Ten Different Cities and All Possible Routes 74

4.1 (A) Schematic Of Tolerance On Two Mating Parts (B) Effect Of Tolerance Stacking (C) Tolerance Stack Up Due To Dimensioning 79

4.2 Schematic Of (A) GO And NO-GO Gauge For Holes (B) GO And NO-GO Gauge For Shafts 80

4.3 Changes In Fan Performance Due To Stagger Variation Of Blades 83

4.4 Changes In Maximum Efficiency Due To Stagger Angle Variation Of Blades . . 83

4.5 Shock Wave Position At 75% Span And Non-Dimensional Flow Rate Of 0.986 For (A) Single Passage 0% Stagger Change (B) Single Passage -2.25% Stagger Change (C) Double Passage 0% And -2.25% Stagger Change 85

4.6 Schematic Showing The Change In Location Of Shock With Change In Stagger Angle 85

4.7 Performance Curve Of Wide-Chord Blade When Subject To Stagger Variation . 86

4.8 Shockwaves In A Wide-Chord Blade : (A) Single Passage Rotor With 0% Change in Stagger (B) Single Passage Rotor With 2.2% Change in Stagger (C) Single Passage Rotor With -2.2% Change in Stagger (D) Double Passage Rotor With 2.2% and -2.2% Change In Stagger Angle 86

4.9 Scatter plot of two different random distributions within a closed interval 88

4.10 TSP Used To Predict The Least Mis-Staggered Arrangement : (A) Distribution Of Blades With Random Stagger Angle (B) Mis-Stagger Matrix (C) Sinusoid Arrangement Having Least Cumulative Mis-Stagger (D) Solution Time History . 89

4.11 TSP Used To Predict The Most Mis-Staggered Arrangement : (A) Distribution Of Blades With Random Stagger Angle (B) Mis-Stagger Matrix (C) Zigzag Arrangement Having Maximum Cumulative Mis-Stagger (D) Solution Time History 89

4.12 Heuristic Arrangements In Case Of NASA Rotor 67 For The Same Set Of Random Staggered Blades With Average Change Of Stagger 0.437% (A) Random Arrangement (B) Linear Arrangement (C) Sinusoid Arrangement (D) Zigzag Arrangement 91

4.13 Performance For Different Combinations Of Random Stagger For NASA Rotor 67 (A) 80% Fan Speed (B) 100% Fan Speed 92

4.14 Heuristic Arrangements In Case Of Wide Chord Blade Rotor For The Same Set Of Random Staggered Blades With Average Change Of Stagger 0.16% (A) Random Arrangement (B) Linear Arrangement (C) Sinusoid Arrangement (D) Zigzag Arrangement 93

4.15 Performance For Different Combinations Of Random Stagger For Wide Chord Blade At 100% Fan Speed 93

4.16 Comparison Of Fan Performance For Different Tip Gaps 95

4.17 Behaviour Of (A) Maximum Pressure Ratio With Respect To Tip Gap (B) Maximum Efficiency With Respect To Tip Gap (C) Stall Margin With Respect To Tip Gap 96

4.18 NASA Rotor 67 Spanwise Profile Of (A) Pressure Ratio (B) Axial Velocity (C) Efficiency For Different Tip Gaps At Same Non Dimensional Mass Flow Rate Of 0.982 96

4.19 Blade Relative Mach Number At 99% Span At A Non Dimensionalised Mass Flow Rate Of 0.982 For (A) Single Passage Tip Gap 0.188% Span (B) Single Passage Tip Gap 0.564% Span (C) Single Passage Tip Gap 0.94% Span (D) Double Passage Tip Gaps Of 0.188% And 0.94% Span 97

4.20 Schematic Showing Location Of Shock In Adjacent Passage Due To Change In Tip Gap 98

4.21 Comparison At 99% Span Of Single Passage Blade With Tip Gaps 0.188% Span And 0.94% With The Respective Individual Blades Of Double Passage Blades With Tip Gaps 0.188% Span And 0.94% Span (Near Peak Efficiency) 99

4.22 Different Low Speed Fans Used In Industry (A) Normalised Pressure Ratio vs Span For Fan A (B) Normalised Pressure Ratio vs Span For Fan B (C) Normalised Pressure Ratio vs Span For Fan C. The Figures Have Been Adapted From Lee et al. (2018) Wherein The Terms OSA, MSA and GWF Represent The Original SA Model, Modified SA Model Based On β-Function And Generalised Wall Function Respectively [Reproduced With Kind Permission Of ASME] 100

4.23 Effect Of Tip Gap On Performance Of Wide Chord Blade 100

4.24 Wide Chord Blade Spanwise Profile Of (A) Pressure Ratio (B) Axial Velocity (C) Efficiency For Different Tip Gaps At Same Non Dimensional Mass Flow Rate Of 0.962 101

4.25 Comparison Of Different Double Passage Vs. Half Annulus Arrangement Performances For The Same Mean Tip Gap In Case Of NASA Rotor 67 102

4.26 A Line Diagram Of Compressor Blades Around The Casing Showing (A) Uniform Tip Gap With Concentric Rotor And Casing (B) Half Annulus Arrangement Of Different Tip Gaps Producing An Effect Similar To Eccentric Rotor 103

4.27 Different Combinations For Same Set Of Random Tip Gap Blades For NASA Rotor 67 With Average Tip Gap Of 0.52% Span (A) Random Arrangement (B) Linear Arrangement (C) Sinusoid Arrangement (D) Zigzag Arrangement 103

4.28 Performance For Different Arrangements Of Random Tip Gaps (NASA Rotor 67) 104

4.29 Schematic Showing Movement Of shock In Adjacent Passages Due To Variation In Tip Gap And Stagger Angle 106

4.30 Changes In Performance Curve Due To Variation Of Tip Gap And Stagger Angle 107

4.31 Changes In Spanwise Pressure Ratio And Efficiency Due To Variation Of Tip Gap And Stagger Angle 108

4.32 Shock Movement In Adjacent Passages Of Double Passage With Tip Gaps 0.188% Span And 0.94% Span Due To Variation Of Stagger Angle By 1° At 98% Span . 109

4.33 Loading At 80% Span From Hub In Blades With Tip Gap Of (A) 0.188% Span (B) 0.94% Span For Baseline Double Passage, LTO-STC : 1° And STO-LTC : 1° 109

4.34 Comparison Of Performance Of Double Passage Baseline And Pseudo Random Varying Case 111

4.35 TSP Analogy For Pseudo Random Variation Of Tip Gap And Stagger Angle : (A) Distribution Of Different Staggered And Tip Gap Blades (B) Distance Matrix (C) Optimal Path (D) Converged Solution History 112

4.36 Optimised Arrangement Using TSP Analogy For Pseudo Random Variation : (A) Arrangement For Blades With Different Tip Gap (B) Arrangement For Blades With Different Stagger Angle 113

4.37 TSP Analogy For Random Variation Of Tip Gap And Stagger Angle : (A) Distribution Of Different Staggered And Tip Gap Blades (B) Distance matrix (C) Optimal Path (D) Converged Solution History 114

4.38 Optimised Arrangement Using TSP Analogy For Random Variation : (A) Arrangement For Blades With Different Tip Gap (B) Arrangement For Blades With Different Stagger Angle 115

5.1 (A) High Pressure Compressor Tip Curl Damage And Missing Liner (B) Rolls-Royce RB 211-524GT Engine - Adapted From Marshall et al. (2013) [Reproduced With Kind Permission Of Rolls-Royce, PLC] 118

5.2 Formation Of Glaze Ice At -5°C, Mixed Ice At -10°C And Rime Ice At -15°C Temperature - Adapted From Wang et al. (2020) 119

5.3 (A) Ice Formation On IGV Of Industrial Gas Turbine And Damage On Compressor Blade Due To Ice Ingestion (B) Installation Of Inlet Hoods At The Intake Of Industrial Gas Turbine - Figures Adapted From Sammak (2006) 120

5.4 (A) Modelled Ash Particles From The Site Of Volcanic Eruption - Figure Adapted From Davison and Rutke (2014) [Reproduced With Kind Permission Of ASME] (B) Operating Envelop In Dust Laden Environment From Rolls Royce - Adapted From Davison and Rutke (2014) [Reproduced With Kind Permission Of ASME] (C) Erosive Loss Kinetics For Nickel At 90° Impact At Different Velocities, Temperature And Fluids As Given In Kang et al. (1987) - Adapted From Birks et al. (1993) [Reproduced With Kind Permission Of Springer Nature] (D) Comparison Of New Compressor Blade And Eroded Compressor Blade As Given In Hamed And Tabakoff (1994) - Adapted From Alqallaf et al. (2020) 122

5.5 (A) Fatigue Failure Of The HPC Blade (Ti-6Al-4V Alloy) In An Industrial Gas Turbine - Adapted From Jasiczek et al. (2013) [Reproduced With Kind Permission Of Springer Nature] (B) Fatigue Failure Of Fan Blade In Rolls-Royce Trent 772B-60 Engines [Reproduced With Kind Permission Of Rolls-Royce, PLC] (C) Region of Crack Initiation Point (Left) And Magnified View Of Fracture Showing Its Propagation (Right) In Fan Blade Of Rolls-Royce Trent 772B-60 Engines - Adapted From ATSB (2020) [Reproduced With Kind Permission Of Rolls-Royce, PLC] 123

5.6 Schematic Showing (A) Comparison Of An Undamaged Compressor Blade With A Compressor Blade Undergoing Tip Curl Damage (B) Comparison Of Recontoured Compressor Blade And Undamaged Compressor Blade (C) Damage Near The Leading Edge and Trailing Edge Of The Compressor Blade Along With Some Pitting Damage (D) A Typical Compressor Blade After Blending Operation. The Schematic For Undamaged Rotor Adapted From Chaganti (2012) 126

5.7 Allowable Damage Limits In A Typical Compressor Blade As Given By Federal Aviation Administration (2018) [Reproduced With Kind Permission From FAA] 126

5.8 Allowable Damage Limits As Given For T63-A-720 Merlin 250 Engine In The TM 55-2840-241-23 Manual (A) Compressor Rotor Blade Leading and Trailing Edge Blend Limits (B) Instruction To Maintain Radius Of LE And TE After Blending Operation (C) Compressor Blade Surface Blending Limits (D) Compressor Rotor Blade Tip Blend Limits (Adapted From TM 55-2840-241-23 Manual) 127

5.9 Revenue Breakdown Of Rolls-Royce Civilian Aerospace Division In 2015 128

5.10 Damaged Blades Used In The Study Of Industrial Gas Turbines 130

5.11 Schematic Of Damage Decomposition Into: (**A**) Different Radial Level Damage. (**B**) Different Chord-Wise Damage. 130

5.12 Effect Of Leading Edge Damage On Performance Of Different Blades 131

5.13 Mach Number Contours At **Same** Non-Dimensional Corrected Mass Flow Rate $\approx \mathbf{1}$: (**A**) Undamaged Blade. (**B**) Chord Damage Of 4%. (**C**) Chord Damage Of 10% And (**D**) Chord Damage Of 18% 132

5.14 Effect Of Tip Gap On The Rotor Blade Of 1-Stage IGT 133

5.15 Span-Wise Comparison Of Choked Mass Flow Rate For 18% Chord Damaged Blade And Undamaged Blade 134

5.16 Influence Of Varying Radial Damages With Constant Chord On 1-Stage IGT . . 134

5.17 Influence Of Varying Chord-Wise Damage At Same Radial Level On 1-Stage IGT135

5.18 Influence Of Same Mean Damage But Different Damage Intensities On Performance Of 1-Stage IGT 136

5.19 Comparison Of Mach Number Contours For : (**A**) Single Passage Simulation For Blade With Damage Level 3 (At Peak Efficiency) (**B**) Double Passage Simulation For Blades With Damage Level 0 and Damage Level 7 (At Peak Efficiency) (**C**) Single Passage Simulation For Blade With Damage Level 3 (At Near Stall) And (**D**) Double Passage Simulation For Blades With Damage Level 0 and Damage Level 7 (At Near Stall) 137

5.20 Different Types Of Damaged Blade Arrangement : (**A**) Typical (Random) Arrangement (**B**) Linear Arrangement (**C**) Sinusoidal Arrangement (**D**) Zigzag Arrangement 139

5.21 Effect Of Arrangement Of Blade With Different Damage Intensities On Performance Of 1-Stage IGT 141

5.22 Stall Margin Comparison Of Different Whole Annulus Cases With Single Passage Damaged Blades 142

5.23 Effect Of Same Total Damage In A Sector With Different Intensities On The Performance Of 1-Stage IGT 143

5.24 Effect Of Number Of Damaged Blades On Performance 144

5.25 Schematic Of Basic Mode Shapes 145

5.26 Laser Deposition With Adaptive Toolpath Method : (A) Used To Repair Blade (B) Used To Repair PT6 Blisk (C) Used To Repair Titanium Blisks (D) Microstructure Of The Laser Generated Compressor Blade - Figures Adapted From Guo and Brommesson (2018) 146

5.27 BlackGold® Coating Developed By MDS Coating Shows : (A) Difference In Erosion Levels Between Coated And Uncoated Blades (B) Impeccable Surface Finish Over An Extended Period Of Time (C) Coated Blade Outperforming The Uncoated Blades For Sand Ingestion And Ash Ingestion (D) Reduced Leading Edge Curling On T-58 Blades While Operating In Desert Environment (E) Resists Fluid Erosion Over A Longer Duration (F) Resists Corrosion Over An Extended Period 147

6.1 Uncertainty Quantification Using Novel Surrogate Model 151

6.2 (A) General Schematic For Constructing Surrogate Model (B) Schematic Of Surrogate Model For Random Stagger Angle Around The Annulus (C) Schematic Of Surrogate Model For Tip Gap Around The Annulus 152

6.3 Schematic Of Sinusoidal Arrangement With Respect To Blade Number For (A) Stagger Angle Variation (B) Tip Gap Variation 153

6.4 CFD Performance Vs. Interpolation Performance (NASA Rotor 67) At 100% Speed For Different Mis-stagger Levels While Maintaining The Same Mean Stagger Angle 156

6.5 Schematic For Different Interpolation Cases For Building Surrogate Model Of Stagger Angle (A) Total 7 Interpolation Points *i.e.* 5 Single Passage and 2 Double Passage Cases (B) Total 10 Interpolation Points *i.e.* 7 Single Passage and 3 Double Passage Cases (C) Total 19 Interpolation Points *i.e.* 13 Single Passage and 6 Double Passage Cases 159

6.6 Schematic For Performance Prediction Of Different Arrangements Of Stagger Angle Using Double Interpolation Method (A) Interpolation For Different Single Passages (B) Interpolation For Different Mis-Staggers 160

6.7 Characteristic Curve From Surrogate Model For Stagger Angle Variation (NASA Rotor 67) At 100% Speed 161

6.8 Mean Absolute Percentage Error Between The Surrogate Model And Full Annulus CFD Simulation 161

6.9 Comparison Of Characteristic Curve From Surrogate Model And Whole Annulus CFD Simulation For Stagger Angle Variation 162

6.10 Schematic Of Performance Prediction For Baseline Surrogate Model And Modified Surrogate Model In Case Of Tip Gap 162

6.11 Comparison Of Slopes Of Actual Temperature Ratio And Scaled Temperature Ratio Vs. Pressure Ratio For A Sample Double Passage Case With Mixed Tip Gaps (A) Pressure Ratio And Actual Temperature Ratio Vs. Mass Flow Rate (B) Y Axis Of Actual Temperature Ratio Shifted To Coincide With Pressure Ratio (C) Pressure Ratio And Scaled Temperature Ratio Vs. Mass Flow Rate (D) Y Axis Of Scaled Temperature Ratio Shifted To Coincide With Pressure Ratio 166

6.12 Comparison Of Surrogate Models For Tip Gap Variation (NASA Rotor 67) At 100% Speed In Case Of Sinusoidal Arrangement And Linear Arrangement . . . 167

6.13 Surrogate Model For Tip Gap Variation (NASA Rotor 67) At 100% Speed In Case Of Zigzag Arrangement And Random Arrangement 167

6.14 Mean Absolute Percentage Error (MAPE) Of Surrogate Models With Respect To Full Annulus CFD Simulation For Tip Gap Variation (NASA Rotor 67) (A) Zigzag Arrangement (B) Random Arrangement 168

6.15 Schematic Depicting The Uncertainty In Stall Mass Flow Rate 170

6.16 Variation Of Stall Margin With Change In Stagger Angle For NASA Rotor 67 And Wide Chord Blade At Respective Design Speed 171

6.17 Manufacturing Tolerance Of Stagger Angle Variation For Nasa Rotor 67 173

6.18 Variation Of Maximum Efficiency With Respect To Different Arrangements Of Stagger Angle At Different Speed For Nasa Rotor 67 174

6.19 Operating Map For NASA Rotor 67 Adapted From Fidalgo et al. (2012) 175

6.20 Experimental Validation At 80% Speed For NASA Rotor 67 175

6.21 Probability Density Function And Reliability Function Of Maximum Efficiency With Respect To Different Arrangements Of Stagger Angle At 100% Speed For Nasa Rotor 67 176

6.22 (A) Scatter Plot Of Maximum Efficiency With Respect To Angle Stagger Angle For Wide Chord Blade (B) Reliability Function Of Maximum Efficiency With Respect To Different Arrangements Of Stagger Angle At Design Speed For Wide Chord Blade 177

6.23 Joint PDF (Z Axis) For Average Stagger Angle (X Axis) And Stall Margin (Y Axis) : Sinusoidal Arrangement Of Blades With Differing Stagger Angle In Case Of NASA Rotor 67 At Design Speed Visualised In (A) XYZ Isometric view (B) YZ Plane (C) XY Plane (D) XZ Plane. 178

6.24 Joint PDF (Z Axis) For Average Stagger Angle (X Axis) And Stall Margin (Y Axis) : Zigzag Arrangement Of Blades With Differing Stagger Angle In Case Of NASA Rotor 67 At Design Speed Visualised In (A) XYZ Isometric view (B) YZ Plane (C) XY Plane (D) XZ Plane. 179

6.25 Joint PDF (Z Axis) For Average Stagger Angle (X Axis) And Stall Margin (Y Axis) : Sinusoidal Arrangement Of Blades With Differing Stagger Angle In Case Of Wide Chord Blade At Design Speed Visualised In (A) XYZ Isometric view (B) YZ Plane (C) XY Plane (D) XZ Plane. 180

6.26 Joint PDF (Z Axis) For Average Stagger Angle (X Axis) And Stall Margin (Y Axis) : Zigzag Arrangement Of Blades With Differing Stagger Angle In Case Of Wide Chord Blade At Design Speed Visualised In (A) XYZ Isometric view (B) YZ Plane (C) XY Plane (D) XZ Plane. 181

6.27 Normalised Histogram Of Random Tip Gaps 182

6.28 Scatter Plot Of Maximum Efficiency Vs Average Tip Gap For NASA Rotor 67 At 100% Speed 183

6.29 Probability Density Function And Reliability Function Of Maximum Efficiency With Respect To Different Arrangements Of Tip Gaps At 100% Speed For NASA Rotor 67 183

6.30 Joint PDF (Z Axis) For Average Tip Gap (X Axis) And Stall Margin (Y Axis) : Zigzag Arrangement Of Blades With Differing Stagger Angle In Case Of NASA Rotor 67 At Design Speed Visualised In (A) XYZ Isometric view (B) YZ Plane (C) XY Plane (D) XZ Plane. 184

6.31 Joint PDF (Z Axis) For Average Tip Gap (X Axis) And Stall Margin (Y Axis) : Sinusoidal Arrangement Of Blades With Differing Stagger Angle In Case Of NASA Rotor 67 At Design Speed Visualised In (A) XYZ Isometric view (B) YZ Plane (C) XY Plane (D) XZ Plane. 185

6.32 Reliability Function Of Stall Margin For NASA Rotor 67 Having Different Arrangements Of Blades With Differing Tip Gaps At 100% Speed 186

Chapter 1

Introduction

1.1 Background

"Uncertainty is an uncomfortable position. But certainty is an absurd one"

The above quote by French philosopher Voltaire aptly summarises the realm of uncertainty quantification. None of the real world systems are devoid of uncertainties in the parameters that define it. A decade back, the design process of an aircraft engine required 90% of experimental rig tests and 10% of computational fluid dynamics. Today, with ever increasing robustness of computational fluid dynamics (CFD) algorithms and widespread availability of high performance computing (HPC) facilities, these numbers are almost inverted (Montomoli et al., 2015). In a turbo-machinery environment, the uncertainties may arise due to varying atmospheric conditions, eccentrically assembled rotors, casing ovalation, manufacturing tolerance, etc. While performing a CFD simulation, the chief sources of uncertainty would be the numerical (turbulence) modelling, accurate 3D representation of the blade geometry and boundary conditions (discussed in detail in chapter 2). Given the omnipresence of uncertainty in experimental tests as well as numerical simulation (Mehta et al., 2016), it becomes crucial to evaluate the propagation of uncertainty through the system. These uncertainties can wreak havoc if not properly quantified. According to Oberkamph and Trucano (2002), the

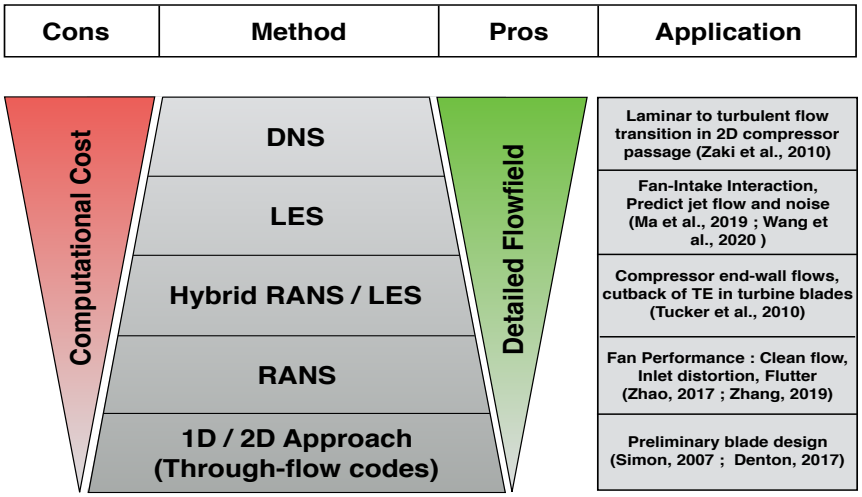


Figure 1.1: Application Of Different Numerical Methods In Turbo-machinery

uncertainties can be classified as either aleatory uncertainty (inherent randomness, irreducible uncertainty) or epistemic uncertainty (lack of knowledge, reducible uncertainty).

In any CFD simulation, the fidelity of the numerical model, its computational cost along with its ability to resolve flow field accurately are of prime concern. Figure 1.1 shows the computational cost for the different numerical methods along with its ability to give detailed flowfield. The red colour and the green colour signify the undesirable and the desirable features of the numerical method respectively. As colour gradient changes from lighter shade to darker shade, the value of the said feature increases. While the Direct Numerical Simulation (DNS) is known to give a very detailed information of the flow-field down to the Kolmogorov scale, it imposes severe penalty with regard to the computation cost. Hence its use is limited to only low Reynolds number components such as low pressure turbines (Tucker, 2014). In comparison, a transonic compressor like NASA Rotor 67 operates typically at a Reynolds number of 1.17×10^6 (Choi et al., 2010). Recently, Zaki et al. (2010) used DNS to study the laminar to turbulent flow transition in the passage of compressor cascade at a Reynolds number of 138,500 and grid size of 84 million. DNS is therefore not feasible for performing a study related to uncertainty quantification (UQ) that mandates large number of simulations to be carried out.

Methods like Large Eddy Simulation (LES), though not as cost prohibitive as DNS, also use very fine mesh. It resolves the larger turbulent scales up to the available grid size and models the

extremely small eddies (Tucker, 2014). Gourdain (2015) calculated the simulation cost ratio between Unsteady Reynolds Averaged Navier-Stokes (URANS) and LES to be 500. Tucker (2014) notes that a good match between LES and experiment was obtained by Tyacke et al. (2012) when studying the labyrinth seals. Recently, Ma et al. (2019) compared LES with Reynolds Averaged Navier-Stokes (RANS) in the study of fan-intake interaction and found that the discrepancy between the RANS and LES is the least when the fan is located closest to the distortion generator. In such cases, only marginal improvement to the accuracy of predictions is possible. In spite of the potential benefits of LES, its success in predicting the compressor performance curve has not been been satisfactory due to its sensitivity to the boundary conditions (discussed in detail in the next chapter).

There are wide range of hybrid RANS-LES techniques with some closer to RANS and others to LES. Tucker (2014) notes that some of these techniques restrict RANS to the near wall zone while few others allow RANS and LES to appear anywhere in the domain depending on the generated grid. In such cases, complex RANS-LES interfaces are generated wherein the RANS layer next to the wall contains high eddy viscosity while the LES layers away from the wall have lesser eddy viscosity. However, there is insufficient opportunity for the scales to develop when transitioning from RANS to LES and this often gives rise to a kink in the velocity profile. The interface between RANS and LES called as "grey area", thus requires very specialised treatment. Notwithstanding the complicated modelling techniques, these methods have found applications in predicting the turbine and compressor endwall flows, jet flows, flow around a fan blade section and a cutback trailing edge (Tucker et al., 2012). Recently, Wang and Yuan (2013) used hybrid RANS-LES to predict compressor corner separation over a range of incidences. However, the prohibitive computational cost of hybrid RANS-LES method makes it an unattractive proposition from a UQ perspective.

On the other hand, simpler methods like through-flow codes used for preliminary design of compressor blades (Cumpsty, 2004) are grossly inadequate to predict the effect of blade-to-blade variation found in the annulus of the compressor. Thus a balance between the fidelity of numerical method and its associated computational cost and accuracy has to be established. The present research aims to maximise the performance and stability boundaries of a compressor

in the face of manufacturing tolerance and/or in-service degradation. RANS simulation has been used by previous researchers (Jennions and Turner, 1993; Choi et al., 2010; Fidalgo et al., 2012; Lee et al., 2018) to predict the performance and stability boundaries of a compressor with a high degree of accuracy. Though RANS simulation presents a good trade-off between computational cost and modelling accuracy, it is infeasible to club it along with Monte Carlo Methods (MCM) due to the colossal number of simulations associated with it. This handicap was overcome by employing a surrogate model (also called as meta-model) that was developed using the data from fewer deterministic RANS simulation. Such surrogate models offer a quick turnaround time and can be easily integrated with MCM (Montomoli et al., 2015). The use of surrogate model in conjunction with MCM aided the study of UQ in the present thesis.

1.2 Motivation

"What we observe is not nature itself, but nature exposed to our method of questioning."

The above quote by German scientist Werner Karl Heisenberg captures the limitations of knowledge and power of imagination. The limitation of our imagination often contributes towards a lack of knowledge; which in turn increases the epistemic uncertainty of the system. Many a time, the researchers simplify the problem at hand by assuming the various uncertain parameters to be independent and identically distributed (i.i.d.) random variable. In a real world system, the parameters need not be identically distributed random variables.

Montomoli et al. (2015) succinctly describes the various research carried out in the last three decades pertaining to the field of uncertainty quantification (UQ) in an aircraft engine. The common thread binding most of this research was the absence of study of combinatorial optimisation. These studies raised a few open ended questions :

- Is there an optimal arrangement for a given set of blades with differing dimensions?
- How significant is the variation in performance and stability for different arrangements?
- How to perform uncertainty quantification of such systems?

Few researchers (Roberts et al., 2002; Zheng et al., 2017; Taylor et al., 2019) have pondered over some of these questions in parts and at times with mixed opinions. This thesis attempts to answer the above questions while maintaining a balance between basic and applied research.

The first challenge that the author faced in the present research was the sheer number of possible configurations. For a fan/compressor with N blades of differing dimensions around its annulus, a total of $(N\text{-}1)!$ unique arrangements are possible. To complicate the matters, each of those N blades are a random variable which are coupled to each other ($i.e.$ the principle of superposition cannot be applied). The application of readily available UQ tools like PCE would have suffered from the problem of "the curse of dimensionality." This implied that a new tool tailor-made for the problem at hand needed to be developed. The second main challenge that the author faced was the credibility and generality of this new UQ tool vis-a-vis the results from RANS simulation. The successful solving of all the above stated problems would culminate in reducing the epistemic uncertainty. Roberts et al. (2013) have shown that an increase of about 0.5% efficiency across fan and compressor can result in fuel savings worth tens of thousands of pounds per engine per year. It would thus also help the engine manufacturers to eke out maximum possible performance while indirectly reducing the carbon footprint.

1.3 Research Objectives

According to John Tukey, an approximate solution of an accurate problem is often far more consequential than an accurate solution of an approximate problem. This thesis deals with the effect of geometric uncertainty in flow past compressor blades. The author has thus desisted from making too many simplifying approximation and has tried to retain the original flavour of the problem. The objectives of the present research are as follows :

(1) Conduct a scalability test of AU3D and mesh convergence test of different test cases to arrive at optimal number of grid points per CPU. Validate the CFD results from NASA Rotor 67 at 100% speed (design speed) against the available experimental data in open literature.

(2) Conduct a series of single passage and double passage simulations (details in chapter 3) for

various manufacturing tolerance to see if any flow physics could be understood and correlations could be obtained at design speed.

(3) Create a random set of NASA rotor 67 blades with differing dimensions within the range of manufacturing tolerance. Based on the flow physics and correlations obtained in the step (1), hypothesise the best configuration and worst configuration for the set of blades with differing dimensions and use CFD to validate it. Use the travelling salesman problem (TSP) analogy to see if these results stack up against those obtained using CFD.

(4) Check if the hypothesis in step (3) is valid at part-speed conditions. For this, NASA Rotor 67 is tested at 80% speed (off-speed condition) and the results are compared with design speed condition. Also check if the hypothesis in step (3) is valid for other blade geometries. In this regard, a low speed, wide-chord blade was created which is representative of the fans used in modern civil aircraft engines.

(5) A study of in-service degradation was conducted on a 1-stage compressor used in a typical high performance industrial gas turbine engine. A set of blades that undergoes different leading edge damage was created as a representative of in-service degradation. Different leading edge damages *i.e.* radial damage and chord-wise damage are considered. It was determined which among these two damages are more crucial. Check whether circumferential redistribution of the random damaged blades can improve the performance and stability boundaries in a compressor.

(6) Develop a surrogate model (meta-model) from the few deterministic RANS data. Check the credibility and generality of the new surrogate model vis-a-vis RANS simulation. Apply, Monte Carlo Method (MCM) on the surrogate model to perform UQ analysis. Investigate the effect of input parameter uncertainty on the estimation of output parameter.

1.4 Dissertation Overview

Chapter 2 presents a detailed literature review of the geometric uncertainties found in axial compressors along with a brief philosophical debate about classification of different uncertainties.

The chapter then details about various tools used in UQ viz. Monte Carlo method, Polynomial Chaos Expansion, Response Surface method and Active Subspace method before proceeding to discuss the limitations in CFD and experimental study. The chapter finally concludes with a discussion on the subject of combinatorial optimisation and its application.

Chapter 3 provides a brief description about the methodology used in the thesis for computing compressor stability and performance. It discusses about the aerodynamic model used in the CFD solver AU3D, boundary conditions and the different test cases that have been considered. It then describes the scalability test and the mesh independence study used to arrive at optimal number of grid points per CPU. The chapter finally concludes with a brief discussion on the open source Genetic Algorithm based Travelling Salesman Problem (GA-TSP) code used in this thesis.

Chapter 4 discusses about the impact of manufacturing tolerance on a compressor of an aero-engine. The chapter starts with an introduction to the subject of metrology and quality control. Various concepts related to tolerances, tolerance stack-up, Go-No Go gauges and selective assembly have been introduced in this section. The effect of stagger angle and tip gap on the performance and stability boundary has then been discussed. NASA Rotor 67 and (low speed) wide-chord blade rotor have been considered as test cases. A heuristic method of rearranging the compressor blades with random dimensions has been compared vis-a-vis GA-TSP. The chapter ends with a discussion on two parameter problem of simultaneous variation of stagger angle and tip gap.

Chapter 5 starts with a detailed background to the different causes of blade damage in the compressor of a gas turbine (both industrial gas turbine as well aero-engines). The problem of icing, ingestion of sand and ash has been discussed at length along with its cost to the industry. The chapter then delves into acceptable limits of damage on the blade using Federal Aviation Administration (FAA) regulations and data from Merlin compressor. A study on the effect of different leading edge damages (radial damage and chord-wise damage) on the performance and stability boundaries of the blades has been conducted. Furthermore, the chapter discusses the effect of blades suffering random leading edge damage throughout the

annulus and how re-arranging these damaged blades can positively impact the performance and stability boundaries in a compressor. Throughout this study, a 1-stage IGT developed with support from Mitsubishi Hitachi Power Systems (MHPS) Limited has been used as a test case. Finally, the chapter underlines the limitations of this study and discusses new emerging technology that can help alleviate some of these problems.

Chapter 6 touches upon the development of surrogate model (also called meta-model). Various assumptions in the model development were listed down and using the first principles a novel double interpolation based surrogate model was developed. The results from the surrogate model were validated against the deterministic RANS simulation for different speeds and compressors. After establishing the generality of the model, a MCM was used in conjunction with it thus paving the way for UQ analysis.

Chapter 7 is the last chapter that lists all conclusion in this research work along with a brief discussion on possible future work.

1.5 Key Achievements

The key achievements of this thesis can be summarised as follows :

- Helps in better understanding of the behaviour of different geometric uncertainties.
- Suggests an optimal arrangement of blades with differing dimensions based on CFD simulations and TSP analogy for single parameter variation as well as two parameter variation.
- Novel surrogate model has been developed which helps perform uncertainty quantification analysis for 50,000 samples of virtual compressor.
- This research would help reduce scrapped blades for an original equipment manufacturer.
- By eking out maximum performance, this research has shown potential to save fuel worth billions of pounds per year to the aircraft industry.

1.6 Publications

(1.) S. Venkatesh, Q. Rendu, M. Vahdati and L. Salles, "Effect Of Manufacturing Tolerance In Flow Past A Compressor Blade", Proceeding of 13^{th} European Conference on Turbomachinery Fluid Dynamics and Thermodynamics, Lausanne, Switzerland, 2019, Paper Number : ETC2019-178.

(2.) S. Venkatesh, Q. Rendu, M. Vahdati and L. Salles, "Effect Of Manufacturing Tolerance In Flow Past A Compressor Blade" (extended work), Journal of Turbomachinery, Article Number : TURBO-19-1105, `https://doi.org/10.1115/1.4052600`.

(3.) S. Venkatesh, K. Suzuki, M. Vahdati, L. Salles and Q. Rendu, "Effect Of Geometric Uncertainty On A One Stage Transonic Compressor Of An Industrial Gas Turbine", Proceedings of ASME Turbo Expo 2020, London, UK, 2020, Paper Number : GT2020-16315.

(4.) S. Venkatesh, Q. Rendu, M. Vahdati and L. Salles, "Development Of A Novel Interpolation Method For Predicting The Compressor Performance Due To Manufacturing Tolerance", Manuscript to be submitted.

Chapter 2

Literature Survey

2.1 The Need For Uncertainty Quantification

"What Preceded The Instant In Which The Challenger Was Lost" (New York Times, 1986)

"With New Equipment, Hubble's Eye Gets A New Lease On Life" (New York Times, 1993)

"Ariane 5 Rocket Explodes Seconds Into Maiden Flight" (Wall Street Journal, 1996)

"INSAT-4C Launch Ends In Watery Grave" (The Times Of India, 2006)

An anonymous quote that neatly sums up the above list of disasters is : "It ain't what you don't know that gets you into trouble. It's what you know for sure that just ain't so." A look at the reasons of the above mentioned disasters would assert the importance of UQ.

In case of Space Shuttle Challenger (1986), it was discovered by NASA that the O-ring seal in solid rocket boosters were not designed to operate at low temperatures, and the morning of the Challenger launch was unusually cold. This led to the failure of O-ring seal at launch and hence the explosion of the Space Shuttle (Rogers et al., 1986). In 1990, the scientists at NASA were distraught to see the relay of fuzzy images by Hubble telescope[1]. It was ascertained that the outer edge of the mirror was ground too flat by a depth of 2.2 micron. New instruments

[1] `https://asd.gsfc.nasa.gov/archive/hubble/missions/sm1.html`

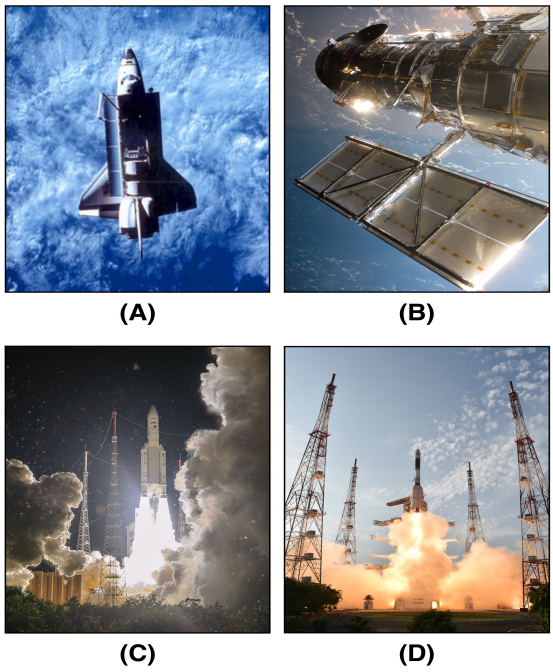


Figure 2.1: Images of (A) Space Shuttle Challenger (Credits : NASA) (B) Hubble Space Telescope (Credits : NASA) (C) Launch of Ariane 5 (Copyrights : ESA/CNES/Arianespace) (D) Launch of GSLV-F05 (Copyrights : ISRO, Reproduced With Kind Permission From ISRO)

had to be installed in 1993 to correct the flaw in Hubble's primary mirror which cost a lot of money in terms of space launch.

The ARIANE 5 disaster (1996) was attributed to the incorrect conversion of sideways velocity of rocket by Inertial Reference System (SRI) which triggered the nozzles of the engine and rocket booster to suddenly swing out of position and initiate a self-destruct mechanism. The SRI used in ARIANE 5 was exactly the same as the one used in the slower moving ARIANE 4 which caused the wrong conversion of velocity from a 64-bit "floating point" format to 16-bit "signed integer" format (Lions et al., 1996). In 2006, India's Geosynchronous Satellite Launch Vehicle (GSLV-F02) carrying the satellite INSAT-4C veered sharply off course and came crashing down into the Bay of Bengal. The failure analysis committee [2] concluded that a probable manufacturing error in one of the strap-on stages (S4) led to a sudden loss of thrust and subsequent loss in control capability.

The uncertainties, if not accounted for, have the capability to destroy the system which can lead to precious loss of time, money and human capital. The uncertainties in any parameter

[2] https://www.isro.gov.in/update/06-sep-2006/gslv-f02-failure-analysis-committee-report

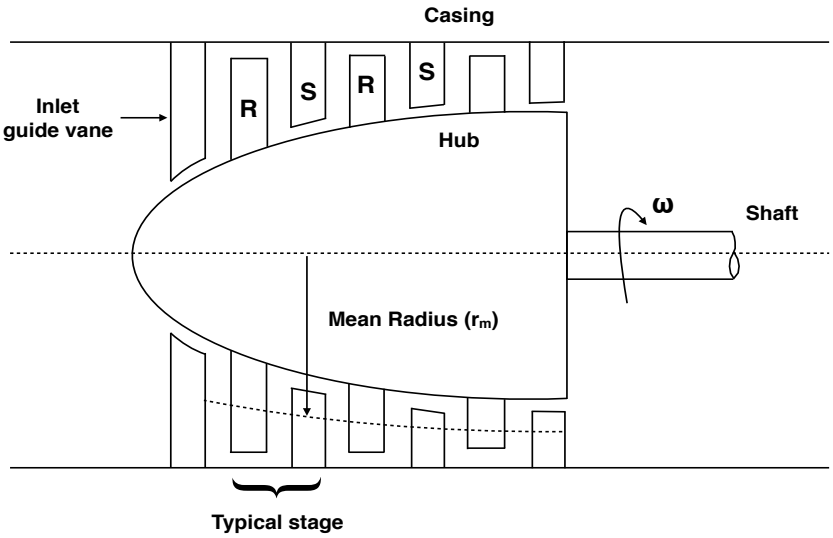


Figure 2.2: Schematic Of An Axial Compressor (Hill and Peterson, 1992)

that define a system can arise due to manufacturing tolerance, change in climate, limitations of measuring instruments, etc. Umpteen examples of parametric uncertainty affecting the flutter boundary in a two-dimensional airfoil can be found in literature (Poirel and Price, 2007; Desai and Sarkar, 2010; Venkatesh et al., 2014). This can be extended to three-dimensional aircraft wings and wind turbine blades by using strip theory and 3D corrections (Opgenoord, 2018). Utmost care must be taken while identifying and quantifying the uncertainties as it has the potential to revolutionise the present day design and certification criteria. The working of an axial compressor along with the different uncertainties affecting it will be discussed in subsequent sections.

2.2 Working Of An Axial Compressor

Though there are a few commonalities between aircraft wings and blades in an axial compressor, any attempt to take over successful concepts from aeronautics into compressor design are not useful (Cumpsty, 2004). A simplified view of an axial compressor is shown as a schematic in fig. 2.2. As can be seen, rows of rotor blades (R), rotating with the shaft at an angular velocity of ω, are each followed by rows of stator blades (S). One rotor blade row along with

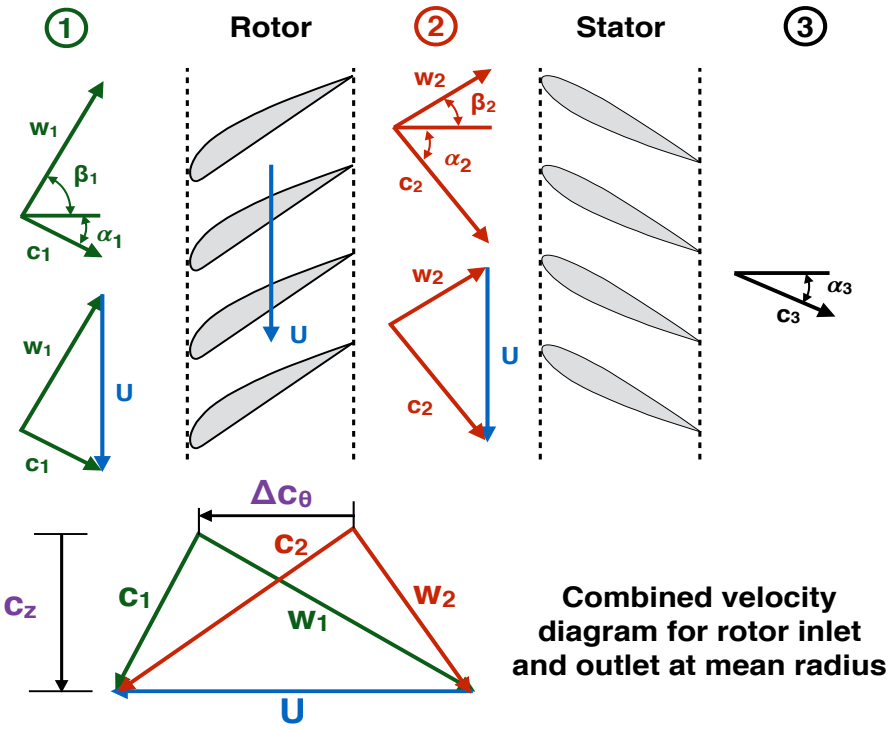


Figure 2.3: Velocity Triangle At Mean Radius Of A Compressor Stage (Hill and Peterson, 1992)

the succeeding stator blade row make up a stage of the compressor. Some compressors have stationary blades at the inlet known as inlet guide vane.

As given in Hill and Peterson (1992), there are two frames of reference in turbomachinery viz. absolute reference frame and relative reference frame. The absolute reference frame is fixed to the frame of the machine and the fluid velocities observed to this frame of reference is denoted by **c** (called as absolute velocities). The relative reference frame, on the other hand, rotates with the rotor (R) of a machine and the fluid velocities observed to this frame of reference is denoted by **w** (called as relative velocities). The vector difference between absolute velocity (**c**) and relative velocity (**w**) is simply the local blade velocity (denoted by **U**).

Fig. 2.3 shows the velocity triangle of an axial compressor stage at mean radius ($\mathbf{r_m}$) wherein station (1) is rotor inlet, station (2) is rotor outlet/stator inlet and station (3) is stator outlet. At mean radius ($\mathbf{r_m}$), the local blade velocity (**U**) is given by $\mathbf{r_m}\ \omega$ where ω is angular velocity of the shaft. From fig. 2.3, it can be seen that the rotor imparts angular momentum to the air as the component of the absolute velocity in the tangential direction (Δc_θ) increases. The rise of Δc_θ and the blade speed **U** are responsible for the pressure rise in a stage of a compressor

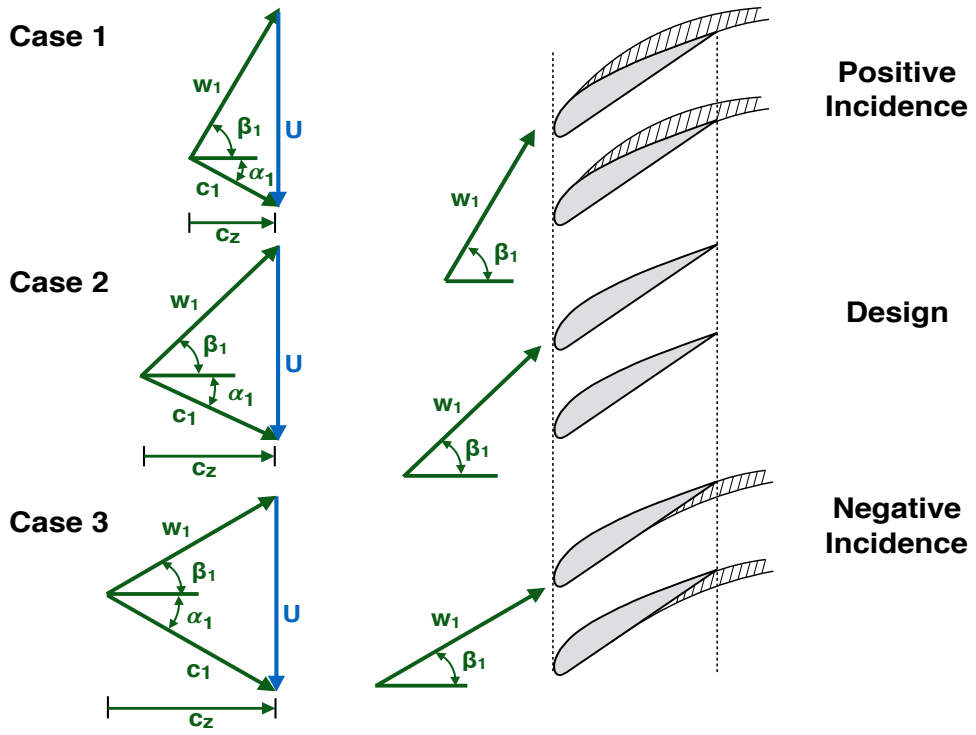


Figure 2.4: Design And Stalling Condition For An Axial Compressor (Hill and Peterson, 1992)

(Hill and Peterson, 1992). As the radius at hub and tip changes, the magnitude and direction (β_1) of relative velocity ($\mathbf{w_1}$) changes. Hence, the fans and compressors have a 3-dimensional twisted shape from hub to tip. The relative inlet flow velocity is supersonic over the entire span in case of a supersonic compressor. According to Cumpsty (2004), the early supersonic compressors used the blade profiles like the double circular arc (DCA) which were suitable for subsonic conditions. However as the time progressed, the blades were modified such that the inlet part of the blade became flatter, camber moved rearwards and thickness became smaller Cumpsty (2004). For a transonic compressor with subsonic velocity at the hub and supersonic velocity at the tip, it is common to see the gradual thinning of airfoil section from hub to tip.

As the operation of an axial compressor departs from the design flow rate, the axial velocity component ($\mathbf{c_z}$) is affected. An axial compressor operating at a different shaft speed will affect the blade speed ($\mathbf{U}$). Any change in $\mathbf{c_z}$ and/or $\mathbf{U}$ will affect the angle β_1 (which is uniquely determined by the value of $\frac{\mathbf{c_z}}{\mathbf{U}}$) at which the flow approaches rotor. As seen in fig. 2.4, a boundary layer separation can be observed for sufficiently large departure from the design point (Hill and Peterson, 1992). Such a flow separation, results in increased viscous mixing loss and hence the efficiency drops below the design value (Hill and Peterson, 1992). The most widely used

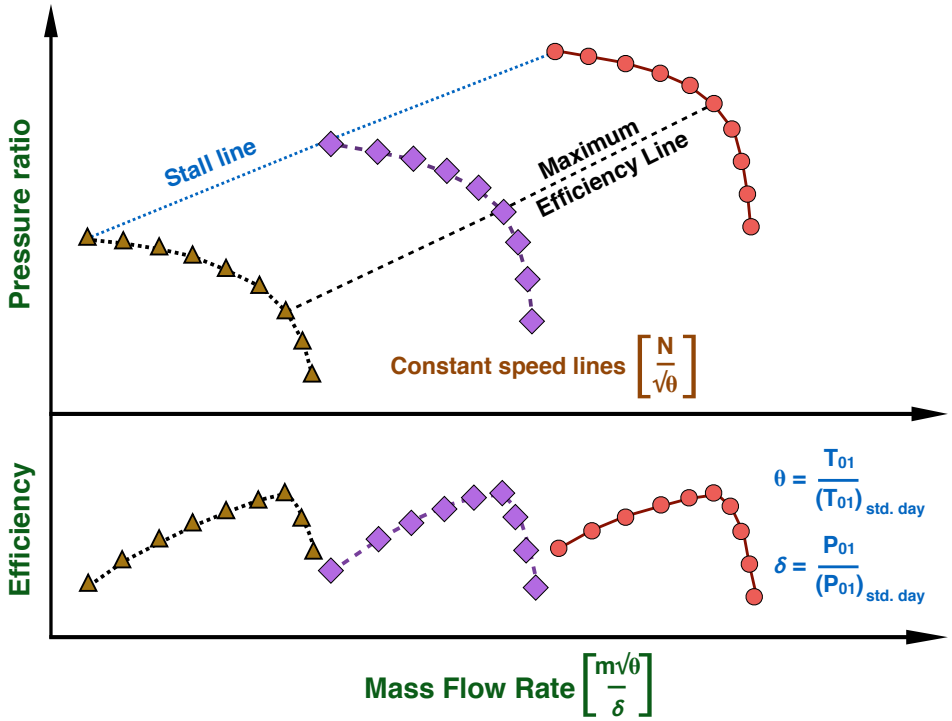


Figure 2.5: Schematic Of A Compressor Operating Map

way to visualise the operation of a compressor is by using "operating map" (Dodds, 2016).

As shown in fig. 2.5, the compressor operating map (also called as characteristic curve) is a graph depicting the pressure ratio and isentropic efficiency against the mass flow rate at different speeds. The mass flow rate and speeds are independent of inlet conditions such that they are valid both at sea-level and altitudes (Dodds, 2016) using the tool of dimensional analysis (Hill and Peterson, 1992). A compressor rig testing setup consisting of a motor (to accurately control the rotational speed of compressor) and a variable area exit nozzle (choked under normal operation) enable the engineers to obtain operating map (Dodds, 2016). A stall line (line connecting the loci of stall points at different speeds) is obtained by gradual closure of variable area nozzle at each speed.

The uncertainties in an axial compressor affect the stability limits (stalling mass flow rate), pressure ratio and efficiency. Zheng and Yang (2016) discuss the influence of tip clearance on performance and matching of multistage axial compressors. It was observed that the front stage tends to work near surge condition while the rear stage tends to work near choke condition as the tip clearance increases resulting in a lower efficiency compared to middle stages. The efficiency

of the whole compressor decreases in parabolic manner and not linearly as previously suggested. The other effects of increased tip clearance are reduced peak pressure ratio and reduced mass flow rate. It thus becomes extremely crucial to identify various sources of uncertainties as its effect can amplify in a multistage axial compressor. The next sections would introduce a brief literature survey on different uncertainties in an axial compressor, the classification of uncertainties and the tools used in uncertainty quantification. This would be followed by limitations of CFD simulations as well as experiments and finally a brief review of combinatorial optimisation and its applications. Due to the novel nature of the present research topic, an effort has been made to cover all the relevant subjects in a comprehensive yet concise manner.

2.3 Geometric Uncertainties In Axial Compressors

The uncertainties in a compressor of a gas turbine engine can occur due to eccentrically mounted rotors giving rise to non-uniform tip gaps, ovalised casing, manufacturing tolerance and in-service degradation. Fig. 2.6 shows a schematic of the various types of uncertainties that maybe encountered in a compressor blade. The uncertainties though different in origin, can sometimes have same effect *e.g.* the leading edge manufacturing tolerance and leading edge erosion damage can be studied together. Similarly, the non-uniform circumferential tip gap which can occur due to differing compressor blade length, whirling rotor, bowed rotor, ovalised casing and eccentrically mounted rotor can be studied together as a single parameter. Some part of the literature survey in this section has been borrowed from Montomoli et al. (2015). The following uncertainties have been considered in case of axial compressor :

2.3.1 Effect Of Tip Gap

The flow-field in the tip region of axial flow compressors has been an active area of research for many decades as it is highly three dimensional and often comprises of tip-leakage vortex, blade boundary layers and shock waves (Thompson et al., 1998). There is a general agreement that larger tip clearances creates large pockets of low energy fluid and this in turn alters the main

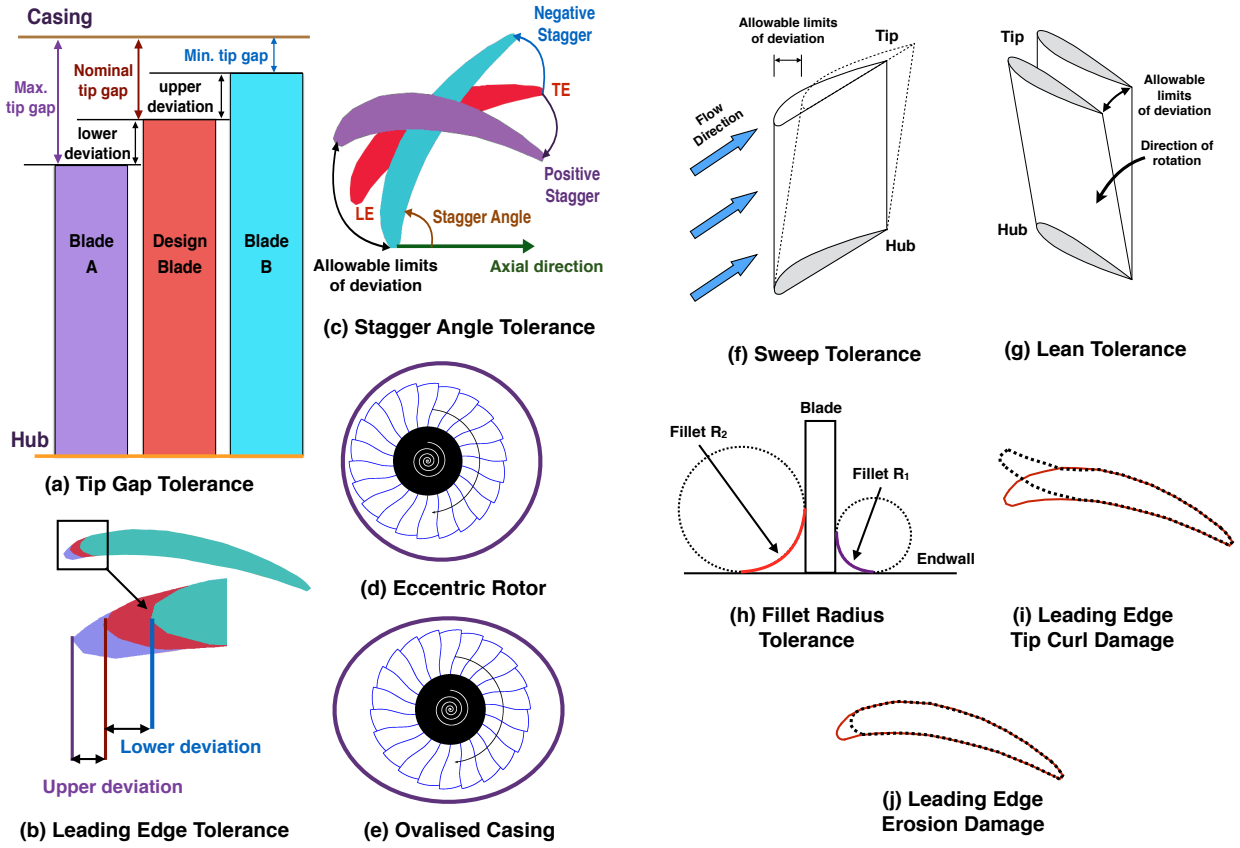


Figure 2.6: Schematic Of Uncertainties In A Compressor Blade

flow. This leads to flow separation and hence stalling of the blade (Suder and Celestina, 1996; Thompson et al., 1998; Beheshti et al., 2004).

The value of an optimum tip gap in a transonic rotor is a subject of dispute in the literature. Thompson et al. (1998) note that in this regard, contradictory results that have been presented in the open literature. Copenhaver et al. (1996) studied the effect of tip clearance on swept transonic rotor both experimentally and computationally for four different tip clearance levels: zero, 0.27, 1.0 and 1.87 percent of tip clearance to tip blade chord ratio and has indicated that the optimum tip clearance is zero. He reasoned that for maximum efficiency and stall margin, the tip gap should be as small as possible (preferably zero). Moore (1982) also studied the effect of tip clearance experimentally at four different tip gaps from 0.5% span (0.61 mm) to 1.5% span (1.78 mm). It was observed that with increasing clearance, the overall performance and stability margin of both the rotor and the stage decreased. He concluded that the optimal tip gap for transonic compressors should be as small as possible (preferably equal to zero).

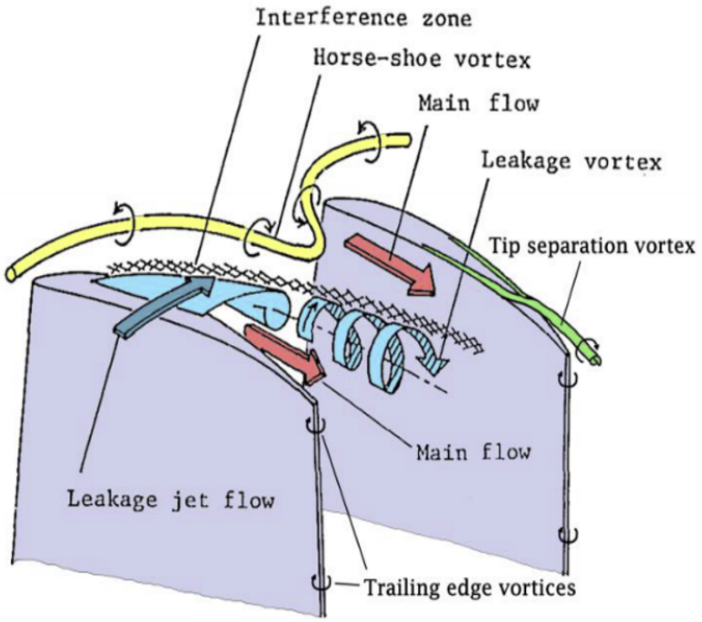


Figure 2.7: Schematic Of Tip Leakage Flow - Adapted From Inoue and Kuroumaru (1989). [Reproduced With Kind Permission From ASME]

On the other hand, Wennerstrom (1984) tentatively concludes from his experimental study about the existence of a non-zero optimal tip gap. He studied the effect of tip gap at three different level of 0.324%, 0.524% and 0.724% of span. Thompson et al. (1998) and Cumpsty (2004) note that Freeman (1985) also was of the opinion that a non zero tip clearance would give best possible performance in case of transonic axial compressors. The difference in the results between different authors could possibly be rotor specific. It was found that the fan tip clearances could also increase by almost 65% because of sand erosion (Ghenaiet et al., 2005).

Graf et al. (1998) conducted an experimental study on non-axisymmetric tip gaps using a low speed compressor. The circumferential tip gaps were changed by radially moving the casing using the shims. It was found that for the same average tip gap, the compressor performance and stability margin decreases with an increase in eccentricity. Furthermore, a two-lobed asymmetry had better performance and stability margin than one-lobed asymmetry.

In case of an industrial gas turbine, the rotor tip gap can be less than 0.5% span on the front stages and more than 5% span at the rear stages (Sakulkaew et al., 2013). For 0.5% to 0.8% span, the change in efficiency is driven by two competing mechanisms : reduced tip leakage mixing loss and increased viscous shear loss as the size of the tip gap reduces. For medium tip

gaps from 0.8% to 3.4% span, the main effect is due to tip leakage mixing loss. In this zone, the efficiency decreases linearly with increase in tip gap size. For rotors with tip gaps beyond the threshold value of 3.4% span, the efficiency is less sensitive to tip gap variation. In such cases, the blade tip is more aft loaded thus reducing the tip flow mixing loss. Fig. 2.7 shows the schematic of tip leakage flow adapted from Inoue and Kuroumaru (1989). As can be seen, the tip leakage flow rolls up into a vortex after interacting with the main flow.

2.3.2 Effect Of Leading Edge

The compressor performance deteriorates due to ingestion of foreign objects which ends up modifying the aerodynamic shape of the blade. Of the various possible foreign object ingestion cases, the impact of the sand ingestion on the blade performance is considered to be very important. This aspect is especially crucial when aircraft operate at places in close proximity to deserts. An experimental study in this regard was done by Balan and Tabakoff (1984) wherein they observed that the sand ingestion resulted in an erosion in the leading edge along with higher roughness (due to pitting erosion) on pressure side. Ghenaiet et al. (2005) observed a reduction of the tip chord by 10% as a result of sand ingestion. Klinner et al. (2014) observed that the leading edge degradation in transonic fans changes the designed shock structures at the leading edge. As a result, there was an overall loss of stage loading by 3.5% followed by a loss of 4% for the overall stage efficiency.

The damage produced can typically vary both radially and in chordwise direction. In fact, the compressor blades of TV3-117 turboshaft suffer from chord length and airfoil thickness reduction above 66% span when operating in extreme desert terrains of Algeria (Dvirnyk et al., 2019). During the engine overhaul, such damaged blades are typically boroblended as well as re-contoured to restore blade performance (Roberts et al., 2002; Taylor et al., 2019). In fact, new airfoils are sometimes mixed with reused parts resulting in wide variety of airfoil geometries within an engine after operation Marx et al. (2014). The maximum chord damage that can be acceptable in a civil aviation turbofan engine is between 4-6% of the nominal chord (Roberts et al., 2002). The foreign object ingestion could also result in a tip curl damage of the

leading edge. As the degree of damage on a single blade increases, the number of stall cells also increase (Li and Sayma, 2015). In case of multiple damaged blades, a large stationary stalled region covering a quarter of annulus along with three other small stall cells rotating around the annulus were also observed.

In spite of the small leading edge radius of the order of 0.1 mm radius (about 0.2% - 0.5% of chord), the geometrical variations of the compressor leading edge can have a strong impact on the single stage as well as on the whole compressor performance (Elmstrom et al., 2011). Montomoli et al. (2015) mention that the boundary layer on the suction side thickens and promotes 3D separation due to small variation in leading edge shape. This effect was shown by comparing two geometries: a circular arc and an elliptic shape of leading edge. It was seen that the flow remained attached and laminar when an elliptic shape leading edge was used. However for circular arc, which is more widely used in aero engines, the flow separation and reattachment was observed which resulted in an increment of profile losses by 30%. In case of transonic compressors, the microscopic variation of leading edge has the potential to modify the suction surface losses by almost 38% with elliptic shape being more efficient.

Another cause of having a distorted leading edge can be a result of the coating on the blades (Elmstrom et al., 2011). While there is evidence that coated compressors can outperform uncoated ones in certain applications, there are situations where this may not be the case (Montomoli et al., 2015). A coated compressor for a naval application was tested by Caguiat (2003). It was observed that there was a loss in maximum power output and an increase in specific fuel consumption (SFC).

2.3.3 Effect Of Stagger Angle

As seen in fig. 2.6, the stagger angle is the angle between the chord-line and the axis of compressor. Stratford and Newby (1977) observed that the stagger variation controls the relative swallowing capacity of each passage between the blades and this in turn determines shock detachment distance at the leading edge. The strength of the shock upstream is determined by

the shock detachment distance. The effect of stagger angle variability resulted in the generation of buzz saw noise.

Wilson et al. (2006) have carried out a study on the effect of static stagger variability on the dynamic untwist behaviour of fan assemblies. The dynamic untwist of a fan assembly is caused due to substantial aerodynamic and centrifugal force. The dynamic untwist, as opposed to cold geometry, determines the actual aerodynamic performance, vibratory response and noise generation. Two cases were considered wherein a solitary blade with a mis-stagger of $\pm 0.2^{\circ}$ was used in an otherwise uniformly staggered fan assembly. Near the choke and stall conditions, the solitary mis-staggered blade predominantly affected the untwist behaviour of the mis-staggered blade itself. Near the maximum efficiency condition, every blade in the assembly was affected by lone mis-staggered blade. A zigzag pattern of circumferential distribution of stagger angle was seen in the compressor assembly. This caused a drastic drop of isentropic efficiency near the maximum efficiency region. Similar conclusion was drawn for when all the compressor blades were randomly mis-staggered. This behaviour is commonly known as Alternating Passage Divergence (APD). Lu (2020) recently furthered the work in this area by suggesting active and passive methods for attenuating the APD phenomenon. Active attenuation involved redesigning of the blade such that it modified the passage geometry while passive attenuation involved using machine learning techniques to identify APD causing mis-stagger pattern *a priori* which could be later modified to avoid APD.

Sladojevic et al. (2007) studied the influence of stagger angle variability using only a small layer at two thirds of the blade span instead of a full 3D blade. This study states the allowable manufacturing tolerance on the stagger angle of the blade to be 0.5°. Three cases of small and large mis-staggering are considered viz. one blade mis-staggered (single blade rotated by 0.2° for small mis-staggering and by 1.7° for large mis-staggering), alternate mis-staggering (every other blade rotated by 0.2° for small mis-staggering and by 1.7° for large mis-staggering) and random mis-staggering (all the blades vary up to $\pm 0.5^{\circ}$ for small mis-staggering and $\pm 2^{\circ}$ for large mis-staggering). It was observed that small mis-staggering did not affect the stability of the system and also did not produce significant shock movement. On the other hand, large mis-staggering caused visible shock movement that can compromise the stability of system.

Ramakrishna and Govardhan (2010) studied the effect of stagger angle variation on forward swept rotors. They have used the following stagger angles variation viz. 0°, 3° and 5°. A general observation in this study was the reduction of losses as the stagger angle increased. Khalid et al. (1999) considered the variation of stagger angle to be ±15° and observed a reduced blockage for an increase in stagger angle. Yoon et al. (2006) studied the effect of stagger angle on tip vortex in axial compressors. Two blades of different stagger angles were considered viz. nominal blade and an increase of 5° from the nominal blade. It was observed that an increase in the stagger angle weakens the tip leakage vortex.

It is important to note that the sign convention of the negative and positive stagger angle used in all the above work is opposite to what has been shown in fig. 2.6. The author feels the present sign convention is more intuitive as a positive stagger angle results in an increase in the incidence angle.

2.3.4 Effect Of Lean, Sweep And Fillet Radius

Denton (2002) studied the effect of lean and sweep on transonic fan performance. Backswept rotor was produced by moving the 25% span section forwards by 1% of its chord, the 50% span section forwards by 3% its chord, the 75% span section backwards by 20% of its true chord and the tip section backwards by 75% of its chord. Forward swept rotor was produced by changing the signs of above blade movement. The leaned rotors were produced by moving the blade sections perpendicular to the local chord lines by the same amount as described above for sweep. To the naked eye, these values don't represent manufacturing tolerance instead they are design changes implemented in the rotor. The main conclusion of this study was that blade sweep has little effect on shock structures near casing though lower down the span there is significant shock sweep and hence decreased shock loss. This however came at the expense of stall margin. Overall, very little change in efficiency was produced by blade sweep or lean though forward lean produces a small increase in mass flow.

Bergner et al. (2005) have studied the effect of sweep in transonic axial compressor. This study indicated that forward swept rotor has beneficial effect on performance and stall margin. Hah

et al. (1998) were of the opinion that forward swept rotor exhibited a higher peak efficiency along with a larger stall margin than the baseline unswept rotor. The aft swept rotor had a same peak efficiency as the unswept rotor along with a smaller stall margin.

Features like fillet radius are often ignored in the design phase but Curlett (1991) showed that variation of fillet radius can lead to alteration of separation size and losses. It was shown that lowest loss occurred with no fillet while highest loss occurred with the largest fillet tested. Similar observation was made by Jongsik (2016) in case of centrifugal compressor.

2.4 Classifying The Uncertainty : Aleatory or Epistemic?

Oberkamph and Trucano (2002) uses aleatory uncertainty to describe the inherent randomness associated with the physical system. This type of uncertainty usually take values in a known range and are described using a probability distribution. This uncertainty is also sometimes referred as stochastic uncertainty, inherent uncertainty and irreducible uncertainty. On the other hand, an epistemic uncertainty is defined as a potential deficiency in any phase or activity of modelling process that is due to lack of knowledge. The fundamental cause of this uncertainty is the incomplete information. Incomplete information is characterised by vagueness, non-specificity or dissonance. Increasing the knowledge base can reduce the epistemic uncertainty and hence also called as reducible uncertainty.

Kiureghian and Ditlevsen (2009) on the other hand argue that any attempt to make the concepts of two uncertainties unambiguous and indisputable seem to slip through fingers. According to them, the classification of an uncertainty should be the prerogative of the modeller. If the modeller sees a possibility of reducing the uncertainty by gathering more data or by refining model, he will characterise it as epistemic uncertainty else it will be characterised as aleatory uncertainty.

To understand the above statements better, Kiureghian and Ditlevsen (2009) give the following example : when the compressive strength of concrete of an existing building is to gauged, the parameter should be classified as epistemic uncertainty if the concrete samples from the building

can be tested to yield that information. In fact, a measurement uncertainty can be introduced if there are alternate methods of testing like nondestructive testing. This measurement uncertainty in itself should be classified as an epistemic uncertainty. Conversely, the compressive strength of the concrete in a future building should be characterised as aleatory uncertainty if there will be no attempt made in control of the concrete production. Until the completion of the building, no amount of testing would reduce the variability in the compressive strength of concrete in future building. Once the building is realised, the aleatory uncertainty transforms into epistemic uncertainty.

In this thesis, the uncertainties in compressor blade dimensions due to manufacturing tolerance and/or in-service degradation are characterised as aleatory uncertainty since they can be described in terms of probability density function. On the other hand, questions like "Is there an optimal arrangement for the given set of random blades? How can UQ be performed on such systems?" are considered as a source of epistemic uncertainty. This line of thinking is consistent with Oberkamph and Trucano (2002) and Loeven (2010). Hesthaven (2010) notes that an epistemic uncertainty is more problematic as it arises because of an insufficient knowledge of the system and/or lack of data.

2.5 Tools In Uncertainty Quantification

Axial flow compressors play an indispensable role in both heavy industries as well as in turbojet engines. As the mass flow rate through the compressor reduces, the pressure rise increases thus improving the power output. However, beyond a critical value of mass flow rate, the steady design flow is no longer stable and risks pushing the compressor into an unstable region (McCaughan, 1990). This point at which the system behaviour changes is known as bifurcation point.

McCaughan (1990) categorises the different flow regimes observed experimentally in the following way : axisymmetric steady (design flow), non-axisymmetric steady (rotating stall), axisymmetric time dependent (deep surge) and non-axisymmetric time dependent (classical

surge). McCaughan (1990) studied the stability limits of an axial flow compressor using bifurcation analysis through which each of the above flow could be characterised and regions of parameter space were located wherein the flow is stable. Liaw et al. (1991) used two parameter bifurcation analysis and characterised the compressor operation into three major zones: the stalled zone, the pre-stall zone, and the normal (unstalled) zone. Furthermore, different dynamical behaviours were shown to exist within each regime of parameter space. Abed et al. (1993) explained the boundary between surge and rotating stall behaviours using bifurcation analysis without delving into detailed flow analysis.

According to McCaughan (1990), a compressor undergoing steady rotating stall has one or more stall cells rotating about the annulus of compressor at around half rotor speed. As the blades of the compressor go in and out of stalled flow regions, it produces severe vibrations if one of the natural frequencies of blade matches the frequency of rotating stall. Choi et al. (2011) have shown that a single mis-staggered blade (bad blade) can cause an asymmetry in the flow and thus trigger rotating stall. It was also seen that the number of stall cells decreases though their size increases with an increase in the fan speed. Similarly, a compressor undergoing surge experiences oscillation of mass flow along the length of compressor. This can be equally detrimental as the compressor experiences reverse flow during a part of the operation. It is therefore imperative, for a designer to know the uncertainties in the nature of flow that develops once the compressor is pushed into an unstable region, as each flow can have different consequences.

The nonlinear dynamics of fluid instabilities such as rotating stall and surge in an axial compressor are typically modelled as subcritical Hopf bifurcation (Lin et al., 2017). Fig. 2.8 shows a subcritical hopf bifurcation in a typical nonlinear system obtained using numerical simulation (Desai, 2011). As seen in the figure, the stationary solution bifurcates to a higher amplitude limit cycle through point B but the large amplitude limit cycle comes back to the stable stationary solution at turning point A and hence exhibits a hysteresis. The unstable branch connecting points A and B is not possible to be obtained by any numerical method and hence has been named as hypothetical branch.

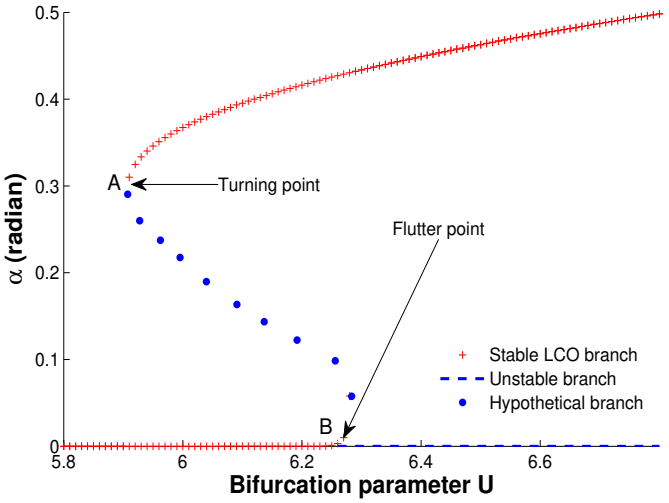


Figure 2.8: Subcritical Hopf Bifurcation As Seen In Desai (2011)

This hysteresis behaviour has also been observed in wind tunnel tests of a large aspect ratio wings (Bunton and Denegi, 2000; Tang and Dowell, 2001). Kartofelev (2020) notes that subcritical Hopf bifurcations are more dangerous and dramatic as the trajectories jump to a distant attractor. The uncertainties can trigger unwanted oscillations of large amplitude prior to the deterministic prediction with catastrophic consequences *e.g.* collapse of Tacoma narrows bridge in 1940 (Kartofelev, 2020). The nonlinear systems are thus very sensitive to parametric uncertainty as they affect the onset of bifurcation point and hence the need for robust uncertainty quantification.

For any model based simulation, the four principal objectives of uncertainty propagation and quantification are : validation, variance analysis, risk analysis and uncertainty management (Maître and Knio, 2010). In the first case, readings from a real world system (susceptible to be affected by uncertainties) are used to validate the simulations. The plotted results must be shown with error bars in the validation task. Variance analysis deals with characterising the robustness of the prediction. This is performed by calculating the variation of system response around its mean value. In risk analysis, the probability that the system response exceeds allowable limits is estimated. This aids in performing the reliability analysis. In uncertainty management, only the dominant uncertainties from multiple sources of uncertainties are identified and modelled so as to minimise the cost of computation. The various tools used in uncertainty quantification are described below :

2.5.1 Monte Carlo Simulation

In a stochastic framework, uncertainty quantification (UQ) of a nonlinear system has been traditionally performed using Monte Carlo Simulation (Desai, 2011). This method is certainly quite popular and simplest to use. An ensemble of realisations corresponding to the input uncertain parameter can be obtained (Hammersley and Handscomb, 1964) provided the variation and distribution of uncertain parameter is known *a priori*. Probability density function (PDF), cumulative distribution function (CDF) and other statistics of the quantities of interest (QoI) are then obtained from the response realisations. MCS involves repeated use of deterministic solver for each realisation of the random parameter that is generated.

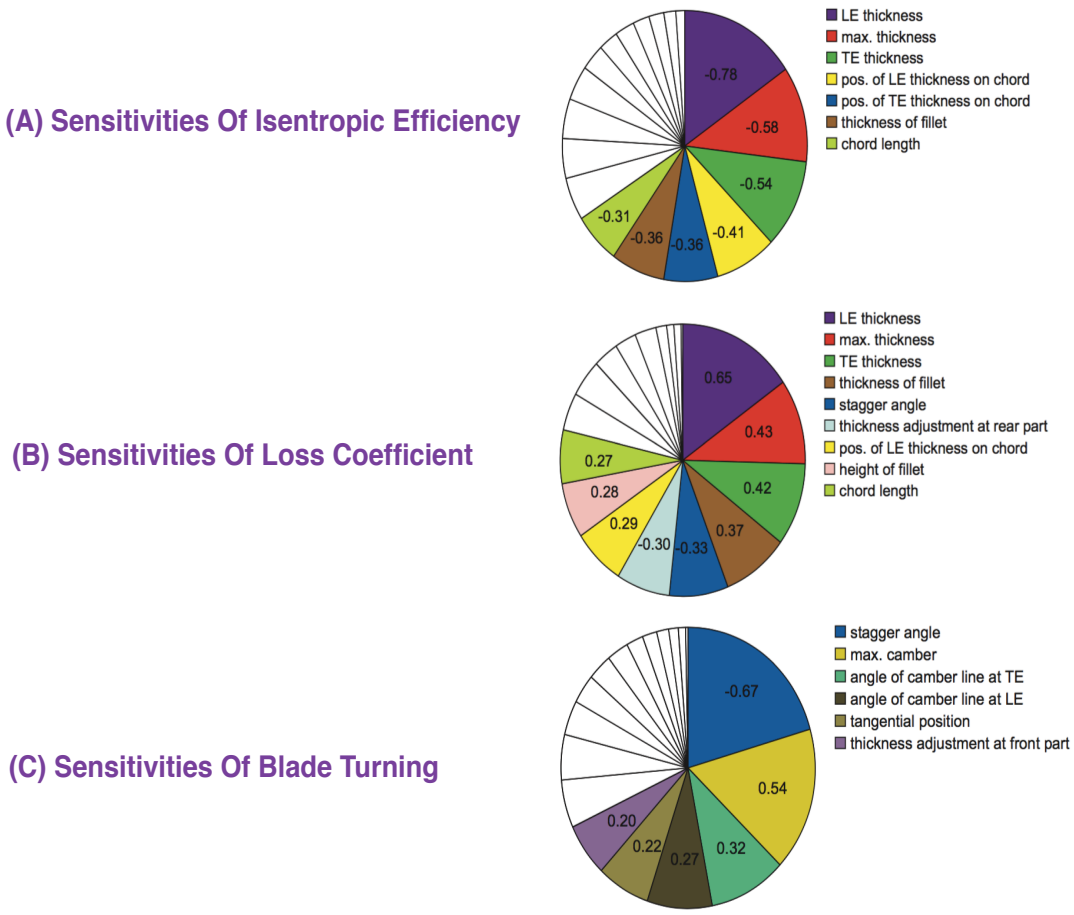


Figure 2.9: Sensitivities From Different Parameters on (A) Isentropic Efficiency (B) Loss Coefficient (C) Blade Turning. Figures Have Been Adapted From Lange et al. (2010) [Reproduced With Kind Permission From ASME]

The order of convergence for MCS is $O(N^{-0.5})$ where N is the number of realisations (Patera and Yano, 2014). This is slow (hence requires large number of realisations) but is also inde-

pendent of spatial dimension (*i.e.* independent of number of uncertain parameters). This can be a drawback as well as an advantage of MCS. If the number of uncertain parameters are less, the convergence of MCS will be very slow. However, if the number of uncertain parameters increase, we enter the realm of curse of dimensionality and in such cases, implementing MCS might be more prudent. Lange et al. (2010) used optical scanner to scan 150 blades. The blades were then used to define geometric variability of the measured data set. The variability of the measured data set was used as an input data of probabilistic 3D simulation. Monte Carlo Method was used to identify the scatter of performance values. It can be seen from fig. 2.9 (A) and (B) that the stage efficiency and the loss coefficient in a rotor shows highest sensitivity to leading edge thickness as a parameter. It was also observed from fig. 2.9 (C) that the turning of the blade was mainly dependent on the stagger angle and the camber profile related parameters.

2.5.2 Surrogate Models

Surrogate models (also sometimes called as metamodels) are quite popular compared to the expensive Monte Carlo Simulation which involves usage of deterministic solver repeatedly for each sample realisation that is generated. There are many types of surrogate models (Samad et al., 2008; Drzewiecki, 2013; Bhosekar and Ierapetritou, 2018) in use today - each with its own application *e.g.* artificial neural network, Kriging, response surface methods, polynomial chaos expansion, etc. One of the main advantage is that these methods are extremely fast and often sample sizes that are encountered in MCS can be used on these methods directly. They can model the impact of rare events directly (Montomoli et al., 2015). These methods are also useful in multi-parameter optimisation study. Samad et al. (2008) used multiple surrogate models to optimise the shape of compressor blade such that it maximises the objective functions (pressure ratio and isentropic efficiency). One of the limitations of these methods is that they are less accurate compared to MCS. In this thesis, we will be briefly touching upon the most popular approaches to build surrogate models viz. polynomial chaos expansion, sensitivity methods and response surface models (Drzewiecki, 2013). In addition to this, a new method

of building surrogate model called "active subspace" has also been described briefly.

2.5.2.1 Generalised Polynomial Chaos Expansion (gPCE)

Botanist Robert Brown (1827) observed that the motion of pollen grains suspended in water kept on changing randomly - which he termed as Brownian motion. Einstein (1905)[3] reasoned that such a motion was due to the collision between pollen grains and tiny water molecules. It was thus possible to work out the number of water molecules hitting a single pollen grain and how fast the molecules were moving just by observing the pollen grains. Jean Perrin (1908)[4] experimentally validated the explanation given by Einstein for which he was awarded Nobel Prize in the year 1926. Wiener (1938), a mathematician, introduced the concept of homogeneous chaos while providing a mathematical description of the Brownian motion. With Weiners theory as the base, Ghanem and Spanos (1990, 1991, 1993) pioneered the development of polynomial chaos expansion (PCE).

The main idea in PCE is to build a polynomial surrogate of the solution in terms of the uncertain parameters (Drzewiecki, 2013). There are 2 types of PCE formulations, intrusive and non-intrusive. In an intrusive formulation, a weak form of the equation is obtained by doing an error minimisation using standard Galerkin projection. The resulting system of equation is modified in terms of chaos coefficients which is then solved for each random mode (Xiu and Karniadakis, 2003). This implies that if an intrusive methodology has to be used, the governing equations and hence the CFD code itself has to be modified. This is easier said than done, especially for well validated industrial CFD codes. In a few cases, the source code may not be available e.g. commercial softwares. These drawbacks of an intrusive formulation resulted in the development of non-intrusive approaches like stochastic collocation (SC) methods and spectral projection methods.

Fig. 2.10 shows the schematic of non-intrusive polynomial chaos expansion. As can be seen, a non-intrusive spectral projection method is based on running a deterministic solver at cer-

[3] `https://nrich.maths.org/6127`
[4] `https://www.nobelprize.org/prizes/physics/1926/perrin/facts/`

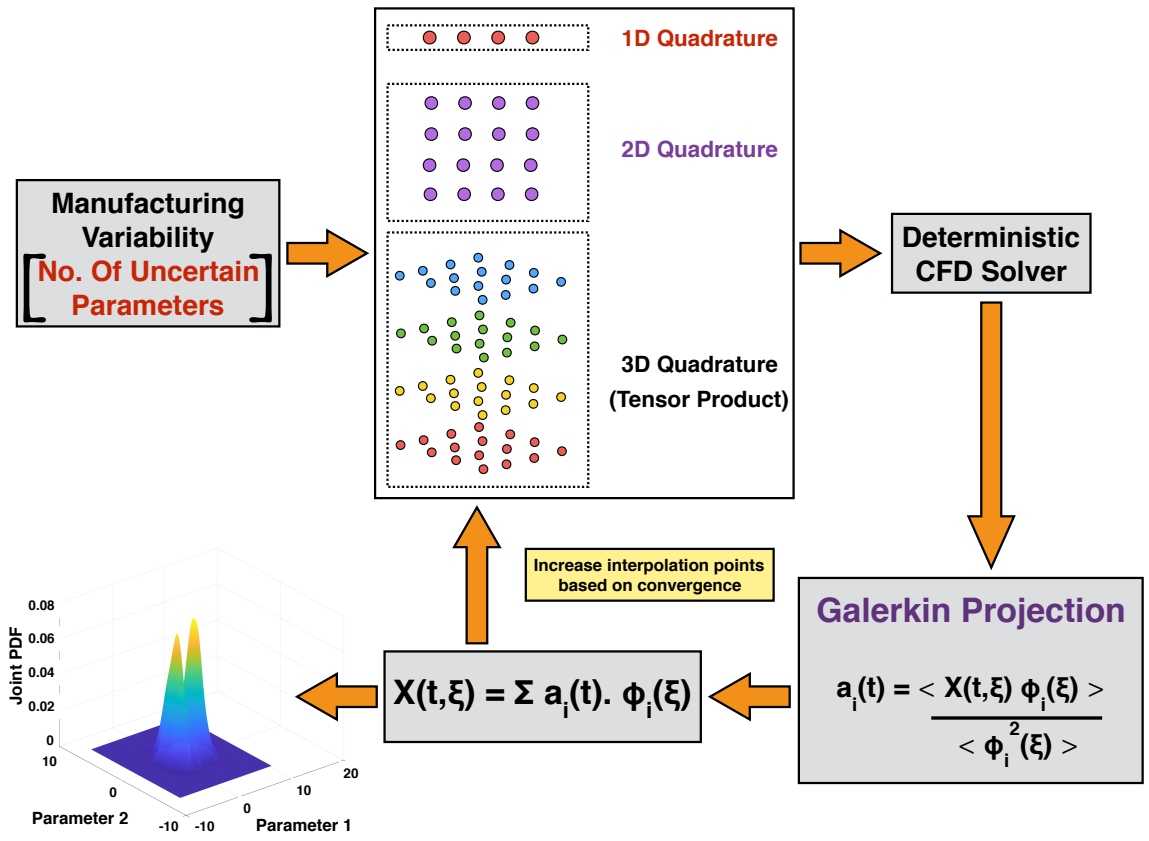


Figure 2.10: Schematic Of Non-Intrusive Polynomial Chaos Expansion

tain at specific collocation points which are nothing but the roots of the chosen order of basis polynomial. This step (also known as pseudo-Monte Carlo Simulation) has been widely used by Maître et al. (2002). These samples of the solution are then used to evaluate the chaos coefficients directly using a projection formula. In collocation method, the problem is collocated at Gauss quadrature points in the probability space and a deterministic solver is used at those collocation points. The co-efficients are then expressed in terms of a polynomial interpolation function. The uncertain system parameter is then written in terms of these N^{th} order polynomial chaos expansion with Lagrange basis polynomials. This method has been used by Loeven et al. (2007) and Sarkar et al. (2009). The Gauss quadrature points can be computed for any arbitrary distributions using for example, the Golub-Welsch algorithm (Golub and Welsch, 1969). The work of generalised polynomial chaos was further developed by not requiring the basis polynomials to be globally smooth and this lead to the development of piecewise polynomial chaos expansion as given by Babuska et al. (2004).

The main drawback of spectral projection method is the number of collocation points (and in turn the deterministic runs) increase rapidly when there are multiple random parameters involved. In such cases, a collocation grid is constructed by using a tensor product of one dimensional quadrature grids in which case non-intrusive methods could become extremely cost prohibitive. Ghisu et al. (2010) used adaptive polynomial chaos in compression system performance analysis. The authors studied the variability in the performance of compressor subject to uncertain operating condition. Seshadri et al. (2013) used stochastic collocation method to study the axial compressor performance subject to varying inlet conditions and geometry changes.

2.5.2.2 Sensitivity Method

Use of Adjoint methods enables the designer to obtain sensitivity derivatives, design optimisation, correction of numerical estimates of quantities of interest, input parameter correction and error propagation (Drzewiecki, 2013). While the calculation of gradients in the adjoint method is independent of number of design variables (Jameson and Kim, 2003), its drawback is the linearisation of Navier-Stokes equations while considering the geometric variability to be small enough (Liefke et al., 2019). As a result, the adjoint method can be applied only when the solution variation is almost linear.

Giebmanns et al. (2013) used an adjoint method to calculate the impact of leading edge geometry variation on a Quasi-3D compressor blade section and the results were compared with the non-linear simulations. It was concluded that results are valid only for small variations of compressor geometry. Adjoint methods are also used extensively in seismic tomography[5] as given in the lecture notes of Bradley (2019).

2.5.2.3 Response Surface Models

Drzewiecki (2013) lists down the several approaches to build response surface models including kriging interpolation, Multivariate Adaptive Regressive Spline (MARS), Alternating

[5] https://cs.stanford.edu/~ambrad/adjoint_tutorial.pdf

Conditional Expectation (ACE) and the Gaussian Process Model. Peter and Marcelet (2008) compared different surrogate models on a stator blade to optimise the local pressure at exit. It was shown that universal Kriging and radial basis function provided best results in terms of approximating exact function. In another study by Samad et al. (2008), the Kriging interpolation fared the worst compared to other surrogate models which were used to optimise the blade shape of NASA Rotor 37 having three design variables (sweep, lean and skew) and the objective functions (pressure ratio and isentropic efficiency).

The accuracy of response surface model is dependent on the number of samples used to build it. Such methods are susceptible to become ill-conditioned if the sample size used to build it is very small (Giunta et al., 2006). Moreover, the response surface models like kriging suffer from severe drawbacks as the dimensions (uncertain parameters) increase. According to Bouhlel et al. (2016), the reason for this is the dramatic increase in the size of covariance matrix as the sampling points increase which makes the inversion of covariance matrix computationally expensive. Bhosekar and Ierapetritou (2018) have reviewed recent advances in surrogate models with regard to modelling, feasibility analysis and optimisation. By applying Kriging and radial basis function on a variety of test problems, they have formulated guidelines for the choice of appropriate surrogate model. They also note that the choice of appropriate surrogate model is based on the type of problem at hand.

2.5.2.4 Active Subspace Based Surrogate Model

As discussed earlier, it becomes extremely cumbersome for a designer to gauge which parameter can be safely ignored and which parameter needs to be considered when there are too many design parameters in consideration. A new set of ideas for reduction of dimension was first proposed by Russi (2010) and was further developed by Constantine et al. (2011) while studying the surrogate model having six input parameters. Instead of identifying a subset of inputs as important, this method determines dominant direction along which the chosen quantity of interest (QoI) varies the most (Seshadri et al., 2017). This method reduces the computational cost and has found application in : (i) The study of safe operating regime of a

hypersonic scramjet (ii) Characterising the relationship between input parameters and output power in a photovoltaic cell (iii) Optimising the shape of an airfoil (Constantine, 2015).

Recently, Seshadri et al. (2017) studied the aerodynamics of fan blade using active subspace. The contours of maximum climb flow capacity (flow capacity at 105% speed of shaft), cruise adiabatic efficiency (at 95% speed of shaft), pressure ratio (to be within certain range of stable fan operation) and sensitivity of manufacturing tolerance are plotted as objective function against a total of 25 design variables. Fig. 2.11 shows the 3D blade parametrisation with 5 degrees of freedom (dof) (Seshadri et al., 2017) : (i) dehedral (ii) sweep (iii) leading edge recambering (iv) trailing edge recambering (v) skew. Each of these parameters are varied at 0, 25, 50, 75 and 100% span and a new blade is generated by radially interpolating these sections. Corresponding to these 25 variables (5 dof and 5 spanwise stations), a design of experiment is conducted by drawing 150 samples using Latin hypercube sampling. For each of these sample, a simulation was run and QoI were computed. Subsequently, a gradient was calculated using the algorithm on pg. 5 of Constantine (2015) along which the QoI exhibit the greatest variability.

Active subspace captures the variation in 25-dimensional space with far fewer dimensions. Fig. 2.12 (A) and (B) shows the geometry changes for minimum and maximum pressure ratio as obtained from the active subspace computation. It was seen that the increase in pressure ratio was obtained by incorporating more camber to the aerofoil sections which increases the flow turning in the compressor. Similarly, fig. 2.12 (C) and (D) shows the geometry changes for minimum and maximum efficiency as obtained from the active subspace computation. It was seen that the reduced curvature of camberline resulted in higher efficiency designs.

Seshadri et al. (2017) used these contours to answer the pedigree design rules : how best to increase fan efficiency; how best to desensitise the blade aerodynamics to impact of manufacturing variations? The former required reduction in both pressure ratio and flow capacity thus leading to reduction in strength of leading edge bow shock wave. While the later required required strictly a reduction in flow capacity. This study was able to give a detailed quantification of aerodynamic trade-offs with regard to blade design. Seshadri et al. (2017) note that active subspace can be interpreted as an *output-based* principal component analysis (PCA) as the

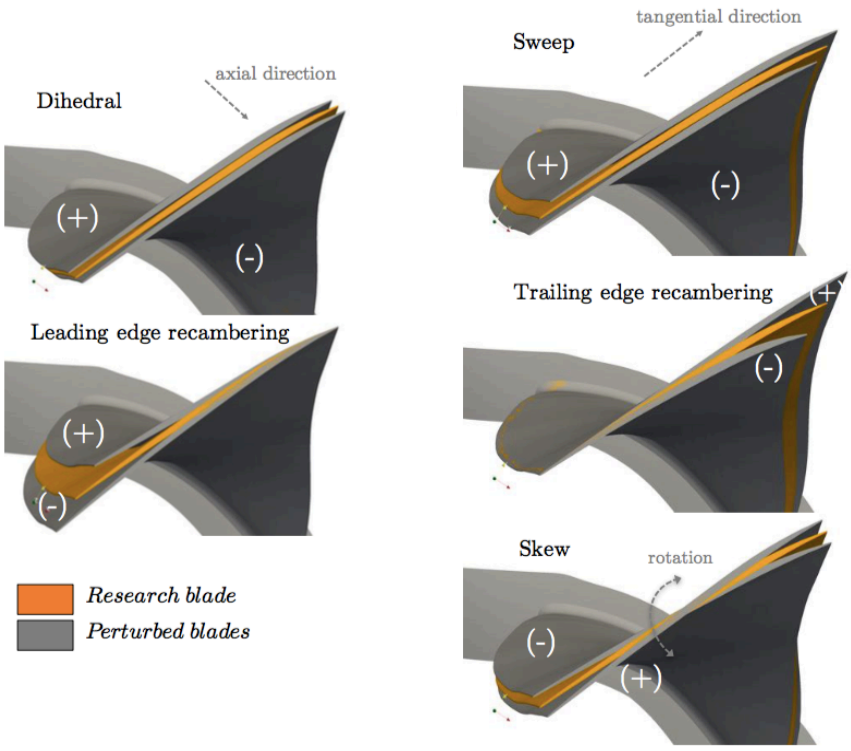


Figure 2.11: 3D Blade Parametrisation Showing 5 Degrees Of Freedom (Both Positive And Negative) From Seshadri et al. (2017) [Reproduced With Kind Permission From ASME]

PCA does not associate variability of inputs to the corresponding model's output. This study however assumes that all the new blade design would have same manufacturing excursions and has neglected the range of design that could be obtained due to manufacturing tolerances.

2.6 Limitations Of CFD And Experiments

"No one believes the CFD results except the one who performed the calculation, and everyone believes the experimental results except the one who performed the experiment"

The above quote by P. J. Roache summarises the limitations of CFD and experiments. As discussed earlier, the first step in the study of uncertainty quantification is the validation of results (Maître and Knio, 2010) wherein the results of CFD and experiments are compared and validated against each other. This makes sure that the essential flow physics is clearly understood and any bias in either the experiment or the simulation could be rectified before proceeding further. While usually, the CFD results are benchmarked and compared against

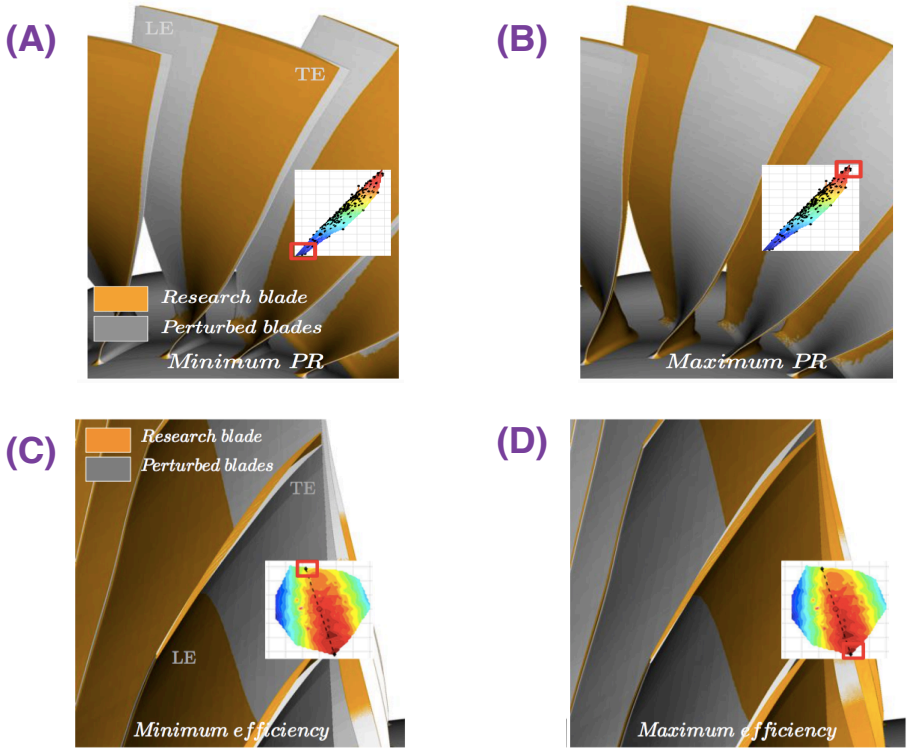


Figure 2.12: Perturbations In Active Subspace Showing (A) Minimum Pressure Ratio Geometry (B) Maximum Pressure Ratio Geometry (C) Minimum Efficiency Geometry (D) Maximum Efficiency Geometry. Figures Adapted From Seshadri et al. (2017) [Reproduced With Kind Permission From ASME]

experimental results to gauge its validity (Mehta et al., 2016), the reverse is also true wherein the CFD results have been successfully used to identify the source of uncertainty in experimental setup (Montomoli et al., 2015). This section has been divided into 2 subsections; each dealing with sources of uncertainty in CFD and experiments respectively.

2.6.1 Limitations In CFD

Though the usage of CFD has become ubiquitous among the engineering community, it is necessary to know the various sources of uncertainty that continues to plague it. The uncertainties in a turbomachinery CFD environment can arise from turbulence modelling, boundary conditions, geometry of the component, mesh quality and the type of simulation used to capture flow physics. Subsequent paragraphs will discuss each of these uncertainties in detail. Part of the literature survey in this section has been borrowed from Montomoli et al. (2015).

2.6.1.1 Turbulence Modelling

As discussed in introduction, though Direct Numerical Simulation (DNS) is known to give flow-field information down to the Kolmogorov scale, its cost prohibitive nature makes it unfeasible to be used in the study of high speed compressor flows. Application of DNS has been restricted to only low Reynolds Number components such as low pressure turbines (Tucker, 2014). Zaki et al. (2010) carried out DNS study of compressor cascade at Reynolds Number of 138,500 using a mesh size of 84 million.

Gourdain (2015) calculated the simulation cost ratio between URANS and LES on the finest grid (about 10^9 points) to be 500. It is therefore unsurprising to find the literature in turbo-machinery application filled with papers pertaining to RANS and to a lesser extent hybrid RANS/LES than a pure LES. Hah (2009) is among the first few to demonstrate improved prediction of total losses in NASA Rotor 37 using LES. A validation of RANS and LES simulation vis-a-vis experimental results were carried out by Gourdain (2015) and Odier et al. (2017). A schematic of the 1-stage compressor used by Gourdain (2015) and Odier et al. (2017) is shown in fig. 2.13(A) and (B) respectively.

Gourdain (2015) compared LES simulation with URANS as well as experimental results of CME2 compressor designed by SNECMA. URANS used two equation model of k-ω while LES used a Wall-Adapting Local Eddy-Viscosity (WALE) model to compute the turbulence effects. Both LES and URANS are solved using CFD code *elsA*. As shown in fig. 2.14(A), both LES and URANS predict the same shape of pressure ratio curve as observed in experiments; though LES over-predicts the experimental data from choke to stall and URANS under-predicted it. The stability limits predicted by URANS and LES matched well with the experiments. From fig. 2.14(B), it can be seen that the shape of isentropic efficiency curve predicted by URANS was much steeper compared to LES though the overall trends were similar to pressure ratio curve wherein URANS under-predicted the experiments while LES over-predicted the experiments. The LES was however found to predict better flow features compared to URANS, especially near the casing.

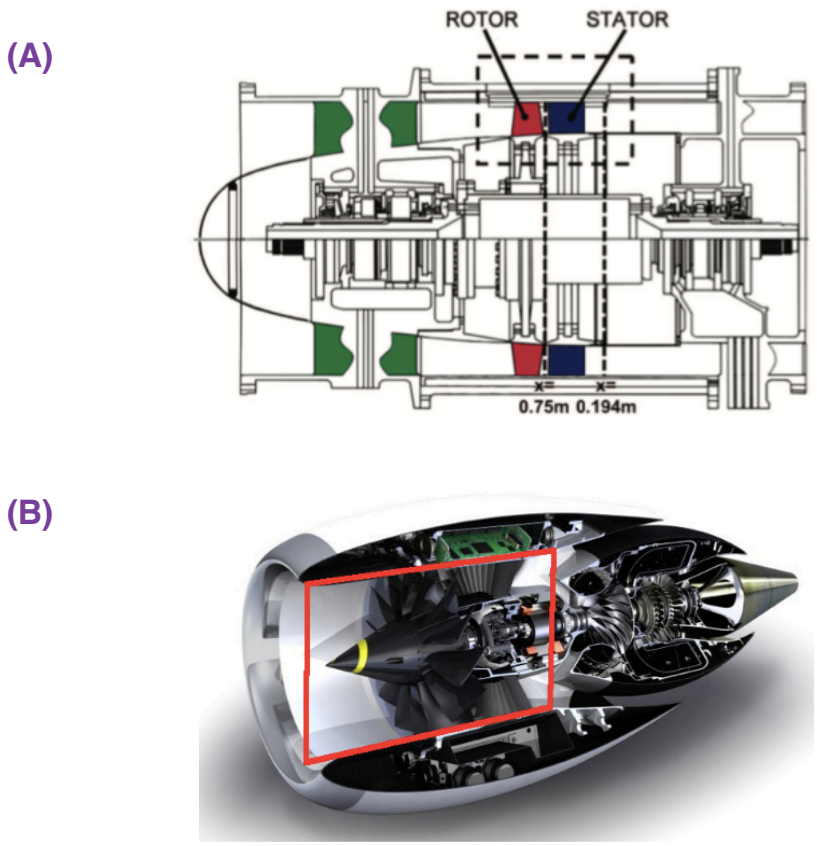


Figure 2.13: (A) Schematic Of The Experimental Setup Used By Gourdain (2015) [Reproduced With Kind Permission From Elsevier] (B) Schematic Of DGEN-380 Turbofan Used By Odier et al. (2017)

Odier et al. (2017) compared LES simulation with both RANS as well as experimental results of a fan stage in an actual turbofan, DGEN-380, intended to power personal light jets. The turbulence closure in RANS is done using one-equation model of Spallart-Allmaras (SA), while in LES, the unresolved turbulent contribution is modelled using WALE subgrid model. LES uses TurboAVBP as CFD solver while RANS is solved using $Fine/Turbo^{TM}$ package of Numeca. Fig. 2.14(C) and (D) shows the comparison of performance curve obtained from LES and RANS vis-a-vis experimental results in Odier et al. (2017). Compared with experimental results, the percentage variation in RANS for the massflow rate, the pressure ratio and isentropic efficiency was 2.95%, 0.44% and 0.93% respectively. Similarly, in case of LES, the percentage variation for the massflow rate, the pressure ratio and isentropic efficiency were 2.12%, -0.08% and -1.63% respectively.

The LES showed reasonable agreement with RANS in terms of average profiles though it ex-

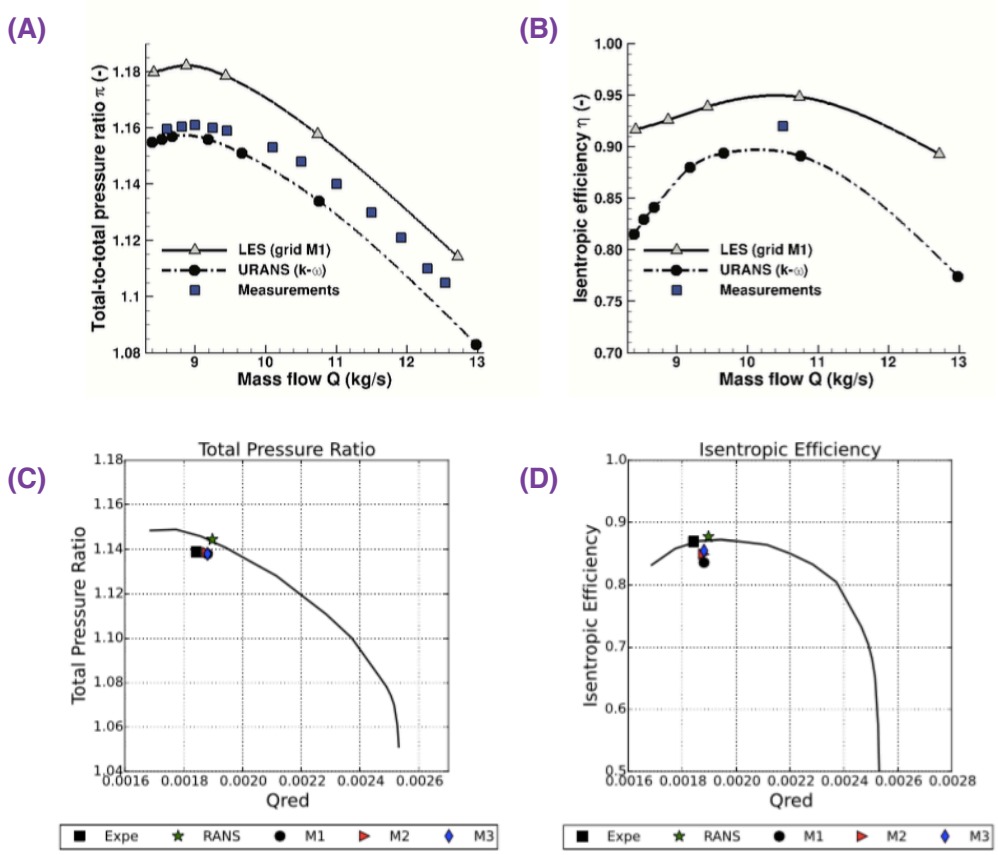


Figure 2.14: Comparison Of Experimental, RANS And LES Performance Curves (A) Pressure Ratio Vs. Mass Flow Rate From Gourdain (2015) [Reproduced With Kind Permission From Elsevier] (B) Efficiency Vs. Mass Flow Rate From Gourdain (2015) [Reproduced With Kind Permission From Elsevier] (C) Pressure Ratio Vs. Mass Flow Rate From Odier et al. (2017) (D) Efficiency Vs. Mass Flow Rate From Odier et al. (2017)

hibited an offset in numerical total temperature, Mach number and static pressure compared to experimental profiles. Gourdain (2015) concluded that LES has potential for better prediction of the turbo-machinery flows. However, it is more sensitive to boundary condition (inflow turbulence, adiabatic walls, etc) along with real geometry effects and thus opens "Pandora's box". Accurate knowledge of boundary conditions would require a more integrated approach with experimentalists. The extremely high computational cost required to perform a large eddy simulation (LES) thus makes it a very unattractive proposition for the purpose of UQ. As seen in the discussion so far, a major drawback of all scale resolving simulation is the requirement of a refined mesh domain to capture small as well as large scales. Thus, the RANS simulation with a turbulence model will remain the workhorse for predicting the compressor stability for the foreseeable future. Duraisamy et al. (2019) have classified the uncertainty in RANS closure

in 4 levels :

Level 1 : The ensemble averaging introduces a loss of information on fluctuating flows that cannot be recovered regardless of the advances in turbulence modelling and hence represents the upper limit to RANS models.

Level 2 : According to Reynolds decomposition, a velocity flow-field can be decomposed into mean part and fluctuating part. When this decomposition is applied to Navier-Stokes (NS) equation, an extra term known as Reynolds Stress Tensor arises and modelling is needed to close these equations. Level 2 uncertainty appears when any approximations are made to compute Reynolds Stress Tensor $i.e.$ Boussinesq eddy viscosity hypothesis : often questionable in complex flows (Perot and Moin, 1996).

Level 3 : This is related to the mathematical form of transport equation $e.g.$ different forms of SA model (Lee et al., 2018)

Level 4 : This uncertainty arises when deterministic values are assigned to the coefficients in the model that are used to calibrate the relative importance of various contributions in the turbulence closure.

Gibson et al. (2017) compared different turbulent models in ANSYS CFX 16.2 with the experimental results of centrifugal compressor using steady state RANS simulation. The models compared were (i) Spallart-Allmaras (SA), (ii) Shear Stress Transport (SST), (iii) modified SST called SST-curvature correction (SST-CC), (iv) Reynolds stress model of Speziale, Sarkar and Gatski (RSM-SSG) and (v) Reynolds stress model (RSM-ω). For global performance parameters, each of the model assessed matched well with experimental results, with a discrepancy below 2% in most cases. SST model was accurate over entire speedline with the advantage of low solve time. SST-CC was more accurate compared to original SST but the solve time was longer (double in some cases). On the other hand, the one dimensional averaging of variables by SA model conceals local flow features and shows the flow structures with high levels of separation. Lee et al. (2018) used a modified SA model based on β-function to predict the fan performance using AU3D CFD code. The computational results were compared against

experimental data and the match was found to be excellent. It is thus seen that tackling of Level 3 uncertainty in RANS closure is useful in terms of predicting the flows in a compressor.

Furthermore, it was shown that the modifications at Level 4 uncertainty of RANS closure is not found to be useful in predicting the flows in a compressor (Xiao et al., 2020b) wherein the uncertainty band of predicted stall mass flow rate does not envelope the measured data. Moreover, re-calibrating the model coefficients leads to contradictory results when different flow quantities are considered (Xiao et al., 2020a).

2.6.1.2 Boundary Conditions

Applying the correct boundary condition is perhaps one of the most important aspects of CFD in the area of turbomachinery. The turbomachinery components are subjected to severe non-uniform conditions whose distributions are yet to be determined with high accuracy (Montomoli et al., 2015). Fan and compressors can be subjected to non-uniform inflow commonly known as inlet distortion which can detrimentally affect the efficiency and stability margin (Zhang, 2019). Such non-uniform inflow conditions can never be avoided during the course of engine operation.

The different types of inlet distortion defined in literature (Mehdi, 2014; Zhang, 2019) are (a) Total pressure distortion (most commonly analysed; caused due to boundary layer ingestion, grounded vortex ingestion and cross wind) (b) Total temperature distortion (main issue for military engines; arises due to ingestion of hot gases when aircraft is operating in thrust reverser, vertical take-off and landing operation) (c) Static pressure distortion (very rare; Harrier aircraft engine had some issues with this type of distortion) (d) Swirl distortion (generated outside the compressor due to cross wind or ingestion of grounded vortex; inside the compressor upstream flow field redistribution can give rise to it).

These inlet distortion could also be (i) Rotating inlet distortion (moves around the annulus; stalled upstream blade row will impose a rotating distortion on downstream blade row) (ii) Abrupt inlet distortion (occurs instantaneously for a short period of time). It is possible that

sometimes two or more of these inlet distortion can act in conjunction *e.g.* the combustor could face both total pressure distortion and total temperature distortion due to the compressor work output (Mehdi, 2014). It is also possible for one type of inlet distortion to generate, amplify or reduce another type of inlet distortion (Zhang, 2019). Sometimes, the different inlet distortions cannot be decoupled so easily *e.g.* there are instances wherein the swirl distortion was taken into account with total pressure distortion as a single problem (Mehdi, 2014). Specifying the correct boundary condition can thus influence the operation of the compressor.

Another source of uncertainty in the boundary condition arises from the treatment of the interface boundaries between the rotating domain and stationary domain. In a turbomachinery environment, either a mixing plane or a sliding plane can be used to treat such interfaces. The mixing plane, as the name suggests, circumferentially mixes out the flow quantities at inlet and exit boundaries of each blade row (Denton, 1992). The circumferential averaging of flow quantities at mixing plane assumes instantaneous mixing of nonuniform flow conditions and as a result can overestimate the mixing loss (Fritsch and Giles, 1995). Cumpsty and Horlock (2006) have given a review of various averaging techniques along with their suitability for different applications. The sliding plane on the other hand, uses a moving grid in rotor frame of references and a stationary mesh in the stator frame of reference. Sayma et al. (2000a) use linear interpolation to compute the boundary fluxes between the inlet and outlet surfaces of rotor and stator at each time instant. A detailed discussion regarding both these methods could be found in Stapelfeldt (2014).

A comparative study between these two methods was carried out by Hongsik et al. (2011) for a GE 1.5 stage compressor (IGV-Rotor-Stator) . It was seen that an identical loading up to the mid-span region is predicted by both mixing plane method as well as sliding plane method while differing mainly towards the tip section. This is because, a mixing plane at the interface boundaries carries out circumferential averaging which cuts off the shock propagation upstream and tip vortex propagation downstream. However, the mixing plane approach has been used widely by many researchers due to its simplicity to calculate the performance characteristics (Hongsik et al., 2011) and also the time required for a sliding plane approach is enormous Stapelfeldt (2014).

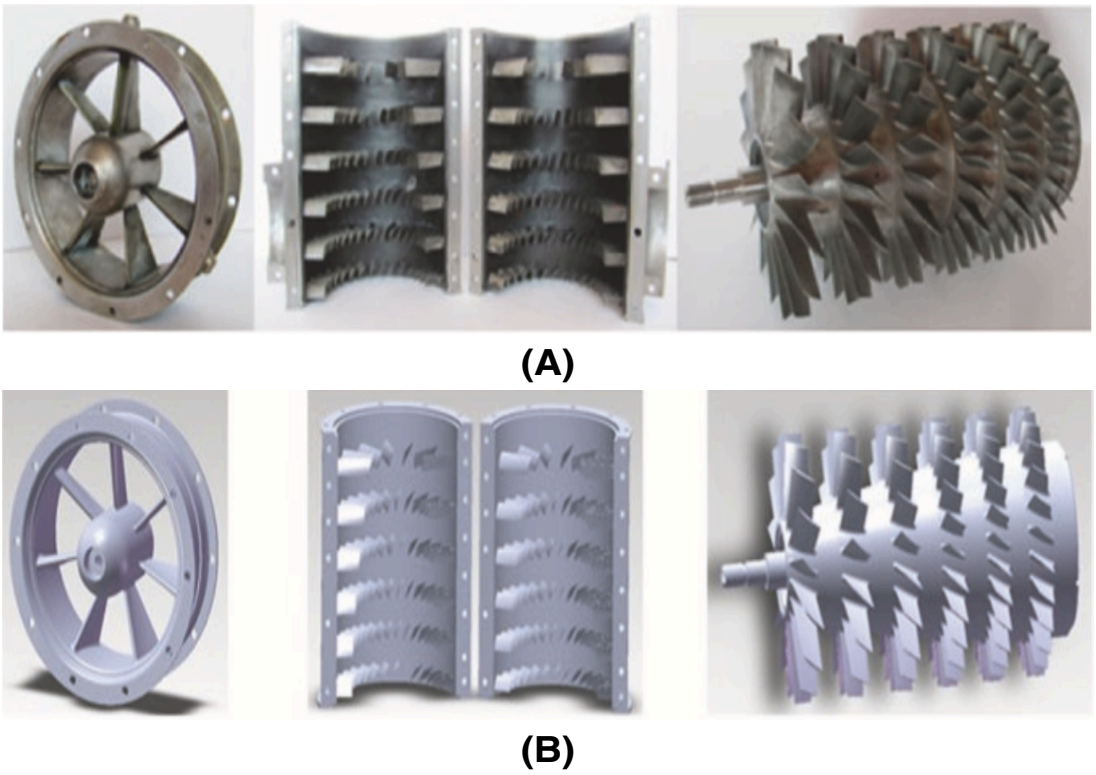


Figure 2.15: (A) Real Geometries In Turbomachinery (B) 3D Optical Scan Geometry. Adapted From Montomoli et al. (2015) [Reproduced With Kind Permission From Prof. F. Montomoli, Imperial College London, UK and Prof. M. Pinelli, University of Ferrara, Italy]

2.6.1.3 Exact Geometry

Due to manufacturing tolerances, a 3D CAD model is not a true replica of the manufactured component. The CAD model would also be ignoring few non-essential features of the manufactured component *e.g.* surface roughness. The CAD model typically consists of features like bolts, brackets, sensors, etc which are non-essential from CFD point of view. The best practice in the industry mandate that these non-essential features be removed before proceeding with the CAD cleanup process. The CAD cleanup process involves patching of holes, connecting the edges/faces and slight modification of the geometry such that the CAD model becomes water-tight (Axerio-Cilies, 2012). This water tight CAD model is used for generating a mesh and further analysis. Thus, there is a considerable difference between the model used for CFD analysis and the real manufactured component.

A UQ study involving the effect of geometric variation could become cumbersome and time consuming due to the large number of CAD geometries that would need to be generated. A

mesh-morphing tool used to generate different samples of geometric variation (Venkatesh et al., 2020) could prove its efficacy under such circumstances. An interesting approach has been to use the geometries of a real compressor for CFD simulation as done by Lange et al. (2010). It involves optical scanning of the compressor geometries which gives a 3D point cloud representing the surface of the blade. From this 3D point cloud, complex geometries as shown in fig. 2.15 can be reconstructed for further analysis (Montomoli et al., 2015). Thus the uncertainty related to reproduction of the exact geometry can be potentially reduced using such techniques.

2.6.1.4 Mesh Dependency

From author's experience of working in industry, though a "perfect mesh" may not exist, the industrial best practices mandate that the mesh should conform to a few mesh quality control parameters *e.g.* minimum and maximum angle, skewness, warpage, aspect ratio, etc. These parameters become even more important when dealing with assemblies that are not symmetric and hence cannot be automated. As discussed in previous section, Axerio-Cilies (2012) says that unwanted features in CAD geometry are deleted during the geometry cleanup process and the CAD geometry is slightly modified at appropriate places before the meshing commences. This directly implies that mesh need not follow the CAD geometry but only needs to capture the physics behind simulation.

Furthermore, the mesh must be coherent with the numerical scheme being used *e.g.* it would be erroneous to perform large eddy simulation with a coarse mesh. A poor grid resolution would result in poor prediction of flow-field (position of shock waves, tip leakage vortex) and also the compressor operating map. Grid independence study is considered as the bedrock of every numerical simulation. A grid convergence entails simulations of at least three different grid sizes before proceeding with numerical campaign. The grid convergence helps minimise the numerical uncertainty in the computation.

2.6.1.5 Steady vs Unsteady

The flow in a turbomachine is inherently unsteady due to different frames of reference. A CFD engineer finds himself at crossroads while studying the rotor/stator interaction in compressors - whether to perform a steady simulation or an unsteady one. This decision can dramatically influence the outcome of the simulation.

In Lee et al. (2018), it was shown that the experimentally measured operating points on the positive part of the slope of the compressor map could only be predicted using a full annulus unsteady simulation as it accurately captures the flow asymmetry at lower flow coefficients. A single passage steady simulation resulted in premature numerical stall. The unsteady simulation helps model several important phenomena :

(i) Flutter, Rotor-Stator Interaction (Li and He, 2005; Zhao, 2016)
(ii) Rotating Stall (Choi et al., 2011; Lee et al., 2018)
(iii) Unsteady Inlet Distortion (Mehdi, 2014; Zhang, 2019)
(iv) Alternate Passage Divergence (Wilson et al., 2006; Lu, 2020)

Rotor-stator interactions can be studied through the following unsteady methodologies as summarised by Montomoli et al. (2015): (a) deterministic stresses approach (b) loosely coupled approach (c) domain scaling approach (d) time lag method (e) generalised shape correction method. However, the amount of inaccuracy of each method cannot be quantified easily given their respective hypotheses. For this reason, it is recommended that rotor-stator interactions be studied by employing full unsteady simulation (Montomoli et al., 2015).

2.6.2 Limitations In Experiments

Pengra and Dillman (2009) lists down the following two types of experimental uncertainties : systematic uncertainty and random uncertainty. Systematic uncertainties arise due to faulty measuring equipment and/or technique used in experiments. On the other hand, random uncertainties may arise due to unpredictable variation in experimental condition, noise, etc.

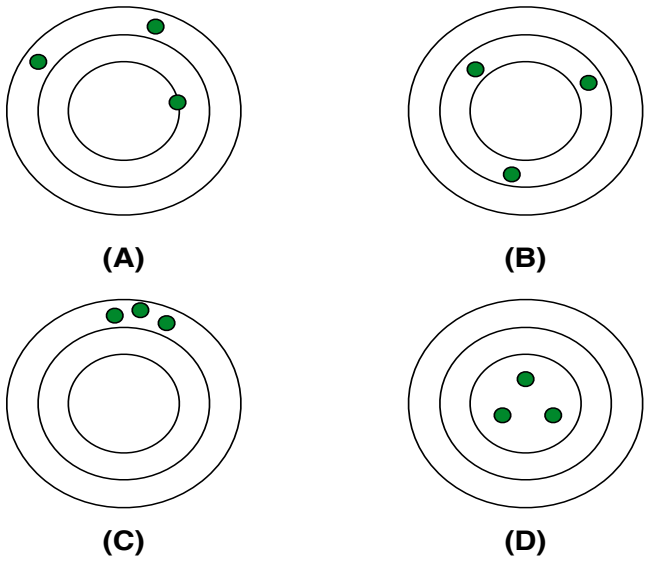


Figure 2.16: Bulls Eye Plot Showing Distinction Between Accuracy And Precision (A) Not Precise and Not Accurate (B) Not Precise But Accurate (C) Precise But Not Accurate (D) Precise and Accurate

According to Bell (2001), repeating the measurement and averaging the quantities of interest (QoI) would give a better estimate of the measurand in case of random uncertainties. For systematic uncertainty, the same unknown affects the measurand each time we try to measure it. In this case, we gain nothing extra by repeating the measurements. Sometimes, systematic uncertainties like "parasitic" resistance in a measurement device like strain gauges are unavoidable (Agilent Technologies, 1999). Thus the measuring equipment should be properly calibrated before taking any reading.

Pengra and Dillman (2009) further note that the random uncertainties are much easier to deal with and to quantify. There is no rule of thumb for gauging the magnitude of systematic uncertainties. The presence of systematic uncertainty implies a certain physics in the analysis has not been accounted for. It requires an experienced and skilful experimenter to see through these uncertainties and avoid it. An experiment with low systematic uncertainty is said to be accurate while an experiment with low random uncertainty is said to be precise. Fig. 2.16 lists four possible types of experiments with the help of a bull's eye plot. Depending on the characterisation of various uncertainties, the experiments are classified as (A) Not Precise and Not Accurate (B) Not Precise But Accurate (C) Precise But Not Accurate (D) Precise and Accurate. Since it is much more difficult to gauge the impact of systematic uncertainties, we

have it in detail in subsequent paragraphs.

2.6.2.1 Limitations Of Measuring Equipments

A classic example of this type of systematic uncertainty is the measurement of tip gap carried out in NASA Rotor 67. Strazisar et al. (1989) note that the measured tip gap in NASA Rotor 67 is 1.016 mm. Since the performance map from CFD did not match the performance map from experiments, researchers started toying with the idea of varying the size of tip gaps computationally. Jennions and Turner (1993) adopted the size of nominal tip gap to be 0.61 mm in their computation and since then many researchers (Arima et al., 1999; Choi et al., 2010) have adopted this value in their CFD computation. Recently, Roberts et al. (2013) studied the effect of ultrapolish on the performance of NASA Rotor 67. The running tip clearance in this study is noted to be approximately 0.5 mm.

The researchers matched the characteristic curve obtained from CFD with that of experiments by changing the parametric values and were able to correctly guess the approximate size of nominal tip gap. This size of nominal tip gap was found to be very close to measured value in later experiments.

2.6.2.2 Limitations Of Experimental Setup

Due to lack of public domain open source data, for decades, NASA Rotor 37 has been one of the most studied test cases that has been used to calibrate and test CFD solvers, turbulence closures etc. In particular this case has been studied extensively due to the mismatch between CFD and experimental results. Seshadri et al. (2014) used uncertainty quantification to prove that the discrepancy between experimental and numerical results was due to uncertainties in experiments rather than numerical accuracy. They successfully showed the presence of hub leakage flow in the test rig which was hitherto previously unknown. This example illustrates the need to go beyond mere benchmarking of experiment and simulation results.

2.7 Combinatorial Optimisation

According to Korte and Vygen (2011), combinatorial optimisation is one of the most important areas of discrete mathematics and has its genesis in the field of combinatorics, operations research and theoretical computer science. They give two real life example that summarises the problem at hand. In the first example, a company with a drilling machine drills holes into printed circuit boards (PCB). Objective is to produce as many printed circuit boards as possible within a given time frame. Though the time to drill a hole is fixed, by minimising the time the machine needs to move from one point to another to drill a hole, the company can increase its production of PCB. The drilling time cannot be optimised (*i.e.* it remains fixed for each hole) but the time required for the machine to move from one point to another can be minimised. In the second example, a set of jobs have to be completed. Each job has a specified processing time and can be done by a subset of the employees. It is assumed that all employees doing a job are equally efficient. One employee can contribute to several jobs but not at the same time. Also, several employees can contribute to the same job at the same time. The objective is to get all jobs done as early as possible.

With thousands of real-life problems being formulated as an abstract combinatorial optimisation problems, this has become a very active area of research. Combinatorial optimisation is a process of finding a maxima or minima of an objective function for a finite, discrete domain but with large number of possible configurations. A few applications of combinatorial optimisation are : (a) A generalised vehicle routing problem such as Theatre Distribution and Vehicle Routing Problem (Gao et al., 2017, pp. 371-385) (b) Simulating the replication behaviour of computer malware as described in (Gao et al., 2017, pp. 401-416) (C) Scalable gene synthesis and amplification of proteins (Tang and Chilkoti, 2016).

In the present thesis, the problem of optimal arrangement of the blades of differing dimensions so as to eke out maximum performance and stability boundaries can be thought of as a problem that falls within the domain of combinatorial optimisation. Further discussion on the methods to solve such problems will be carried out in the next chapter.

2.8 Chapter Summary

This chapter started with the need of performing an uncertainty quantification in the real world systems surrounding us. Four examples were considered to drive home its importance : (i) NASA's Challenger Space Shuttle disaster (ii) NASA's Hubble Space Telescope rectification (iii) ESA's Ariane 5 disaster (iv) ISRO's GSLV-F05 disaster. The chapter then delved into the working of an axial compressor and geometrical uncertainties associated with it. Various parameters like tip gap, stagger angle, shape of leading edge, lean, sweep and fillet radius were taken into consideration based on the previous research works. The allowable values of these parameters along with their effect on compressor performance and stability were discussed at length. Most of these research consider all the blades in the compressor to undergo same geometric variation (single passage simulations).

When doing UQ due to parametric variation, a brute force Monte Carlo Simulation has a very slow convergence and hence the surrogate models (which provides a quick turn around time) are usually preferred. Various surrogate models like PCE, Response Surface Models, etc have been discussed. The chapter also lists down various limitations of CFD simulation and experiments which would help a researcher quantify different uncertainties. The chapter ends with a discussion on combinatorial optimisation. Combinatorial optimisation is a process of finding a maxima or minima of an objective function for a finite, discrete domain but with large number of possible configurations.

The detailed literature survey helped identify that combinatorial optimisation of different blade arrangements as a potential area which could have an immediate impact in academia as well as industrial perspective. Hence in this thesis, all the blades in a compressor undergo simultaneous parametric variation and the focus is on establishing a rule of thumb for optimal arrangement that helps eke out maximum performance and stability margin.

Chapter 3

Methods

"If you can't describe what you are doing as a process, you don't know what you are doing" - Edwards Demings.

This chapter briefly introduces the aerodynamic model employed by the CFD solver followed by a brief description of the different test cases used in this work. This work encompasses the study of tip loaded blade and part span loaded blade used in the compressors of aero-engines along with a 1-stage compressor used in a typical industrial gas turbine. The chapter also details the various boundary conditions, meshing strategy used to study the different test cases, the scalability study and mesh convergence results. Finally, a brief description of open source genetic algorithm (GA) based TSP solver that has been used in the present work for the combinatorial optimisation study has been given.

3.1 Numerical Methodology

The two main objectives of this thesis are : (i) establish a rule of thumb for optimised arrangement of compressor blades having differing dimensions due to geometric variability (ii) develop a surrogate model that can be used to predict the performance of compressor having geometric

variability. The in-house CFD solver, AU3D, developed at Imperial College London-VUTC with support from Rolls-Royce over 25 years was used for this purpose.

AU3D is a three dimensional, time-accurate, viscous, compressible Reynolds-averaged Navier-Stokes (RANS) solver. The solver, based on a cell-vertex finite volume methodology, is implicit and second-order accurate in space and time. This solver has been optimised for simulating both aerodynamic as well as aeroelastic phenomena and has been successfully used to predict the design and off-design conditions (Vahdati and Imregun, 1996; Choi et al., 2011; Dodds and Vahdati, 2015; Lee et al., 2018; Zhao et al., 2018). Throughout the present study, the calculations performed are purely aerodynamic in nature with no prescribed vibration being applied to the blade. The solver also incorporates a wall function for faster computation. As discussed in the Chapter 1, RANS simulation presents a good trade-off between computational cost and modelling accuracy. Moreover, the sheer number of computations that need to be carried out for testing various parametric cases makes RANS simulation an ideal candidate in the present case.

The solver operates on a semi-structured mesh with hexahedral elements found around the airfoil and prismatic elements in rest of the passage. The boundary layer region in rotor-to-rotor grid has a body-fitted O grid while rest of the region is unstructured. The tip clearance geometry is meshed by triangulating the blade tip and mapping extra layers over the tip. The mesh is represented using an edge-based data structure and is presented to the solver as a set of node pairs connected by edges. Furthermore, the edge weights at the inter-cell boundaries is computed such that it allows the solver to have a unified data structure and conceal the nature of the semi-structured grid from the main calculation loops. The numerical fluxes are evaluated along the edges of the grid while the flow variables are represented on the nodes of the grid.

The numerical fluxes are evaluated using the Jameson- Schmidt-Turkel scheme. Additionally, a pressure switch which reverts to first order Roe scheme in the vicinity of discontinuities, has been used for numerical robustness. A central differencing scheme has been applied along with a mixture of second and fourth-order artificial dissipation for stabilisation. The solver uses the one-equation Spalart-Allmaras (SA) model (Spalart and Allmaras, 1992) to evaluate

the turbulent eddy viscosity. The parameters in SA model can be adjusted to achieve a good agreement up to the stability limit when compared with the experimental data (Lee et al., 2017, 2018). This agreement is typically obtained by comparing the pressure ratio and and the overall radial distribution of the quantities of interest. In the present work, the said parameters of SA model have been held constant for all the test cases. Furthermore, techniques like residual smoothing and local time stepping have been used to accelerate the steady-state flow computations. Further information regarding the solver is given by Sayma et al. (2000b)

3.2 Test Cases

To demonstrate the generality of the models developed in this project for different design of fan/compressors, three test cases have been considered : (i) Tip Loaded NASA Rotor 67 (ii) 1-stage high performance 3D transonic compressor used in a typical industrial gas turbine (IGT) industry (iii) Part Span Loaded 3D rotor - representative of a fan in civil aircraft engine. NASA Rotor 67 as shown in fig. 3.1 was selected as an initial test case due to the availability of experimental (Strazisar et al., 1989; Roberts et al., 2013) and computational results (Adamczyk et al., 1993; Jennions and Turner, 1993) from past studies. Such tip loaded fans are typically found in military aircraft engines.

The 1-stage transonic fan used typically in an industrial gas turbine (IGT) as shown in fig. 3.2, was developed at Imperial College London (UK) with support from Mitsubishi Hitachi Power Systems Ltd (Japan) as a second test case. Typically, an aero-engine fan blade is lighter with high aerodynamic loading; and thus susceptible to aeroelastic instabilities like flutter. In contrast, the blades in the compressors of land based industrial gas turbines (IGT) are more rigid and less susceptible to instabilities like flutter (Suzuki et al., 2020). However, as the demand in the industry grows with regard to increased airflow and power output to meet its economic targets (Suzuki et al., 2018), the front stages of IGT compressors are moving towards longer blades and thus starting to resemble the aero-engine fan blades (Suzuki et al., 2018). This concept is similar to increased fan diameter in aero-engines which takes advantage of more

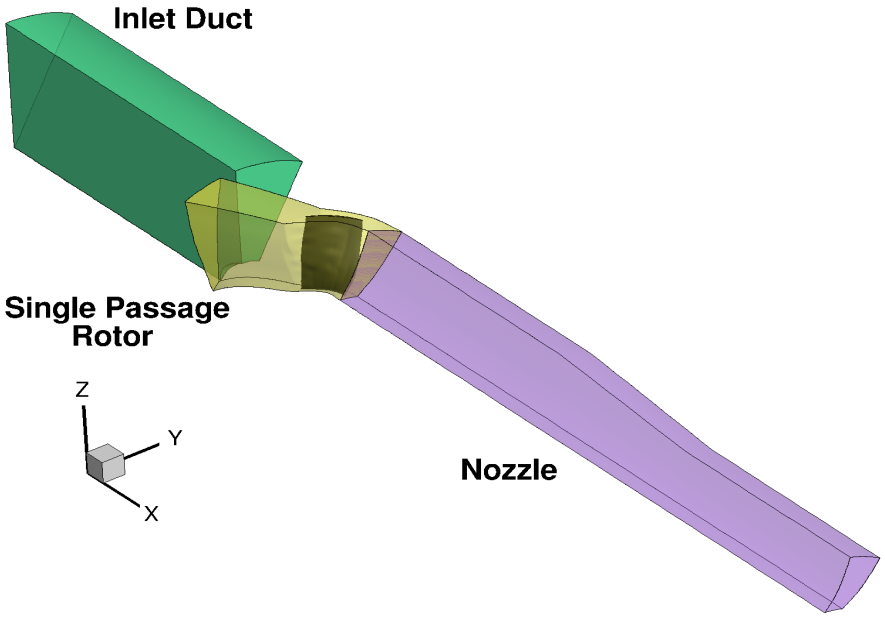


Figure 3.1: Computational Domain Of NASA Rotor 67

bypass airflow to increase the propulsive efficiency and reduce the specific fuel consumption.

The open-source software MULTALL (Denton, 2017) has been used to design the front stage of the IGT compressor. MULTALL (Denton, 2017) is a 3D CFD solver with an added feature to perform quasi-3D blade-to-blade calculation and axisymmetric throughflow calculation. MULTALL is combined with 2 functions : 1D mean-line program that can generate velocity triangles (MEANGEN) and blade geometry generation and manipulation program (STAGEN). Fig. 3.4 shows the flowchart of the open-source turbomachinery design software MULTALL (Denton, 2017). Representative values of pressure ratio, mass flow rate, RPM, etc are considered from the specification for existing machines[1] in the market. The velocity triangles are generated for the tip, mean and hub streamlines using MEANGEN (Denton, 2017). In contrast to the military aircraft engines, the civil aviation turbofan engines have in recent years started migrating towards the low specific thrust cycles. This transition to low specific thrust cycles is a direct consequence of requiring improved specific fuel consumption. This mandates the development of high mass flow and low-pressure ratio fan designs (Lee et al., 2017). With this as base, a low-speed, part span loaded, wide chord blade rotor was developed as a third test case as shown

[1] https://www.mhps.com/products/gasturbines/lineup/m501j/index.html

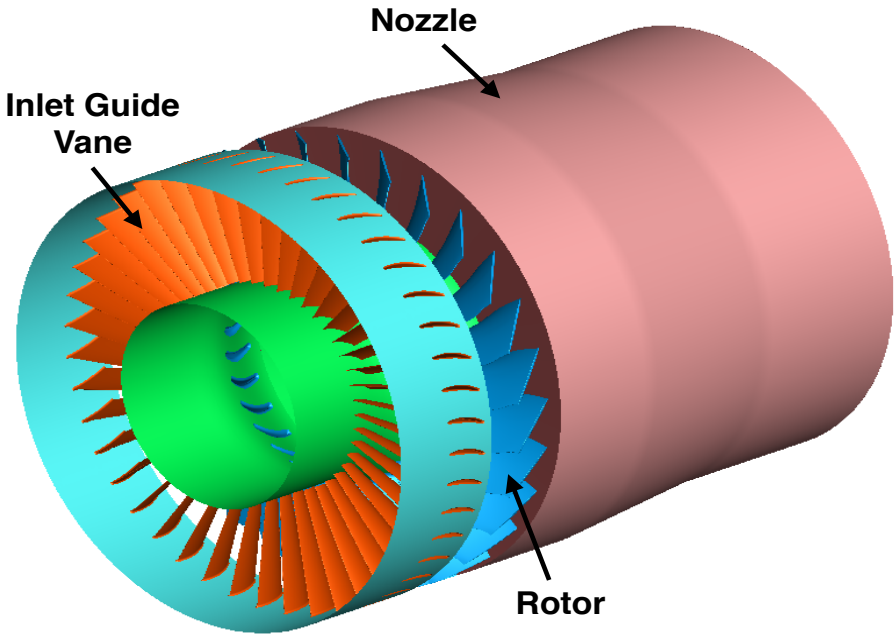


Figure 3.2: Computational Domain Of 1-Stage Compressor Used In A Typical IGT

in fig. 3.3. While the inlet and outlet casing diameters of both NASA Rotor 67 and wide chord blade rotor were kept same, the hub diameter of the former is slightly larger than the later.

Table 3.1: Blade Design Control Parameters

No.	Design Parameter	Category
1	Blade Count	Blade
2	Incidence Angle	Blade Section
3	Deviation Angle	
4	Front Camber	
5	Front Chord	
6	Maximum Thickness	
7	Location of Maximum Thickness	
8	Leading Edge Radius	
9	Trailing Edge Radius	
10	Polynomial Order For Thickness Distribution	
11	Axial Gap	Blade
12	Sweep	

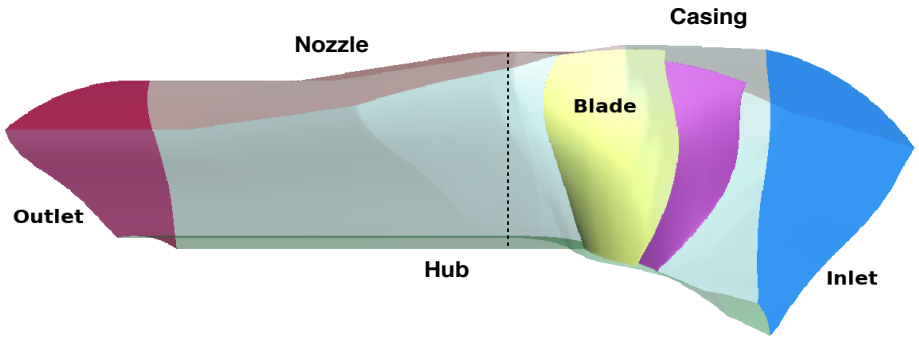


Figure 3.3: Computational Domain Of Wide Chord Blade

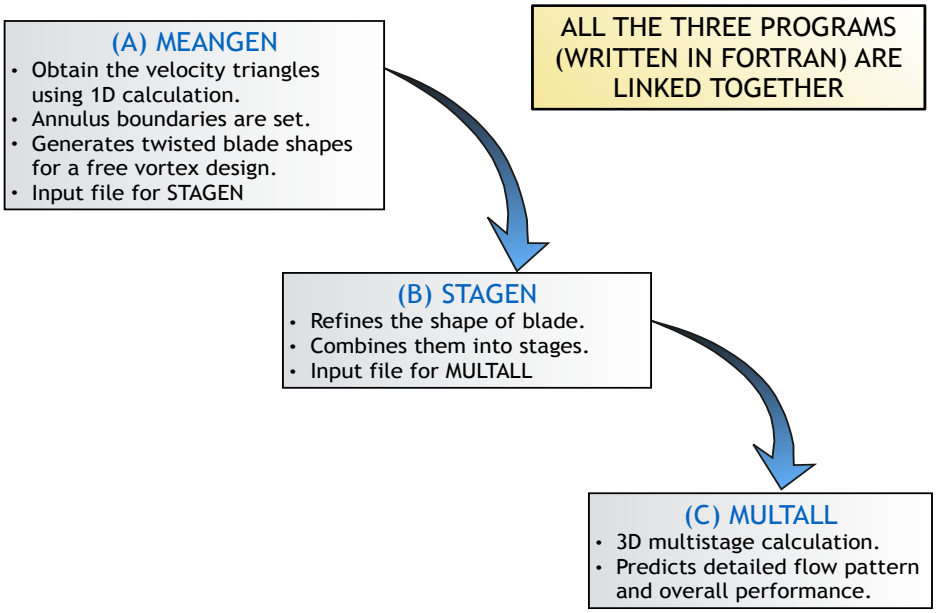


Figure 3.4: Functions Used In MULTALL (Denton, 2017)

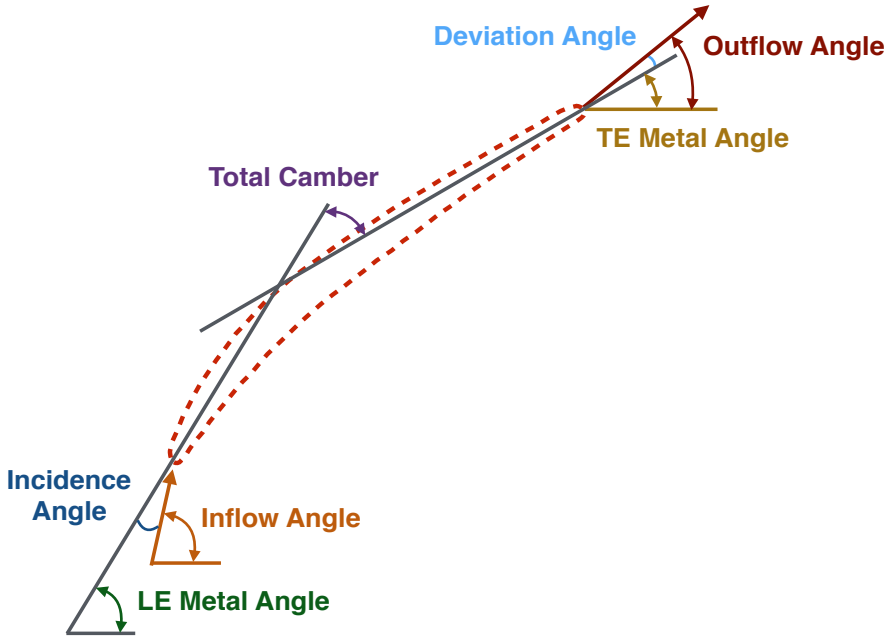


Figure 3.5: Parameterisation Of Blade Section

For the purpose of blade geometry design, a Controlled Diffusion Airfoil (CDA) generation toolkit was developed at ICL (UK) in association with MHPS Ltd. (Japan). The purpose of this toolkit was to handle the different geometries, allow flexibility in varying the 1-stage compressor set-up and provide input to in-house mesh generation software. This toolkit is based on parameterisation used in STAGEN (Denton, 2017) and uses the following independent shape parameters as shown in table 3.1. Fig. 3.5 shows the usage of double arcs to define the total camber. The camber line of the airfoil is defined using parameters 4 and 5 in the *table* 3.1 while the thickness of the airfoil is distributed on the camber line using parameters 6-10 in the *table* 3.1. The three airfoils at tip, mean and hub are radially stacked with the centroid of each airfoil placed on stacking line.

Table 3.2 provides a brief comparison of the various test cases viz. NASA Rotor 67, wide chord blade and 1-stage IGT compressor in terms of number of blades, pressure ratio, nominal tip gap, hub-tip ratio, mass flow rate per unit area and non-dimensional design speed. Fig. 3.6 shows the difference between the three testcases by comparing the spanwise profile of normalised pressure ratio at respective peak efficiency condition. As can be seen, both NASA Rotor 67 and rotor of IGT is highly tip loaded while the wide chord blade is part span loaded. The difference in design architecture between these blades will enable one to compare and rank the

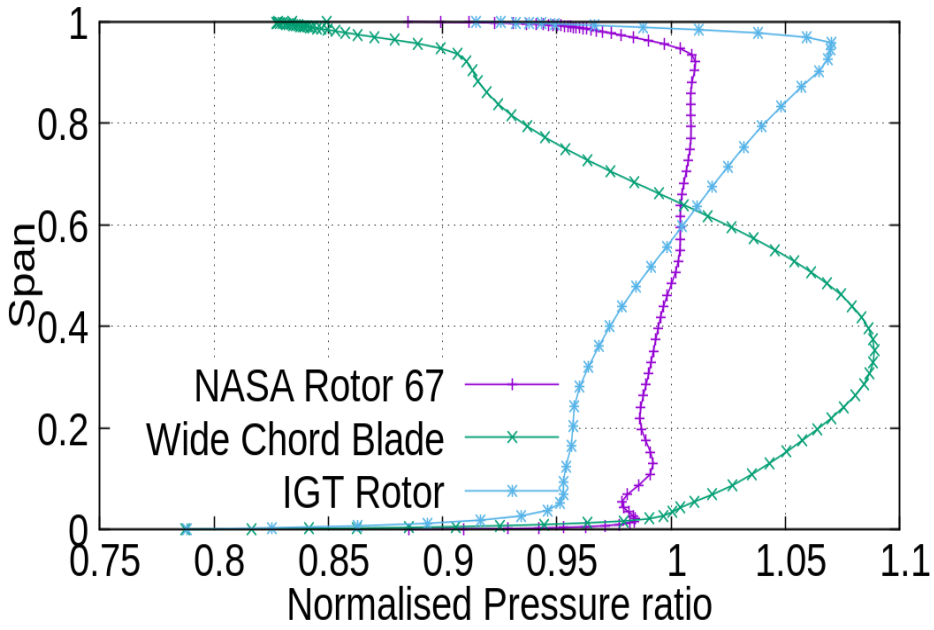


Figure 3.6: Normalised Pressure ratio Of Different Blades At Respective Peak Efficiency

effects of manufacturing tolerance (specially tip gap variation) on aerodynamic stability (stall) for different loading distributions.

Table 3.2: Comparison of Different Test Cases

Design Specifications	NASA R67	Wide Chord Blade	1-Stage IGT
Number of Blades	22	18	28
Nominal Tip Gap	0.376% span	0.45% span[2]	0.33% span[3]
Pressure Ratio	1.63	1.26	1.78
Hub-Tip Ratio (Inlet-Exit)	0.375 - 0.478	0.247 - 0.32	0.5 - 0.583
Non Dimensional Mass Flow Rate (Q)	0.0277	0.031	0.0295
Non-Dim. Rotational Speed ($ND/\sqrt{RT_{01}}$)	14.156	11.106	15.022

[2,3] The value of nominal tip gap has been chosen based on past experience

3.3 Boundary Conditions

Fig. 3.7(A) shows the schematic of computational domain in the present research. As can be seen, depending on the test case at hand, it consists of (a) Inlet duct or Inlet Guide Vane (IGV) (b) Rotor Domain (c) Nozzle. For the ease of visualisation, different blade rows in fig. 3.7(A) has been shown with gaps. As is the usual practice, the interface between a stationary and a rotating blade row is modelled as mixing plane in all the steady computations. The mixing

planes used circumferentially mix out the flow quantities at the inlet and the exit boundaries of each blade row as given in Denton (1992).

To predict the performance and stability margins of a rotor (in the presence of any geometric variability) computationally, it is necessary to include all the blades of the rotor domain. When all the blades in the rotor have the same geometric dimension (ideal scenario), we can take advantage of the symmetry and use a single blade along with the use of periodic flow condition at the passage boundaries. Such a sector is called as single passage rotor domain. A double passage rotor domain can be used to model the behaviour of two different blades that are arranged alternately. Similar to the single passage rotor domain, a periodic flow condition is imposed on the passage boundaries of double passage rotor domain due to repeating symmetric pattern. It is to be noted that a double passage computation cannot be carried out if odd number of blades are present in the rotor. Fig. 3.7(B) shows a schematic of the single passage rotor domain and double passage rotor domain respectively. It can be seen that the imposition of periodic flow condition at the passage boundaries reduces the size of the computational domain and thus the time required to solve it compared to a full annulus CFD simulation. In case of single passage rotor domain, the passage boundaries are represented by set of periodic surfaces P_1 and P_2 while for double passage rotor domain, the passage boundaries are represented by the periodic surfaces P_1 and P_3. As a general rule, any number of passage 'n' can be used in computation provided the pattern of 'n' is repeating throughout the annulus. In other words, previous statement could also be reframed as the total number of blades 'N' has to be a multiple of the number of passage 'n' being used in computation. A whole annulus simulation has been performed when the given geometry lacks any symmetry. This method of solving a turbo-machinery problem is ubiquitous to a lot of research papers found in the literature (Wilson et al., 2006; Stapelfeldt, 2014). However, Hsu and Hoyniak (2011) have used 3-blade model, 5-blade model, 7-blade model and 11-blade model to study the influence coefficient method in flutter and forced response of a disk consisting of 24 blades.

The operating point of the rotor is controlled by variable area nozzle. The flow through the nozzle is controlled by changing the area ratio which is achieved by changing the angle of the nozzle. The total pressure, total temperature and flow angles are specified as the inlet boundary

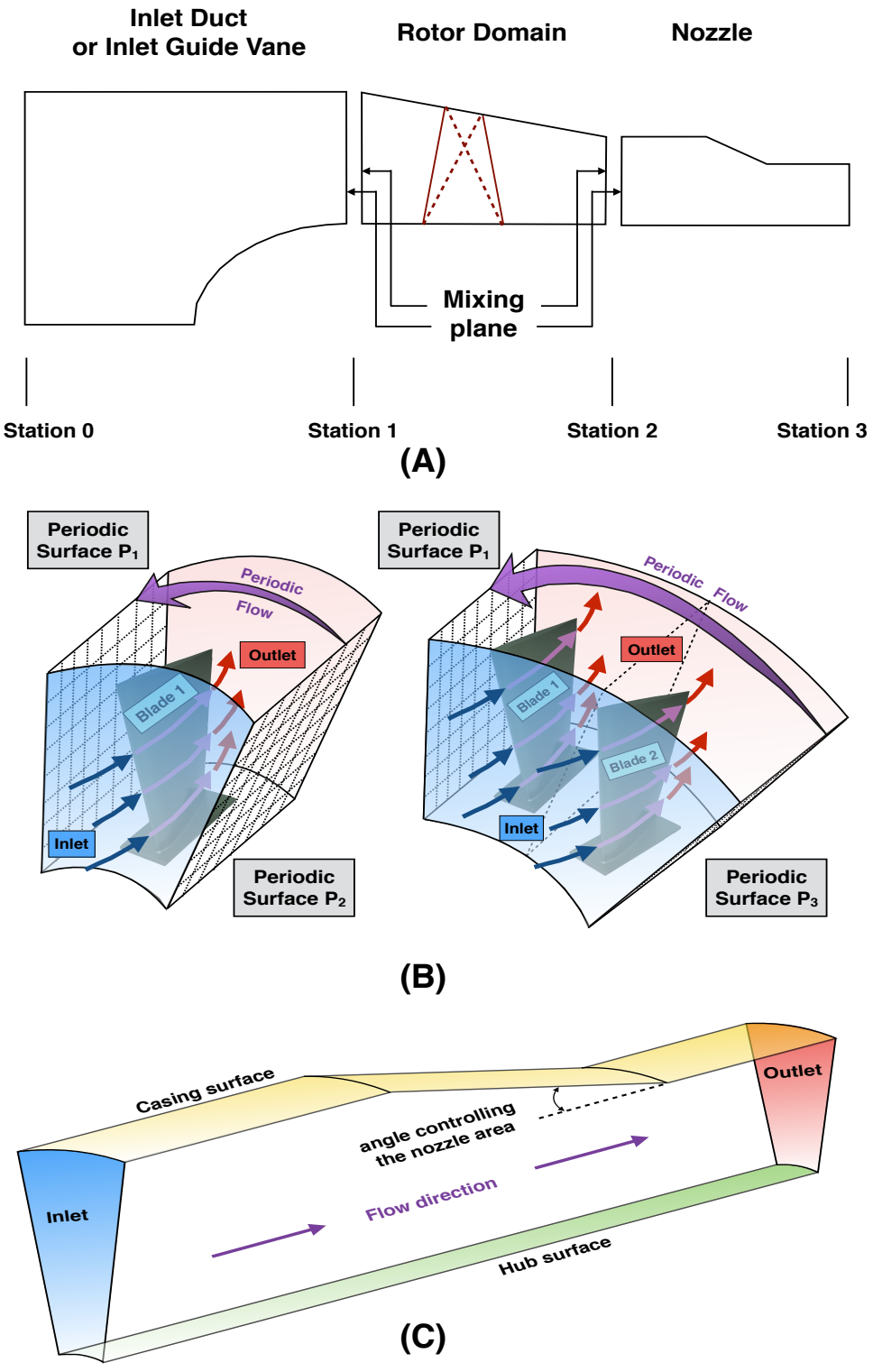


Figure 3.7: Schematic Showing (A) Computational Domain (B) Single Passage Rotor Domain (Left) And Double Passage Rotor Domain (Right) (C) Variable Area Nozzle

condition at Station 0 and a choked nozzle is used at the outlet at Station 3 in fig. 3.7(A). A choked nozzle ensures that disturbance from the exit does not propagate upstream and the flow becomes independent of the exit condition (Vahdati et al., 2005). As the rotor operating point moves from choke to stall, the nozzle is closed gradually in discrete steps as shown in fig. 3.7(C) which ensures a gradual reduction of mass flow rate accompanied by a corresponding increase in pressure ratio.

3.4 Mesh Generation

Fig. 3.8(A) shows the mesh corresponding to NASA Rotor 67. As seen in the figure, the mesh is semi-structured with the boundary layer region around the airfoil having a body-fitted O grid while rest of the region is unstructured. NASA Rotor 67 has been studied for different tip gaps. Fig. 3.8(B) shows a schematic of the radial mesh spacing adopted for gridding blades with different tip gaps. As can be seen, the entire region has been divided into 3 distinct parts. In part (I), the radial layers for the smallest blade A is chosen such that it is fine towards the blade tip and the hub while gradually coarsens towards the mid span region (this mesh will be used as it is in the largest blade including the intermediate ones). The part (II) starts from the tip gap region for the largest blade up-to the blade tip of the smallest blade. This region is equispaced such that all the intermediate tip gap sizes can be covered. All the remaining area up-to the casing forms part (III) of the region. The mesh spacing in part (III) has been kept the same as that in part (II) though it can be made finer according to the need. With this spacing, the grid on the periodic boundary will be independent of the tip gap size while ensuring a similar mesh count for rotors with different tip gaps. The same meshing parameters have been used in case of wide chord blade as used in NASA Rotor 67 since the size of the two computational domains are similar and comparable.

In this thesis, a study related to damaged blades has been considered in the rotor of 1-Stage IGT. Seven levels of damage have been considered with each level indicating progressively higher damage both chord-wise as well as radially. A mesh-morphing tool has been used to generate

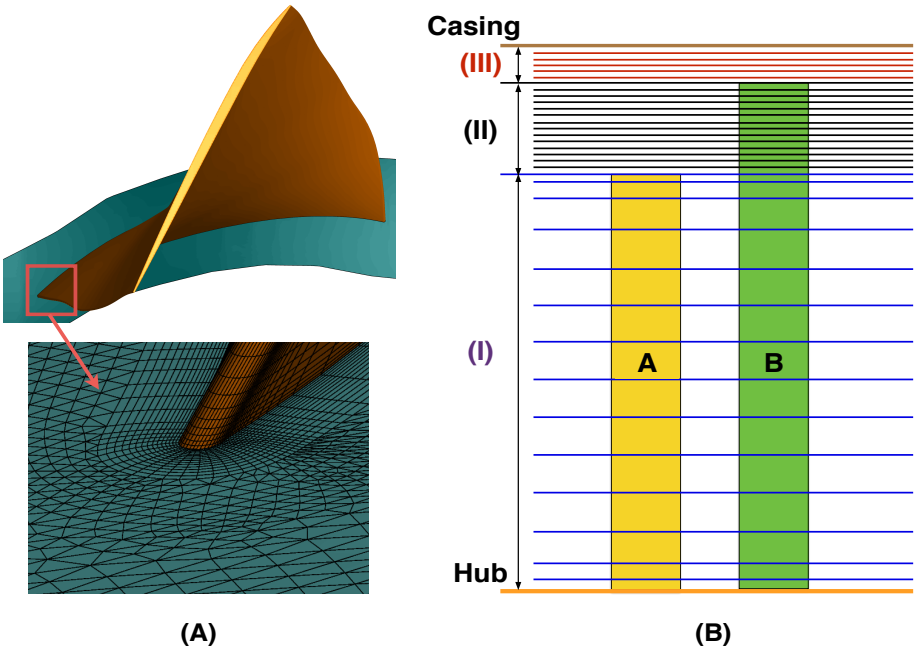


Figure 3.8: (A) Mesh Around The Blade Of NASA Rotor 67 (B) Radial Mesh Strategy In Case Of Blades With Different Tip Gaps

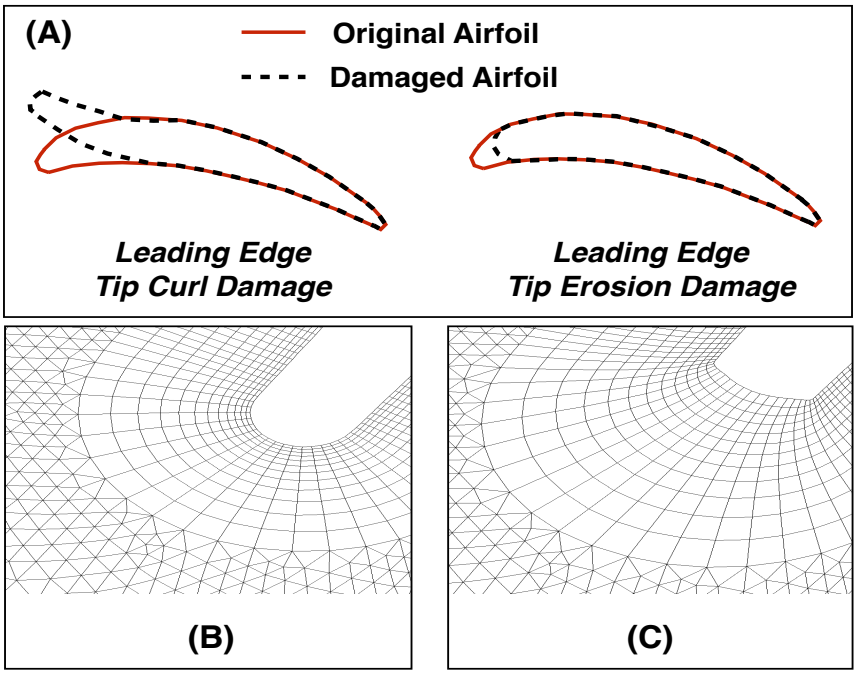


Figure 3.9: (A) Schematic Of Different Leading Edge Damages (B) Mesh Around Undamaged Rotor Blade Of 1-Stage IGT (C) Mesh Around Damaged Rotor Blade Of 1-Stage IGT

damaged blades from the datum mesh of blade having nominal tip gap of 0.33% of span. The damage could be classified as either leading edge curl damage or leading edge erosion damage as shown in Fig. 3.9(A) (Roberts et al., 2002; Li and Sayma, 2015). The present paper does not consider the leading edge tip curl damage at the rotor tip. Fig. 3.9(B) and (C) show the mesh around the undamaged blade and leading edge damaged blade respectively. The damage has been represented in terms of a hyperbolic tangent function as it has a gradually increasing slope which represents the actual blended blade better. It also has an added advantage of the mesh not getting distorted while undergoing mesh morphing as there is no drastic change of slope.

3.5 Scalability Test

A scalability study is performed to decide the optimal number of mesh points per CPU. This study is also important from the perspective of building a data driven surrogate models as it allows researchers to plan and schedule the simulations required for building surrogate model. Future researchers would have to do a similar scalability study for the hardware and the CFD code they would be using.

Scalability analysis can be performed in two ways: (A) strong scalability analysis (B) weak scalability analysis. In case of strong scalability, the problem size remains the fixed and the number of CPUs increase. The objective in this case is to find the "sweet-spot" wherein the computation can be completed in reasonable amount of time without wasting time due to parallel bottlenecks. On the other hand, in case of weak scalability, the workload assigned to each CPU remain the same which implies that problem size increases proportionally with an increase in the number of processors. It is difficult to obtain strong scalability with higher number of processors since the communication overhead also increases proportionally. On the other hand, most programs are linearly scalable even at higher processor counts when testing the weak scalability. This is because the amount of work done by each processor in an ideal case is almost constant and hence the communication overhead also remains almost constant

Lantz, 2015[4]. Both the scalability analyses have been done in the present study.

Scalability study in the present thesis has been conducted using the high performance computing (HPC) services available at Imperial College London, UK. The HPC services are upgraded regularly with newer computing architecture keeping in view the evolving research requirements. With each such upgrade, the maximum number partitions per job and the total number of CPUs per researcher is rationed accordingly. While the absolute time required to solve the problem would reduce with each such upgrade, the scalability study would be still be dependent on the efficient parallelisation of the AU3D code and as such this study would give a direction on the optimal number of partitions and also the mesh points per CPU. In the present scalability study, a single passage of rotor of NASA rotor 67 has been considered with the mesh size progressively increasing from 19 million up to 102 million. Each of these meshes have been partitioned into 12, 24, 36, 48, 60, 72 and 96 parts and solved on CX1 computer cluster at Imperial College London, UK. The average (wall) time required to run 50 time steps has been plotted against the number of CPUs for all the cases (the average wall time was obtained by repeating the same computation 7 times). A wall time instead of CPU time has been used as it includes both the calculation of algorithm and the communication between the processors.

As seen in fig. 3.10, the time required to solve is directly proportional to the mesh size and is inversely proportional to the number of partitions. To get a better picture, for each mesh size we non-dimensionalize the time required to solve 50 time steps with different partitions with respect to the baseline time for 12 partitions of the mesh size under consideration. As seen in fig. 3.11, a scalability of almost 5.5 to 6 is obtained for 96 partitions of all the different meshes under consideration (ideal case should have been 8). The divergence between actual scaling and ideal scaling starts amplifying after 36 partitions.

As the mesh size does not increase in exact proportion to the number of processors, it is difficult to make sure that the workload assigned to each CPU remains the same as the problem size increases. Hence, the mesh size and the number of partition are chosen such that an approximate value of 1 million mesh points per CPU are obtained. A weak scalability study for the same is

[4] `https://www.cac.cornell.edu/education/training/stampedejan2015/scalability.pdf`

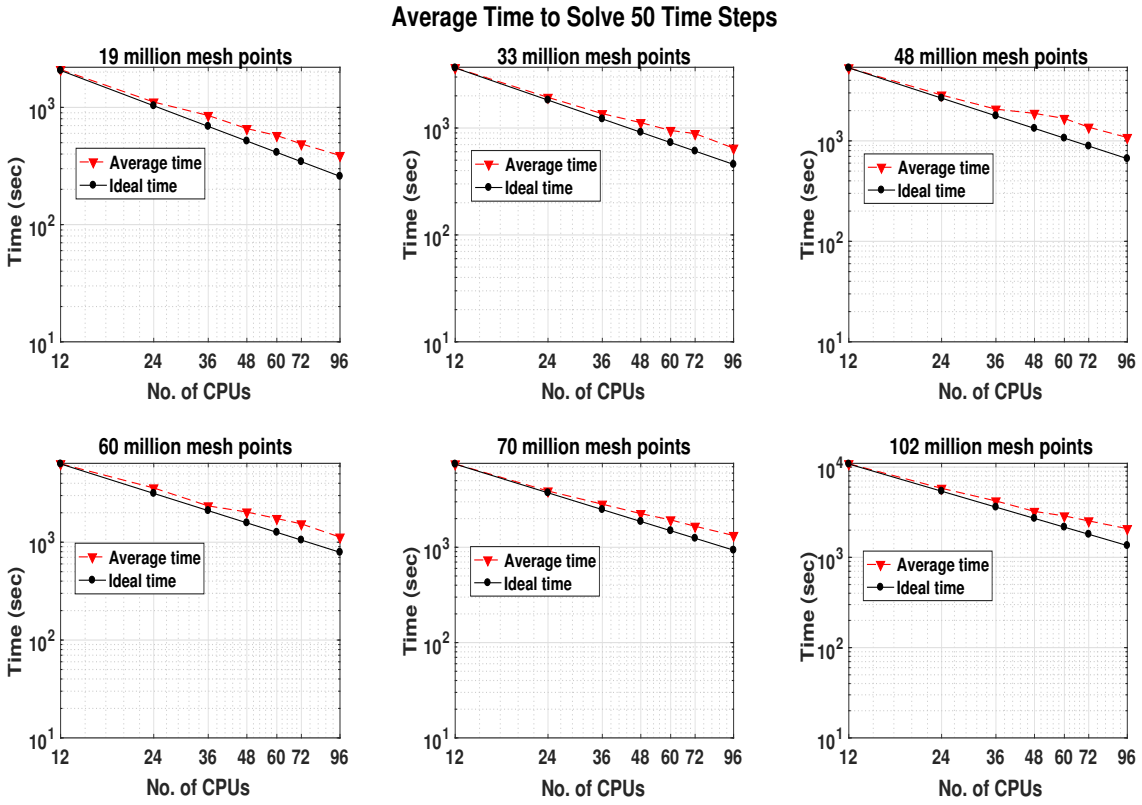


Figure 3.10: Time Required to Solve In AU3D For Different Meshes Sizes

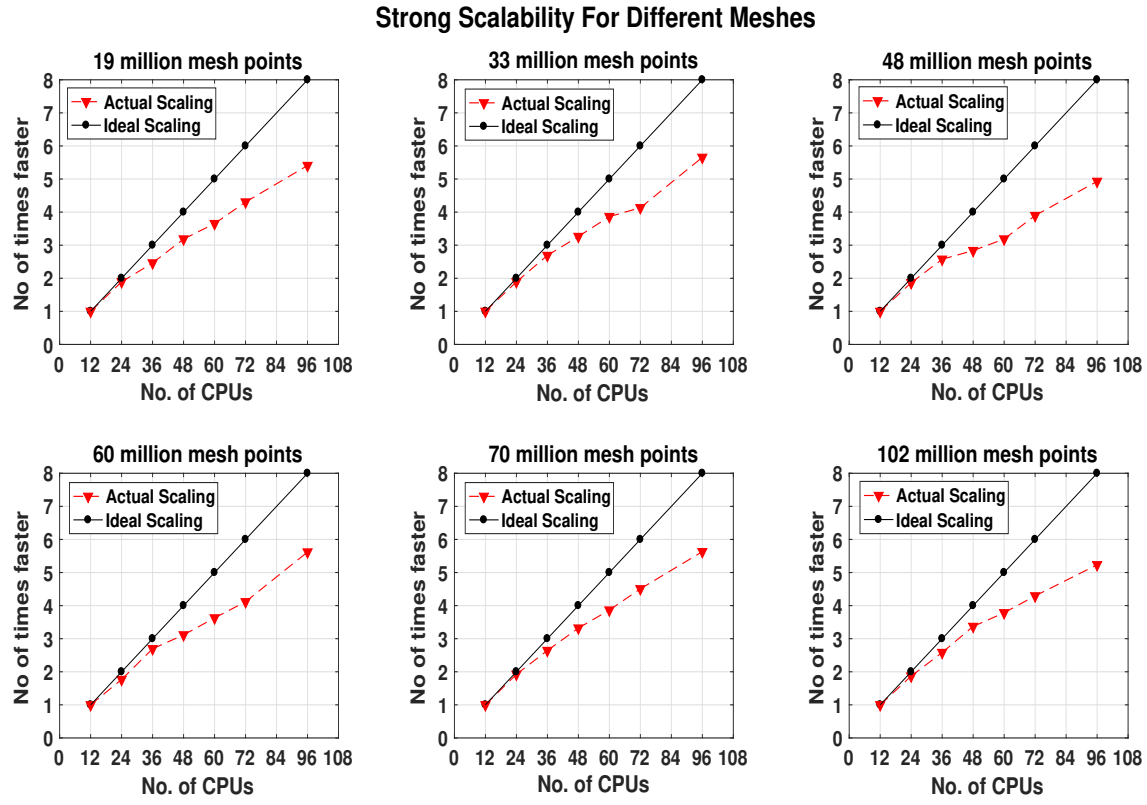


Figure 3.11: Strong Scalability Test For Different Meshes In AU3D

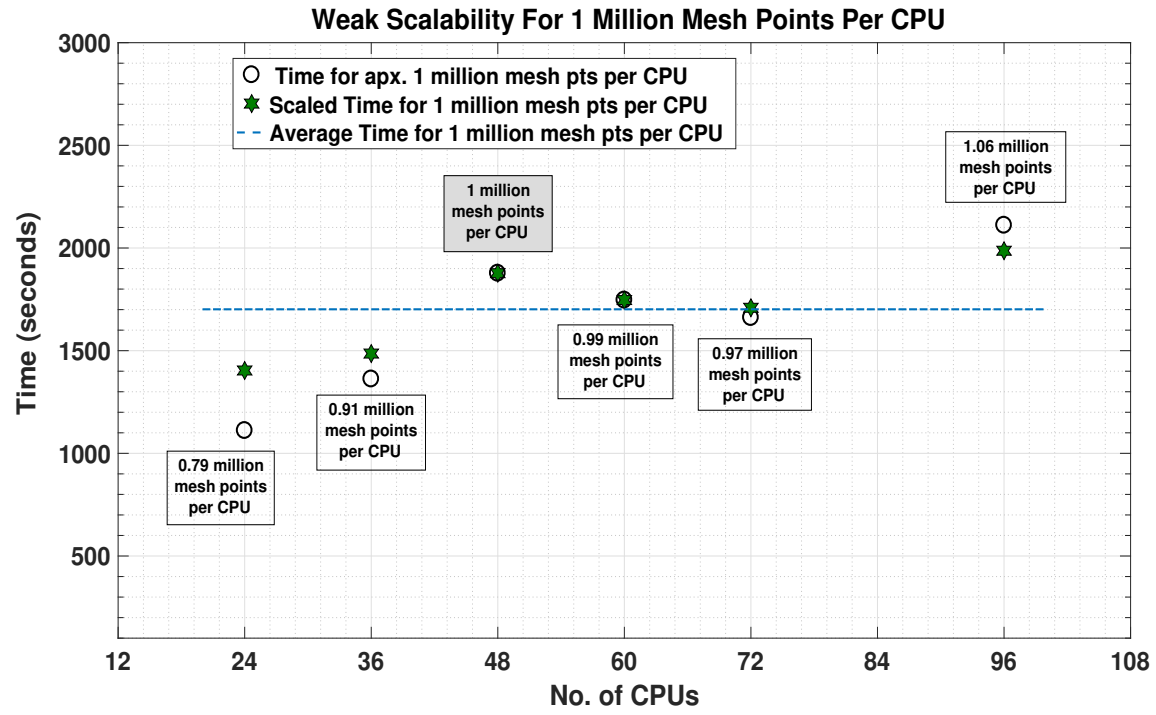


Figure 3.12: Weak Scalability Test For 1 Million Mesh Points Per CPU In AU3D

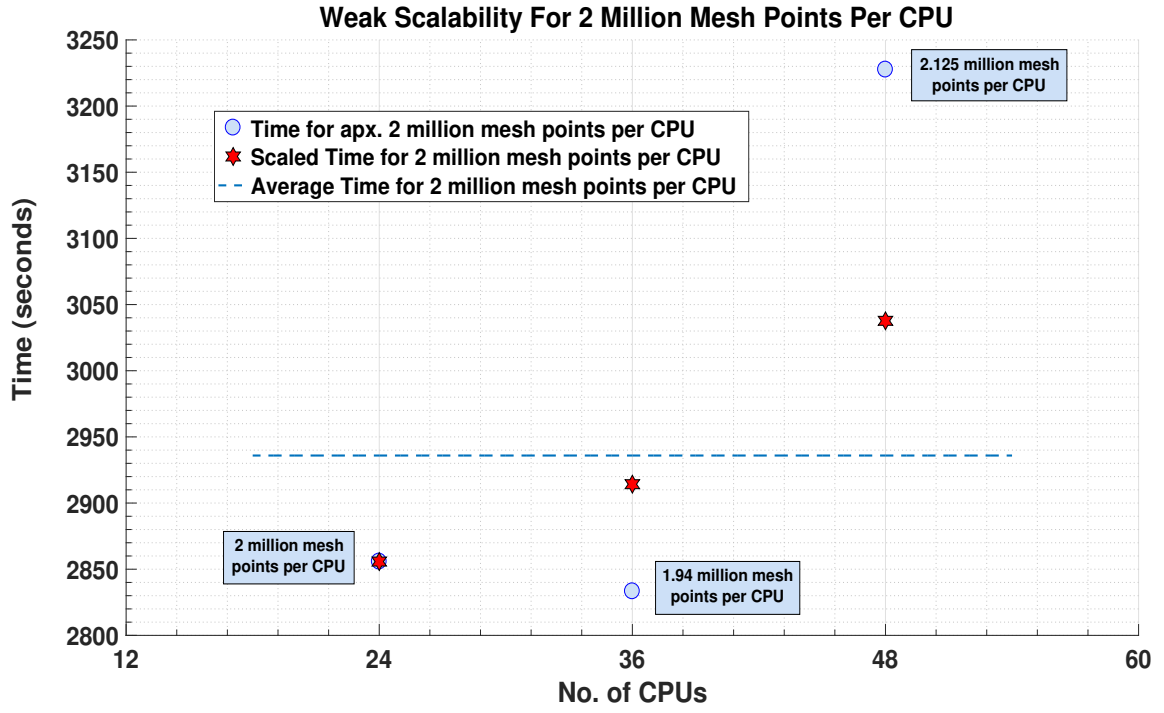


Figure 3.13: Weak Scalability Test For 2 Million Mesh Points Per CPU In AU3D

shown in fig. 3.12 and fig. 3.13 respectively. In fig. 3.12, the time required to solve approximately 1 million mesh points per CPU is linearly scaled such that it now represents the time required to solve exactly 1 million mesh points per CPU. An average time from different cases of 1 million mesh points per CPU is plotted to show the spread of time required for each case of 1 million mesh points per CPU. Similar steps are repeated incase of weak scalability study of 2 million mesh points per CPU as shown in fig. 3.13. From the average time required to solve the two cases of 1 million mesh points per CPU and 2 million mesh points per CPU, it can be seen that it takes 73% more time in the later case for solving twice as many mesh points per CPU. While a case with less than 1 million mesh points per CPU would result in a faster computation, the accuracy of the results might be negatively affected due to coarser mesh (this has to be confirmed using mesh convergence study). This study thus establishes a mesh limit of approximately 1 million mesh points per CPU and number of partitions to be equal to or less than 36.

As said earlier, with each upgrade of HPC architecture over a period of time, the maximum number partitions per job and the total number of CPUs per researcher gets rationed. The latter upgrades[5] allowed partitions of 24, 48 (Job Class : singlenode) and multiples of 32 up to 512 (Job Class : general; poor interconnecting network). The domain size was thus fixed to a maximum of 24 partitions with approximately 1 million mesh points per CPU subjected to mesh independence study.

3.6 Mesh Independence Study

Similar to the earlier scalability study, a mesh independence study is also important while building a data driven surrogate model. It is necessary that researchers choose an optimal grid size in terms of solve time as well as converged values. It would also help researchers assess the prediction of quantities of interest (QoI) by the surrogate model vis-a-vis a CFD simulation. All the performance curves shown in this paper have been computed using a steady RANS solver.

[5] https://www.imperial.ac.uk/admin-services/ict/self-service/research-support/rcs/computing/job-sizing-guidance/high-throughput/

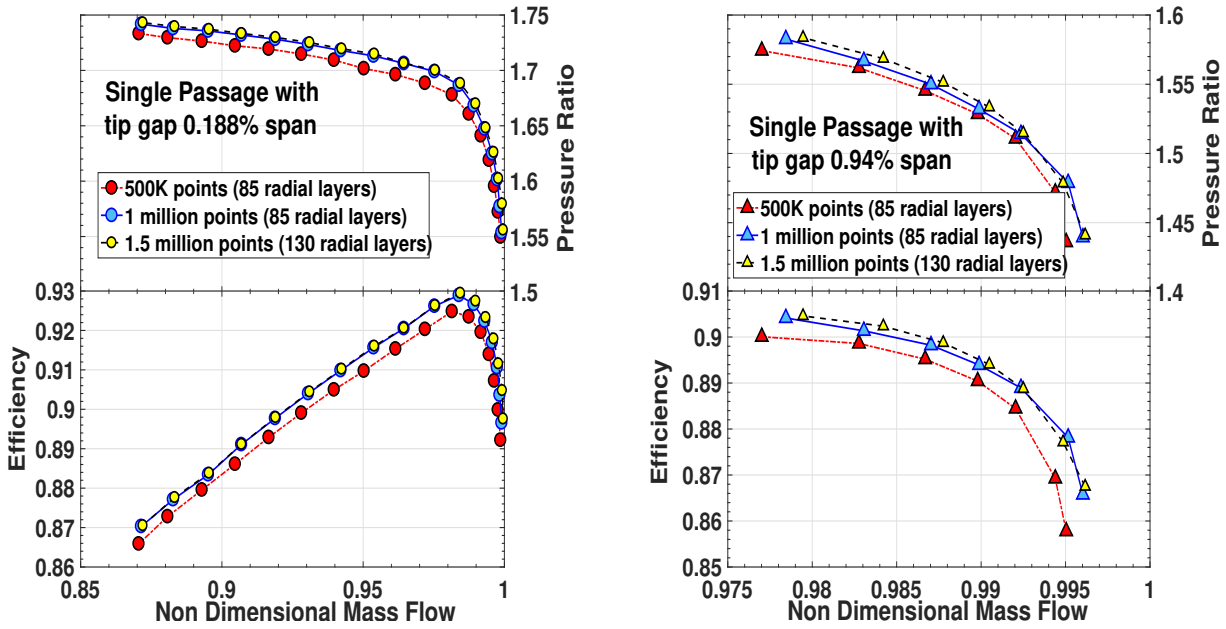
In case of NASA Rotor 67, many papers have adopted the nominal tip gap to be 0.61 mm in their computation (Arima et al., 1999; Choi et al., 2010) which can be traced back to Jennions and Turner (1993). A summary of all the values of different nominal tip gaps found in literature is listed in table 3.3. Five different tip gap sizes have been used in this study viz. 0.3 mm (≈ 0.188% span), 0.6 mm (≈ 0.376% span), 0.9 mm (≈ 0.564% span), 1.2 mm (≈ 0.752% span) and 1.5 mm (≈ 0.94% span). The nominal tip gap size is considered to be 0.6 mm (≈ 0.376% span) which is in line with the previous parametric studies performed using discrete tip gaps in case of NASA Rotor 67 (Adamczyk et al., 1993; Jennions and Turner, 1993). Table 3.4 shows a mesh convergence study been performed to check on the blades with maximum (0.94% span) and minimum (0.188% span) tip gaps in single passage (uniform tip gap) and double passage (alternate arrangement) simulation with mesh refinement in both blade-to-blade direction as well as radial direction (mainly in the tip gap region).

Table 3.3: Uncertainty In Nominal Tip Gap Of NASA Rotor 67 As Found In Literature

Method	Nominal tip gap	Range of tip gap
Experimental (Strazisar et al., 1989)	1 mm	-
Experimental (Roberts et al., 2013)	0.5 mm	-
Computational (Adamczyk et al., 1993)	0.225 mm	0-1.225 mm
Computational (Jennions and Turner, 1993)	0.61 mm	0.3-1.22 mm

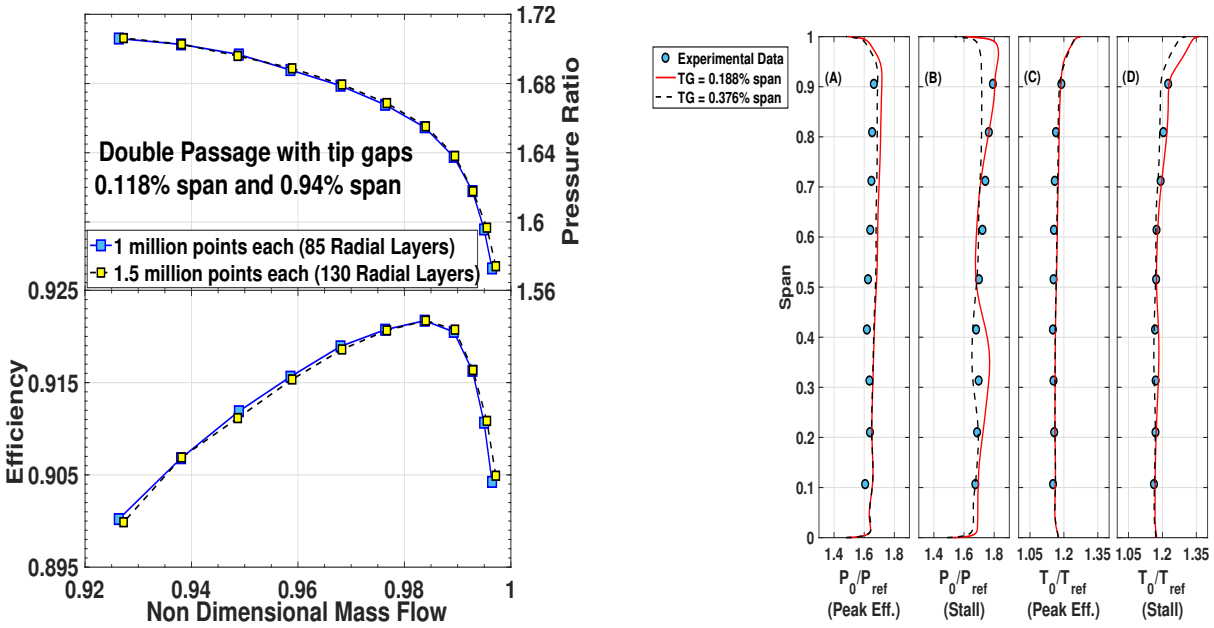
It can be seen from fig. 3.14 (A), (B) and fig. 3.15 (A) all the three cases have converged at a per passage mesh count of 1 million. Unless otherwise stated, all the performance curves in this paper pertaining to NASA Rotor 67 has been non-dimensionalised with respect to the choke mass flow with tip gap of 0.188% span (34.7 kg/sec). From fig. 3.15 (B), it can be seen that the results from the converged solution matched well with the experimentally available results from Strazisar et al. (1989). It has to be noted that the latest running tip gap mentioned in the Roberts et al. (2013) is 0.5 mm (≈ 0.3% span) and hence the experimental data in fig. 3.15 (B) is compared with the results for tip gaps 0.188% span and 0.376% span.

Two sets of measurement data has been noted in literature survey with regard to NASA Rotor 67, viz. Strazisar et al. (1989) and Fidalgo et al. (2012). As discussed earlier, the running



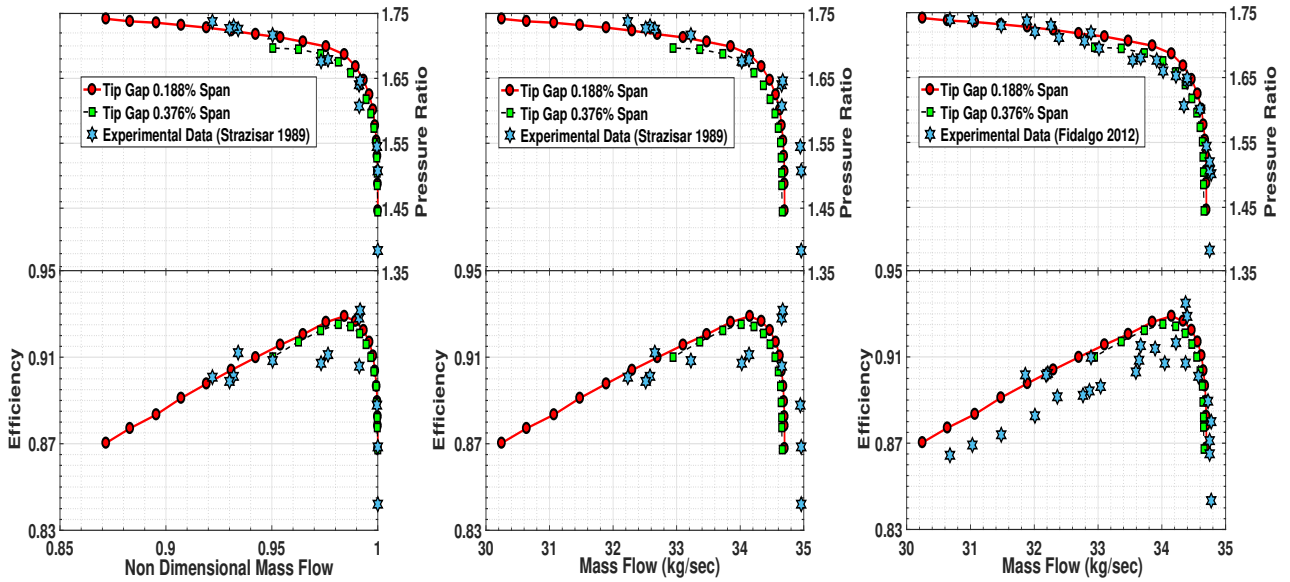
(A) Single Passage 0.188% Span Tip Gap (B) Single passage 0.94% span tip gap

Figure 3.14: Mesh Convergence For Different Single Passage Tip Gaps Of NASA Rotor 67 At 100% Speed



(A) Mesh Convergence For Double Passage With Tip Gaps Of 0.188% Span And 0.94% Span (B) Experimental Data vs. Simulation Results For NASA Rotor 67 At 100% Speed

Figure 3.15: NASA Rotor 67 At 100% Speed (A) Mesh Convergence Of Double Passage Mixed Tip Gaps (B) Span-Wise Experimental Data (At Peak Efficiency, Stall) vs Simulation Results



(A) Normalised : Experimental (Strazisar et al., 1989) vs Numerical

(B) Absolute : Experimental (Strazisar et al., 1989) vs Numerical

(C) Absolute : Experimental (Fidalgo et al., 2012) vs Numerical

Figure 3.16: Uncertainty In Experimental Data Of Performance Curve For NASA Rotor 67

tip gap measured by Strazisar et al. (1989) was 1 mm. It was observed that Fidalgo et al. (2012) reported a few extra points all along the performance curve that were not reported in the original report of Strazisar et al. (1989). Apart from this, Roberts et al. (2013) conducted experimental measurements to study the effect of superpolish on performance of NASA Rotor 67. For the same rotor speed and performance, they noted the running tip gap to be 0.5 mm.

Fig. 3.16 shows the comparison of the two sets of experimental data has been done with respect to computational data having tip gaps 0.188% span (0.3 mm) and 0.376% span (0.6 mm). As seen in fig. 3.16(A), the mass flow rate data from experiment (Strazisar et al., 1989) as well as the computation has been normalised with respect to respective choke mass flow rate. Fig. 3.16(B) and (C) show the comparison between experiment and computation at absolute mass flow rate for Strazisar et al. (1989) and Fidalgo et al. (2012) respectively. It can be seen that the computational results match very well with the experimental results. Similar such match between experimental and computational result in case of NASA Rotor 67 can be observed in Liou and Yao (2014).

Comparison of the relative Mach number contour obtained between CFD and Laser Doppler Velocimetry (LDV) in Strazisar et al. (1989) is shown in fig. 3.17, fig. 3.18 and fig. 3.19. The

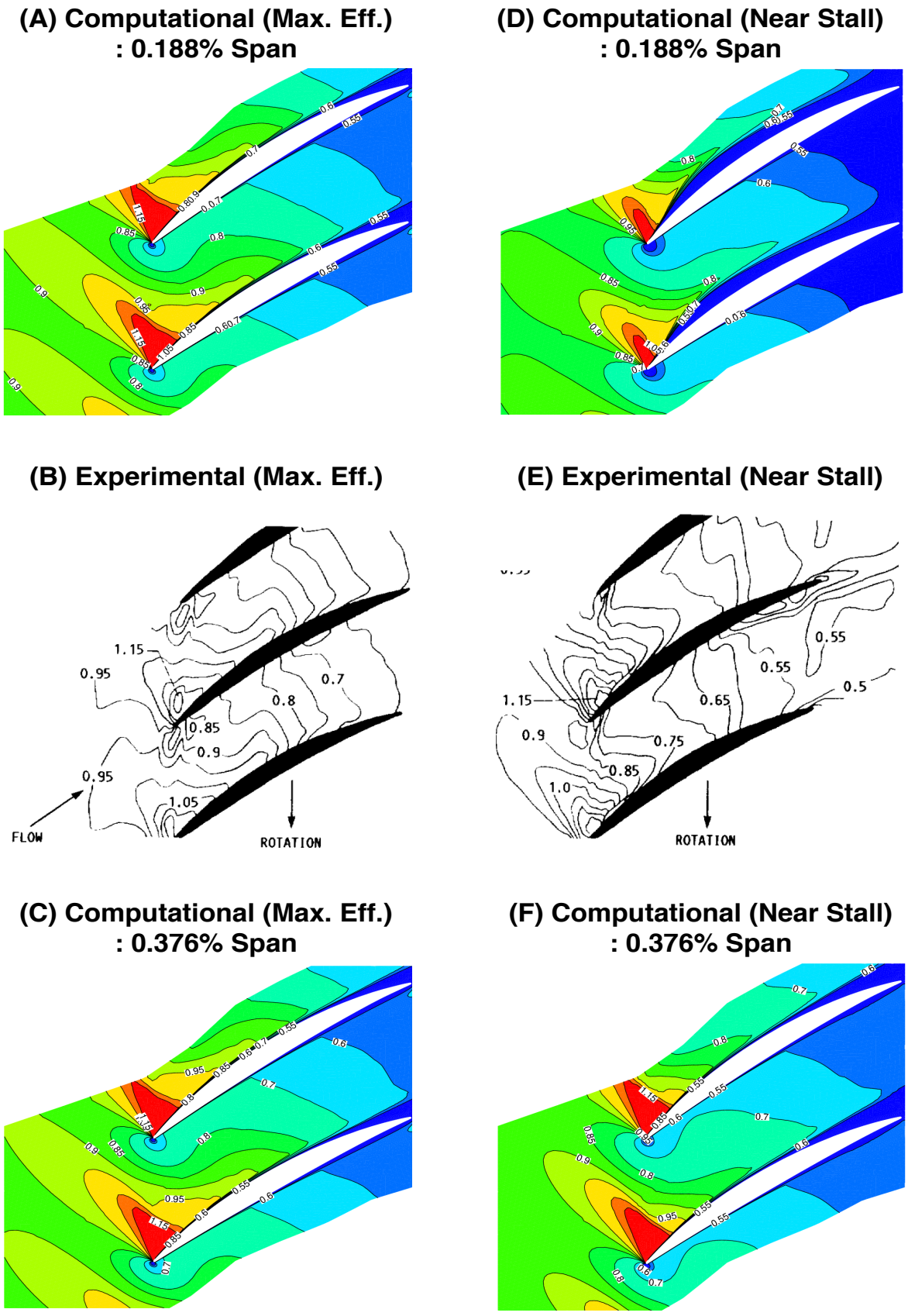


Figure 3.17: Experiment vs. Computational (tip gap of 0.188% span and 0.376% span) Flow Field At Maximum Efficiency (A, B and C) And Stall (D, E and F) At 30% Span From The Hub

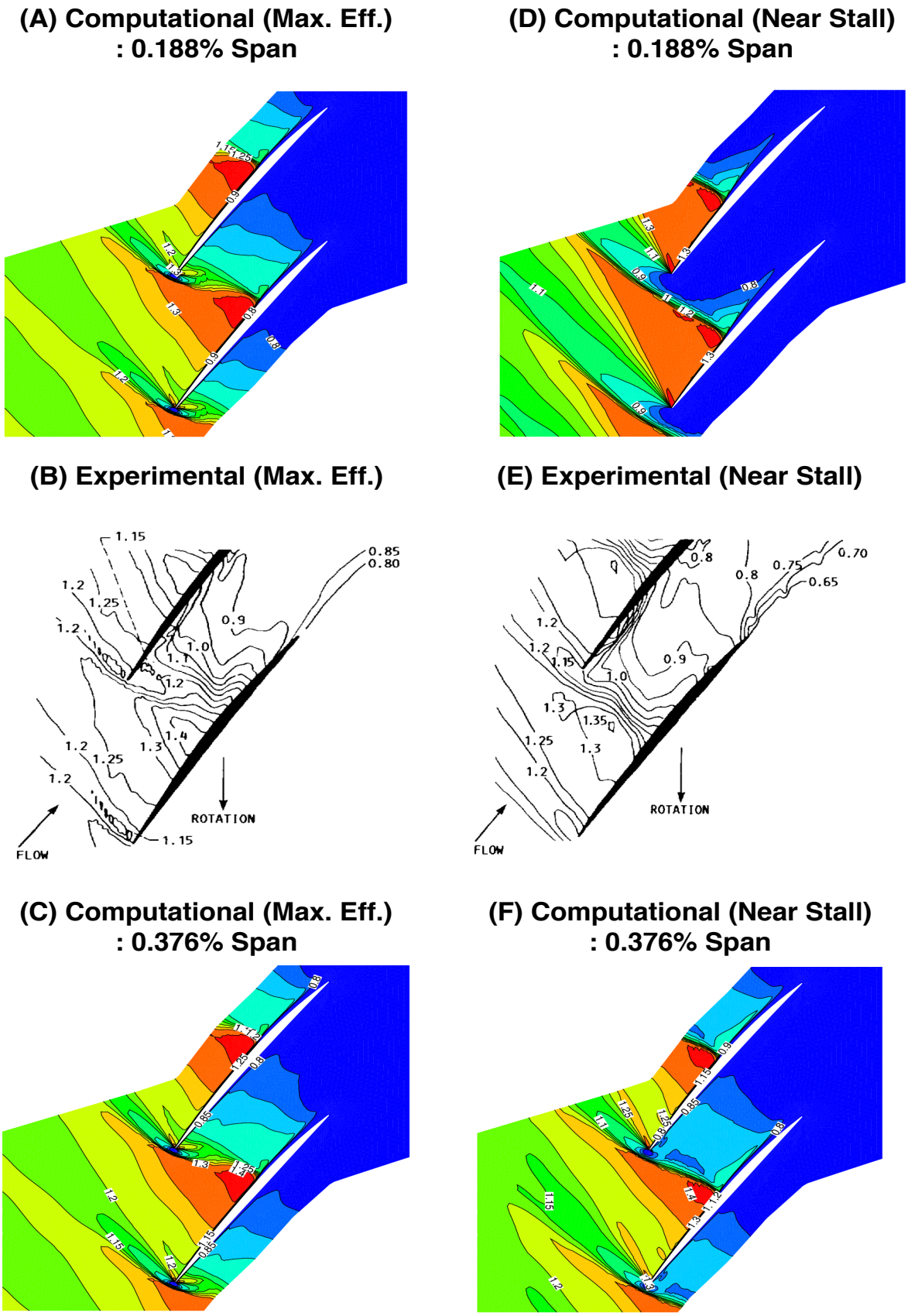


Figure 3.18: Experiment vs. Computational (tip gap of 0.188% span and 0.376% span) Flow Field At Maximum Efficiency (A, B and C) And Stall (D, E and F) At 70% Span From The Hub

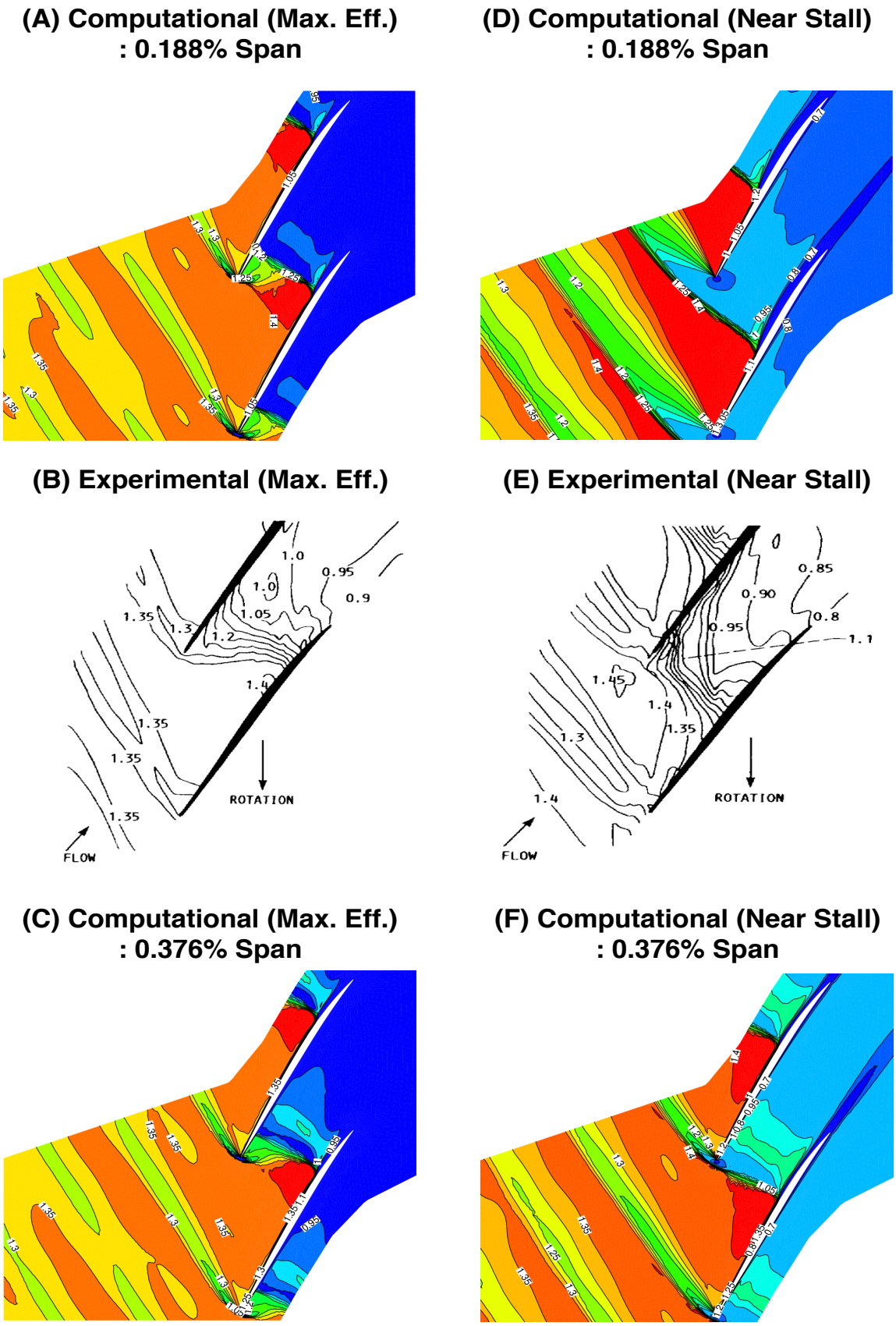
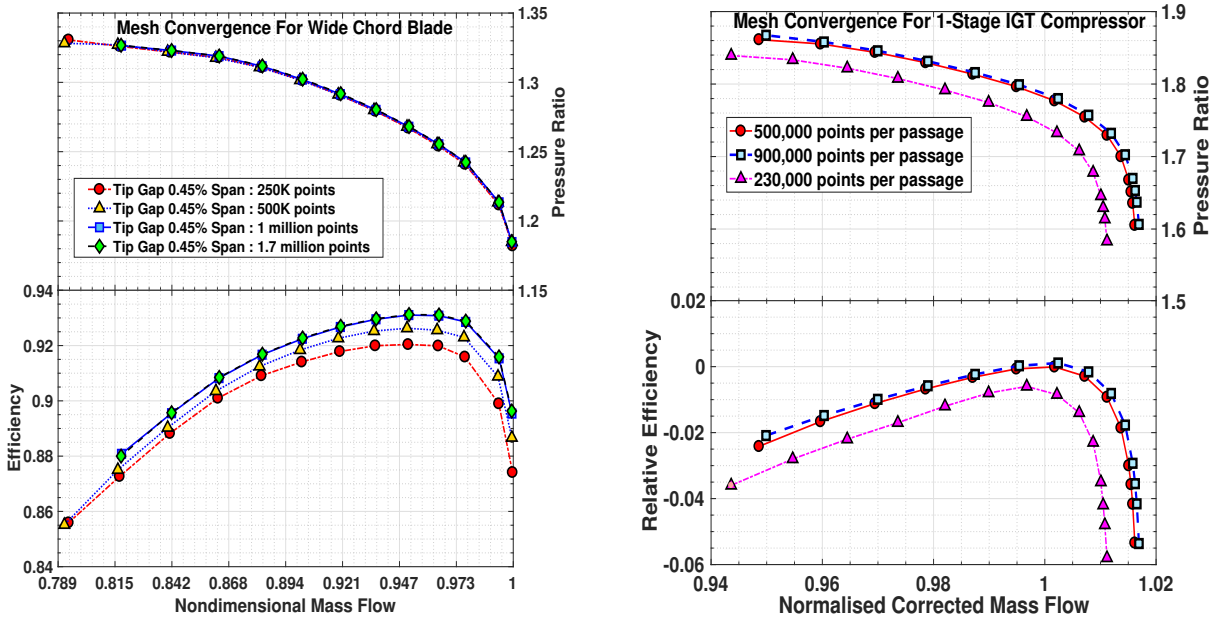


Figure 3.19: Experiment vs. Computational (tip gap of 0.188% span and 0.376% span) Flow Field At Maximum Efficiency (A, B and C) And Stall (D, E and F) At 90% Span From The Hub

Table 3.4: Mesh Convergence Study Of NASA Rotor 67

Case (Tip gap in % span)	Radial layers (Blade+Tip Gap)	Mesh count (million)
Uniform (0.188%)	85 (82+3)	0.5
Uniform (0.188%)	85 (82+3)	1
Uniform (0.188%)	130 (118+12)	1.5
Uniform (0.94%)	85 (70+15)	0.5
Uniform (0.94%)	85 (70+15)	1
Uniform (0.94%)	130 (70+60)	1.5
Alternate (0.188% and 0.94%)	85 (mixed)	2×1
Alternate (0.188% and 0.94%)	130 (mixed)	2×1.5

comparison has been carried out at peak efficiency as well as near stall condition at spans of 30% from hub, 70% from hub and 90% from hub. As seen, the position as well as strength of shockwave is reproduced very well. Strazisar et al. (1989) report about higher experimental uncertainty in the regions of high velocity gradients as the seeding particles may fail to follow the flow. The regions may occur at rotor passage shock and/or wake of the blade.



(A) Mesh Convergence For Wide Chord Blade (B) Mesh Convergence For Rotor Of 1-Stage IGT

Figure 3.20: Mesh Convergence At 100% Speed (A) For Wide Chord Blade (B) Transonic Rotor In 1-stage IGT

The casing diameter of the wide chord blade has been kept the similar to that of NASA Rotor 67. The hub diameter in case of wide chord blade is slightly smaller (and blade height of wide

chord blade is slightly bigger) than that of NASA Rotor 67. The number of blades in a wide chord rotor is 18 and the nominal tip gap is 0.45% span. The parameters used for meshing the wide chord including the radial gridding across the span of the blade is kept exactly same as that used for NASA Rotor 67.

In the next step, a grid convergence study is performed for the wide chord blade. It can be seen from fig. 3.20 (A) the mesh for wide chord blade converges at a per passage mesh count of 1 million points. The converged mesh consisted of a total of 85 radial layers along the span of the blade (including 9 radial layers in the tip gap region).

Finally, a mesh convergence study of 1-stage IGT was also carried out. A number of rotor meshes were generated by systematically varying the total number of radial levels (45 to 80) and also the blade-to-blade mesh for rotor domain (700 to 18,000 nodes per radial layer). Fig. 3.20 (B) shows the mesh convergence for 1-stage transonic rotor used in IGT. It can be seen that the convergence has been obtained at a mesh count of approximately 500,000 points per passage. The number of blades in the rotor of 1-stage IGT is 28 while the nominal tip gap is 0.33% span. This reference mesh consisted of 50 radial layers along the span (including 10 in the tip gap region). The IGV consists of 44 blades and a reference mesh of 0.44 million points per passage has been used in all the calculations. The performance curve for 1-Stage IGT has been depicted using normalised corrected mass flow (NCMF) and relative efficiency (RE) due to proprietary issues.

$$\begin{aligned} NCMF &= \frac{CMF}{C_1} \\ RE &= \eta - C_2 \end{aligned} \tag{3.1}$$

In the above equations, CMF is the corrected mass flow of compressor, η is isentropic efficiency of the compressor, C_1 is the corrected mass flow at design point and C_2 is isentropic efficiency at design point respectively. The constants C_1 and C_2 are used to normalise the parameters.

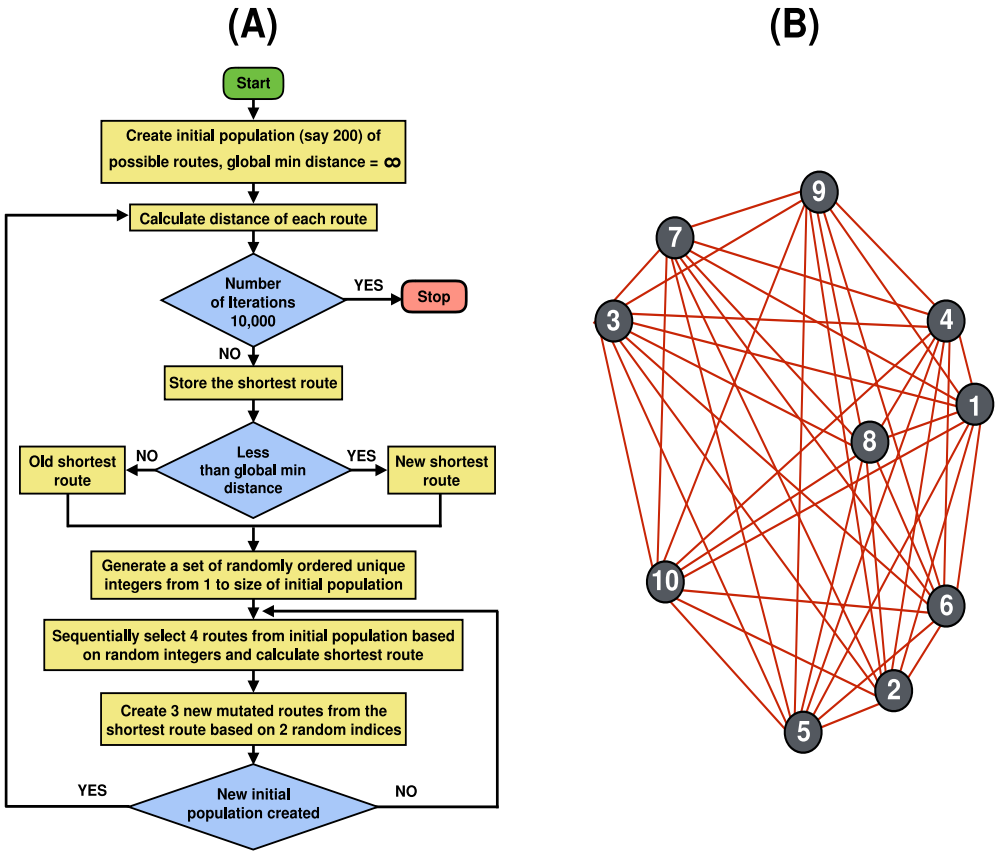


Figure 3.21: (A) Flowchart Of Travelling Salesman Problem Using Genetic Algorithm Adapted from (Kirk, 2014) (B) Schematic of Travelling Salesman Problem With Ten Different Cities and All Possible Routes

3.7 Travelling Salesman Problem

The travelling salesman problem (TSP) is a subset of combinatorial optimisation problem. It can be stated as the shortest route a salesman takes while travelling a number of cities such that he visits all the cities (in his itinerary) exactly once before returning home. This is a classic combinatorial optimisation problem that falls under the category of NP-hard (Awad et al., 2009) and is thus notoriously difficult to solve (Wang and Hong, 2010).

Awad et al. (2009) have made a comparative study of using genetic algorithm (GA) with other applied optimisation methods (linear, dynamic, Monte Carlo and heuristic search methods). It was concluded that a GA based approach provides an efficient search method with a significant lowest distance solution. It was further observed that a brute force exhaustive search algorithm fares worse as the number of nodes (cities) increase beyond 15.

Table 3.5: Example Of A Genetic Algorithm Used For Generating 3 Mutated Routes From The Shortest Route. Adapted from (Kirk, 2014)

Index Of City	1	2	3	4	5	6	7	8	9	10
Shortest Route (Iter 2)	1	6	2	10	3	8	4	7	5	9
Genetic Algorithm With 2 Random City Index e.g. (3,7)										
Flip Route	1	6	4	8	3	10	2	7	5	9
Swap Route	1	6	4	10	3	8	2	7	5	9
Slide Route	1	6	10	3	8	4	2	7	5	9

Fig. 3.21(A) and fig. 3.21(B) shows the flowchart of genetic algorithm used to solve TSP using an open source MATLAB code (Kirk, 2014) and a schematic of 10-city travelling salesman problem respectively. As seen in fig. 3.21(A), an initial population of the possible routes for travelling the 10 cities are created for which the distance is calculated. The shortest route detected in this first step is stored for future comparison. In the second step, a number of possible routes with randomly ordered cities are generated. These routes act as a set of newly created population which would be later subjected to mutation. 4 routes are out of this newly created population are randomly selected and shortest distance amongst them is calculated and stored. This step is repeated until there are no realisations left in the newly created population.

Three new mutated routes are then created for each shortest route stored in the second step as shown in *Table* 3.5. The first mutated route is a flip route wherein the order of all the cities between the two random city indices are flipped while keeping the rest of the city order the same as the parent route (shortest route). The second mutated route is a swap route wherein the two cities represented by the two random city indices are interchanged while the rest of the city order is the same as the parent route (shortest route). The third mutated route is a slide route wherein all the cities between and including the two random city indices are circular shifted. These mutated routes along with the shortest routes stored in second step help create a set of new population. The shortest route calculated from this new population is compared with the shortest route obtained in the first step and the procedure repeats till convergence is obtained.

3.8 Chapter Summary

Three test cases viz. NASA Rotor 67, wide chord blade rotor and 1-stage IGT rotor used in the present thesis have been compared with respect to their pressure ratio, number of blades, rotational speed, pressure ratio and mass flow rate. It was shown that 1-stage IGT rotor was highly tip loaded, NASA Rotor 67 was moderately tip loaded and wide chord blade rotor was part span loaded.

The simulation strategy with respect to single passage, double passage and full annulus simulation was discussed. A chocked nozzle ensures the disturbance from the exit does not propagate upstream while the rotor is throttled from choke to stall by gradually closing the nozzle area. The meshing strategy has been chosen such that the grid on the periodic points will be independent of the tip gap size while ensuring similar mesh count for rotors with different tip gaps.

A scalability study in conjunction with mesh convergence study allows the domain size to be fixed to maximum of 24 partitions with approximately 1 million mesh points per CPU. Validation of NASA Rotor 67 with respect to flow field at peak efficiency and near stall condition has been carried out at 30% span from hub, 70% span from hub and 90% span from hub. In addition, characteristic curve at design speed predicted by CFD has been validated against experimental data given by various researchers. Uncertainty in the experimental data as given in different literature has also been recorded. The radial profiles of temperature ratio and pressure ratio at peak efficiency condition and near stall condition has been compared against experimental data given in literature. Finally the genetic algorithm based travelling salesman problem has been discussed which will be used in next chapter for optimal arrangement problem.

Chapter 4

Study Of Manufacturing Tolerance On Aircraft Engines

"The great differentiator in business is when an organisation steps out on its own and creates value from something never tried before or uses common fundamentals to drive significant value improvements in a clever way" - Kerry Baskins (Modern Manufacturing Vol. 2)

This chapter gives a brief introduction to metrology and quality control which deals with measurements and tolerance planning - a tool used in industries to represent and control the variations in manufactured components. The chapter then probes into the effect of manufacturing tolerance on NASA rotor 67 and the wide chord blade. Stagger angle variation and tip gap variation have been chosen as parameters of interest in this chapter. Unlike the previous research works which considered the effect of manufacturing tolerance on single passage case (*i.e.* all blades in a compressor were assumed to undergo same geometric variation), this research will study the performance and stability margin when all the blades in the compressor undergo simultaneous geometric variation. Parts of this chapter has been published in ETC Conference (Paper Number : ETC2019-178) and the extended work has been published in the Journal of Turbomachinery (Article Number : TURBO-19-1105).

4.1 Engineering Metrology And Quality Control

No two manufactured parts are exactly the same. This may arise due to wear of machining tools, different lubricants or coolants used during the manufacturing process (Britton, 2000), changes in ambient atmospheric conditions, different jigs and fixtures used in production, etc. Thus, acceptable variations in the dimensions of component are always applied such that the functionality is not adversely affected while also maintaining a low cost of production. As shown in fig. 4.1(A), each of the two mating parts (hole and shaft), have upper and lower limit of variation and the difference between the these two limits is called as tolerance. Allowance is difference between the lower limit of hole and upper limit of shaft. While positive allowance would give clearance fit, negative allowance would result in an interference fit.

The subject of Metrology deals with the science of measurements. Dimensional metrology is a branch of Metrology which concerns with the measurement of dimensions of a part. Dimensional metrology consists of (a) Linear measurements (b) Angular measurements (c) Geometric form measurements *i.e.* roundness, straightness, flatness, cylindricity (d) Geometric relationship *i.e.* parallel, perpendicular, concentric, runout (e) Surface finish/texture. This in depth classification of the different types of dimensions and the associated tolerances was a direct result of the USA finding it difficult to assemble the manufactured parts though they were made to specifications during the World War 2. This forms the basis of Geometric Dimensioning and Tolerancing (Cogorno, 2006).

As the manufactured parts vary due to the tolerances associated with it, tolerance control is one of the most important areas associated with regard to quality control in the industries. According to Britton (2000), tolerance control is achieved in 2 ways : process control and product control. In process control, the sources of variation are controlled directly or indirectly by measurement and compensation. The tolerance planning is possible only if the process control is stable (predictable). An important feature of tolerance planning is calculating the tolerance stackup or tolerance accumulation. According to Britton (2000), "tolerance stackup is inevitable when a surface not directly referred to by a dimension is used for location." A mismatch of two different assemblies can be seen clearly in fig. 4.1(B) that shows the effect of

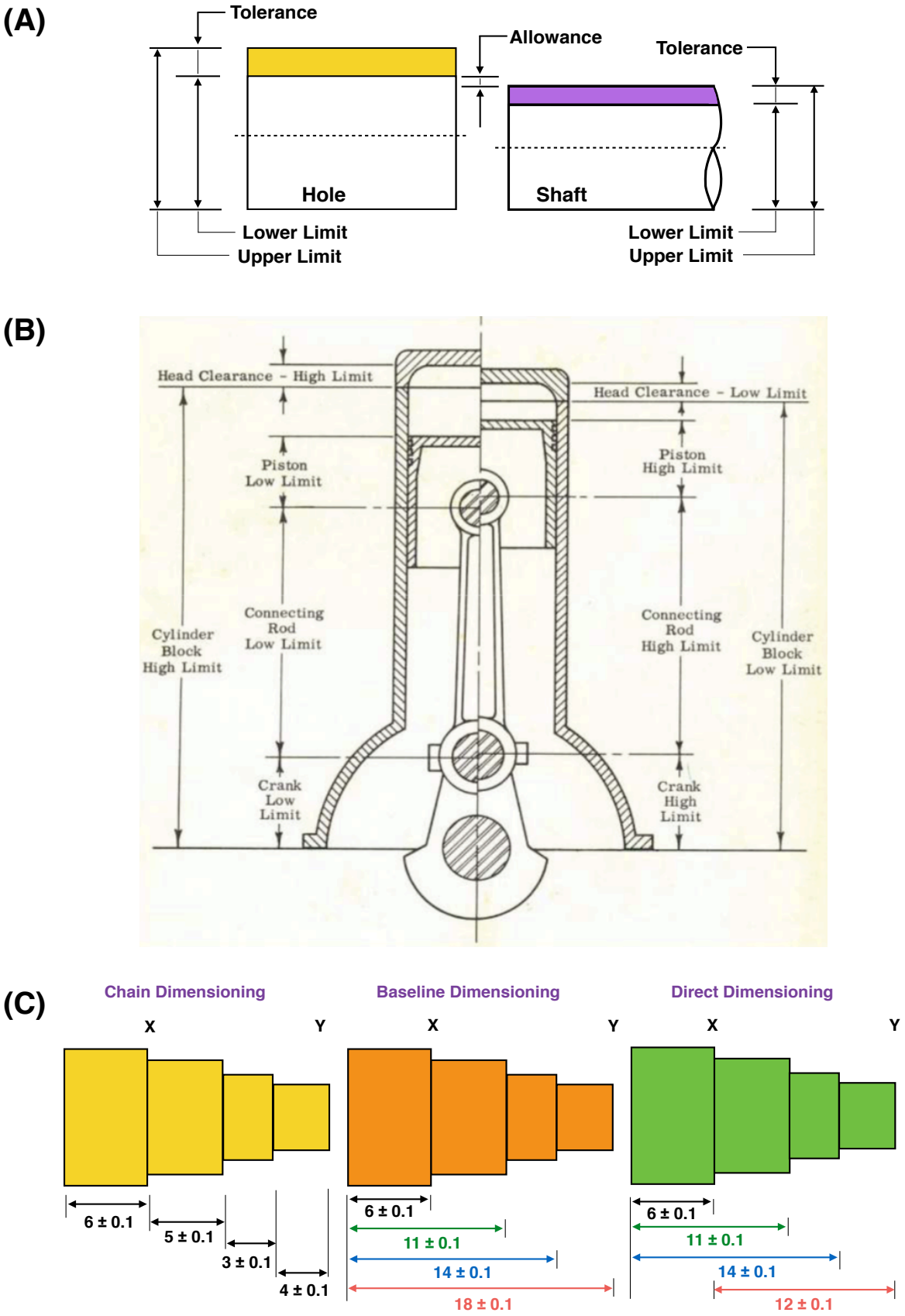


Figure 4.1: (A) Schematic Of Tolerance On Two Mating Parts (B) Effect Of Tolerance Stacking (C) Tolerance Stack Up Due To Dimensioning

tolerance stack up in an engine consisting of crank, connecting rod, piston and cylinder head[1]. The negative effect of tolerance stackup can be minimised by carefully selecting and placing the dimensions. It can be seen in fig. 4.1(C) that chain dimensioning produces maximum tolerance accumulation points X and Y while direct dimensioning produces the least tolerance accumulation.

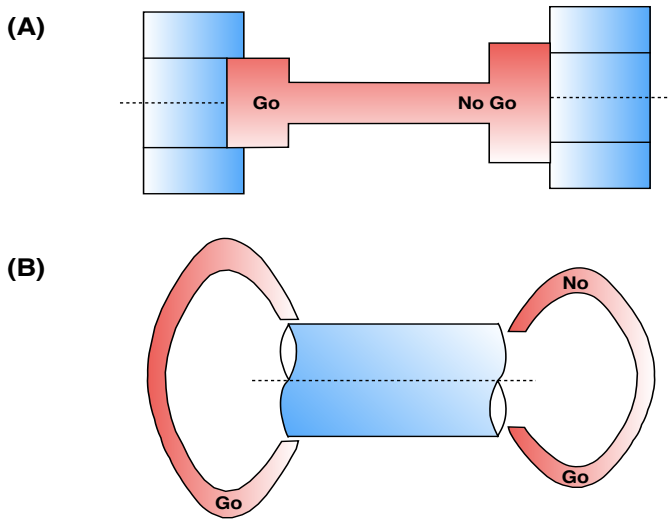


Figure 4.2: Schematic Of (A) GO And NO-GO Gauge For Holes (B) GO And NO-GO Gauge For Shafts

The tolerance control achieved by means of product control relies on inspection of parts. In this method, the parts are inspected by either measurement equipments (vernier calliper, profilometers, etc) or by limit gauges (also called Go and No-Go Gauge). Limit gauges do not give the accurate value of the dimensions. Instead, they are used to determine whether the manufactured component lies within the upper and lower limit of variation. Fig 4.2 (A) and (B) shows the Go and No-Go Gauge used for holes and shafts respectively. These gauges are simple to use and have a quick turnaround time in terms of inspecting the components. The components that exceed the specified dimensional limits are usually scrapped off. This helps in maintaining an inventory of interchangeable parts that enhances the production rate while reducing assembling cost at the same time.

In some special cases, the lower limit of the component mating with the higher limit of another component might produce a fit which may not fully satisfy functional requirements of

[1] https://home.iitk.ac.in/~nsinha/Metrology.pdf

the assembly. Under such circumstances, the industry adopts "Selective Assembly" wherein both the mating parts are measured and sorted in groups by dimension, prior to the assembly process. This method helps in assembling the upper limit of hole with the upper limit of shaft and the lower limit of hole with the lower limit of shaft such that appropriate clearances can be maintained thereby satisfying all the functional requirements of the assembly. Thensen and Jantayavichit (1999) describe that certain components in scroll compressor for automotive application cannot be manufactured economically with required precision using standard high volume machining practices. Selective assembly can provide a cost effective solution for obtaining an extremely tight tolerance under such circumstances. This method also has the potential to reduce the scrap (Eger et al., 2018) as an oversize shaft can be mated with an oversize hole provided other functions in the assembly are not compromised. These methods are extremely popular in automotive industries which deals with components that are manufactured at a large scale.

Sidwell (2004) has shown through his research that selective assembly of turbine blades leads to minimising the impact of manufacturing variability while improving the flow and oxidation life for majority of the turbine blade rows. The blades were classified into different groups based on passage flow capability. The Rolls-Royce PLC.[2] FY-2019 report shows that RR sold 510 widebody engines in 2019 including 106 engines of Trent 7000 (which equals to 1 engine of Trent 7000 being released every 3.5 days approximately). Each new generation of engine is different from its predecessor in terms of flow specifications, compressor pressure ratio, turbine inlet temperatures, etc and hence employing modular design concepts for fan/compressor/turbine blades might not be possible between different platforms of the same original equipment manufacturer (OEM). More often than not, even a small gain in efficiency across fan and compressor would outweigh the cost benefit from a modular design and as such the fan and compressor blades (also turbine blades) are tailor made for different platforms. Thus, the major impediment to implementing the idea of selective assembly in the aero-engine industry would be the absence of fan/compressor/turbine blades being produced at large scale. With this background, the present research considers only the tolerance control obtained through product control by mea-

[2] https://www.rolls-royce.com/~/media/Files/R/Rolls-Royce/documents/investors/2019-fy-press-release.pdf

suring the dimensions of each blade (possibility of reducing the scrap by means of redistribution of compressor blades circumferentially) while ignoring the practicality of selective arrangement due to the absence of parts being produced at large scale.

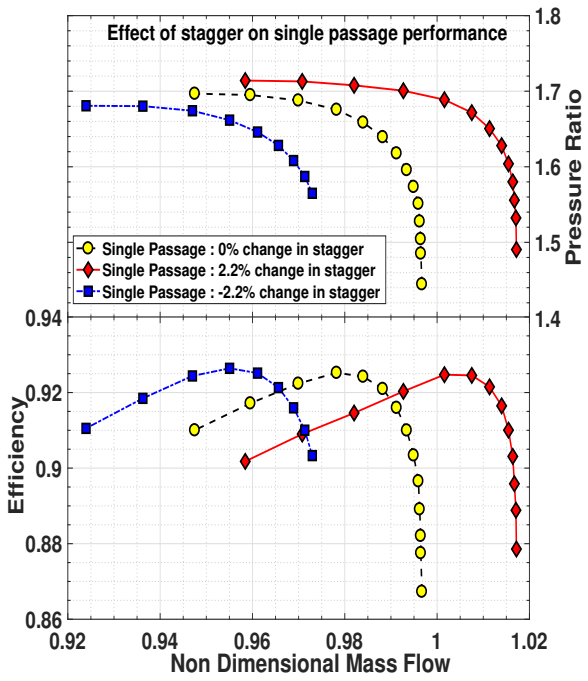
4.2 Compressor Stagger Angle

4.2.1 Single and Double Passage Simulation Of NASA Rotor 67

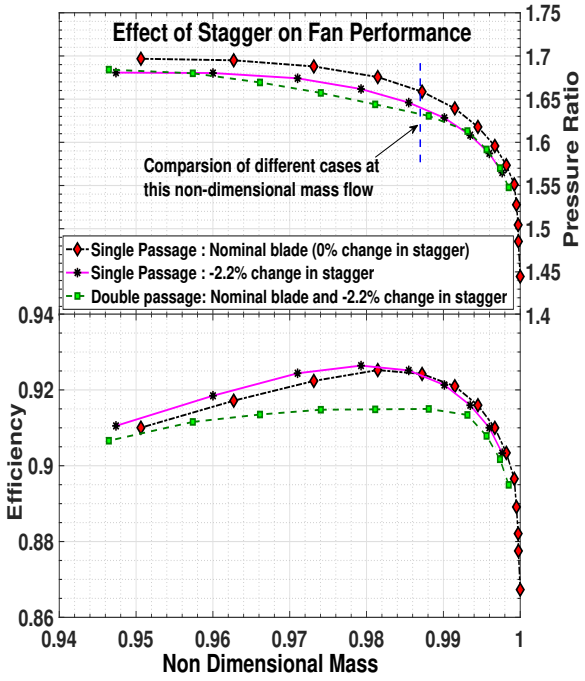
As mentioned earlier in the literature survey, a stagger angle variation up to 1° (Wilson et al., 2006; Sladojevic et al., 2007; Zheng et al., 2017) is allowed as manufacturing tolerances. When a system is designed for certain tolerance limits and a component exceeds that limit, there is a chance of system failure (Bazovsky, 2004). Thus any blade that exceeds the prescribed limit is scrapped off, resulting in a financial loss to the manufacturer. With this rationale, the present thesis considers the stagger variation to be within ± 1.5° (± 2.25% change of stagger) from the datum stagger angle, as a way to check if these losses could be mitigated. The stagger angle varies along the span linearly with zero at the hub and ± 1.5° at the tip.

The fan blade with nominal tip gap size (0.376% span) was considered and the stagger angle was gradually changed in steps of ± 0.75% relative to the datum stagger angle (± 0.5°). The effects of stagger angle variation on the rotor performance was studied by juxtaposing the five cases of (**I**) Single passage domain with nominal blade (also called as 0% change in stagger angle) (**II**) Single passage domain with a blade of 2.25% change in stagger angle (**III**) Single passage domain with a blade of -2.25% change in stagger angle (**IV**) Double passage domain with blades of 0% and 2.25% change in stagger angle and (**V**) Double passage domain with blades of 0% and -2.25% change in stagger angle.

For single passage cases, a blade having ± 2.25% change in stagger angle causes the mass flow rate to change by ± 2% on either side of the baseline blade as shown in fig. 4.3(A). Hence the mass flow rate for each of the above mentioned case was non-dimensionalised with respective choking mass flow rate which makes a one-to-one comparison between different cases

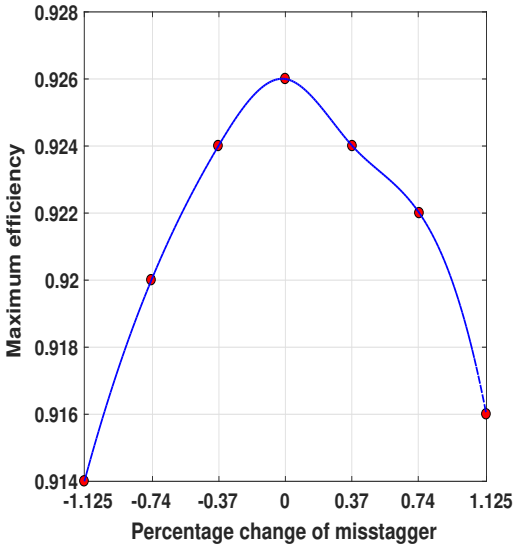


(A) Single Passage Blade With -2.25% Stagger Variation, 0% Stagger Variation And 2.25% Stagger Variation

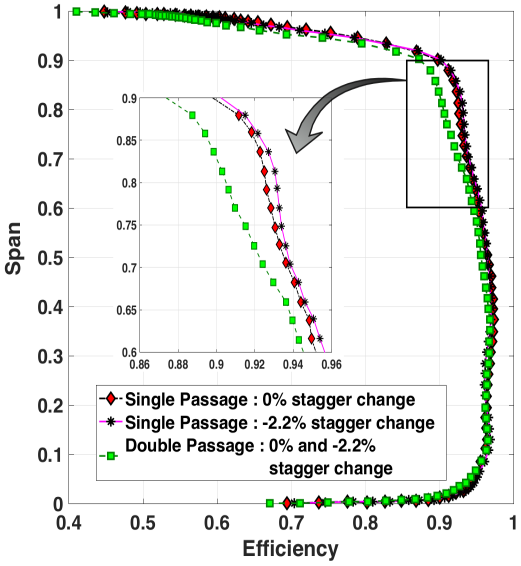


(B) Comparison Of Single Passage Uniform Staggered Blades And Double Passage Non-Uniform Staggered Blades

Figure 4.3: Changes In Fan Performance Due To Stagger Variation Of Blades



(A) Effect Of Mis-Stagger On Maximum Efficiency



(B) Spanwise Maximum Efficiency for Uniform Staggered Blades And Mis-Staggered Blades

Figure 4.4: Changes In Maximum Efficiency Due To Stagger Angle Variation Of Blades

simpler. For brevity, the results of only case (**I**), (**III**) and (**V**) are presented in fig. 4.3(B) and a comparison between these cases are made at the non-dimensional mass flow rate of 0.986 (marked by vertical blue dashed line). These points depict the behaviour of the respective cases

as they are near maximum efficiency. It was seen that the peak efficiency of 92.5% is observed for all the single passage cases; whereas for a double passage case, the peak efficiency drops to about 91.5%. Fig. 4.4(A) shows that as the mis-stagger decreases, the peak efficiency increases. It can also be seen that this curve is unsymmetric on either side of maximum efficiency of the baseline case (the reason for this behaviour will be discussed later). A span-wise comparison of efficiency between cases (**I**), (**III**) and (**V**) is presented in fig. 4.4(B).

It can be seen that the case (**V**) starts to lose its efficiency from 60% span upwards compared to case (**I**) and (**III**). Hence a blade-to-blade view at 75% span for case (**I**), (**III**) and (**V**) respectively is used to compare the difference in flow-fields as shown in fig. 4.5. The non-dimensionalised static pressure in fig. 4.5(A), (B) and (C) shows that both the single blade cases *i.e.* case (**I**) and (**III**), have symmetric shock waves which are close to the entrance of the blade passage while the case (**V**) with blades of different stagger angles has unsymmetrical shock waves (Wilson et al., 2006). This implies that when one of the blade is having peak efficiency, the other blade is choked (or stalled) and hence the assembly will always be less efficient than the single passage cases. A schematic explanation of the mechanism of change in location of shock wave for a double passage case with different stagger blades is shown in fig. 4.6. It can be seen that in case of extreme mis-staggering, one of the passages behaves like a nozzle while the other behaves like a diffuser thus resulting in unsymmetrical shock waves. Moreover, due to asymmetrical aerofoil used in the compressor blades, the area of nozzle and diffuser formed in a double passage computation of case (**IV**) differs from that of case (**V**), thus resulting in different losses in the two cases. This can be clearly seen in fig. 4.4(A) which shows an unsymmetric shape about the 0% mis-stagger. Thus the change in passage area because of change in stagger angle results in a drop of performance compared to the baseline case of uniform passage area.

4.2.2 Single and Double Passage Simulation Of Wide Chord Blade

The wide chord blade has been subject to stagger angle variation of $\pm$ 1.5° ($\pm$ 2.2% change of stagger). Four cases have been considered :

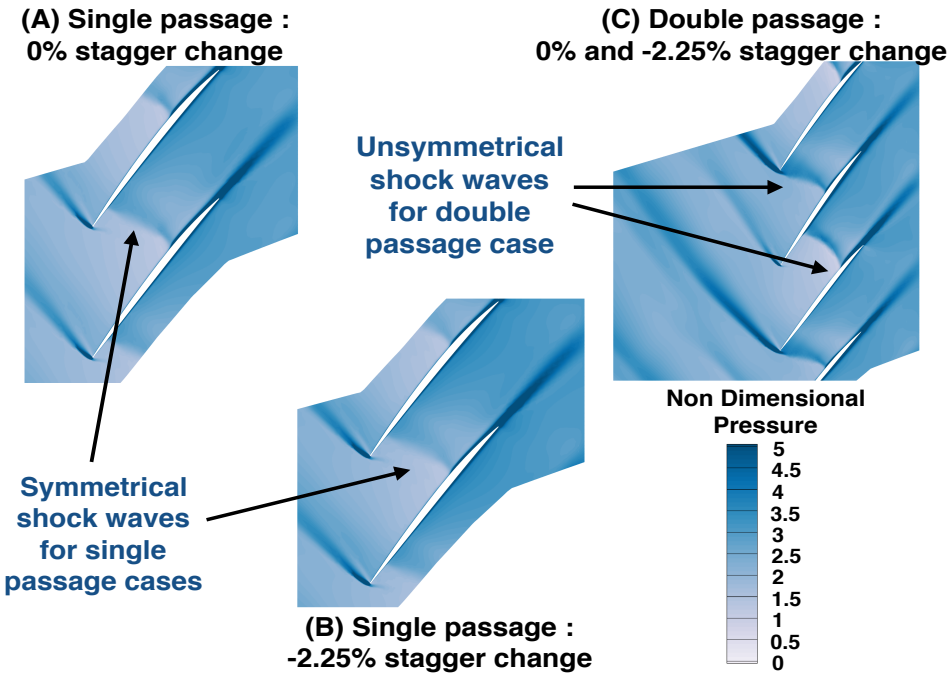


Figure 4.5: Shock Wave Position At 75% Span And Non-Dimensional Flow Rate Of 0.986 For (A) Single Passage 0% Stagger Change (B) Single Passage -2.25% Stagger Change (C) Double Passage 0% And -2.25% Stagger Change

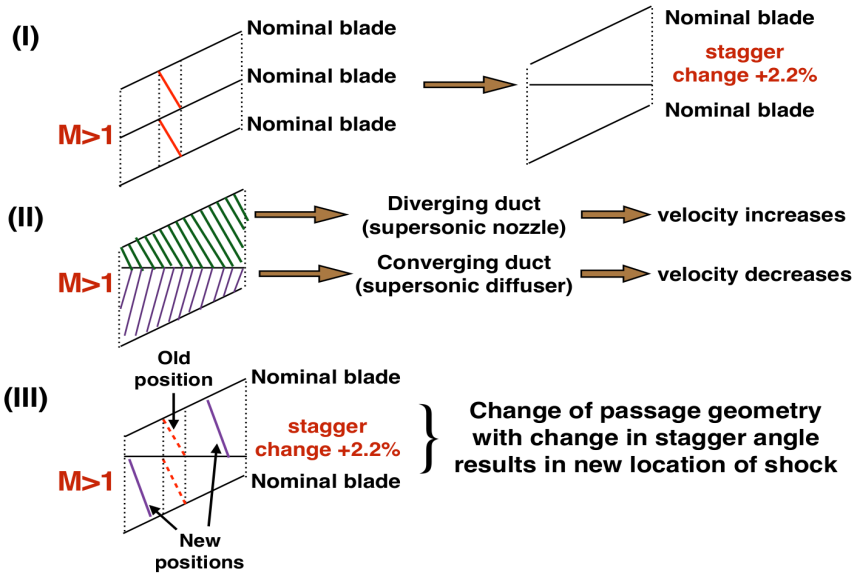


Figure 4.6: Schematic Showing The Change In Location Of Shock With Change In Stagger Angle

(A) Single passage wide chord blade with 0% change in stagger (baseline) (B) Single passage wide chord blade with 2.2% change is stagger (C) Single passage wide chord blade with -2.2% change in stagger (D) Double passage wide chord blades with 2.2% change in stagger and -2.2% change in stagger

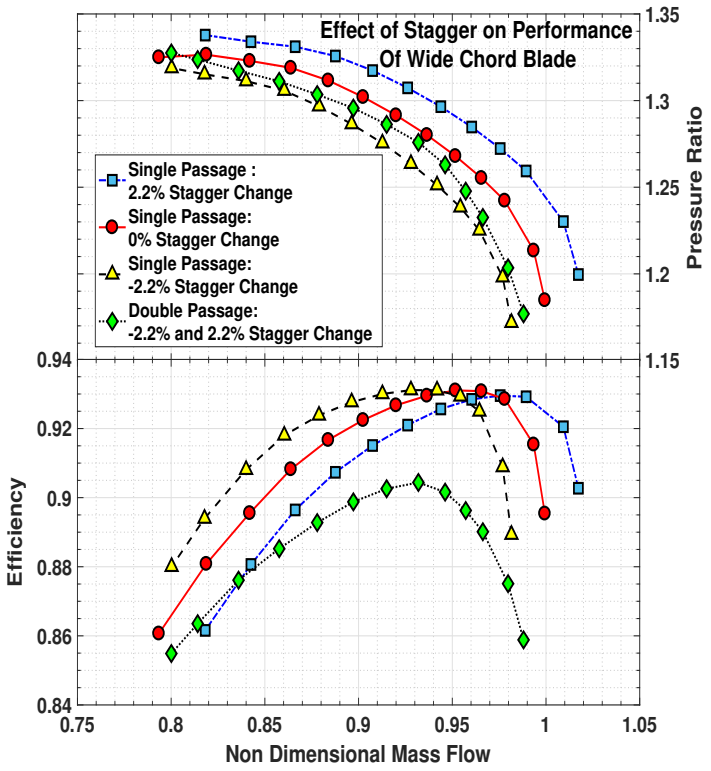


Figure 4.7: Performance Curve Of Wide-Chord Blade When Subject To Stagger Variation

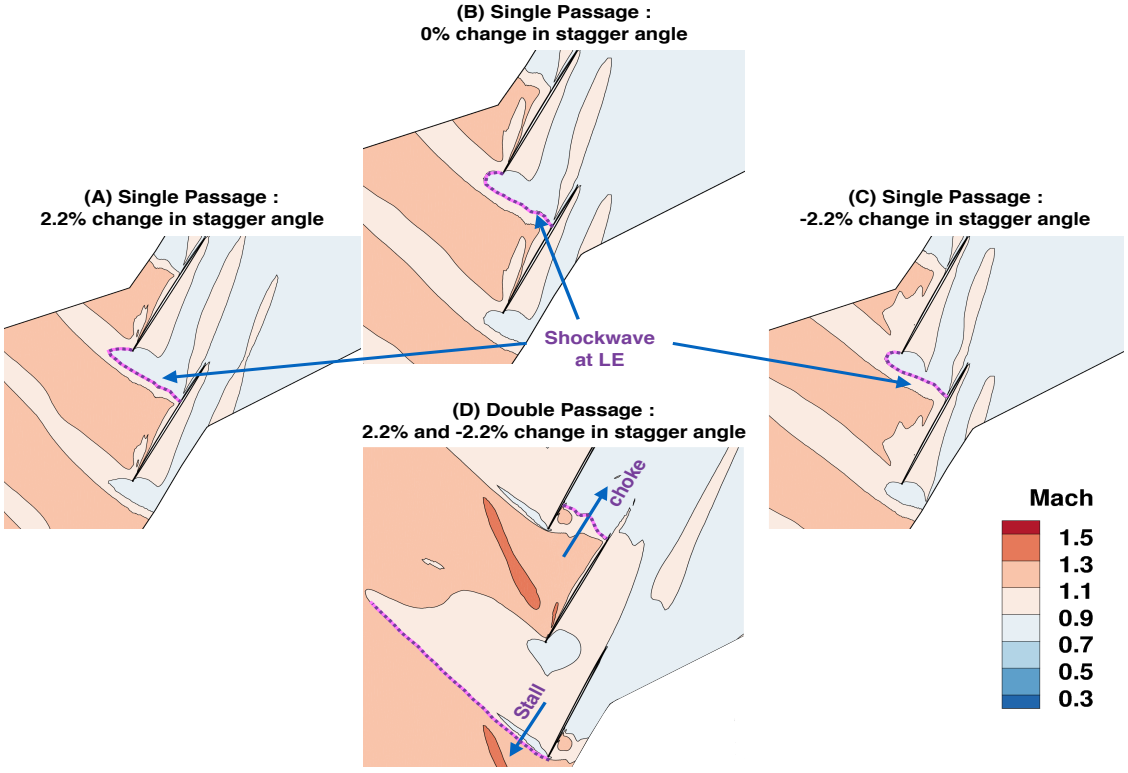


Figure 4.8: Shockwaves In A Wide-Chord Blade : (A) Single Passage Rotor With 0% Change in Stagger (B) Single Passage Rotor With 2.2% Change in Stagger (C) Single Passage Rotor With -2.2% Change in Stagger (D) Double Passage Rotor With 2.2% and -2.2% Change In Stagger Angle

The average stagger of case (D) is zero while mis-stagger between the two blades is 1.5° (2.2% change in mis-stagger). Fig. 4.7 shows the performance curve of wide chord blade while it is subject to stagger variation. It can be seen that a change in stagger angle by 2.2% for single passage cases causes the choke mass flow rate to shift by almost 1.5% on either side of the baseline case. It can also be seen that the maximum efficiency of case (D) is the worst compared to the single passage cases of (A), (B) and (C). All the single passage cases have a maximum efficiency of 93% while the double passage case has a maximum efficiency of 90.5%. The reason for this can be seen in fig. 4.8 wherein all the single passage cases have shock wave near the leading edge and thus undergoing peak efficiency. However for double passage rotor with 2.2% and -2.2% change in stagger angle blades, a non-symmetric shock wave exists with one of the passage undergoing choke while the other passage undergoes stall. Thus the case (D) is less efficient compared to cases (A), (B) and (C). This result for wide chord blade is similar to the previous results of NASA Rotor 67 having different stagger angle blades.

4.2.3 Full Annulus Simulation Of NASA Rotor 67 And Wide Chord Blade

Though the manufacturing tolerances are generally assumed to have Gaussian distribution, in the present thesis a uniform distribution has been considered. For a closed interval [a,b] the uniform distribution is known to be maximum entropy distribution (Park and Bera, 2009) and as shown in fig. 4.9, a uniform distribution represents a design space much better compared to Gaussian distribution which is concentrated towards the mean.

Two terms have been introduced in this section viz. overall average stagger angle ($\mathbf{S_{ave.\ overall}}$) and cumulative mis-stagger ($\mathbf{C-MIST}$). These two terms are global parameters for the entire annulus and are used to determine the best (or worst) arrangement. A comparison of the GA based TSP (Kirk, 2014) has been carried out vis-a-vis heuristic method of arrangement

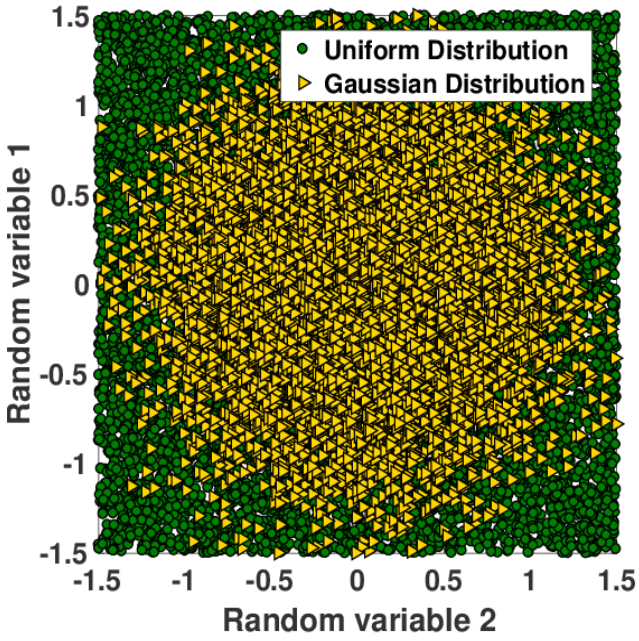


Figure 4.9: Scatter plot of two different random distributions within a closed interval

developed by the author.

$$S_{ave.\ overall} = \frac{\sum_{i=1}^{N} S_i}{N} \tag{4.1}$$

$$C - MIST = \sum_{i=1}^{N} \frac{\sqrt{(S_i - S_{i+1})^2}}{2} \tag{4.2}$$

In the above equations, $\mathbf{S_i}$ is the stagger angle of the 'i' th blade. As there are $\mathbf{N}$ blades in the compressor, the term $\mathbf{S_{N+1}}$ is the same as $\mathbf{S_1}$ in the equation 4.2. It should be noted that there maybe various arrangements which can have the same (minimum/maximum) C-MIST and even a GA based TSP algorithm gives only an approximate solution (Awad, 2009). As seen in equation 4.2, the cumulative mis-stagger is equal to summation of all the mis-stagger between two adjacent blades throughout the full annulus. Fig. 4.10(A) shows the distribution of blades with differing stagger angle. As can be seen, each blade in the compressor has a unique stagger angle which implies all the blades have a random dimension associated with them. The mis-stagger between each of these blades are calculated and represented in fig. 4.10(B). This mis-stagger matrix is similar to the distance matrix (which represents the distances of all the cities with respect to each other) in a conventional TSP. Similar to the

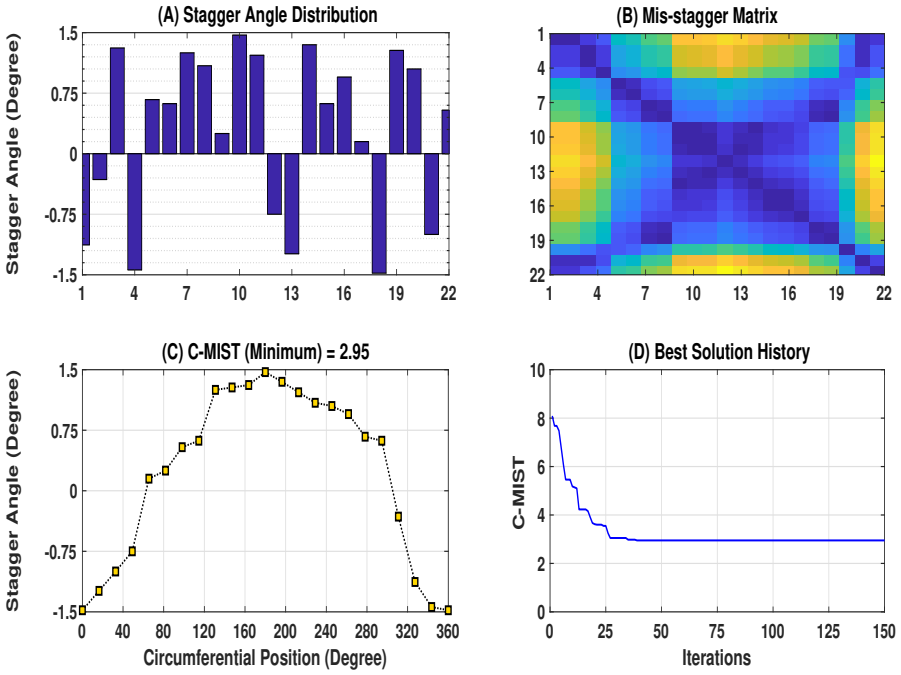


Figure 4.10: TSP Used To Predict The Least Mis-Staggered Arrangement : (A) Distribution Of Blades With Random Stagger Angle (B) Mis-Stagger Matrix (C) Sinusoid Arrangement Having Least Cumulative Mis-Stagger (D) Solution Time History

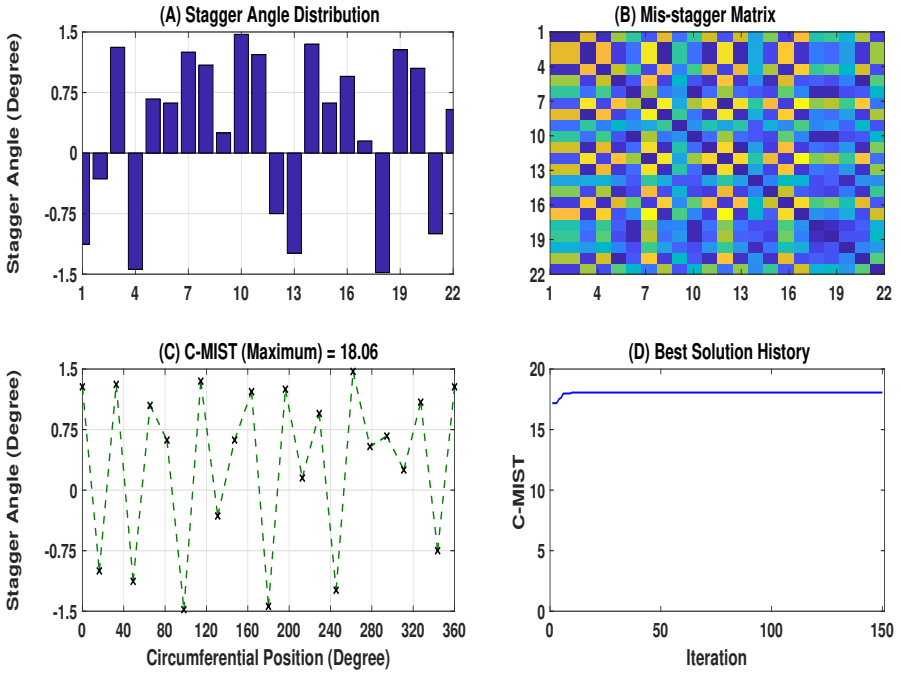


Figure 4.11: TSP Used To Predict The Most Mis-Staggered Arrangement : (A) Distribution Of Blades With Random Stagger Angle (B) Mis-Stagger Matrix (C) Zigzag Arrangement Having Maximum Cumulative Mis-Stagger (D) Solution Time History

Table 4.1: Heuristic Method For Different Arrangement Of Stagger Angle (NASA Rotor 67)

(I)	(II)	(III)	(IV)	(V)	(VI)
Random	Linear	Sine Order	Zig Order	Sinusoidal (II and III)	Zigzag (II and IV)
-1.13	-1.48	**12**	**22**	1.47	1.47
-0.32	-1.44	**11**	**2**	1.31	-1.44
1.31	-1.24	**13**	**20**	1.25	1.31
-1.44	-1.13	**10**	**4**	1.09	-1.13
0.67	-1	**14**	**18**	0.95	1.25
0.62	-0.75	**9**	**6**	0.62	-0.75
1.25	-0.32	**15**	**16**	0.54	1.09
1.09	0.15	**8**	**8**	0.15	0.15
0.25	0.25	**16**	**14**	-0.75	0.95
1.47	0.54	**7**	**10**	-1.13	0.54
1.22	0.62	**17**	**12**	-1.44	0.62
-0.75	0.62	**6**	**11**	-1.48	0.62
-1.24	0.67	**18**	**13**	-1.24	0.67
1.35	0.95	**5**	**9**	-1	0.25
0.62	1.05	**19**	**15**	-0.32	1.05
0.95	1.09	**4**	**7**	0.25	-0.32
0.15	1.22	**20**	**17**	0.62	1.22
-1.48	1.25	**3**	**5**	0.67	-1
1.28	1.28	**21**	**19**	1.05	1.28
1.05	1.31	**2**	**3**	1.22	-1.24
-1	1.35	**22**	**21**	1.28	1.35
0.54	1.47	**1**	**1**	1.35	-1.48

shortest route taken by a travelling salesman to cover all the cities, fig. 4.10(C) shows that the least cumulative mis-stagger around the annulus of a compressor is obtained when the blades are sinusoidally arranged. Fig. 4.10(D) shows the solution convergence history using GA-TSP. It can be seen that the solution converges after approximately 40 iterations. Similar results for maximum cumulative mis-stagger is plotted in fig. 4.11. As can be seen, fig. 4.11(A) and (B) shows the distribution of blades with differing stagger angle and the mis-stagger matrix respectively. Fig. 4.11(C) shows that the maximum cumulative mis-stagger around the annulus of a compressor is obtained when the blades are arranged in a zigzag manner and fig. 4.11(D) shows the solution convergence history using GA-TSP. It can be seen that the solution converges to a maximum cumulative mis-stagger of 18.06 after approximately 15 iterations.

The heuristic method for different arrangement in case of NASA rotor 67 has been shown in table 4.1. Column (**I**) represents the random arrangement of different staggered blades in a compressor. Column (**I**) has been rearranged in column (**II**) such that the stagger angle increases monotonically; called as linear arrangement. The blades in column (**II**) have been sorted as shown in column (**III**) such that the value of stagger angle initially decreases and then increases. This arrangement shown in column (**V**) resembles a sine wave and hence called

as sinusoid arrangement. Similarly, the blades in column (**II**) have been sorted in column (**IV**) such that the stagger alternately increases and then decreases. This arrangement shown in column (**VI**) resembles a zigzag pattern and hence called as a zigzag arrangement. All these four arrangements have been shown in fig. 4.12 along with respective C-MIST values.

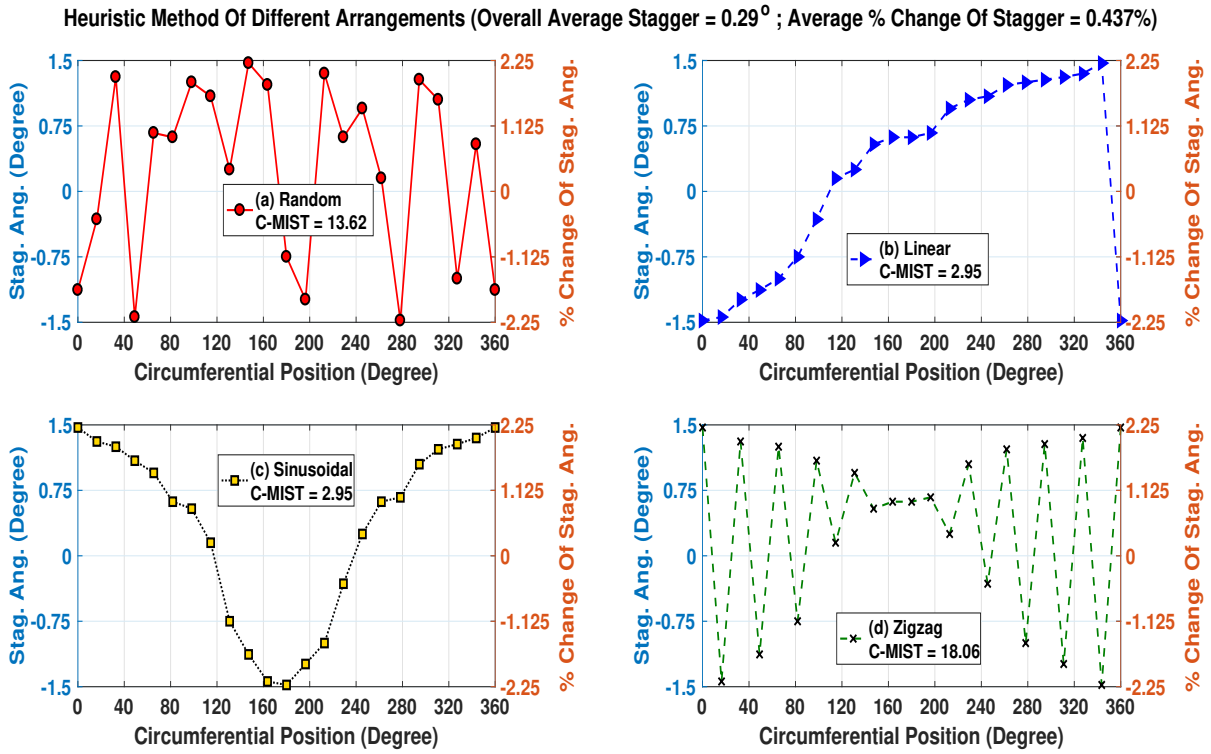
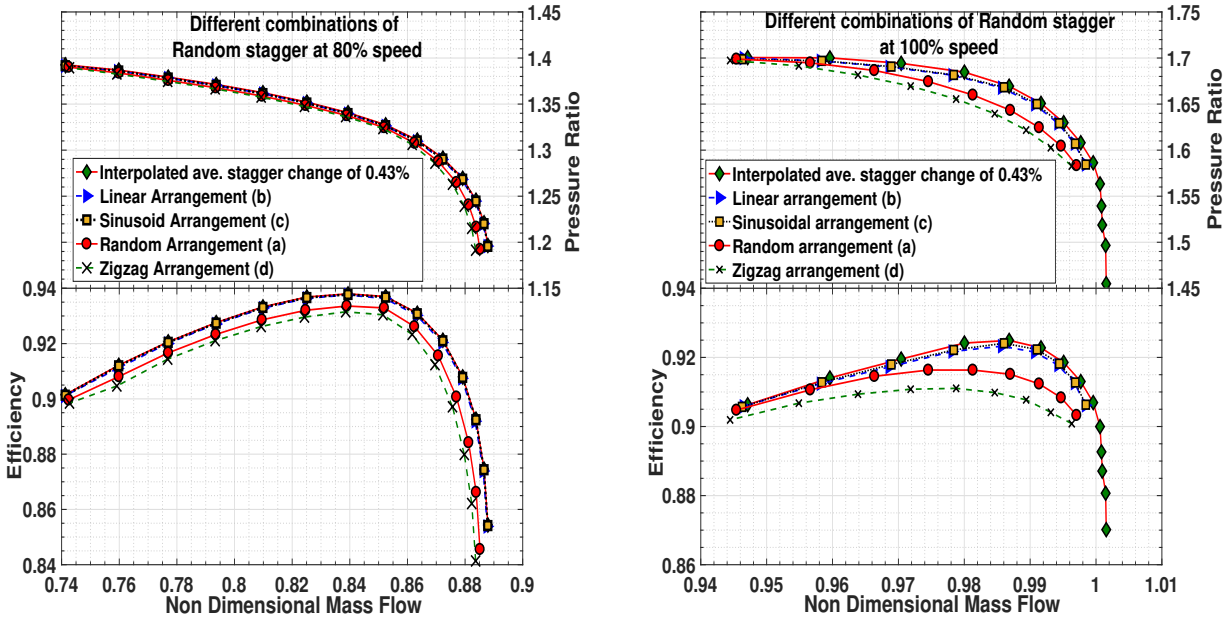


Figure 4.12: Heuristic Arrangements In Case Of NASA Rotor 67 For The Same Set Of Random Staggered Blades With Average Change Of Stagger 0.437% (A) Random Arrangement (B) Linear Arrangement (C) Sinusoid Arrangement (D) Zigzag Arrangement

Thus, for a given set of uniformly distributed random staggered blades between ± 2.25% (as shown in fig. 4.12(A)) if the arrangement is smooth as shown in fig. 4.12(B) and fig. 4.12(C), the cumulative mis-stagger (C-MIST) between successive blades is minimum which would maximise the performance of the compressor. On the other hand, an arrangement that maximises the value of C-MIST between two successive blades (as shown in fig. 4.12(D)), will minimise the performance of the compressor. It can also be seen that the value of C-MIST in case of heuristic arrangement shown in fig. 4.12(C) and fig. 4.12(D) matches with the arrangement predicted by GA-TSP as shown in fig. 4.10(C) and fig. 4.11(C).

Fig. 4.13(A) and (B) shows that the sinusoidally and linearly arranged blades around the whole annulus have the best performance; while the zigzag arrangement has the worst performance.



(A) Fan Performance At 80% Speed (B) Fan Performance At 100% Speed

Figure 4.13: Performance For Different Combinations Of Random Stagger For NASA Rotor 67 (A) 80% Fan Speed (B) 100% Fan Speed

The performance of all other random arrangements lie between these two extremities. No difference in the stability margin is observed for different configurations. The difference in maximum efficiency between sinusoidal arrangement and zigzag arrangement is almost 1.5% at 100% speed while and around 0.75% at 80% speed. As the relative Mach number at the inlet of the blade reduces with reduction in compressor speed from 100% to 80%, the shock losses proportional to $(M-1)^3$ (Cumpsty, 2004) also start decreasing. Thus the difference between the value of peak efficiency for different arrangement also reduces. It can also be seen that at 80% speed, the range of compressor (mass flow rate at choke - mass flow rate at stall) increases compared to 100% speed (Cumpsty, 2004; Kurzke, 2011)

For the wide chord blade rotor, different arrangements for blades with random stagger angle viz. random, linear, sinusoid and zigzag was carried out as shown in fig. 4.14(A), (B), (C) and (D) respectively. It was observed that sinusoid and linear arrangement performed the best while zigzag arrangement had the worst performance as shown in fig. 4.15. The stability margin for different arrangements were unaffected. This analysis for wide chord blade was carried out at its design speed. The difference in maximum efficiency between sinusoidal arrangement and zigzag arrangement is almost 1.2%.

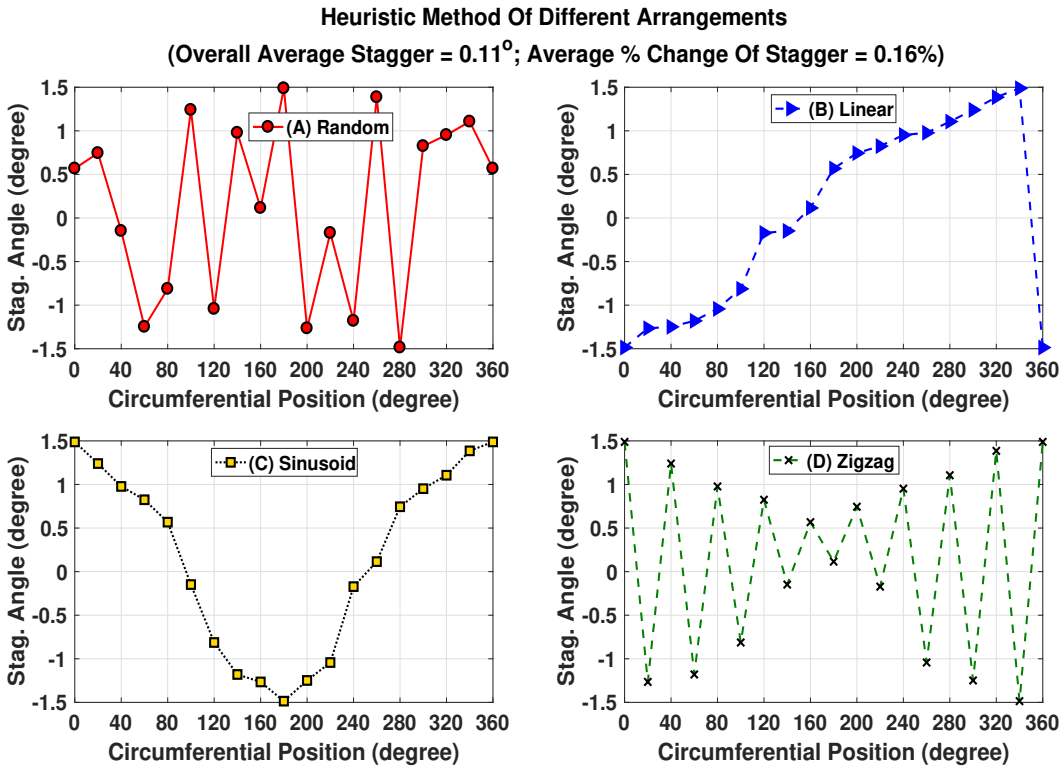


Figure 4.14: Heuristic Arrangements In Case Of Wide Chord Blade Rotor For The Same Set Of Random Staggered Blades With Average Change Of Stagger 0.16% (A) Random Arrangement (B) Linear Arrangement (C) Sinusoid Arrangement (D) Zigzag Arrangement

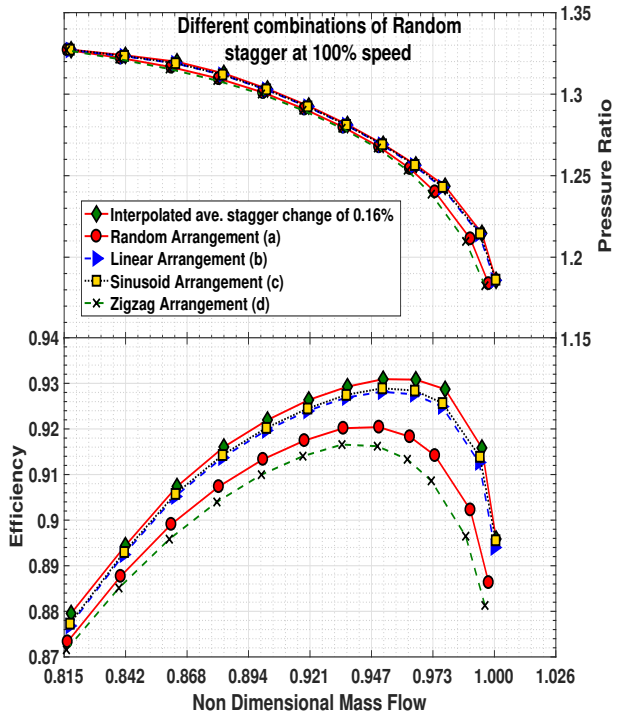


Figure 4.15: Performance For Different Combinations Of Random Stagger For Wide Chord Blade At 100% Fan Speed

Zheng et al. (2017) also observed that the sinusoidal arrangement works best though they have not evaluated the minima of possible performance. While there maybe other combinations which give similar high performance, the aim of this research was to establish a rule of thumb for the best possible arrangement. The sinusoidal arrangement can also have an added advantage of a reduced "Alternate Passage Divergence" as shown in Lu et al. (2018). It can thus be concluded that the change in passage area (as a result of change in stagger angle between various blades) is the driver behind fall of efficiency in different arrangements. A similar view was also shared by Isomura (1996) wherein he quoted (pg. 137) the following :

"In a transonic fan, the shock position is defined by the inflow Mach number, the pressure ratio and the passage area contraction, but not directly by the incidence angle ... the change in the stagger angle can cause the blade passage throat area to change, and will result in a change of the inflow Mach number. Therefore an incidence angle change affects the shock position indirectly instead of directly."

4.3 Compressor Tip Gap

4.3.1 Single and Double Passage Simulation Of NASA Rotor 67

Sakulkaew et al. (2013) noted that in an industrial gas turbine, the rotor tip gap can be less than 0.5% span on the front stages and more than 5% span at the rear stages. Single passage rotor domain was generated for five different tip clearances: 0.188% span, 0.376% span, 0.564% span, 0.752% span and 0.94% span which are representative of the manufacturing tolerance. This tip gap variation could also occur in a refurbished blade with a smaller stall margin (SM) because of damage at the tip during the course of operation. The **SM** is defined below:

$$\mathbf{SM} = \left[\frac{(\mathbf{PR})_{\mathbf{stall}} \times (\dot{\mathbf{m}})_{\mathbf{ref.}}}{(\mathbf{PR})_{\mathbf{ref.}} \times (\dot{\mathbf{m}})_{\mathbf{stall}}} - \mathbf{1}\right] \times \mathbf{100} \tag{4.3}$$

where PR is Pressure ratio and $\dot{m}$ is mass flow rate (Moore, 1982; Beheshti et al., 2004). In addition to this, double passage rotor configurations with two different tip gaps for all the possible combinations from above tip gaps have been generated.

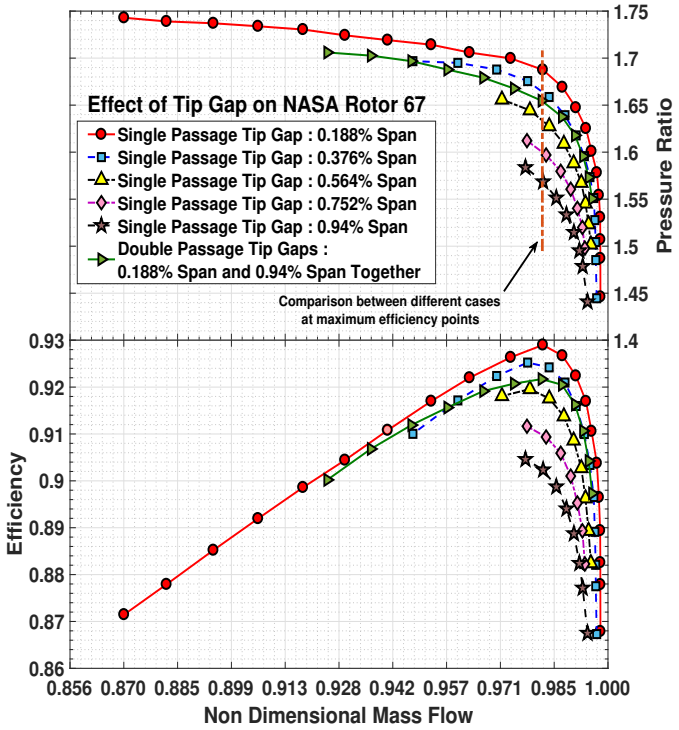
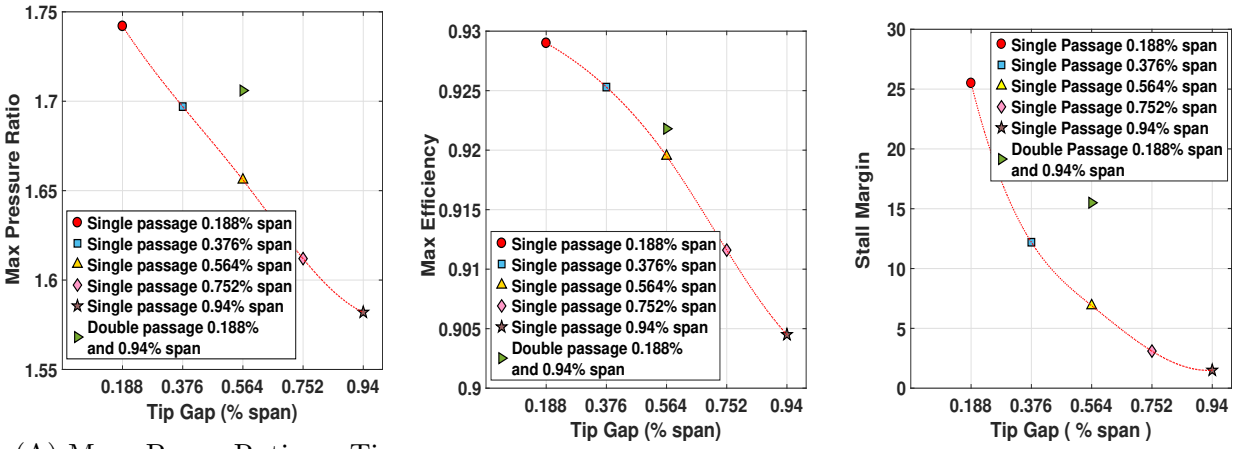


Figure 4.16: Comparison Of Fan Performance For Different Tip Gaps

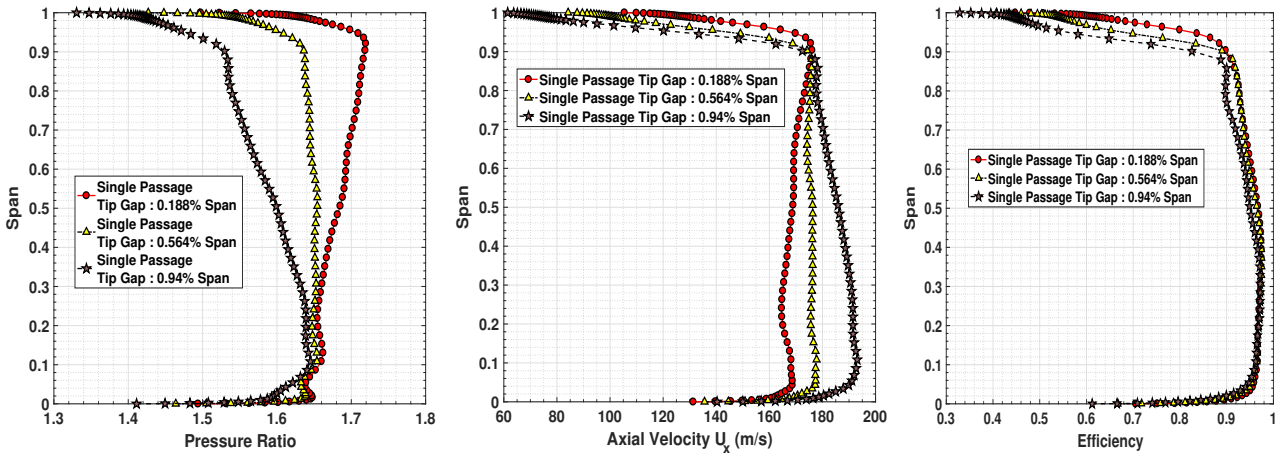
As seen in fig. 4.16, an increase in tip gap size causes a decrease in pressure ratio, decrease in efficiency and an increase in the stalling mass flow rate. These trends are shown in fig. 4.17(A), (B) and (C) where the variation of maximum overall pressure ratio, maximum overall efficiency and stall margin plotted against the tip gap size. Similar trends were obtained by Moore (1982), Adamczyk et al. (1993) and Beheshti et al. (2004). Moreover, it can be observed from fig. 4.17(C) that the stall margin (SM) is higher for double passage rotor with tip gaps of 0.188% span and 0.94% span compared to single passage with (average) tip gap of 0.564%. Fig. 4.18 shows spanwise profiles of different QoI at the same non dimensional mass flow rate (vertical orange line marked in fig. 4.16). Fig. 4.18(A) shows the spanwise profile of pressure ratio for different tip gaps. It can be seen that there is a loss of pressure ratio from 20% span upwards. Fig. 4.18(B) shows the axial velocity across the span of NASA Rotor 67. It can be seen that higher blockage for bigger tip gaps causes a low momentum flow near the tip gap region. Since the comparison is made at same mass flow rate, a redistribution of axial velocity

takes place across the span and hence large differences in different axial velocity profiles are seen. Fig. 4.18(C) shows the spanwise plot of efficiency for different tip gaps. The spanwise efficiency for different tip gaps starts deviating from 40% span onwards and above 90% span, the difference in efficiency for blades with smaller tip gap and blades with larger tip gap is more pronounced.



(A) Max. Press. Ratio vs Tip Gap (B) Max. Efficiency vs Tip Gap (C) Stall Margin vs Tip Gap

Figure 4.17: Behaviour Of (A) Maximum Pressure Ratio With Respect To Tip Gap (B) Maximum Efficiency With Respect To Tip Gap (C) Stall Margin With Respect To Tip Gap



(A) Press. Ratio vs Span (B) Axial Velocity vs Span (C) Efficiency vs Span

Figure 4.18: NASA Rotor 67 Spanwise Profile Of (A) Pressure Ratio (B) Axial Velocity (C) Efficiency For Different Tip Gaps At Same Non Dimensional Mass Flow Rate Of 0.982

For brevity, the Mach number contours of only single passage tip gaps of 0.188% span, 0.564% span, 0.94% span and double passage with tip gaps 0.188% span and 0.94% span together are shown in fig. 4.19(A), (B), (C) and (D) respectively. All the contours in fig. 4.19 have been

plotted at 99% span and a non dimensional mass flow rate of 0.982 which are the points near peak efficiency. An increase in the tip gap causes the size and strength of tip leakage vortex to increase which in turn creates a large zone of low momentum fluid as seen in fig. 4.19(B) and (C). It can also be seen from fig. 4.19(D) that the low momentum fluid in double passage case with tips gaps 0.188% and 0.94% span is much smaller than single passage tip gaps of 0.564% span and 0.94% span. These pockets of low energy fluid produce a region of blockage which causes the main flow to be diverted around it. The altered main flow due to the blockage creates an adverse pressure gradient which leads to flow separation and hence the blade stall (Thompson et al., 1998; Beheshti et al., 2004). The low momentum fluid in the flow-fields shown in fig. 4.19(B) and (C) are very similar and hence stalling mass flow rate of both the tip gaps (viz. 0.564% span and 0.94% span) are very close to each other.

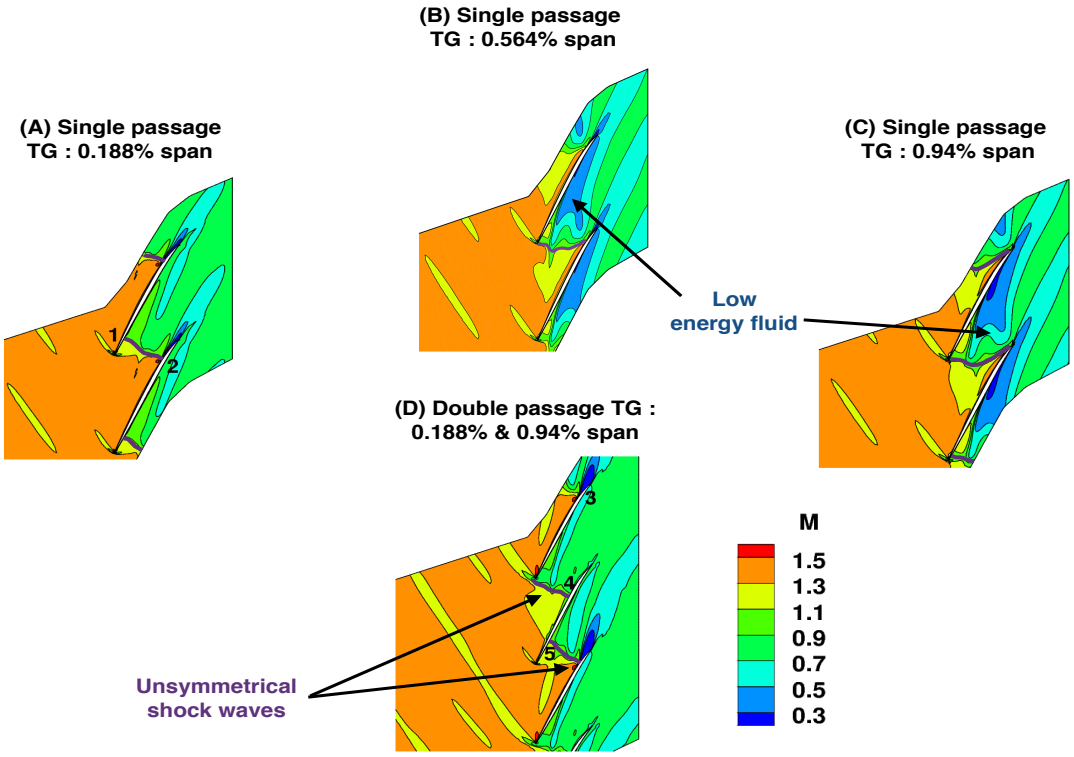


Figure 4.19: Blade Relative Mach Number At 99% Span At A Non Dimensionalised Mass Flow Rate Of 0.982 For (A) Single Passage Tip Gap 0.188% Span (B) Single Passage Tip Gap 0.564% Span (C) Single Passage Tip Gap 0.94% Span (D) Double Passage Tip Gaps Of 0.188% And 0.94% Span

A schematic explanation of the mechanism of shock location for a single passage with tip gap of 0.188% span vis-a-vis a double passage with tip gaps of 0.188% and 0.94% together is shown in fig. 4.20. Both of these cases are compared at the same mass flow rate. A single passage

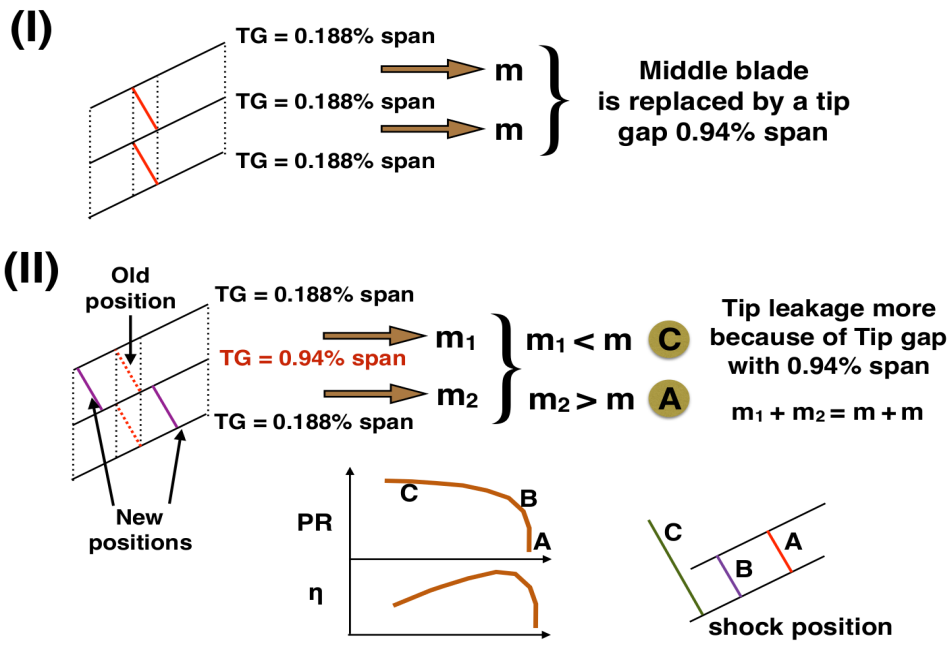
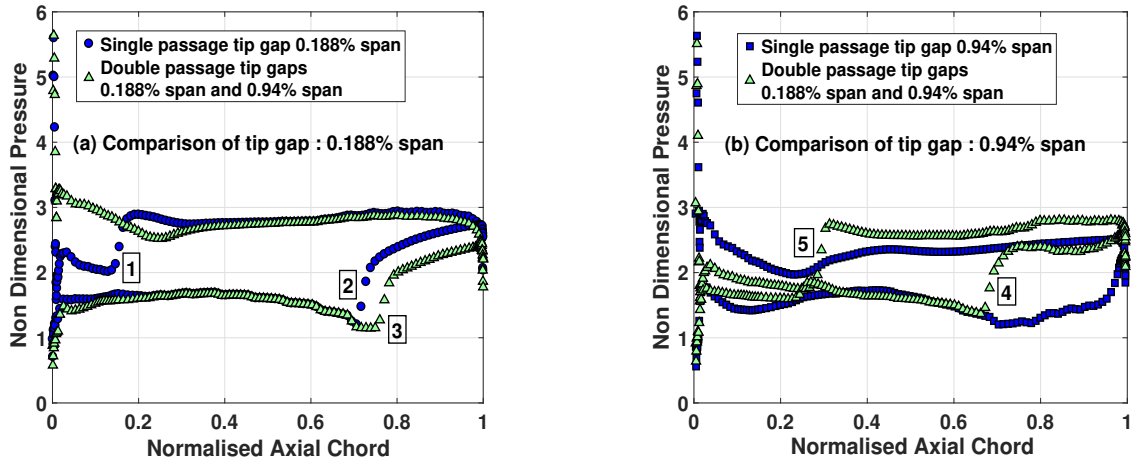


Figure 4.20: Schematic Showing Location Of Shock In Adjacent Passage Due To Change In Tip Gap

case has a uniform mass flow rate from all its passage and thus has symmetric shocks in all the passages. In case of double passage, it can be seen that the higher tip leakage flow due to the larger tip gap blade causes the mass flow rate from one of the passages to drop thus pushing it towards stall. To compensate for this drop in mass flow rate, the other passage undergoes an increased mass flow rate thus causing it to become choked. Due to the location of shock waves in the double passage case, the larger tip gap blade becomes "unloaded" while the smaller tip gap blade becomes "more loaded" as seen in fig. 4.21(A) and (B). Here, the blade loading of single passage tip gaps of 0.188% span and 0.94% span is compared with the individual blades of double passage tip gaps of 0.188% span and 0.94% span. The numbers marked (1-5) on this plot corresponds to the numbers marked (1-5) on Mach number contours shown in fig. 4.19(A) and (D) at 99% span. The shock wave location in a single passage simulation with tip gap 0.188% span has been marked by a line joining points 1 and 2 in fig. 4.19(A). The flow-field of double passage rotor having alternate tip gaps of 0.188% span and 0.94% span is shown in fig. 4.19(D). As discussed earlier, one of the passage is pushed towards stall while the other passage undergoes choked condition. The location of shock wave positions have been marked by points 3, 4 and 5. Hence in the presence of a blade with smaller tip gap, the blade with larger tip gap becomes less loaded than it would have been if all the blades had same tip gaps.



(A) Comparison Of 0.188% Span Tip Gaps (B) Comparison Of 0.94% Span Tip Gaps

Figure 4.21: Comparison At 99% Span Of Single Passage Blade With Tip Gaps 0.188% Span And 0.94% With The Respective Individual Blades Of Double Passage Blades With Tip Gaps 0.188% Span And 0.94% Span (Near Peak Efficiency)

4.3.2 Single Passage Simulation Of Wide Chord Blade

As discussed earlier, the civil aviation turbofan engines have started migrating towards the high mass flow, low-speed fan designs (Lee et al., 2017) as a way to improve the specific fuel consumption. The low-speed fan blades employ a wide chord based design and are typically part-span loaded as seen in Lee et al. (2018). A plot of span-wise pressure ratio for these low speed fans used in the industry is shown in fig. 4.22. It can be seen that the pressure rise in these kind of blades is obtained mainly from the mid-span region.

The wide chord blade test-case used in the present thesis has been tested for different tip gaps similar to NASA Rotor 67 and its performance is shown in fig. 4.23. It can be seen that this fan compared to tip loaded fans like NASA Rotor 67 is less sensitive to tip gap variation. There is no drastic reduction in pressure ratio, efficiency and stability margin. Also, it can be seen in fig. 4.24 (A), (B) and (C) that the pressure ratio, axial velocity and efficiency across the span does not vary appreciably with changes in tip gap size. It can be concluded that the wide chord blades are less sensitive to manufacturing tolerance (for tip gap as a parameter) and hence there would be no appreciable effect with respect to blade rearrangement problem considered in the present thesis. Thus there would be no further investigation with regard to CFD simulation of full annulus wide chord blade with random tip gaps.

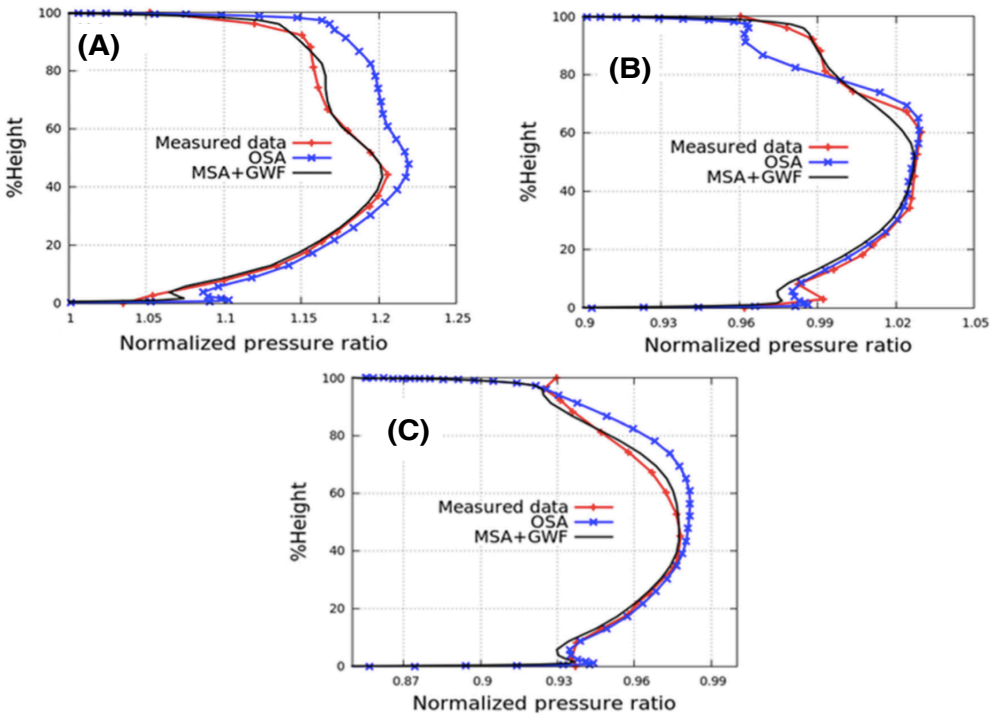


Figure 4.22: Different Low Speed Fans Used In Industry (A) Normalised Pressure Ratio vs Span For Fan A (B) Normalised Pressure Ratio vs Span For Fan B (C) Normalised Pressure Ratio vs Span For Fan C. The Figures Have Been Adapted From Lee et al. (2018) Wherein The Terms OSA, MSA and GWF Represent The Original SA Model, Modified SA Model Based On β-Function And Generalised Wall Function Respectively [Reproduced With Kind Permission Of ASME]

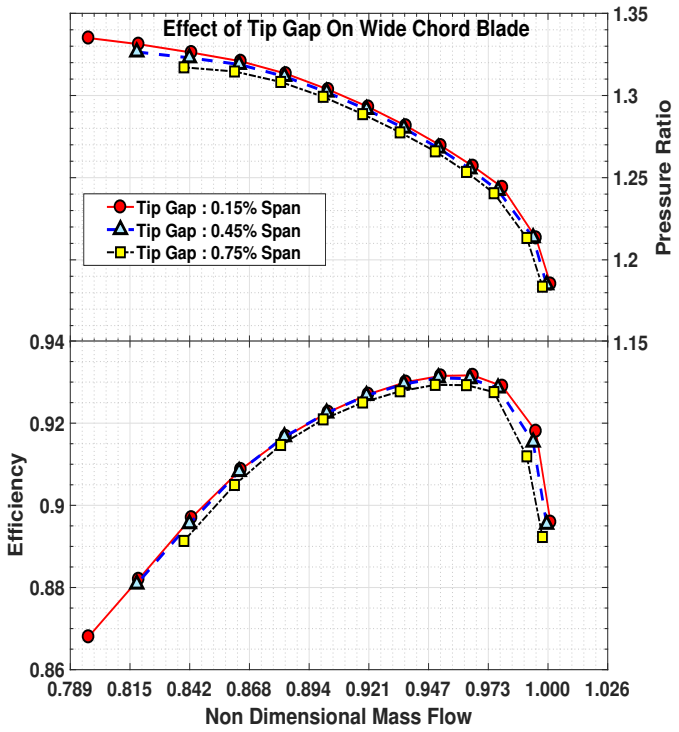
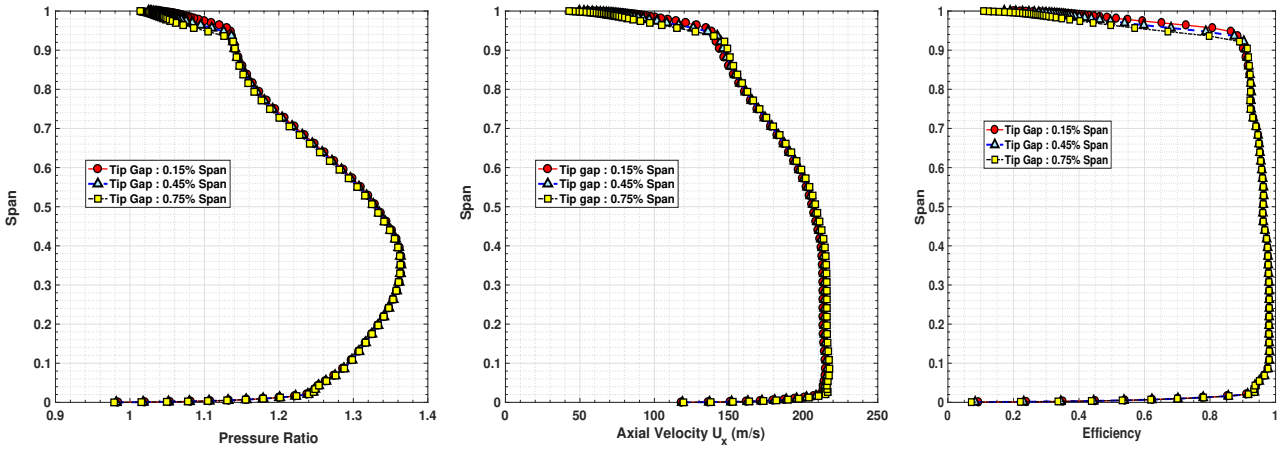


Figure 4.23: Effect Of Tip Gap On Performance Of Wide Chord Blade



(A) Press. Ratio vs Span (B) Axial Velocity vs Span (C) Efficiency vs Span

Figure 4.24: Wide Chord Blade Spanwise Profile Of (A) Pressure Ratio (B) Axial Velocity (C) Efficiency For Different Tip Gaps At Same Non Dimensional Mass Flow Rate Of 0.962

4.3.3 Full Annulus NASA Rotor 67

Another study was conducted to see the effects of arranging 11 blades of 0.188% span tip gap in one half of the annulus and 11 blades of 0.94% span tip gap in the other half of annulus (also called "half annulus arrangement") and was compared with double passage (zigzag pattern) tip gaps of 0.188% span and 0.94% span. It can be seen in fig. 4.25 that the performance and the aerodynamic stability of the double passage with tip gaps 0.188% span and 0.94% span was much better than half annulus arrangement of the tip gaps 0.188% span and 0.94% span. Similar tests were performed for blades with tip gaps 0.376% span and 0.752% span. The performance of double passage with tip gaps 0.376% span and 0.752% span matches closely with the single passage tip gap of 0.564% span as does the half annulus arrangement with tip gaps 0.376% span and 0.752% span. This implies that the type of arrangement plays no further role in eking out any extra performance when the manufacturing tolerance is very close to the mean value.

One interesting way to look at the uniform tip gap and half annulus arrangement case would be as shown in fig. 4.26 (A) and (B). It can be seen that the half annulus arrangement of non-uniform tip gaps introduces an effect similar to eccentrically mounted rotor which can be termed as induced eccentricity. In this regard, Graf et al. (1998) conducted an experimental

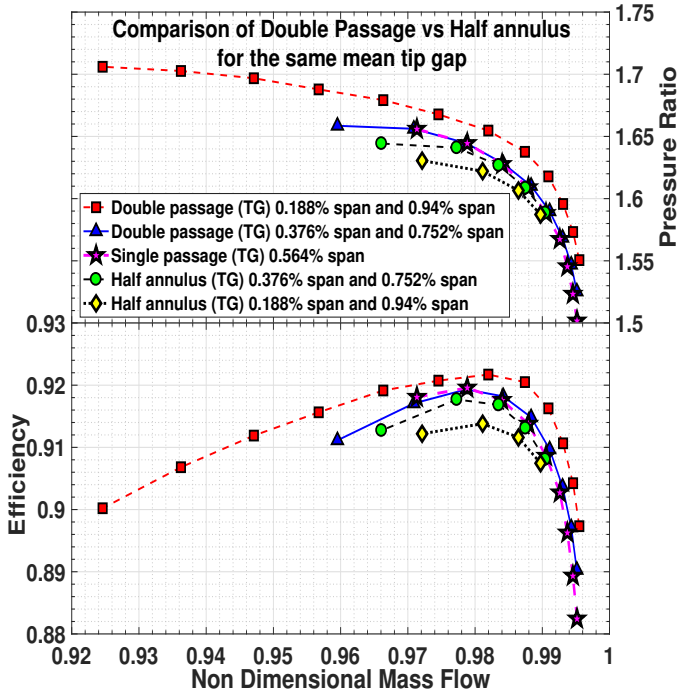


Figure 4.25: Comparison Of Different Double Passage Vs. Half Annulus Arrangement Performances For The Same Mean Tip Gap In Case Of NASA Rotor 67

study on a subsonic axial compressor having a non-axisymmetric tip clearance. They observed that an eccentrically mounted rotor has a smaller stability margin compared to a rotor having uniform clearance of average same level. This is similar to the results shown in fig. 4.25 wherein the half annulus arrangement with tip gaps 0.188% span and 0.94% span stalls earlier compared to single passage tip gap of 0.752% span. With a reduction of this induced eccentricity, the performance of half annulus arrangement with tip gaps 0.376% span and 0.752% span approaches the performance of single passage tip gap with 0.564% span. Graf et al. (1998) have also tested the compressor for one lobed clearance asymmetry and two lobed clearance asymmetry which is akin to half arrangement and quadrant arrangement respectively. Graf et al. (1998) observed that two lobe asymmetry performs better than one lobe asymmetry. In the present research, it is observed that the performance of zigzag pattern (11 lobed clearance asymmetry) is much superior to that of half annulus arrangement (1 lobe).

It can thus be hypothesised that when faced with random tip gaps in a whole annulus which are not close to mean value, the best arrangement would be to have a larger tip gap between two smaller ones also called as “zigzag arrangement” around the full annulus to obtain maximum efficiency, pressure ratio and stall margin. The word “random” in the context of tip gaps is

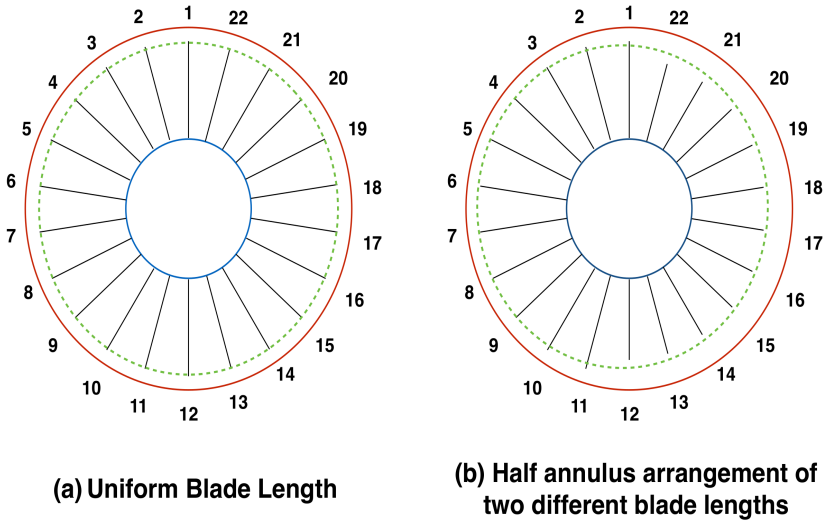


Figure 4.26: A Line Diagram Of Compressor Blades Around The Casing Showing (A) Uniform Tip Gap With Concentric Rotor And Casing (B) Half Annulus Arrangement Of Different Tip Gaps Producing An Effect Similar To Eccentric Rotor

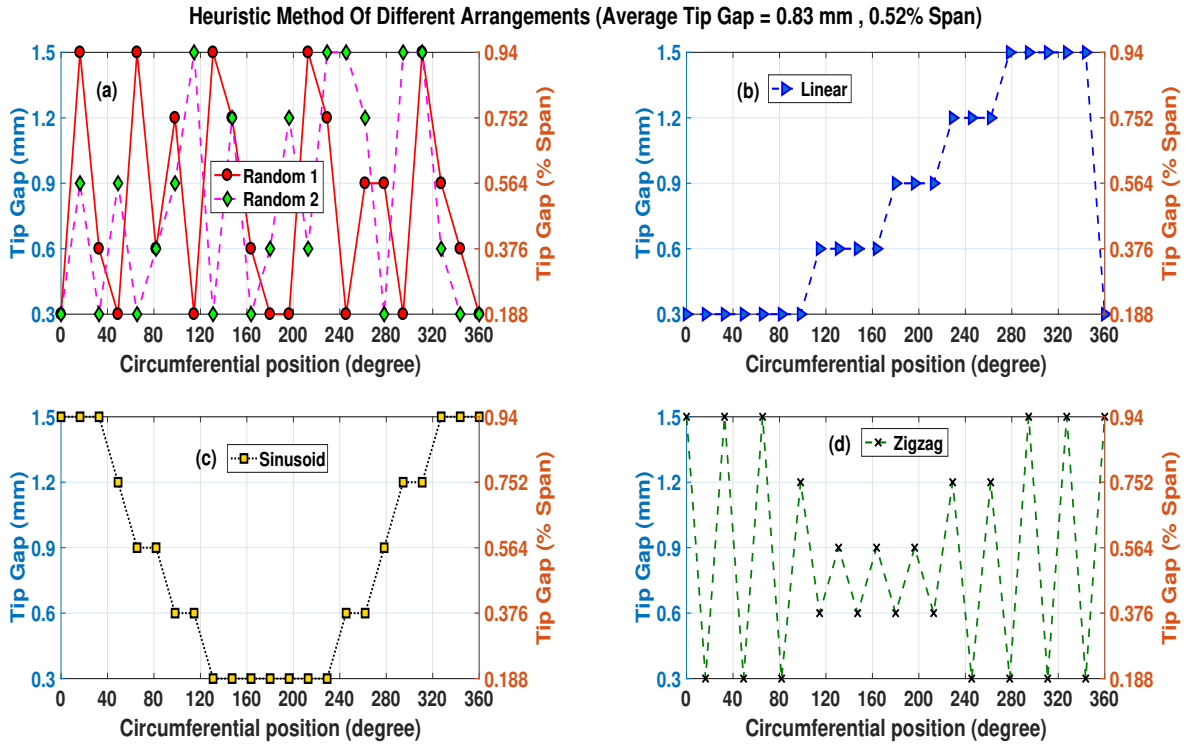


Figure 4.27: Different Combinations For Same Set Of Random Tip Gap Blades For NASA Rotor 67 With Average Tip Gap Of 0.52% Span (A) Random Arrangement (B) Linear Arrangement (C) Sinusoid Arrangement (D) Zigzag Arrangement

a slight misnomer as there are only 5 discrete tip gaps in this study. Instead, a uniformly distributed random integer between 1 to 5 was generated with "1" implying 0.188% span tip

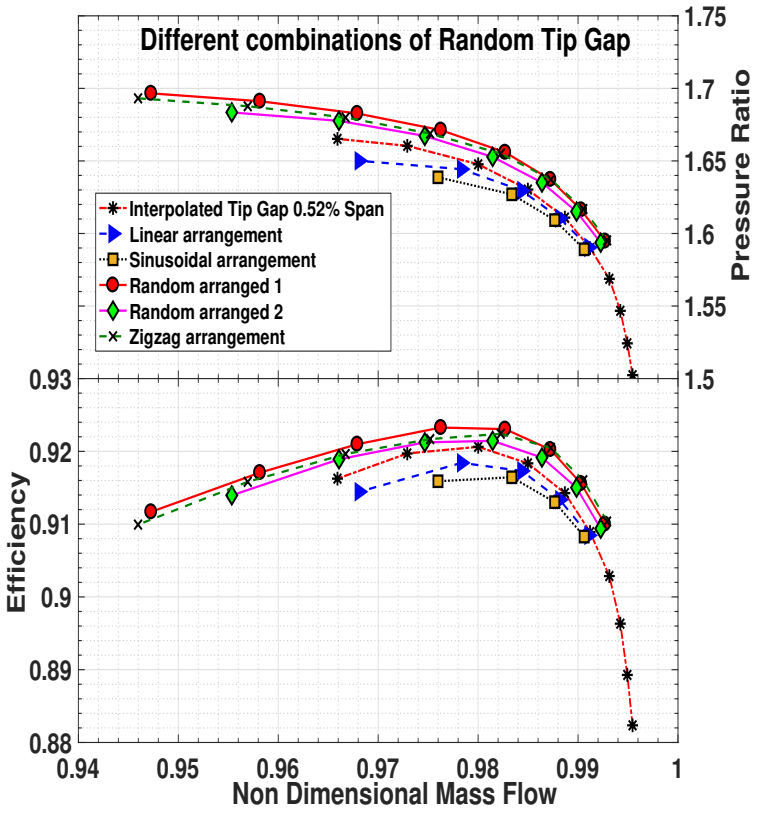


Figure 4.28: Performance For Different Arrangements Of Random Tip Gaps (NASA Rotor 67)

gap and "5" implying 0.94% span tip gap. Fig. 4.27(A) shows the random arrangement of the different tip gaps while fig. 4.27(B), (C) and (D) show the linear, sinusoid and zigzag arrangement respectively for the same set of random blades. Fig. 4.28 shows the corresponding performance of all the different arrangements described in fig. 4.27. It can be seen that sinusoidal arrangement stalls earliest whereas the zigzag arrangement stalls the last on comparison with interpolated performance of single passage average tip gap of 0.52% span which implies that the performance of all the random combination lie in between these two extremities as seen from the performance of "Random arranged 1" and "Random arranged 2". It should be noted that for any arrangement, there are two combinations that are possible: (a) Clockwise (b) Anticlockwise. There were no major difference in the performance curve exhibited by the two combinations.

4.4 Two Parameter Variation : Stagger And Tip Gap

In previous sections, using single passage and double passage CFD simulations, it was hypothesised that the best arrangement for stagger angle as a parameter of variation mandated the mis-stagger between two successive blade to be minimum. The heuristic algorithm showed that both linear arrangement as well as sinusoidal arrangement exhibited the minimum mis-stagger and the subsequent use of deterministic whole annulus CFD simulation confirmed that both the arrangements showed equivalent performance. Furthermore, a GA based TSP analogy confirmed that sinusoidal arrangement does in fact exhibit minimum mis-stagger (akin to minimum distance in TSP). It must be noted that there is no unique solution in this 1D TSP as many different combinations can exhibit an equivalent minimum mis-stagger. The aim of this research is to establish a rule of thumb which is backed up by CFD, mathematical and physical theory. Similar conclusions were drawn about worst arrangement for stagger angle wherein a zigzag kind of arrangement exhibited maximum mis-stagger (akin to maximum distance in TSP) represented the lower limit of compressor performance. In contrast, for tip gap as a parameter of variation, the best and worst arrangement were zigzag arrangement and sinusoidal arrangement respectively.

The optimal arrangement for a 2 parameter problem is more complicated than the previous two previous two cases of single parameter variation because the optimal arrangement in this case would be driven by two opposite mechanisms *i.e. minimum distance* for stagger angle variation and *maximum distance* for tip gap variation. The author would be only analysing the NASA Rotor 67 as a test case for the 2 parameter problem variation.

A double passage case with tip gaps 0.188% span (0.3 mm) and 0.94% span (1.5 mm) is chosen as a the baseline case. 2 cases have been considered :

(I) **L**arge **T**ip gap with Stagger **O**pen and **S**mall **T**ip gap with Stagger **C**losed (LTO-STC)
(II) **S**mall **T**ip gap with Stagger **O**pen and **L**arge **T**ip gap with Stagger **C**losed (STO-LTC).

It is to be noted that when one of the blade is opened, simultaneously, the other blade is closed by same measure which ensures that the mis-stagger increases but mean stagger re-

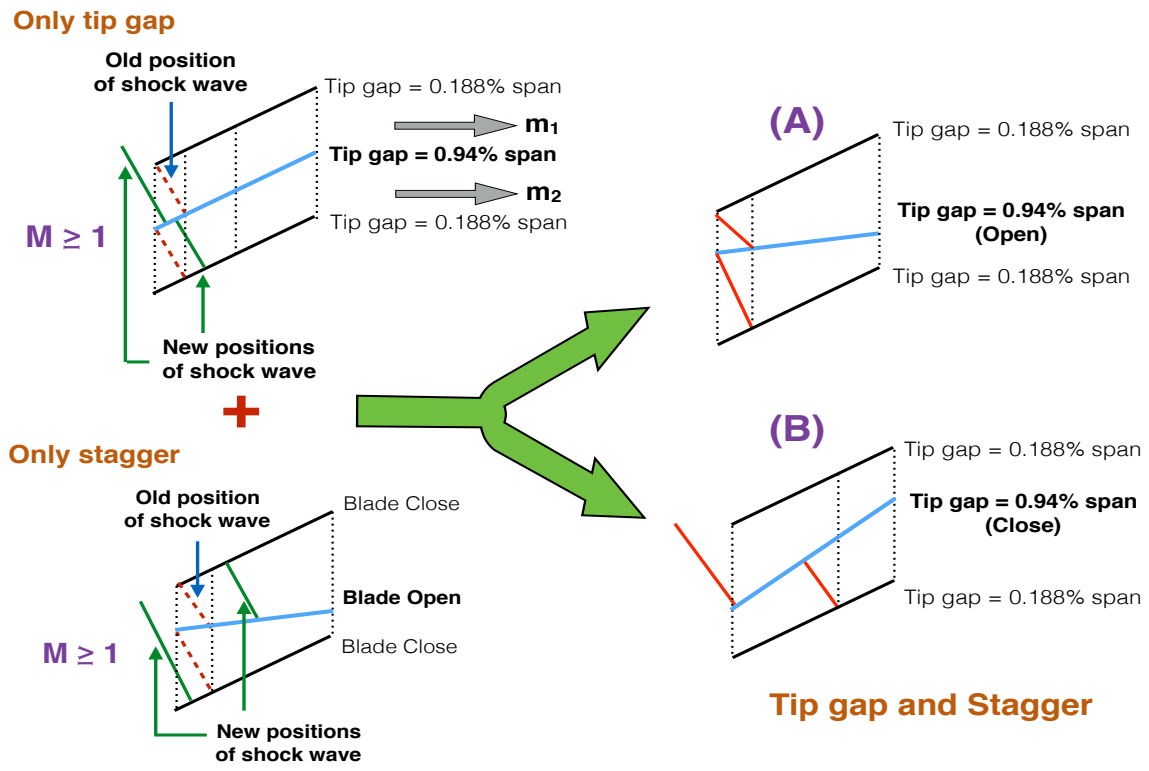


Figure 4.29: Schematic Showing Movement Of shock In Adjacent Passages Due To Variation In Tip Gap And Stagger Angle

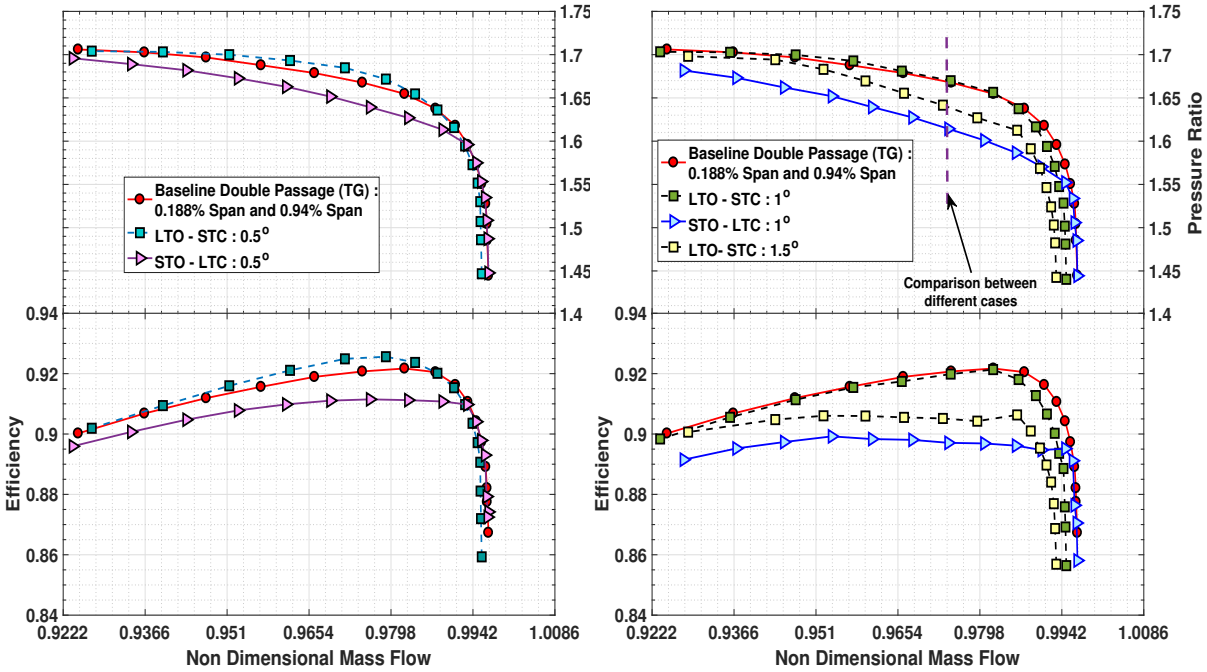
mains unaffected. For each of the 2 cases, the stagger angle has been changed in steps of 0.5° (0.75% relative to the datum stagger angle), 1° (1.5% relative to the datum stagger angle) and 1.5° (2.25% relative to the datum stagger angle). In this section, further discussion has been kept succinct by referring to the tip gap and stagger angle in terms of % span and degree(°) respectively.

The movement of shock waves due to non-uniform tip gap blades and non-uniform staggered blades in adjacent passages was shown in fig. 4.6 and fig. 4.20 respectively. It can be seen that the usage of non-uniform blades resulted in asymmetric shock waves being produced in the adjacent passages. This implies that one of the blade undergoes choke while the other one is in a condition of maximum efficiency. For a two parameter variation case, the author has built a theory for shock wave movement using the prior experience from single parameter variation case. Fig. 4.29 shows the schematic of the theory. As seen in the figure, two distinct possibilities emerge :

(A) The mis-staggering of blade alleviates the asymmetric shock waves being produced due to

the usage of non-uniform tip gap blades (LTO-STC)

(B) The mis-staggering of blade aggravates the asymmetric shock waves being produced due to the usage of non-uniform tip gap blades (STO-LTC)



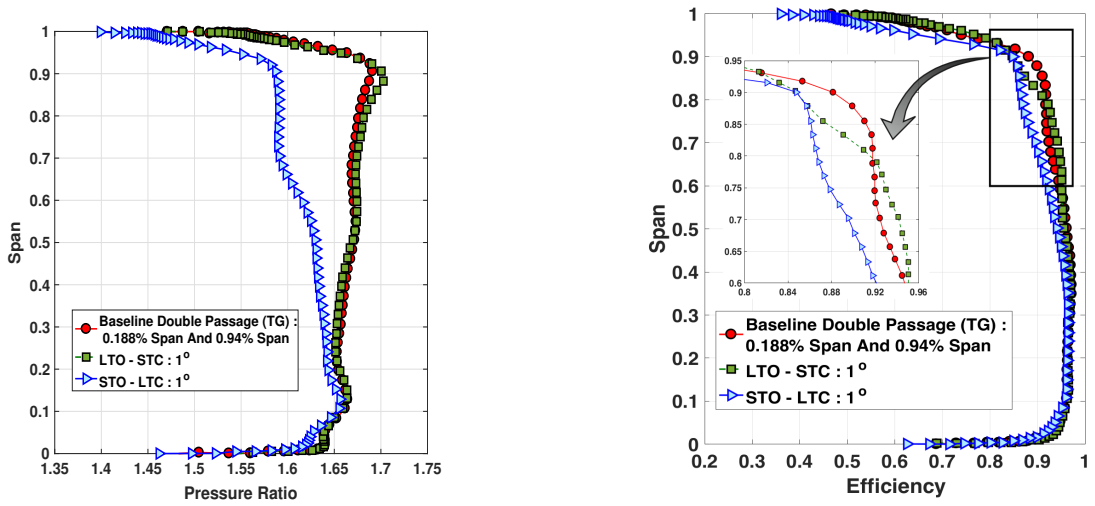
(A) Performance Curve For Double Passage Non-Uniform Tip Gap With Mis-Stagger Of 0.5°

(B) Performance Curve For Double Passage Non-Uniform Tip Gap With Mis-Stagger Of 1° And 1.5°

Figure 4.30: Changes In Performance Curve Due To Variation Of Tip Gap And Stagger Angle

Fig. 4.30 (A) and (B) shows the performance of double passage rotor of NASA Rotor 67 when the tip gap and stagger angle vary simultaneously. It can be seen from fig. 4.30 (A) that the performance of LTO-STC by 0.5° is better than the baseline case while that of STO-LTC by 0.5° is worser than the baseline case. This behaviour of the rotor is exactly as per the theory shown in fig. 4.29. It should be noted that room (or window) for alleviating the asymmetric shock waves in case of blades with non-uniform tip gaps by way of mis-staggering them is very small. The shock waves would be asymmetric if there is excessive mis-staggering of the blades and as a result the performance would deteriorate compared to the baseline case. This can be seen from fig. 4.30 (B) wherein the performance of LTO-STC by 1.5° deteriorates compared to baseline case.

Fig. 4.31(A) shows the spanwise pressure ratio for baseline case, LTO-STC by 1° and STO-LTC



(A) Effect Of Variation Of Tip Gap And Stagger Angle On Spanwise Pressure Ratio

(B) Effect Of Variation Of Tip Gap And Stagger Angle On Spanwise Efficiency

Figure 4.31: Changes In Spanwise Pressure Ratio And Efficiency Due To Variation Of Tip Gap And Stagger Angle

by 1°. It can be seen that the pressure ratio for both baseline case as well as LTO-STC by 1° is almost the same while the case of STO-LTC by 1° shows deterioration of pressure ratio from 20% span onwards. Similarly fig. 4.31(B) shows the spanwise efficiency for the same 3 cases and it can be seen that both baseline case as well as LTO-STC by 1° exhibit similar behaviour while the case of STO-LTC by 1° shows the deterioration of efficiency from 50% span onwards.

Fig. 4.32 shows the movement of shock waves at 98% span in LTO-STC by 1° and STO-LTC by 1° as compared to the baseline case using CFD. The pink line (in case of LTO-STC and STO-LTC) represents the original location of shock wave as observed in baseline case whereas the green line represents the actual location of shock waves. It can be seen that the movement of shock waves in case of STO-LTC by 1° makes the two adjacent passages more stalled and more choked compared to the baseline case. In case of LTO-STC by 1°, it can be seen that the position of shock waves have been interchanged compared to the baseline. The passage in the baseline case that was undergoing maximum efficiency, now undergoes choke while the other passage in the baseline case that was undergoing choke, now undergoes maximum efficiency.

Fig. 4.33(A) compares the loading on blade with smaller tip gap of 0.188% span for baseline case, LTO-STC by 1° and STO-LTC by 1°. Similarly, fig. 4.33(B) compares the loading on blade with larger tip gap of 0.94% span for baseline case, LTO-STC by 1° and STO-LTC by

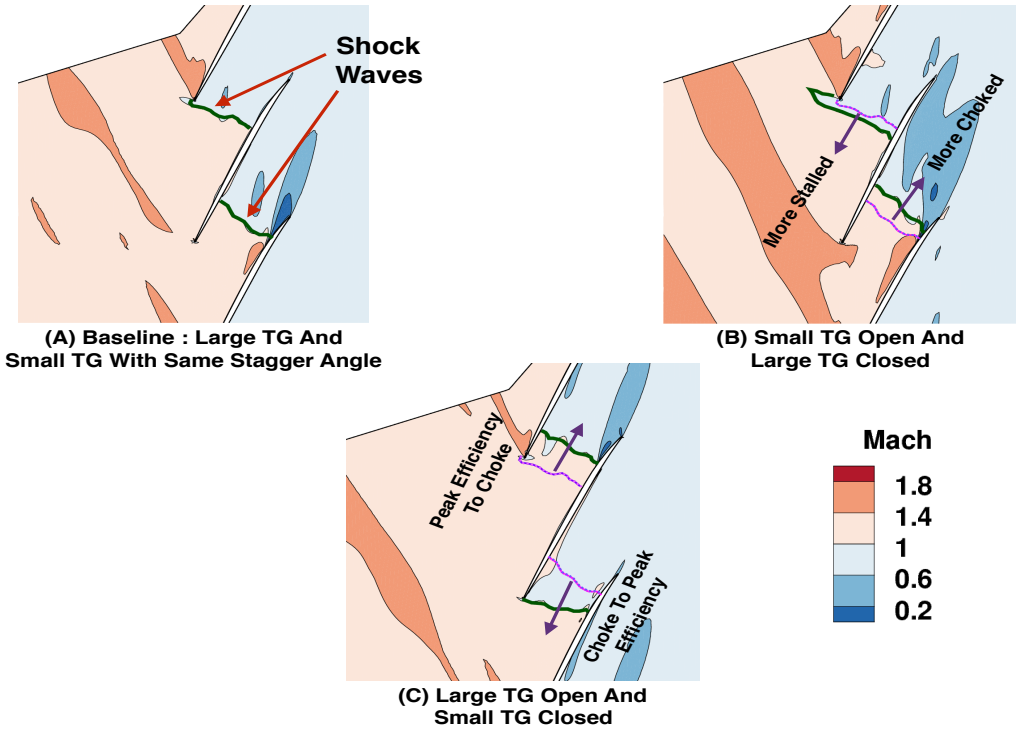


Figure 4.32: Shock Movement In Adjacent Passages Of Double Passage With Tip Gaps 0.188% Span And 0.94% Span Due To Variation Of Stagger Angle By 1° At 98% Span

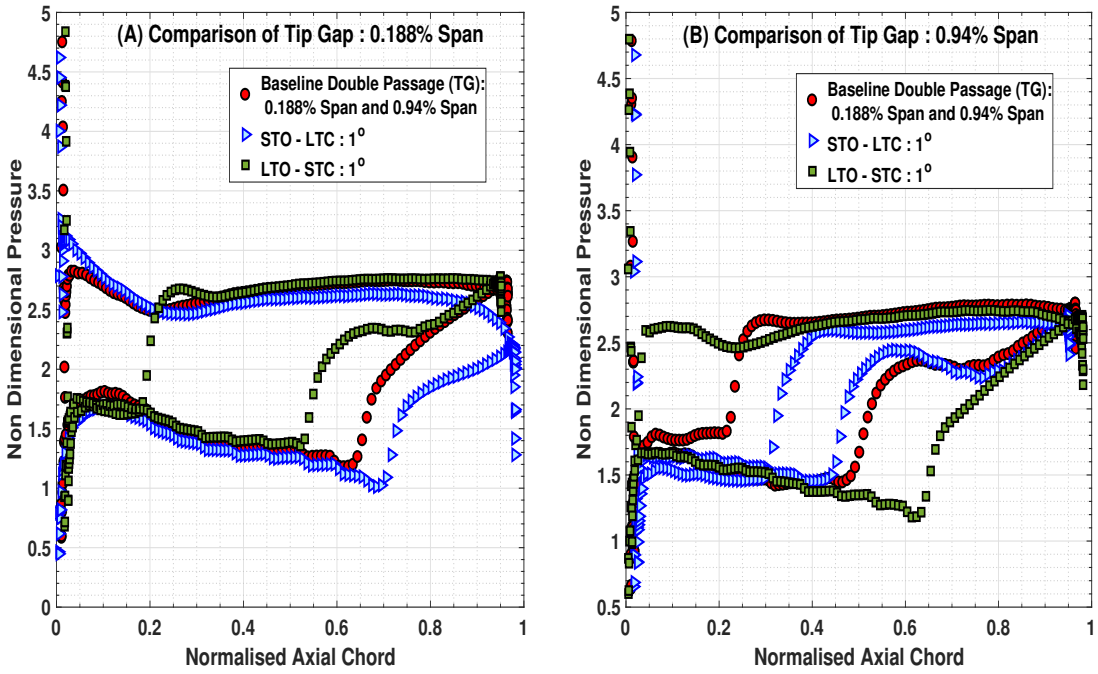


Figure 4.33: Loading At 80% Span From Hub In Blades With Tip Gap Of (A) 0.188% Span (B) 0.94% Span For Baseline Double Passage, LTO-STC : 1° And STO-LTC : 1°

1°. It can be seen in fig. 4.33(A) that the blade with smaller tip gap in the LTO-STC by 1° is less loaded compared to the blade with smaller tip gap in baseline case. However, the blade

with larger tip gap in LTO-STC by 1° is more loaded compared to the blade with larger tip gap in the baseline case as seen in fig. 4.33(B) and this compensates the loss of loading on blade with smaller tip gap. Also, it can be seen in fig. 4.33(A) that the blade with smaller tip gap in STO-LTC by 1° is slightly more loaded compared to blade with smaller tip gap in the baseline case. However, this is accompanied with very little loading of the blade with larger tip gap in STO-LTC by 1° compared to blade with larger tip gap in the baseline case as seen in fig. 4.33(B).

However, the above cases do not represent the true effect of manufacturing tolerance. In real scenario, each blade would have varying tip gaps as well as stagger angle. The aim of this work is to establish a rule of thumb for arranging them optimally so as to eke out maximum performance and stability margin. However before tackling such a complex problem, "a pseudo random" varying case has been generated which consists of :

(i) 6 blades with tip gap of 0.188% span and stagger angle of 1°
(ii) 5 blades with tip gap of 0.188% span and stagger angle of -1°
(iii) 6 blades with tip gap of 0.94% span and stagger angle of -1°
(iv) 5 blades with tip gap of 0.94% span and stagger angle of 1°

Thus there are 11 blades with tip gap of 0.188% span and 11 blades with tip gap of 0.94% span. Also, there are 11 blades with stagger angle of 1° and 11 blade with stagger angle of -1°. The variation in this case is done under controlled atmosphere rather than a machine generated random values and hence the name "a pseudo random" varying case. It must be noted that the pseudo random varying case has only 4 unique (distinct) blades (rest of them are repetition). It is known from the previous section that zigzag arrangement for tip gap would give maximum stability margin, maximum efficiency and maximum pressure ratio. For stagger angle variation, a smooth sinusoidal/linear arrangement would give maximum efficiency. Intuitively, the best arrangement in this case (order is important) should consist of two half arrangements such that in one half of the annulus, there are alternate (i) and (iv) blades while in the other half of annulus, there are alternate (iii) and (ii) blades. This ensures all the blades are zigzag arranged for tip gaps and stagger angle is distributed smoothly. Any other arrangement either

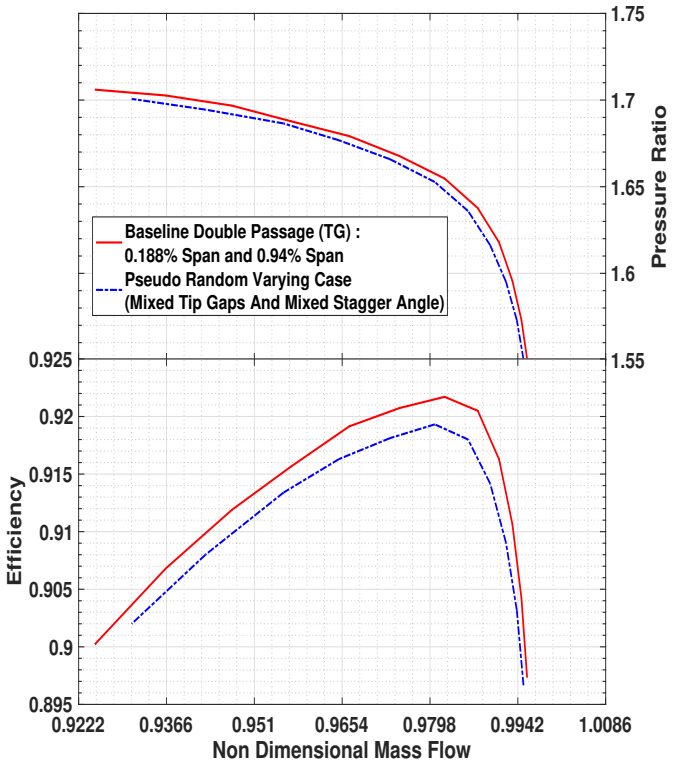


Figure 4.34: Comparison Of Performance Of Double Passage Baseline And Pseudo Random Varying Case

disturbs the smooth distribution of stagger angle (and in turn increase the cumulative mis-stagger throughout the annulus) or disturbs the zigzag arrangement of tip gap. As seen in fig. 4.34, the performance and stability margin of optimally arranged pseudo random varying case matches very closely with that of baseline case of double passage with blades of tip gaps 0.188% span and 0.94% span. A similar optimal arrangement can also be arrived at using TSP algorithm (albeit with some modification).

$$d \quad = \quad min \left(\sum_{i=1}^{N} \sqrt{(dx_i^2 + dy_i^2\ )} \right) \tag{4.4}$$

The euclidean distance (d) is minimised as shown in equation 4.4, to get the shortest path for N cities in TSP. The longest path can be defined as the inverse of minimum distance problem. As discussed earlier, the optimal configuration of stagger angle is given by the shortest distance path while that for the tip gap is given by the longest distance path. When these two parameters vary simultaneously, the true global optimum would be zigzag variation of tip gap followed by smooth variation of stagger angle (because the behaviour of tip gap variation is more non-linear

compared to behaviour of stagger angle variation). This can be obtained by defining the new euclidean distance d_1 to be given by

$$d_1 = min\left(\sum_{i=1}^{N}\sqrt{\left(dx_i^2 + \frac{1}{dy_i^2}\right)}\right) \tag{4.5}$$

The magnitude of stagger angle ($\pm$ 1.5°) is comparable to the magnitude of tip gap (0.188% span - 0.94% span). Of the two varying parameters, tip gap is more non-linear compared to stagger angle. To make sure the true global optimal arrangement is zigzag arrangement of tip gap followed by smooth stagger angle variation (and not vice versa), the magnitude of stagger angle is reduced by a factor of 1000 (an arbitrary large number which is used to artificially inflate the magnitude of tip gap vis-a-vis stagger angle).

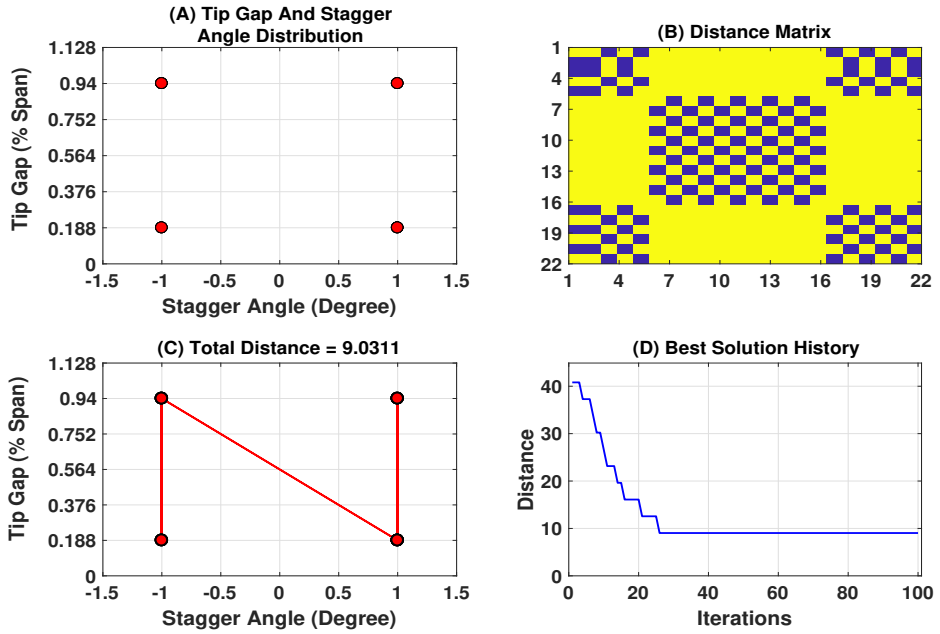
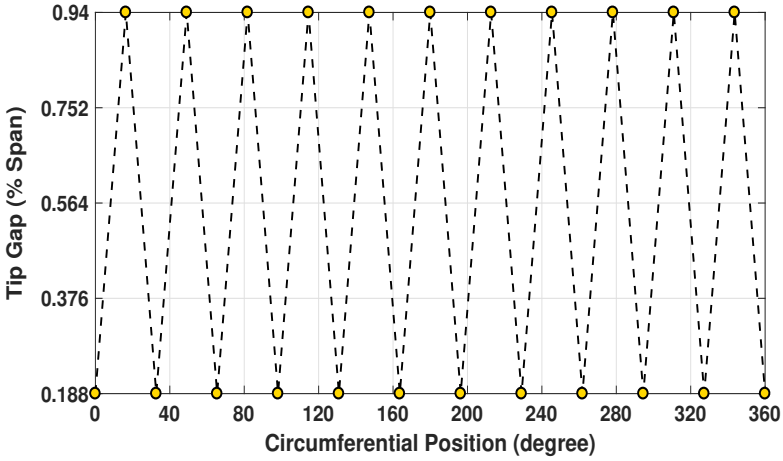
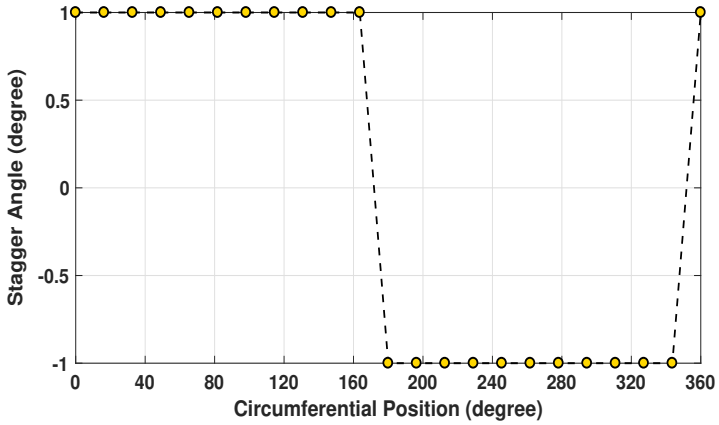


Figure 4.35: TSP Analogy For Pseudo Random Variation Of Tip Gap And Stagger Angle : (A) Distribution Of Different Staggered And Tip Gap Blades (B) Distance Matrix (C) Optimal Path (D) Converged Solution History

In a conventional TSP, each city is defined by its latitude and longitude. In the present 2 dimensional optimisation case, the blades are defined using their stagger angle and tip gap size. Fig. 4.35(A) shows the distribution of blades with different tip gaps and stagger angle for pseudo random variation case. 4 circles are visible in this plot as there are only 4 unique blades in this case as discussed earlier. The distance d_1 of each blade is calculated with respect to every other blade in the design space and the resulting distance matrix is shown in fig. 4.35(B).



(A) Circumferential Variation Of Tip Gap



(B) Circumferential Variation Of Stagger Angle

Figure 4.36: Optimised Arrangement Using TSP Analogy For Pseudo Random Variation : (A) Arrangement For Blades With Different Tip Gap (B) Arrangement For Blades With Different Stagger Angle

This distance matrix does not hold any physical meaning as the magnitude of stagger angle is reduced by using a large number and also the new euclidean distance (d_1) is not the same as conventional euclidean distance (d). Fig. 4.35(C) shows the route taken to find the global optimal solution and Fig. 4.35(D) shows the converged solution history.

The optimal arrangement of the blade has been plotted in fig. 4.36(A) and (B). It can be seen that this arrangement represents the true global optimum wherein a zigzag variation for tip gap is followed by smooth variation for stagger angle. This method of arrangement can thus be extended to cases wherein both the tip gap as well as stagger angle are completely random. Fig. 4.37(A) shows the distribution of blades with random stagger angle and random tip gap variation. It can be seen that there are 22 circles which implies that all the blades in

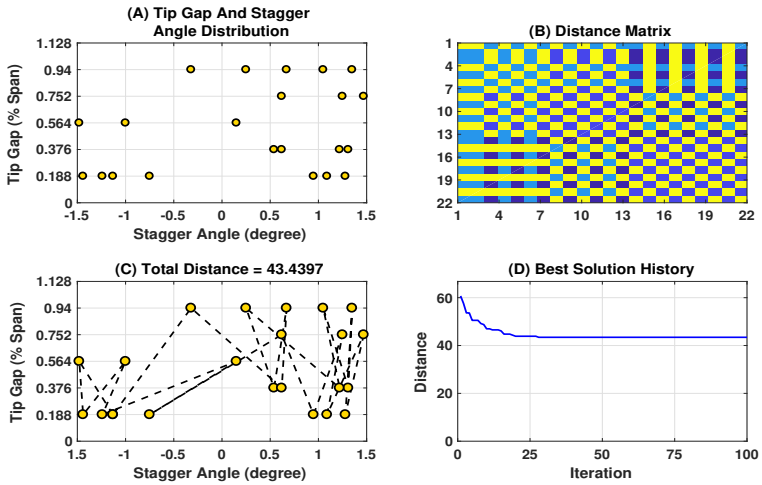
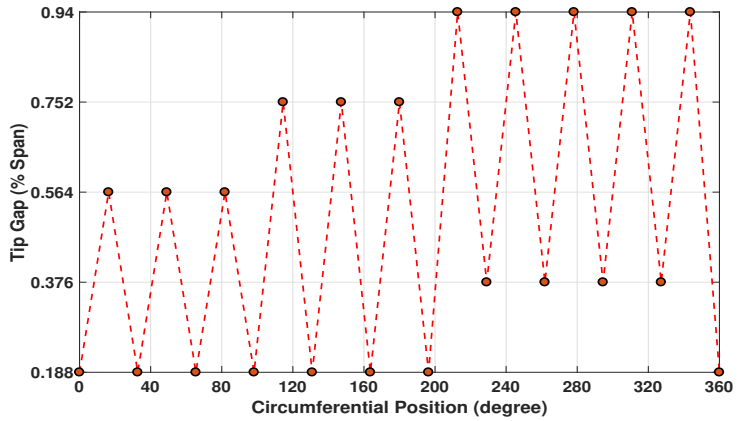


Figure 4.37: TSP Analogy For Random Variation Of Tip Gap And Stagger Angle : (A) Distribution Of Different Staggered And Tip Gap Blades (B) Distance matrix (C) Optimal Path (D) Converged Solution History

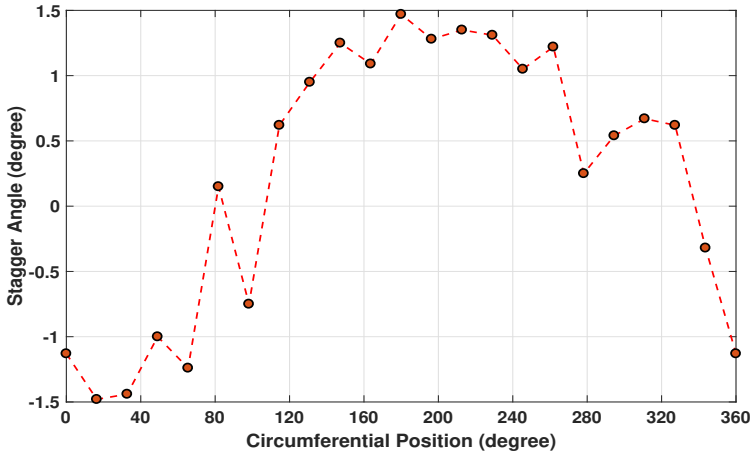
the compressor are unique. This figure represents the true effect of manufacturing tolerance wherein all the compressor blades would have differing stagger angle as well as differing tip gaps.

The distance matrix based on the new euclidean distance d_1 is shown in fig. 4.37(B). The distance matrix represents the distance of each blade with respect to every other blade in the compressor based on new euclidean distance d_1. As discussed previously, this distance matrix does not hold any physical meaning as the magnitude of stagger angle is reduced by using a large number and also the new euclidean distance (d_1) is not the same as conventional euclidean distance (d). Fig. 4.37(C) shows the route taken to find the global optimal solution while fig. 4.37(D) shows the converged solution history.

Fig. 4.38(A) and (B) shows the arrangement of blades with random tip gap and blades with random stagger angle based on optimal route predicted in fig. 4.37(C). It can be seen that the blades with random tip gaps are arranged in zigzag order and simultaneously the blades with random stagger angle has been arranged in such a way that the stagger angle variation between two adjacent blades is minimum. The advantage of this method is that the blades could be more efficiently arranged using multidimensional TSP when three or more parameters vary simultaneously. It has to be noted that the distance is always defined using euclidean norm and hence the terms involving cross products 'xy' are ignored.



(A) Circumferential Variation Of Random Tip Gap



(B) Circumferential Variation Of Random Stagger Angle

Figure 4.38: Optimised Arrangement Using TSP Analogy For Random Variation : (A) Arrangement For Blades With Different Tip Gap (B) Arrangement For Blades With Different Stagger Angle

4.5 Chapter Summary

The chapter starts with a detailed introduction to the subject of metrology and quality control wherein various concepts like tolerance control, tolerance accumulation, Go-No Go gauges and selective assembly were discussed. Two parametric uncertain parameters were considered namely, Tip gap and Stagger angle. A series of single passage and double passage simulations were performed which helped understand the underlying flow physics.

In case of stagger angle variation, as the mis-stagger increases the maximum efficiency of the compressor decreases. This was attributed to one of the passage undergoing choke or stall while the other passage undergoes maximum efficiency condition. Both NASA Rotor 67 as well

as wide chord blade exhibited this kind of behaviour. It was thus hypothesised that smoother redistribution of stagger angle would give better performance. For this a heuristic based method of arranging the blades was developed. It was found that both sinusoidal arrangement and linear arrangement exhibited lowest cumulative mis-stagger while a zigzag arrangement had the largest cumulative mis-stagger. This result was further backed up using a genetic algorithm based code used to solve Travelling Salesman Problem. A full annulus CFD simulation at design speed and off-design speed for NASA Rotor 67 confirmed that sinusoidal and linear arrangement gave best performance while zigzag arrangement gave the worst performance. Similar results were also observed for wide-chord blade rotor.

For tip gap variation, it was found that the performance and stability limit reduces as the size of tip gap increases in a single passage CFD simulation. Moreover, an alternate arrangement of blades with small tip gap and large tip gap had better stall margin compared to the half annulus arrangement of blades with small tip gap and large tip gap. In case of alternate arrangement, the blade with smaller tip gap unloads the blade with larger tip gap thereby delaying the onset of stall. It was thus hypothesised that a zigzag arrangement wherein the largest tip gap blade is sandwiched between two smallest tip gap blades would give the best performance and stability margin. A full annulus CFD simulation at design speed for NASA Rotor 67 confirmed that the zigzag arrangement gave best performance and stability margin while sinusoidal arrangement exhibited the worst performance and stability margin. The wide chord blade which is part span loaded is not very sensitive to variations in tip gap and hence not studied.

When both the stagger angle and tip gap undergo simultaneous variation, it was observed that the double passage case of large tip gap open and small tip gap closed performed better than the baseline double passage case of large tip gap and small tip gap up to a certain threshold of mis-stagger after which its performance deteriorates. The double passage case of small tip gap open and large tip gap closed has a loss of performance from the beginning. It can thus be seen that the principle of superposition cannot be applied when the two parameters are coupled to each other. Furthermore, by changing the definition of euclidean distance, the GA-TSP can be used to arrive at best arrangement when both these parameters undergo simultaneous random variation.

Chapter 5

Study of In-service Degradation In An Industrial Gas Turbine

"It's better to lead change than follow it" - Jeff Martin (Jetblue Airways)

This chapter gives a detailed background regarding the types of damaged blades, its causes and the cost to industry. The literature focusses on both aero-engines as well as industrial gas turbines. The chapter then looks into the allowable damage limits in compressor blades as given by the Federal Aviation Administration (2018) and legacy data for Merlin Engine.

The chapter then introduces the effect of geometric variability due to damage suffered by the compressor blade using single passage and double passage simulations. The damage on each blade is then considered to be completely random and best arrangement has been proposed based on the flow physics obtained through CFD simulation. Finally, the limitation of this study along with modern developments on ways to alleviate this problem has been given. Parts of this chapter have been published in ASME TurboExpo, 2020 (Paper Number : GT2020-16315).

5.1 Background To Damaged Blades In Compressors

In the previous chapter, it was seen that reducing the tip gap has a positive impact on pressure ratio, efficiency and stall margin. However, this can also give rise to increased tip rubbing incidents which can damage the blade as well casing. This is usually exacerbated due to factors like centrifugal forces acting on blades of an off-centered rotor, different thermal expansion of blade and casing due to different materials being used to manufacture it and heavy landings which distorts the casing (Arzina, 2011). These kind of damages are primarily due to poor manufacturing and assembly (without due regard for manufacturing tolerances and/or tolerance stackup) along with secondary reasons like faulty operation of the machine. In extreme cases of high tip rubbing forces, the blades can fracture and subsequently destroy the the next set of blades resulting in total annihilation of blades also called as "de-cobbing". Damage to the engine that results due to the broken off pieces from upstream engine parts are usually classified under impact damage (more specifically "Known Object Damage").

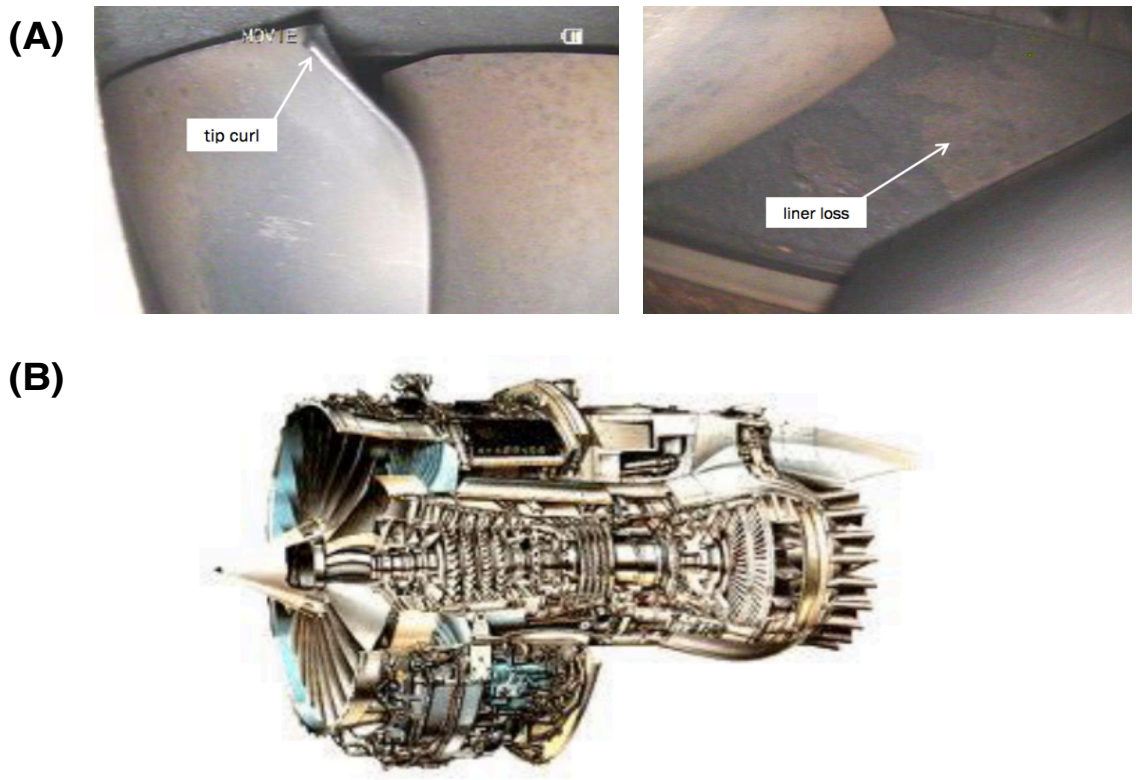


Figure 5.1: (A) High Pressure Compressor Tip Curl Damage And Missing Liner (B) Rolls-Royce RB 211-524GT Engine - Adapted From Marshall et al. (2013) [Reproduced With Kind Permission Of Rolls-Royce, PLC]

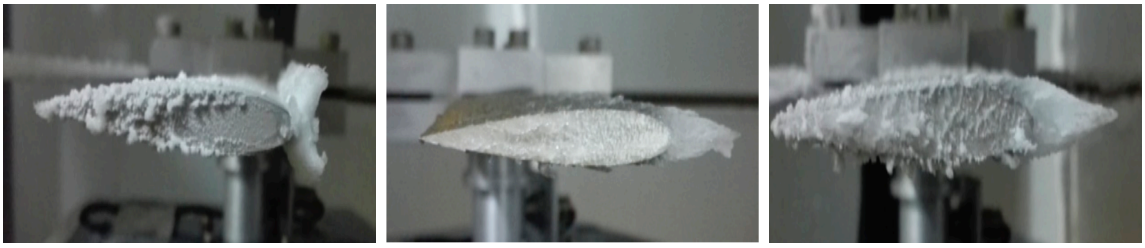


Figure 5.2: Formation Of Glaze Ice At -5°C, Mixed Ice At -10°C And Rime Ice At -15°C Temperature - Adapted From Wang et al. (2020)

Tip-rubbing is a significant contributor to excessive engine maintenance at the least and engine failures at worst. Arzina (2011) notes that in 1973, National Transportation Safety Board (NTRB) recorded a case of mid-air disintegration of engine fan assembly due to interaction between fan blade tip and casing. In fact, Kascak et al. (1987) accredited 10.2% of the 275 reported jet engine failures between 1962 and 1975 to the rub-related phenomena as cited in Arzina (2011). A common defect observed in the blade due to the tip rub phenomena is tip curl damage (though it can also occur due to variety of other reasons like surge of compressors and impact damage). Fig. 5.1(A) shows the tip curl damage and missing liner in a high pressure compressor (HPC) of Rolls-Royce RB 211-524GT (shown in fig. 5.1(B)) engine due to possible surge of compressor during the Sydney-Aukland flight (Marshall et al., 2013).

According to Aust and Pons (2019), the impact damage can further arise due to (a) Organic (birdstrike) (b) Poor maintenance practice (left behind hand tools in engine assembly, improper assembly-disassembly) (c) Foreign Object Damage (ingestion of ice, sand, ash, ground debris). Birdstrikes (relevant only to aero-engines) can prove hazardous to human life in the worst case scenario. McFann (2005) has listed the causes of all accidents in different platforms in US Airforce. Malfunctioning of engine caused due to birdstrike included prominent platforms like C-5, C-130, KC-10, B-1B, B-52 and F-15. A total of 4477 birdstrikes costed approximately $52 million in FY 2004. This included the cost towards engine repair, engine replacement, aircraft structure repair and loss of aircraft (due to damaged engine).

The author has ignored discussing the damage due to poor maintenance practice as these are human errors that can be eliminated and has concentrated on foreign object damage (FOD).

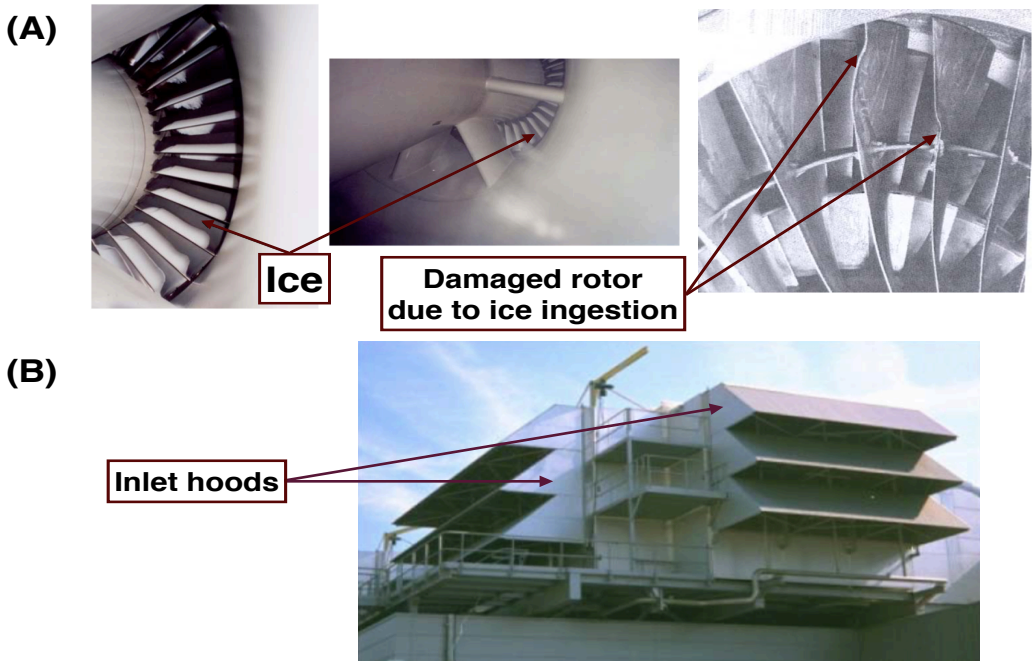


Figure 5.3: (A) Ice Formation On IGV Of Industrial Gas Turbine And Damage On Compressor Blade Due To Ice Ingestion (B) Installation Of Inlet Hoods At The Intake Of Industrial Gas Turbine - Figures Adapted From Sammak (2006)

An industrial gas turbine typically operates in regions like tropics, dessert, polar regions and at seas (Loud and Slaterpryce, 1991). Icing is major problem that is encountered while operating a gas turbines in polar regions as it can modify the shape of the leading edge by either sticking to the blade surface or by causing dents on the blade surface due to high velocity impact. It can thus trigger instabilities like stall/surge with a potential to cause flame-out event by entering the combustion chamber (Kundu, 2015).

The formation of ice on the blades is highly dependent on factors like relative humidity, ambient temperature, air velocity, droplet size along with rotation speed and radius of curvature of the blade (Sammak, 2006; Wang et al., 2020). Precipitate icing can be in the form of hail, snow, freezing rain, ice fog, ice crystals and super cooled water droplets (Sammak, 2006). Hails can cause severe damage to the engine cowling as well as the rotor blades. Lockheed Constellation suffered simultaneous failure of all four engines when encountering hail (Souter and Emerson, 1952). Rasmussen et al. (2006) observed an accretion of freezing drizzle on the jet engine fan blades and cowling which are subsequently shed during the take off. Due to this shedding, United Airlines suffered damage to their 12 B737-300 engines which cost them over $2 million.

The condensate icing comes into picture when the air stream in the inlet (bellmouth) accelerates to a high velocity that in turn causes a drop in the static temperature of the air (Sammak, 2006). Under such situations, the air might become saturated with the water vapour condensing on the surface of the intake system. For the ice formation to take place on the surface, the surface temperature has to be below the air saturation temperature as well as below the freezing point of water (Stewart, 2001). Three types of ice can form on the rotor blades depending on the ambient temperature. Fig. 5.2 shows the formation of glaze ice at -5°C, mixed ice at -10°C and rime ice at -15°C (Wang et al., 2020). The rime ice contains a high amount of trapped air and is therefore less dense, more brittle compared to glaze ice (Sammak, 2006).

An important objective while operating at a temperature of -40°C in polar region is to prevent ice formation on the Inlet Guide Vanes (IGVs). The formation of ice leads to performance loss and blockage of inlet filtration equipment causing the gas turbine to ingest unfiltered air. In extreme cases, a chunk of ice striking the rotor blade tends to deflect the blade tip about its neutral axis; which if high enough, can cause mechanical interference with the trailing edge of the inlet guide vane. This can result is some metal shedding which in turn can affect the subsequent stages of the compressor (Dickson, 1976). Fig. 5.3(A) shows the condensate ice formation on the IGV and the damage suffered by the rotor blades due to its ingestion. The installation of inlet hoods at the intake of IGT as shown in fig. 5.3(B) causes the air to rise vertically before entering the system. This leads to separation of precipitate icing (hail, snow) due to their high inertia (Sammak, 2006). However, it allows particles like mist of size less than 10 μm to enter the system. Hence IGT suffers predominantly from condensate icing problem unlike aero-engine which suffers from both precipitate icing as well as condensate icing.

Erosion-corrosion mechanism is major factor that degrades the blade surfaces of compressor. This is very dynamic in nature as one effect influences the other and hence cannot be decoupled. This typically occurs due to ingestion of abrasive particles (like sand and ash) and the wear is highly dependent on the angle at which hits the surface, the velocity of the particle, temperature and the chemicals present in the atmosphere. It is further complicated by the fact that certain metals oxidise slowly (copper, lead) while few other oxidise fast (aluminium). This oxide layer can either form uniform, non-porous protective layer or it can be a porous layer which allows

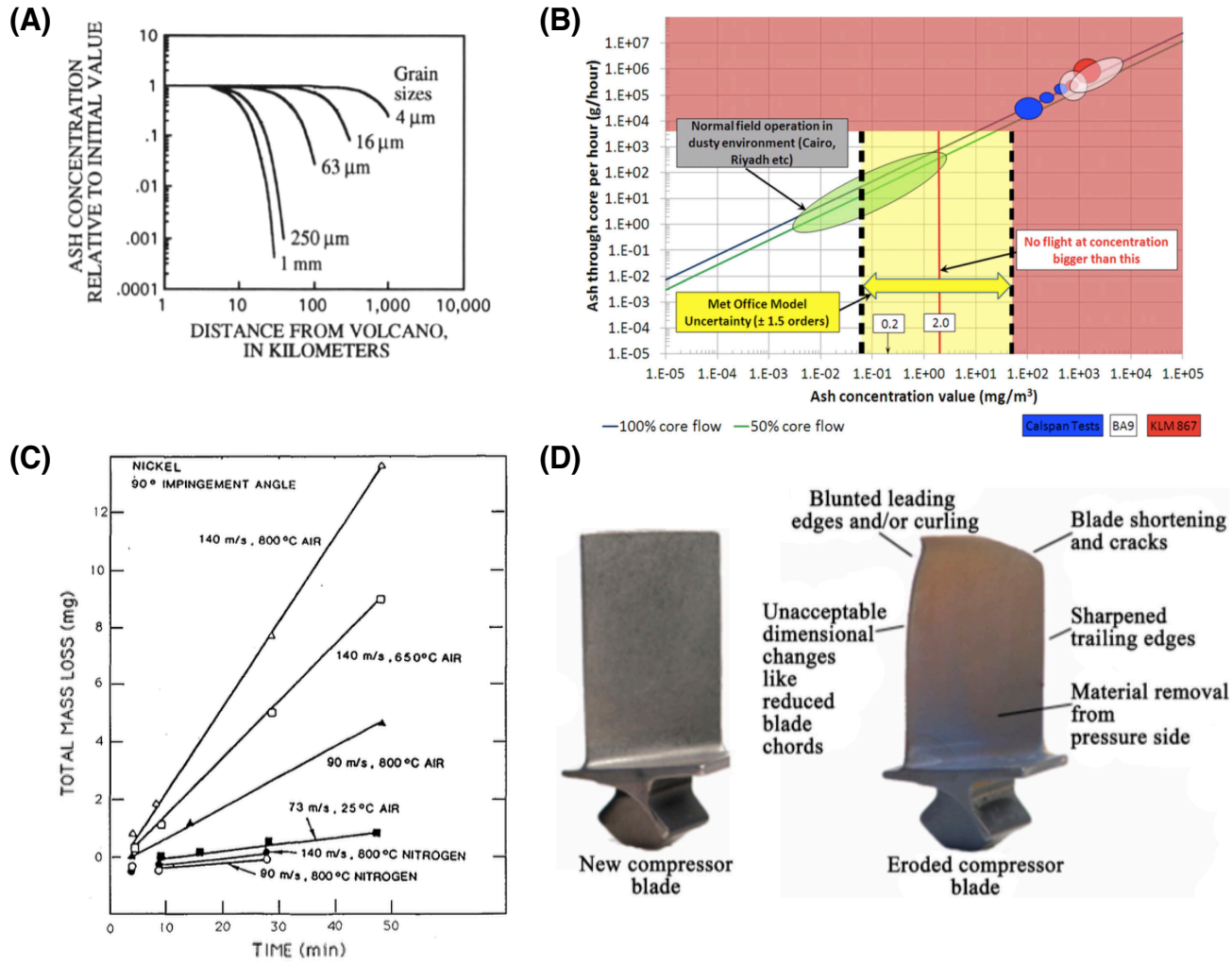


Figure 5.4: (A) Modelled Ash Particles From The Site Of Volcanic Eruption - Figure Adapted From Davison and Rutke (2014) [Reproduced With Kind Permission Of ASME] (B) Operating Envelop In Dust Laden Environment From Rolls Royce - Adapted From Davison and Rutke (2014) [Reproduced With Kind Permission Of ASME] (C) Erosive Loss Kinetics For Nickel At 90° Impact At Different Velocities, Temperature And Fluids As Given In Kang et al. (1987) - Adapted From Birks et al. (1993) [Reproduced With Kind Permission Of Springer Nature] (D) Comparison Of New Compressor Blade And Eroded Compressor Blade As Given In Hamed And Tabakoff (1994) - Adapted From Alqallaf et al. (2020)

oxygen to react with the exposed metal surface (John, 1992). The mechanical properties of the oxide layer (also called as film or scale) in terms of its resistance to abrasion would further decide the dynamics of erosion-corrosion mechanism. Moreover, the mechanism of erosion for ductile material is different from that of brittle materials (Alqallaf et al., 2020) and many materials exhibit ductile-to-brittle transition depending on the temperature. It is therefore important to develop materials that are not only capable of bearing the load during operation of turbo-machinery but also be able to resist the wear and tear due to erosion-corrosion mechanism.

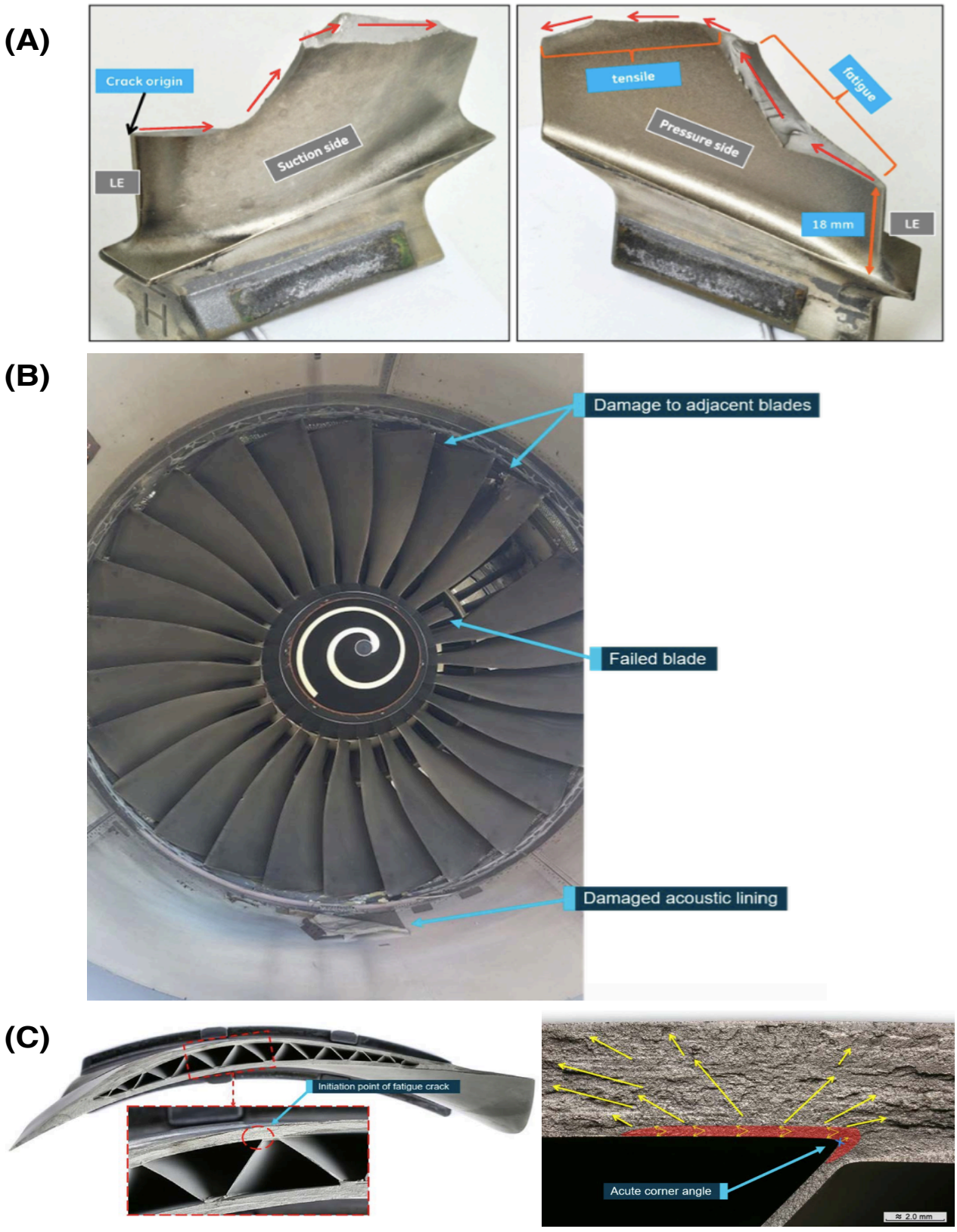


Figure 5.5: (A) Fatigue Failure Of The HPC Blade (Ti-6Al-4V Alloy) In An Industrial Gas Turbine - Adapted From Jasiczek et al. (2013) [Reproduced With Kind Permission Of Springer Nature] (B) Fatigue Failure Of Fan Blade In Rolls-Royce Trent 772B-60 Engines [Reproduced With Kind Permission Of Rolls-Royce, PLC] (C) Region of Crack Initiation Point (Left) And Magnified View Of Fracture Showing Its Propagation (Right) In Fan Blade Of Rolls-Royce Trent 772B-60 Engines - Adapted From ATSB (2020) [Reproduced With Kind Permission Of Rolls-Royce, PLC]

Fig. 5.4(A) shows the ash concentration in the atmosphere from the site of volcanic eruption site - the figure has been adapted from Davison and Rutke (2014). It can be seen that 4 μm particles can be found even at a distance of 1000 km from eruption site. These kind of plots are for guidance only as the dispersal would strongly depend upon the prevailing wind conditions, etc. Fig. 5.4(B) shows the volcanic ash flight envelope as given by Rolls-Royce - the figure has been adapted from Davison and Rutke (2014). It clearly demarcates the (red) area wherein the operation of engine has to be avoided. Davison and Rutke (2014) have listed the significant incidents in the near past when flights encountered ash concentration above the allowable limit. British Airways Boeing 747 encountered volcanic ash near Indonesia in 1982 and experienced a flame out on all four engines within 80 seconds of entering the ash. It was able to restart and land safely but the repairs cost an estimated $ 80 million. In 1980, a C-130 aircraft powered by four T56 turboshaft engines encountered ash cloud from Mount St. Helen. Two of the engines had to be shut down before landing. During inspection it was found that all the 14 compressor stages in one of the engines had shown FOD and erosion. The HPC erosion resulted in 1% efficiency and surge margin decrease.

Fig. 5.4(C) shows the erosion rate for Nickel as given in Kang et al. (1987) at different impinging velocity, temperature and the surrounding fluid - the figure has been adapted from Birks et al. (1993). It shows that at higher velocity and temperature, the material removal rate is high. Also seen is that the material removal rate is extremely low when the impingement occurs in an inert atmosphere of nitrogen compared with that of air. This clearly shows erosion-corrosion dynamics at play. Fig. 5.4(D) shows the difference in new compressor blade and an eroded compressor blade as given in Hamed and Tabakoff (1994) - the figure has been adapted from Alqallaf et al. (2020). It can be seen that the damaged blade has reduced chord length, blunted leading edge and also some material removed from the pressure side. As discussed in literature survey, the ingestion of sand causes the tip chord to be eroded by 10% along with 65% increase in tip clearances (Ghenaiet et al., 2005). The compressor blades of TV3-117 turboshaft also suffered from chord length and airfoil thickness reduction above 66% span when operating in extreme desert terrains of Algeria (Dvirnyk et al., 2019)

According to Jasiczek et al. (2013), a major consequence of the impact damage and pitting ero-

sion/corrosion is that they introduce regions of small notches and microcracks. Left untreated, these notches and microcracks prove to be the cradle of premature crack initiation sites which can subsequently lead to fatigue failure of the compressor blades. Fig. 5.5(A) shows the fatigue failure of a high pressure compressor (HPC) blade in an industrial gas turbine (Jasiczek et al., 2013). The red arrows in the figure represent the direction of crack propagation. Approximately 60% of the fracture path was due to fatigue and the rest was due to ductile overload. This liberated blade caused further damage of all the other blades. Similarly, fig. 5.5(B) shows fan blade failure of Trent 772B-60 Engines. The ATSB (2020) in its report revealed that the "fatigue failure had initiated on the inner surface of the panel at the acute corner of a membrane-to-panel bond" as shown in fig. 5.5(C). A chordwise initial crack propagation was observed before it propagated towards the outer airfoil surface. The remaining fracture surface was angled which implied a ductile overstress failure.

5.2 Maintenance, Repair And Overhaul (MRO)

A boroscope is used to visually inspect the damages on the compressor blades and the acceptable limits to the damage of the compressor blades is decided based on where it occurs along the span. A schematic depicting the comparison of undamaged rotor blade and blade undergoing tip curl damage is shown in fig. 5.6(A). The tip curl damage is typically blended out during maintenance and overhauling of the engine as per the publication by Hamilton (1992) for T700 engine. Fig. 5.6(B) shows the schematic of undamaged rotor blade and re-contoured blended blade. It can be seen that the re-contoured compressor blade has a chord reduction near the tip region (Roberts et al., 2002). The colour scheme on the undamaged blade is such that inner 50% of blade is represented by blue colour and the outer 50% of the blade is represented by red colour. For the damaged blade, the outer 50% of the blade is represented by orange colour.

Fig. 5.6(C) shows the damage near the leading edge and trailing edge of the compressor blade along with some pitting damage (corrosion/erosion). Such damages are typically blended out if they are within the allowable limits as per the maintenance manual[1] of Allison Gas Turbine

[1] http://aviationmiscmanuals.tpub.com/TM-55-2840-241-23/css/TM-55-2840-241-23_161.htm

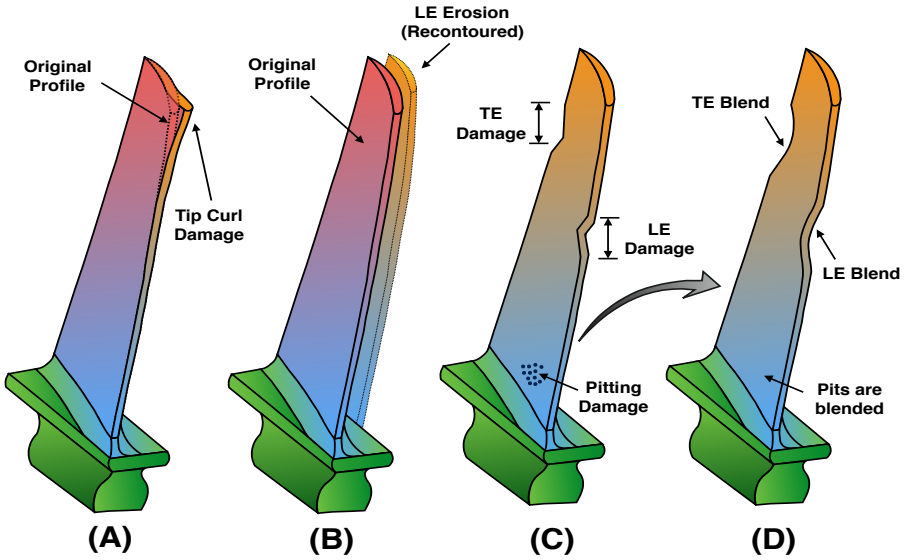
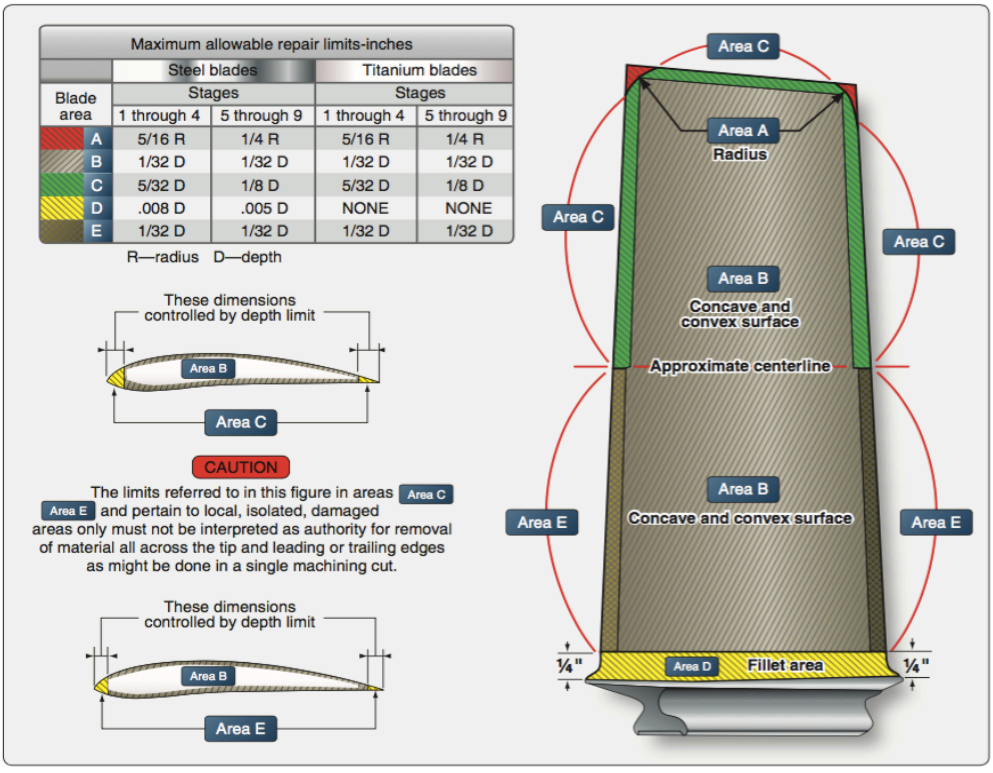


Figure 5.6: Schematic Showing (A) Comparison Of An Undamaged Compressor Blade With A Compressor Blade Undergoing Tip Curl Damage (B) Comparison Of Re-contoured Compressor Blade And Undamaged Compressor Blade (C) Damage Near The Leading Edge and Trailing Edge Of The Compressor Blade Along With Some Pitting Damage (D) A Typical Compressor Blade After Blending Operation. The Schematic For Undamaged Rotor Adapted From Chaganti (2012)



Maximum allowable repair limits-inches				
	Steel blades		Titanium blades	
Blade area	Stages		Stages	
	1 through 4	5 through 9	1 through 4	5 through 9
A	5/16 R	1/4 R	5/16 R	1/4 R
B	1/32 D	1/32 D	1/32 D	1/32 D
C	5/32 D	1/8 D	5/32 D	1/8 D
D	.008 D	.005 D	NONE	NONE
E	1/32 D	1/32 D	1/32 D	1/32 D

R—radius D—depth

Figure 5.7: Allowable Damage Limits In A Typical Compressor Blade As Given By Federal Aviation Administration (2018) [Reproduced With Kind Permission From FAA]

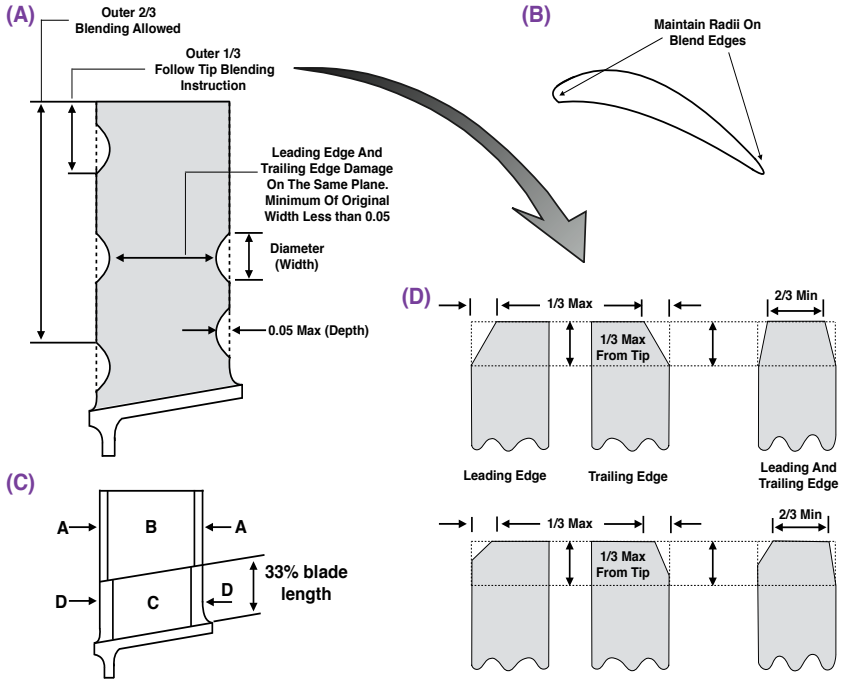


Figure 5.8: Allowable Damage Limits As Given For T63-A-720 Merlin 250 Engine In The TM 55-2840-241-23 Manual (A) Compressor Rotor Blade Leading and Trailing Edge Blend Limits (B) Instruction To Maintain Radius Of LE And TE After Blending Operation (C) Compressor Blade Surface Blending Limits (D) Compressor Rotor Blade Tip Blend Limits (Adapted From TM 55-2840-241-23 Manual)

T63-A-720 Merlin 250 Engine. Fig. 5.6(D) shows the schematic of a typical compressor blade after blending operation. The blending operation is done to minimise the stress concentration (Federal Aviation Administration, 2018) at the nicks, kinks, pits, etc. According to Navy Training Publications Centre (1971), the width of the blend must be four times its depth. There is no open source material available regarding the maintenance and overhauling of industrial gas turbines due to proprietary issues. Hence, the author has used Federal Aviation Administration (2018), maintenance manual for Allison Gas Turbine Model and Navy Training Publications Centre (1971) as a reference. It must be noted that the IGT fan blades are solid as opposed to hollow fan blades of aircraft engines and hence more leeway might be permitted.

As seen in fig. 5.7 shows allowable damage limits in a typical compressor blade as given in Federal Aviation Administration (2018). Similar allowable limits was also given in pg. 167 of Navy Training Publications Centre (1971). While the Federal Aviation Administration (2018) gives an overview of the types of damage and methods to rectify the damage on a typical compressor blade, it notes maintenance personnel should look into engine manufacturers

overhaul instruction manual for the exact details on allowable limits. Maximum damage limit with regard to LE, TE, concave surface, convex surface and tip is prescribed for a T63-A-720 Merlin 250 Engine as per TM 55-2840-241-23 Manual. Fig. 5.8(A) shows allowable damage limits for LE and TE of the blade. Fig. 5.8(B) specifically instructs that the radius of curvature at LE and TE has to be maintained after blending operation. Surface blending limits and tip blending limits can be seen in fig. 5.8(C) and (D) respectively. The TM 55-2840-241-23 manual is more conservative insofar as to repairing the damage in the inner 33% of the span from root compared to 50% of span limit given in Federal Aviation Administration (2018). From the TM 55-2840-241-23 manual, it was observed that the blending operation is allowed from 66% span (from hub) up to the tip where maximum allowable damage is 33% chord (seen in fig. 5.8(D)).

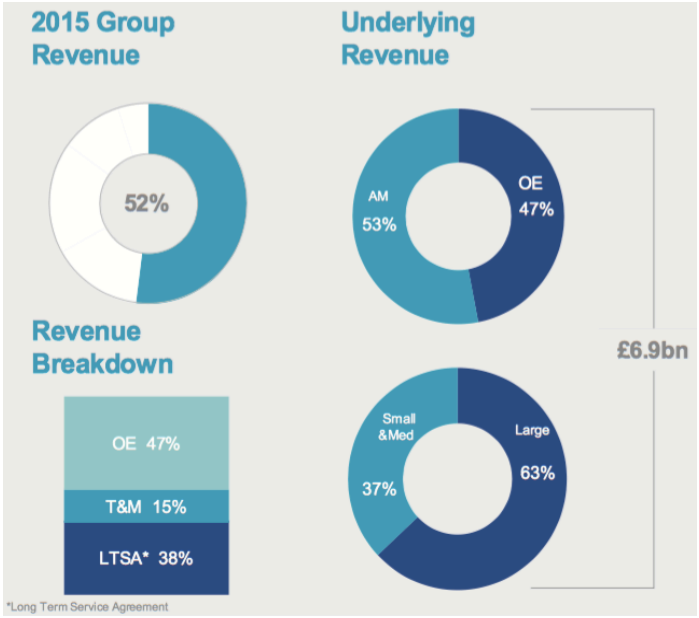


Figure 5.9: Revenue Breakdown Of Rolls-Royce Civilian Aerospace Division In 2015

The MRO market is one of the areas which provides the original equipment manufacturer (OEM) with a steady stream of revenue. Fig. 5.9 shows that the After Market[2] services contributed to nearly 53% of the revenue in 2015. If the cost to repair a blade is lesser than the cost to replace it with a new one, it would add further revenue to the OEMs. The present study of damaged blades of an industrial gas turbine has a potential to reduce the number of scrapped blades and help with the re-certification criteria.

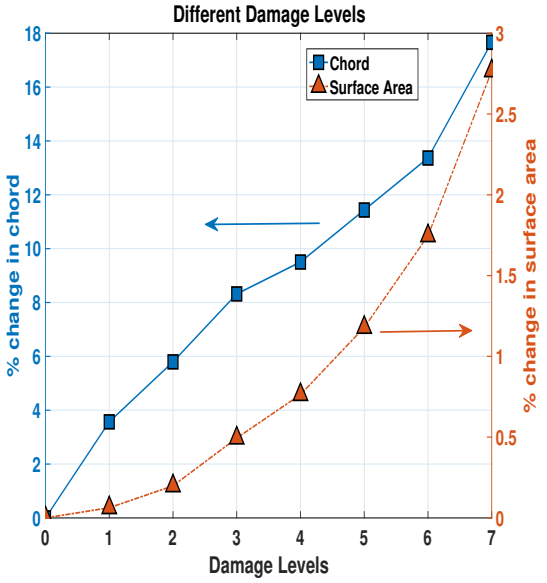
[2] https://www.rolls-royce.com/~/media/Files/R/Rolls-Royce/documents/investors/capital-markets-day/civil-after-market-value.pdf

5.3 Behaviour Of Damaged Blades And Blades With Different Tip Gaps

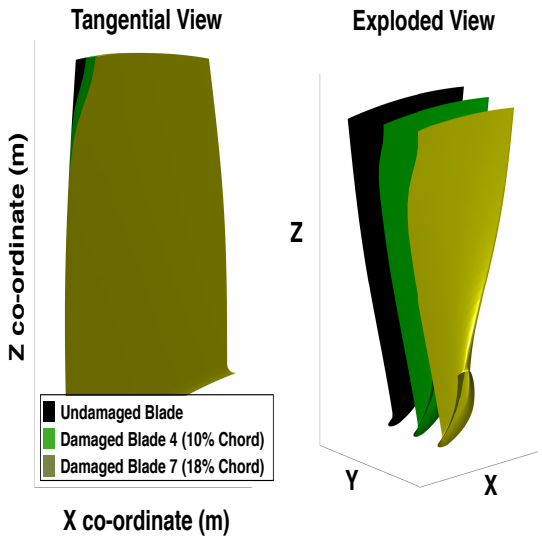
The maximum chord damage that can be acceptable in a civil aviation turbofan engine is between 4-6% of the nominal chord (Roberts et al., 2002). In fact, NASA stage 35 was tested for erosion of leading edge of the blades (Roberts et al., 2002) with a gradual increase of damage from onwards of 50% span up to the tip of the blade where 5% chord damage was observed. Merlin 250 Engines (used predominantly in military aircrafts) allowed a maximum of 33% chord damage. In an industrial gas turbine industry, blades in the field are inspected regularly according to a preset damage criteria (which is typically less than 10% chord). The current practice is to replace the compressor blades having damage more than the allowable limit. This research focuses on a way to reuse them by rearranging them favourably and therefore the highest damage considered in terms of percentage of chord at the tip is 18% of nominal chord (in between the allowable damage of civil aviation gas turbine and Merlin 250 Engines) with the damage starting from approximately 65% span as also considered by Dvirnyk et al. (2019). The damage has been represented in terms of a hyperbolic tangent function. This section covers the parallels and anomalies between the performance behaviour of damaged blades as well as blades with different tip gaps.

The study of stall margin (SM) of damaged blades has been split into two parts : (A) radially increasing damage with same chord-length (B) chord-wise increasing damage with same radial level. The SM is defined as given in equation 4.3 in chapter 4.

All the simulations for testing the stability limits of individual damaged blades is done using single passage simulation unless mentioned otherwise. This study would further the knowledge in identifying the more crucial type of damage. A total of 7 types of damaged compressor blades were generated, namely damaged blade 1, 2, 3, 4, 5, 6 and 7. Each of these blades represent increased intensity of damage both radially as well as chord-wise as shown in Fig. 5.10(A). The three dimensional visualisation of these damaged blades is shown in Fig. 5.10(B) (the scale of X, Y and Z axes are not equal in Fig. 5.10(B) due to proprietary reasons). Moreover at damage



(A) Different Damage Levels In Terms Of Percentage Change In Chord And Percentage Change In Area



(B) Different Views Of Damaged Blade

Figure 5.10: Damaged Blades Used In The Study Of Industrial Gas Turbines

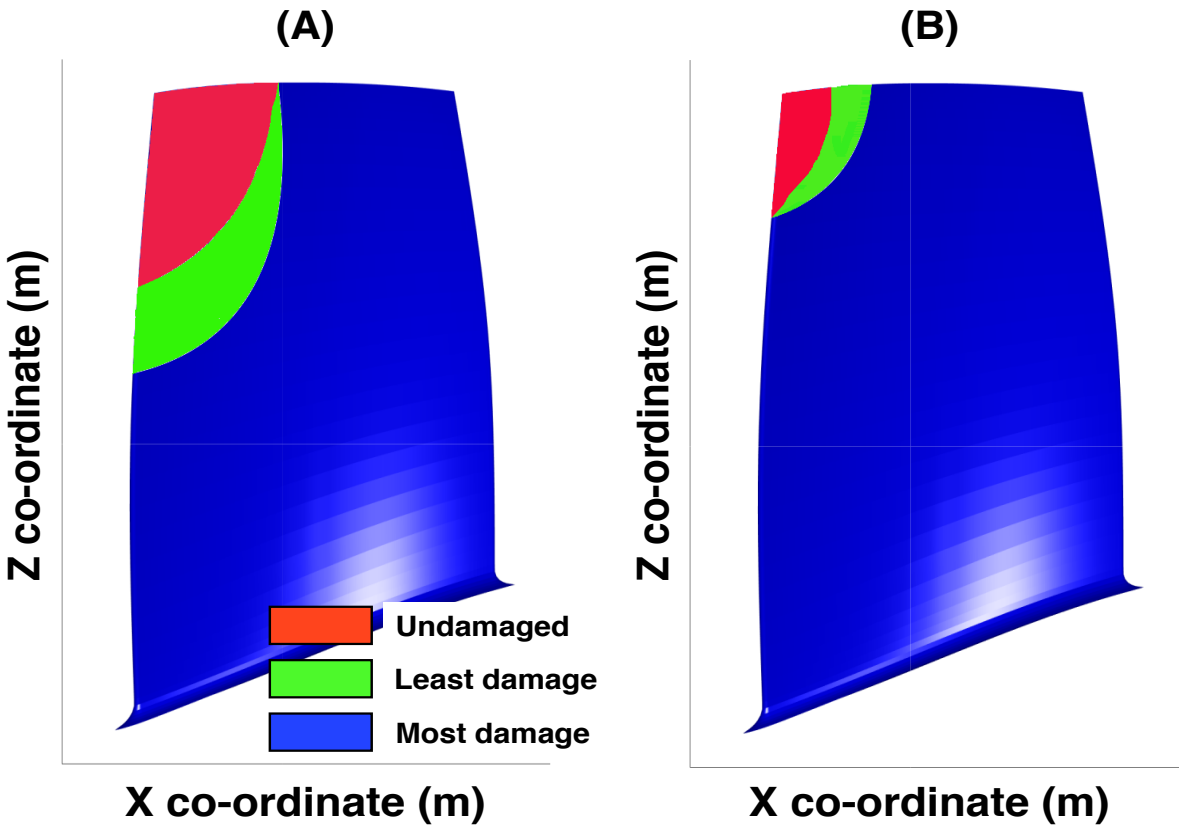


Figure 5.11: Schematic Of Damage Decomposition Into: (**A**) Different Radial Level Damage. (**B**) Different Chord-Wise Damage.

level 4 and damage level 6, additional blades are generated such that same chord-wise damage but different radial level damage as shown in Fig. 5.11(A). They are divided into 4 categories : "Most damaged, More damaged, Less damaged and Least damaged".

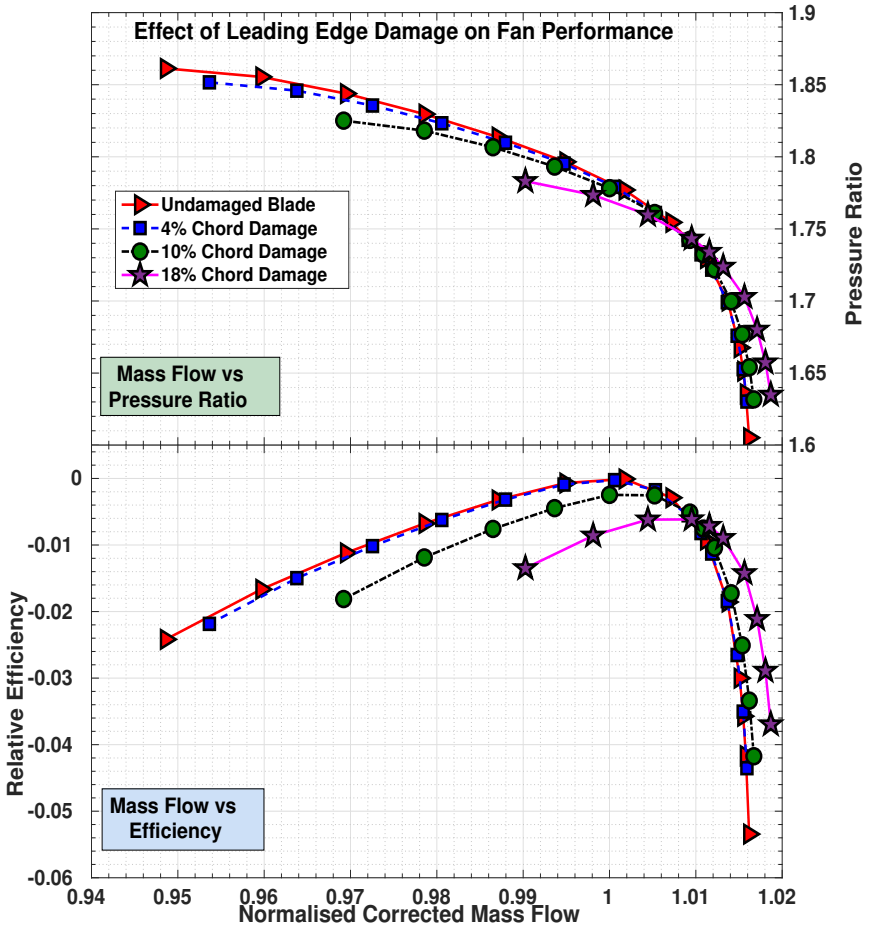


Figure 5.12: Effect Of Leading Edge Damage On Performance Of Different Blades

Two additional damaged blades with varying chord-wise damage are generated at a radial level corresponding to damage 5 (see Fig. 5.11(B)). These three blades are divided into 3 categories : "Most damaged, Intermediate damaged and Least damaged".

The sensitivity of each of the above two parameters has been studied in terms of stall margin. Also, three blades with different tip gaps viz. 0.33% of span, 0.66% of span and 1% of span have been generated. All the results have been reported in terms of Normalised corrected mass flow (NCMF) and Relative efficiency (RE) as said in Chapter 3.

In the first stage, the computations were performed by assuming all the blades have the same damage (single passage simulation). From Fig. 5.12, it can be seen that an increase in the

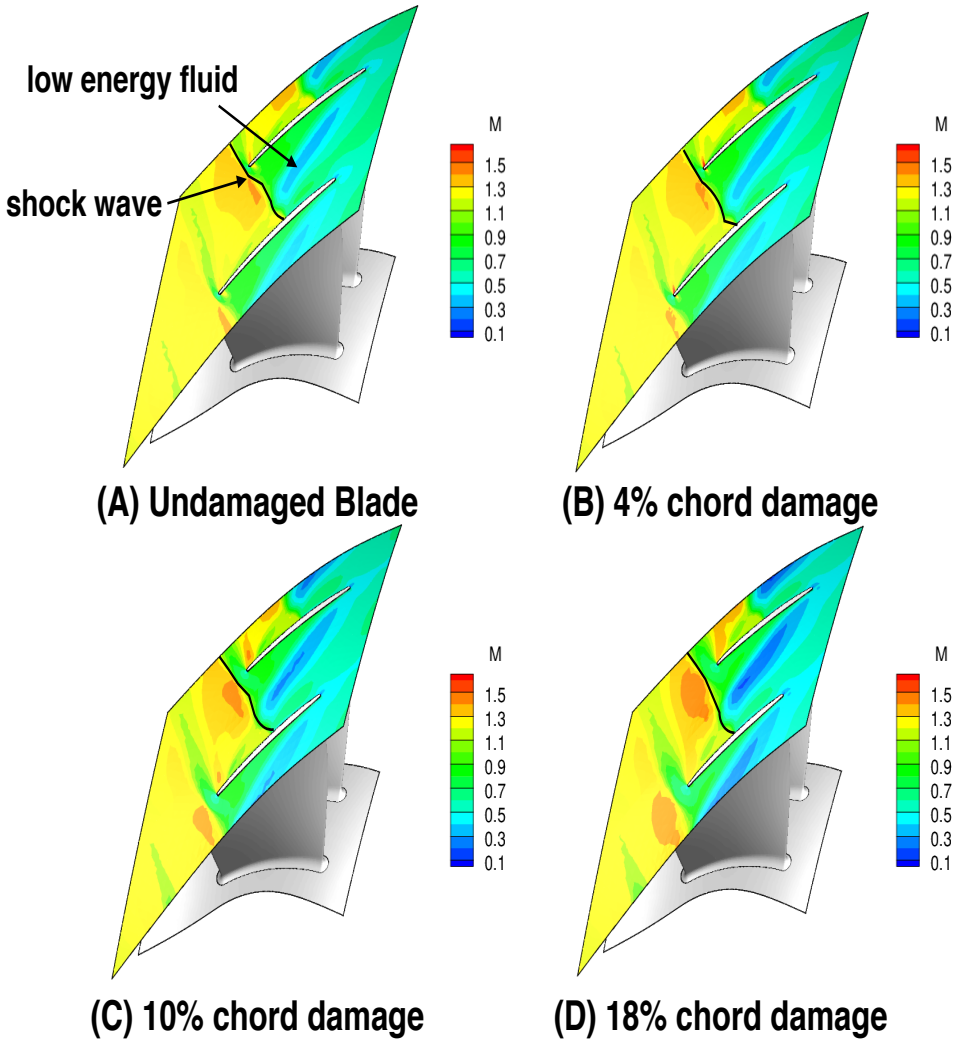
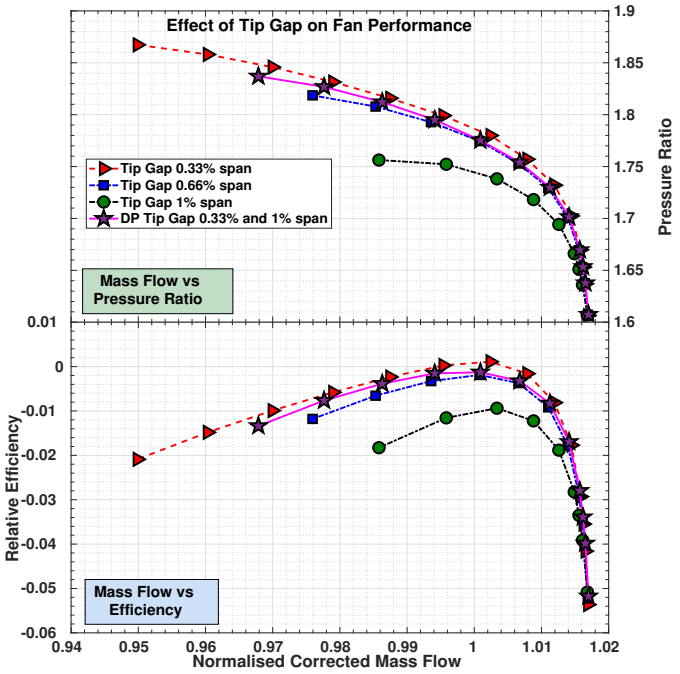
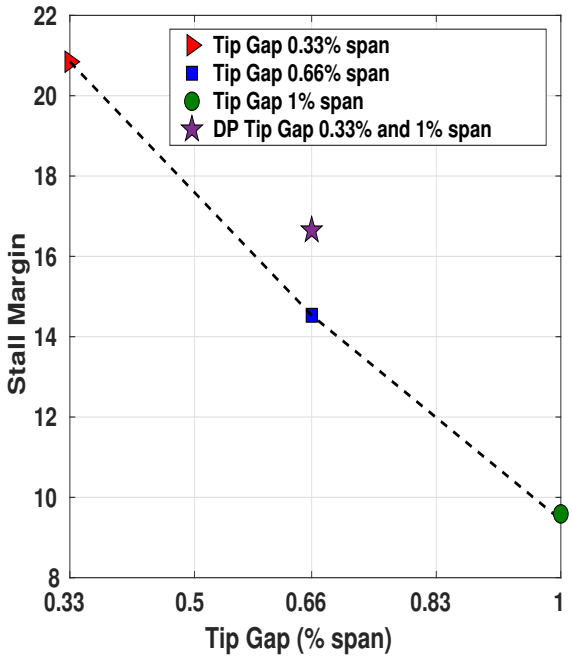


Figure 5.13: Mach Number Contours At **Same** Non-Dimensional Corrected Mass Flow Rate $\approx$ **1** : (**A**) Undamaged Blade. (**B**) Chord Damage Of 4%. (**C**) Chord Damage Of 10% And (**D**) Chord Damage Of 18%

damage intensity causes a drop in performance along with the stability margin. As can be seen in the Mach number contour plot shown in Fig. 5.13, an increasing damage causes a larger zone of low momentum fluid to be created due to the interaction of shockwaves and increased tip leakage flow. This low momentum fluid produces a region of blockage which creates an adverse pressure gradient causing the blade to stall. Also, the location of shock wave in 18% chord damage case as compared to an undamaged blade makes it more prone to stall (Hah et al., 1998). A similar kind of behaviour with respect to the increasing size of tip gaps has been observed in the literature (Adamczyk et al., 1993; Beheshti et al., 2004; Venkatesh et al., 2019). As seen in Fig. 5.14(A), increasing the size of tip gap (single passage simulation) causes the performance and the stability margin to deteriorate similar to the study of NASA rotor 67



(A) Performance Of The Blades With Different Tip Gaps



(B) Stall Margin Of The Blades With Different Tip Gaps

Figure 5.14: Effect Of Tip Gap On The Rotor Blade Of 1-Stage IGT

in chapter 4 (Venkatesh et al., 2019). Also seen in Fig. 5.14(A) and Fig. 5.14(B), wherein the double passage (which models alternate blades with tip gaps 0.33% of span and 1% of span) has better pressure ratio, efficiency, stalling mass flow rate and SM compared to the single passage blade with tip gap 0.66% of span similar to Venkatesh et al. (2019).

One major difference between the performance of different single passage cases for damaged blades and blades with different tip gaps as observed in Fig. 5.12 and Fig. 5.14(A) is that of the choked mass flow rate in the two cases. While the choked mass flow rate for different tip gap remains mostly unchanged, in case of damaged blades, a rightward shift of choked mass flow occurs for an increase in the damage intensity. Reason for this kind of behaviour is the prevalence of a bigger throat area from approximately 65% span onwards for the higher damage intensity blades. This can be clearly seen in Fig. 5.15 wherein the choked mass flow rate for 18% chord has higher mass flow rate from 60% span onwards compared to undamaged blade. The increase in annulus area with an increase in the span causes a discernible increase of choked mass flow for higher damage intensity blade.

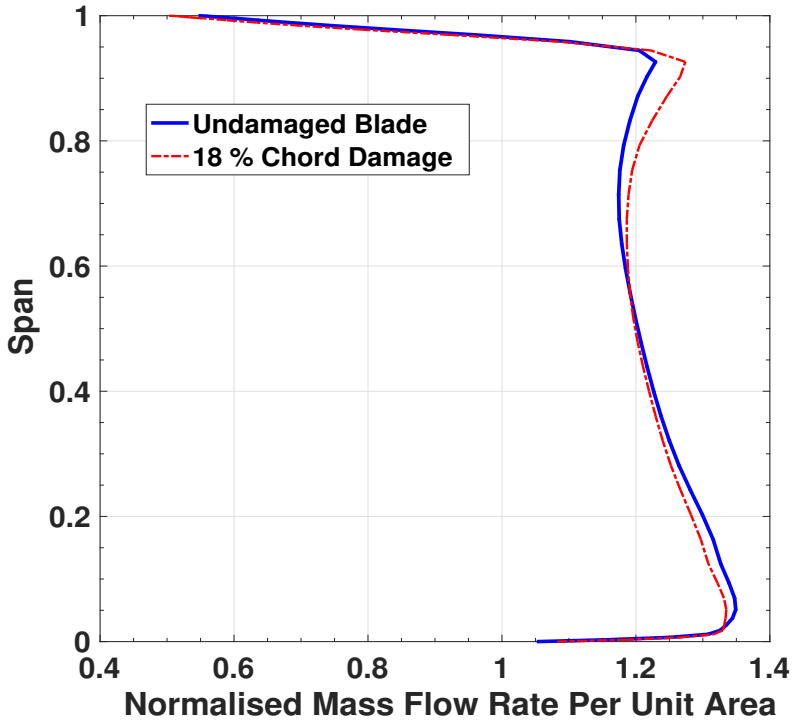
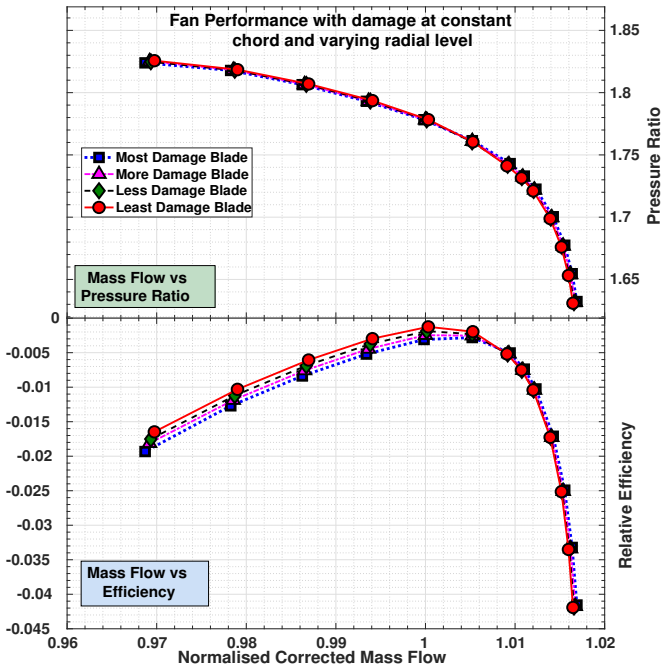
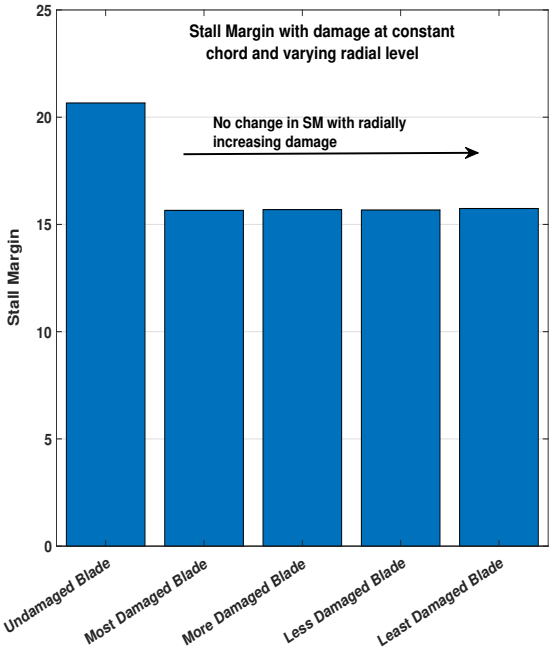


Figure 5.15: Span-Wise Comparison Of Choked Mass Flow Rate For 18% Chord Damaged Blade And Undamaged Blade

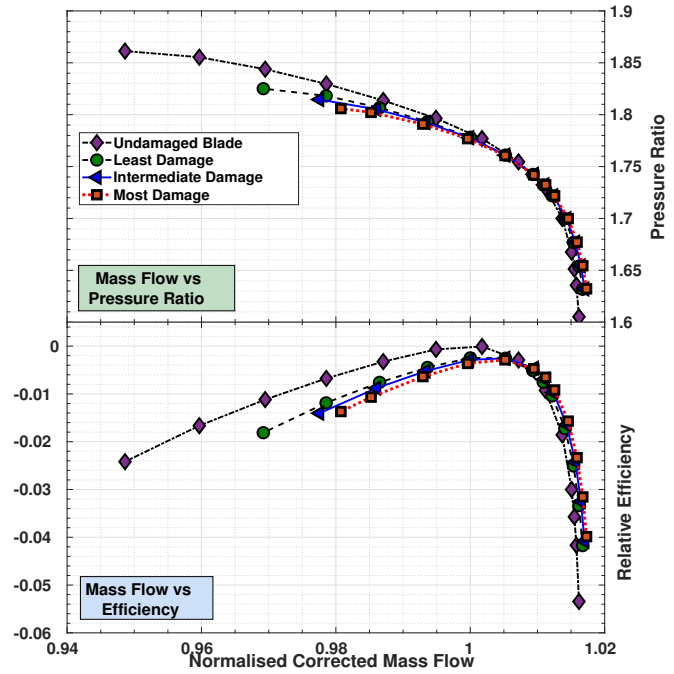


(A) Effect Of Varying Radial Level Damage With Constant Chord On Performance Curves

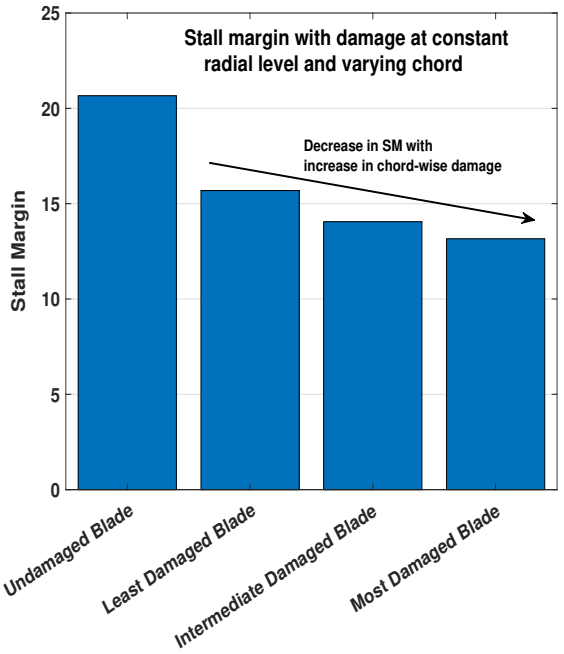


(B) Effect Of Varying Radial Level Damage With Constant Chord On Stall Margin

Figure 5.16: Influence Of Varying Radial Damages With Constant Chord On 1-Stage IGT



(A) Effect Of Varying Chord-Wise Damage At Same Radial Level On Performance Curves

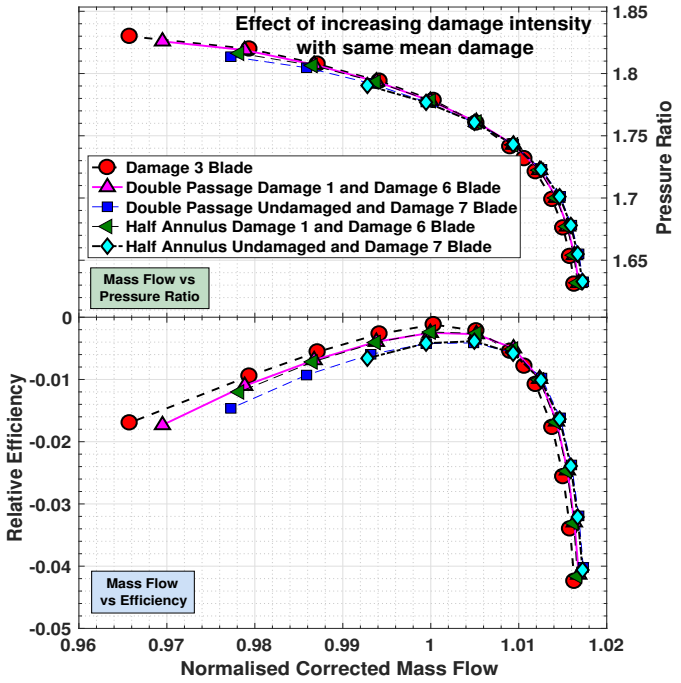


(B) Effect Of Varying Chord-Wise Damage At Same Radial Level On Stall Margin

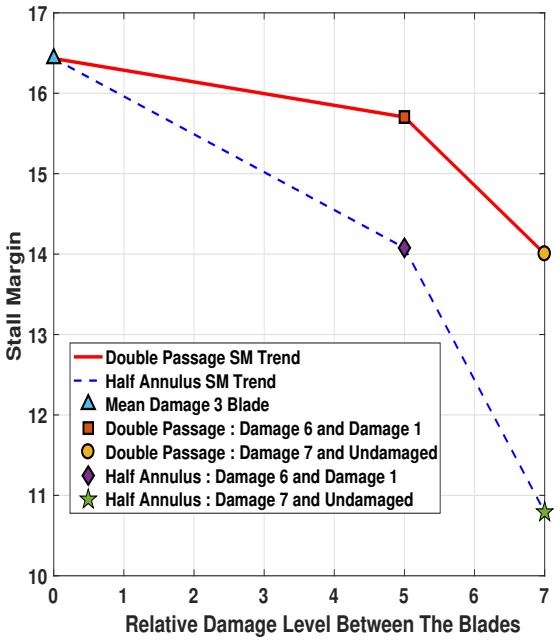
Figure 5.17: Influence Of Varying Chord-Wise Damage At Same Radial Level On 1-Stage IGT

Having established that higher damage causes higher loss in performance and stability boundaries, the study of the chord-wise damage and radial damage was undertaken. All the calculations in this case is performed using single passage computation of IGV, Rotor and Nozzle. It can be seen from Fig. 5.16(A), that the performance curves of the all the radially damaged blade profiles at chord length corresponding to damage level 4 (viz. most damaged blade, more damaged blade, less damaged blade and least damaged blade) look very similar with negligible difference in the efficiency. Consequently, Fig. 5.16(B) shows that all these damaged blades have exactly the same SM. A similar set of results are obtained when the computation is performed for radially damaged blades at chord length corresponding to damage level 6 (not shown for the sake of brevity). Thus the radial extent of the damage does not have significant influence on performance. On the flip side, it can be seen from fig. 5.17(A) that an increasing chord-wise damage at a constant radial level has a detrimental impact on the stability of compressor. The pressure ratio and efficiency curves of the most damaged blade follows that of the least damaged blade before stalling prematurely. Consequently, the SM plot shows a decreasing trend as the damage intensity increases as seen in Fig. 5.17(B). It can thus be surmised that the SM is

affected majorly by the chord-wise damage compared to radial damage. More importantly, the loss in surface area is a derived quantity resulting from either chord-wise damage and/or radial damage and hence should not be used as a parameter for determining the loss in SM.



(A) Effect Of Same Mean Damage But Different Damage Intensities On Performance Curves



(B) Effect Of Same Mean Damage But Different Damage Intensities On Stall Margin

Figure 5.18: Influence Of Same Mean Damage But Different Damage Intensities On Performance Of 1-Stage IGT

Finally, a series of single passage, double passage and half annulus arrangement (whole annulus) simulation is performed such that the mean damage remains the same for all the cases (but the damage intensities vary). As seen in fig. 5.10(A), damage level 7 has a chord loss of 17.75%, damage level 3 has a chord loss of 8.25% and damage level 0 is the undamaged blade. Together, blades with damage level 0 and damage level 7 have approximately the same average chord loss as the blade with damage level 3. Similarly, the blades with damage level 6 (having a chord loss of 13.25%) and damage level 1 (having a chord loss of 3.25%) together have the same average chord loss as blade with damage level 3. Thus a double passage simulation (which implies alternate arrangement of blades) and a half annulus arrangement simulation is performed considering blades with damage level 0 and damage level 7. This is compared with the single passage simulation results of blade damage level 3. Similar comparison can be made for blades with damage level 1 and damage level 6.

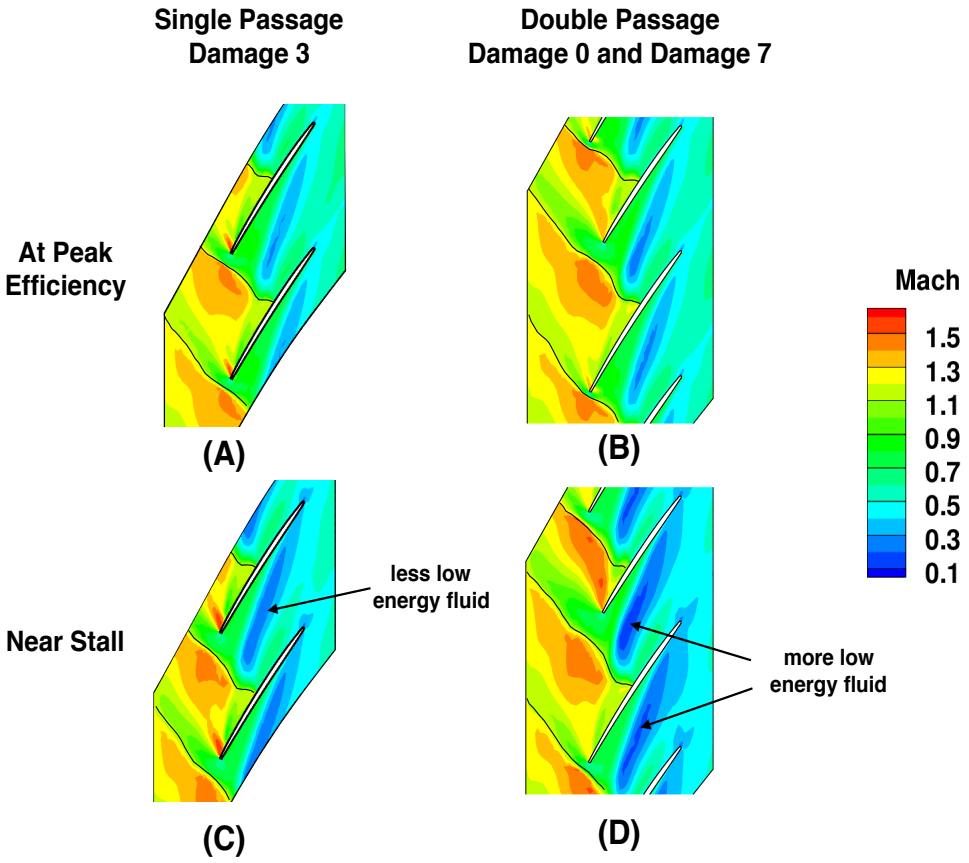


Figure 5.19: Comparison Of Mach Number Contours For : (**A**) Single Passage Simulation For Blade With Damage Level 3 (At Peak Efficiency) (**B**) Double Passage Simulation For Blades With Damage Level 0 and Damage Level 7 (At Peak Efficiency) (**C**) Single Passage Simulation For Blade With Damage Level 3 (At Near Stall) And (**D**) Double Passage Simulation For Blades With Damage Level 0 and Damage Level 7 (At Near Stall)

From fig. 5.18(A), it can be seen that the single passage simulation of blade with damage level 3 performs the best while half annulus arrangement simulation of blades with damage level 0 and damage level 7 performs the worst. The performance of double passage simulation of blades with damage level 0 and damage level 7 falls in between the extremes. Since single passage simulation with damage level-3 considers the same blade to be distributed throughout the annulus, the relative damage level of the blade with respect to itself is zero. For double passage and half annulus arrangement simulations carried out with blades with damage level 6 and damage level 1, the relative damage level is 5. Similarly, in case of double passage simulation and half annulus arrangement simulations for blades with damage level 7 and damage level 0, the relative damage level is 7. Fig. 5.18(B) shows the stall margin with respect to the relative damage levels for different cases in fig. 5.18(A). The trend line shows that the stall

margin reduces as the damage intensity increases for the same mean damage (irrespective of the arrangement). Fig. 5.19(A) shows the Mach number contour of single passage simulation for blade with damage level 3 at peak efficiency condition while fig. 5.19(B) shows the Mach number contour of double passage simulation for blades with damage level 0 and damage level 7 at peak efficiency condition. Similarly, fig. 5.19(C) shows the Mach number contour of single passage simulation for blade with damage level 3 at near stall condition and fig. 5.19(D) shows the Mach number contour of double passage simulation for blades with damage level 0 and damage level 7 at near stall condition. Comparing the Mach number contours of fig. 5.19, it can be inferred that the increase in damage intensity (for same mean damage) causes a larger zone of low energy fluid to be created thereby making it stall earlier.

This result is contrary to the earlier study of tip gaps (Venkatesh et al., 2019) in which it was shown that double passage blades with different tip gaps works the best amongst all the arrangements and always performs better than the single passage blade having average tip gap (in the limiting case when manufacturing tolerances are close to nominal, all the arrangements give same performance as the nominal blade). It was seen that the low momentum fluid produced in the double passage mixed tip gap case was less than the single passage with average tip gap case and hence the double passage mixed tip gap case stalls later.

5.4 Optimised Arrangement Of Random Damaged Blades

The problem of optimised arrangement is a subset of combinatorial optimisation which has its genesis in the field of applied mathematics, computer science and management studies; with applications ranging from logistics, vehicle routing and gene synthesis to name a few. Its application to the field of turbo-machinery bedecks it with another layer of complexity : understanding the flow physics. In the earlier study regarding optimised arrangement of random tip gaps (Venkatesh et al., 2019), it was proved that a zigzag arrangement (largest tip gap sandwiched between two smallest tip gap) works better than any other arrangement. Though the random tip gap was initially introduced as an effect of manufacturing tolerance,

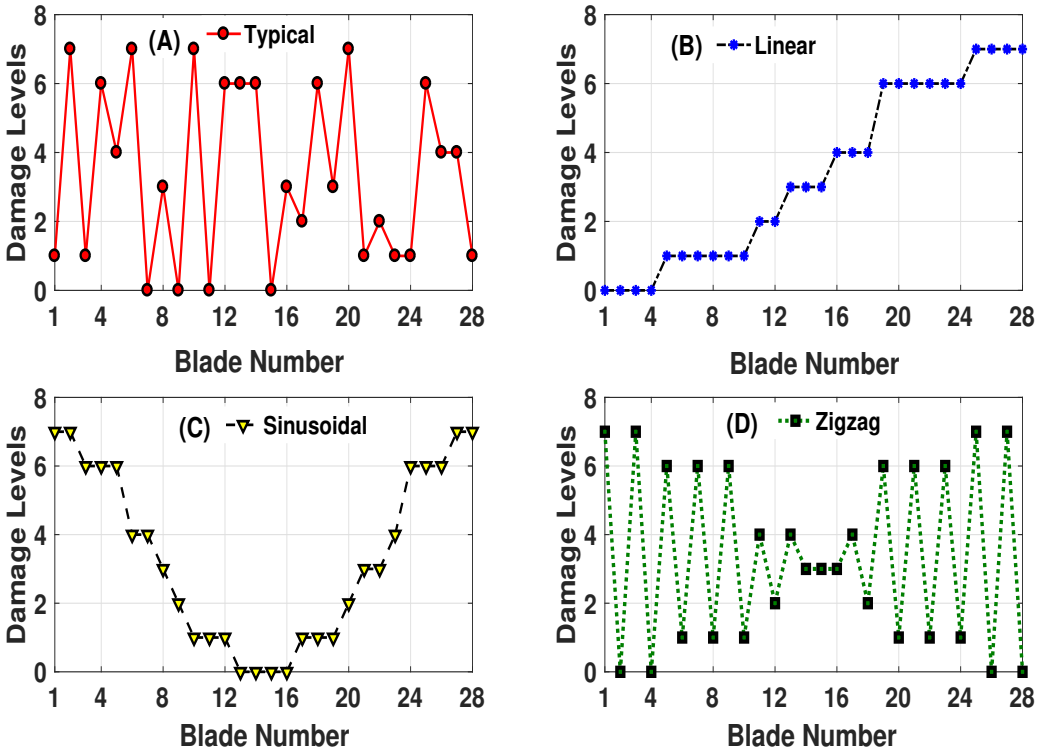


Figure 5.20: Different Types Of Damaged Blade Arrangement : (**A**) Typical (Random) Arrangement (**B**) Linear Arrangement (**C**) Sinusoidal Arrangement (**D**) Zigzag Arrangement

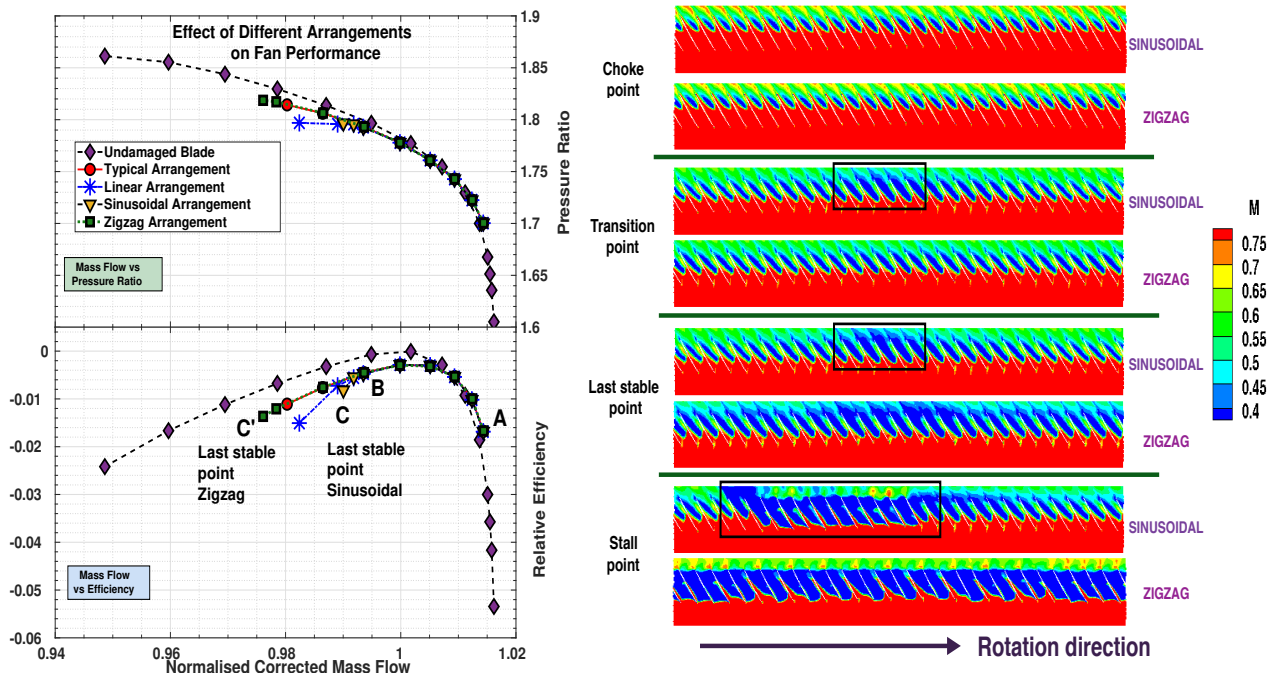
after further deliberation it was felt that it could also be considered as a manifestation of in-service degradation. Hence it was argued that the best possible performance from a compressor can be eked out by arranging the blade with the worst SM in between the blades with best SM.

In regard to answering the question asked in the first section about the optimal arrangement for a given set of random damaged blades, a set of uniformly distributed random integers between **0** to **7** were generated, where " **0** " represents undamaged blade and " **7** " represents damaged blade 7. These set of damaged blades are then arranged in four different ways viz. typical (random), linear, sinusoidal and zigzag as shown in Fig. 5.20. This way of studying the problem of combinatorial optimisation was also carried out in previous chapter wherein the effect of manufacturing tolerance was dealt with (Venkatesh et al., 2019).

As seen in Fig. 5.21(A), the zigzag arrangement has better pressure ratio and stability margin compared to rest of the arrangements and represents a maxima for the given set of random damaged blade. On the other hand, sinusoidal arrangement performs the worst and it stalls

prematurely. This behaviour of zigzag arrangement (for the given set of random damaged blades) wherein it gives a maxima performance is consonant with the zigzag arrangement for random tip gaps seen in previous chapter (Venkatesh et al., 2019). However, it is to be noted that this result is also in complete contradiction to the results obtained by Roberts et al. (2002) who said that the type of arrangement has no significant difference between the various performances. Roberts et al. (2002) have considered 3 different arrangements : (1) Alternate nominal chord blade and damaged short chord blade around the annulus (2) Half annulus of nominal chord blades and half annulus of damaged short chord blade (3) Alternating quadrants of nominal chord blades and damaged short chord blades. However, the maximum chord damage that they have considered is 5% which is too small a value to affect the performance significantly. In chapter 4 (Venkatesh et al., 2019), a similar study conducted for tip gaps shows that the type of arrangement has negligible effect on the performance if the manufactured blades with tip gaps are very close to nominal value. However, if the manufactured blades with tip gaps are not close to the blade with nominal tip gap, the type of arrangement has a significant impact on the performance. Extending the same argument, herein maximum chord damage of 18% is almost 4 times the value used by Roberts et al. (2002) and hence a significant deviation in the results. It can be seen from Fig. 5.12 that the difference in performance between undamaged blade and damaged blade 1 having 4% chord damage is minimal. Usage of these two blades for testing performances of various combinations would draw similar conclusions as that obtained by Roberts et al. (2002).

It is also important to dwell upon the reason that triggers premature stall in sinusoidal arrangement. It can be seen in Fig. 5.21(A) that the performance curve of sinusoidal arrangement follows that of zigzag arrangement from point A (choke side) up to point B (intermediate point) before the sinusoidal arrangement stalls prematurely. Point C and C$'$ are the last stable points in sinusoidal arrangement and zigzag arrangement respectively after which both of them stall. The flow-field at these points is shown in Fig. 5.21(B) wherein the blue colour represents the region of low momentum fluid. It can be seen from this plot that at choke point, both the flow fields seem similar. However at the intermediate point, some localised blockage (marked by a rectangle) is introduced in sinusoidal arrangement which is not seen in a zigzag arrangement.



(A) Effect Of Damaged Blade Arrangement On Performance Curves

(B) Flow-Field At The Tip Layer Sinusoid Arrangement Vs Zigzag Arrangement

Figure 5.21: Effect Of Arrangement Of Blade With Different Damage Intensities On Performance Of 1-Stage IGT

This blockage can be seen to grow at the last stable point for sinusoidal arrangement, though the difference in the mass flow rate between intermediate point and last stable point is not huge. At stall point, it can be seen that half of the annulus is blocked with low momentum fluid in a sinusoidal arrangement thereby causing it to stall. On the contrary, the zigzag arrangement can be seen to undergo an almost uniform stall inception and hence has better stability margin. The SM of each of these four cases is plotted against the different SP damaged blade cases in Fig. 5.22. The average chord damage for the given set of random damaged blades was calculated and the SM for all these arrangements were plotted against average chord damage. It can be seen that the SM for all the above arrangements is less than the single passage case of blade having the same chord damage. The result is on expected lines as the trend-line (in fig. 5.18(B)) for the stall margin with respect to the relative damage levels shows that the increase in damage intensity causes the tip leakage flow to also increases thereby making it stall earlier.

Finally, the authors recognise that only a sector of rotor annulus may be damaged due to

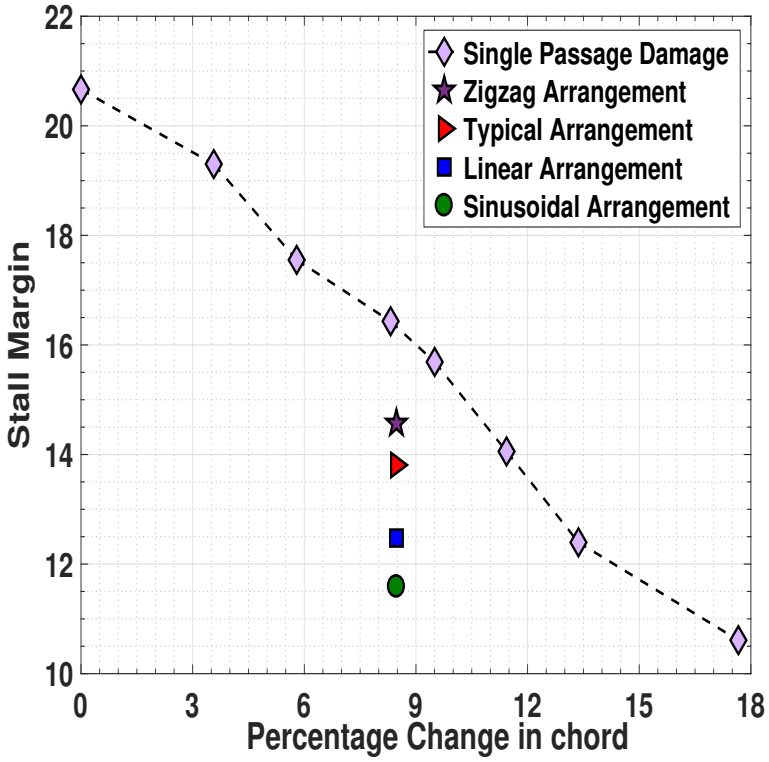
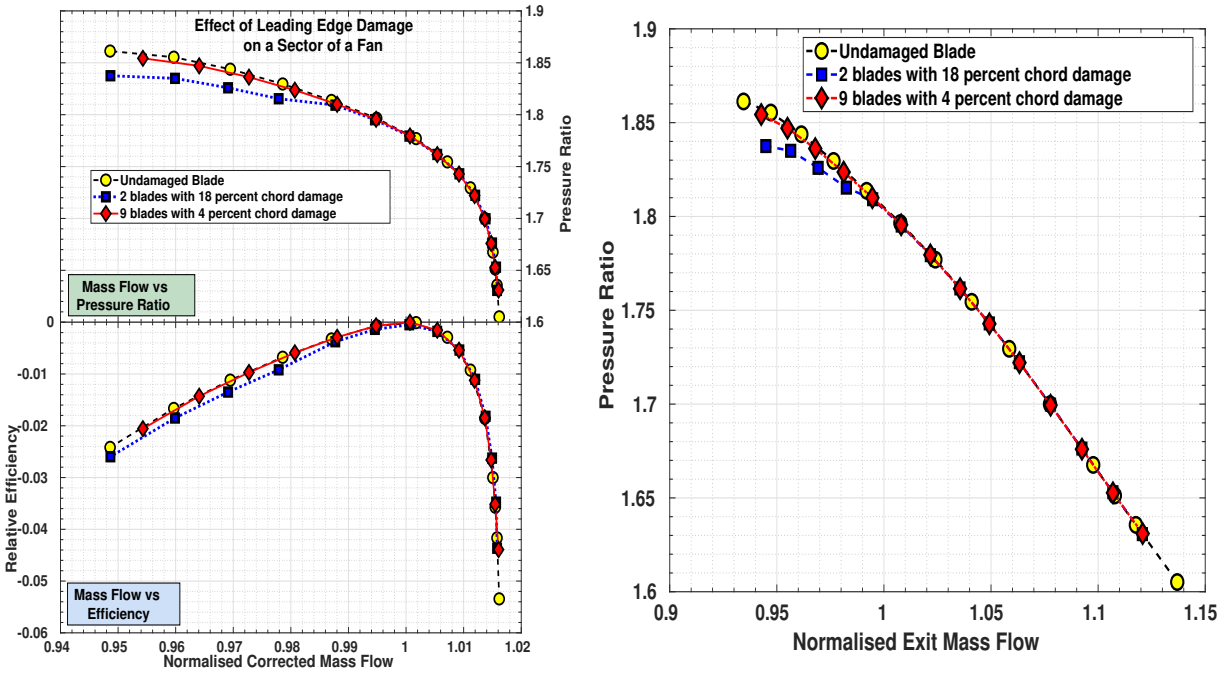


Figure 5.22: Stall Margin Comparison Of Different Whole Annulus Cases With Single Passage Damaged Blades

foreign body impact and all the damaged blades may or may not suffer from the same damage. Different rotors can also have same total damage but with different distribution of damage intensities on damaged blades. On the similar lines of Taylor et al. (2019), two cases were considered : (**A**) 2 blades with 18% damage (**B**) 9 blades with 4% damage. The intent was to see if there was any difference in the behaviour between the present 1-stage transonic compressor of an industrial gas turbine and the low speed compressor test rig used by Taylor et al. (2019). It can be seen from Fig. 5.23(A) that case (**A**) and case (**B**) have negligible difference in the stalling mass flow rate though the performance curve of case (**B**) is closer to undamaged rotor blade in the entire range of operation when compared to case (A). This behaviour is different from the low speed compressor of Taylor et al. (2019) wherein their equivalent of case (**B**) initially follows the performance curve of undamaged blade but stalls earlier compared to case (**A**). Fig. 5.23(B) shows the comparison of the performance of Case (**A**) and Case (**B**) above plotted against exit mass flow function, which indicates a slight loss in stall margin for case (**A**). The conclusion of this case is similar to the fig. 5.18 where we saw that a uniform mean



(A) Performance For Same Total Damage In A Sector Of The Fan

(B) Exit Mass Flow Function For The Same Total Damage In A Sector Of The Fan

Figure 5.23: Effect Of Same Total Damage In A Sector With Different Intensities On The Performance Of 1-Stage IGT

damage on all blades performed better than the case where different damage intensities were distributed throughout the annulus. In that case, higher relative damage intensity between the blades resulted in lower stall margin. In this case, case (**B**) has the less damage more evenly spread out in the sector compared to case (**A**) which has more damage less evenly spread out (the mean damage of both the cases are same).

The authors have also tested a case wherein the damage around the annulus increases progressively. In this study, the number of adjacent blades that undergo damage increases progressively until it covers half of the annulus. It can be seen from Fig. 5.24 that the stalling mass flow rate for the case with half of the annulus consisting of damaged blades is almost the same as the case where all the blades have undergone same damage. The threshold limit for performance in this case is 6 damaged blades next to each other and the performance is same as the case where all the blades are damaged. Overhauling of the case with half the annulus filled with damaged blades with an intention to eke out the maximum performance and stability results in an alternately arranged undamaged blade and damaged blade. It can be seen from Fig. 5.24

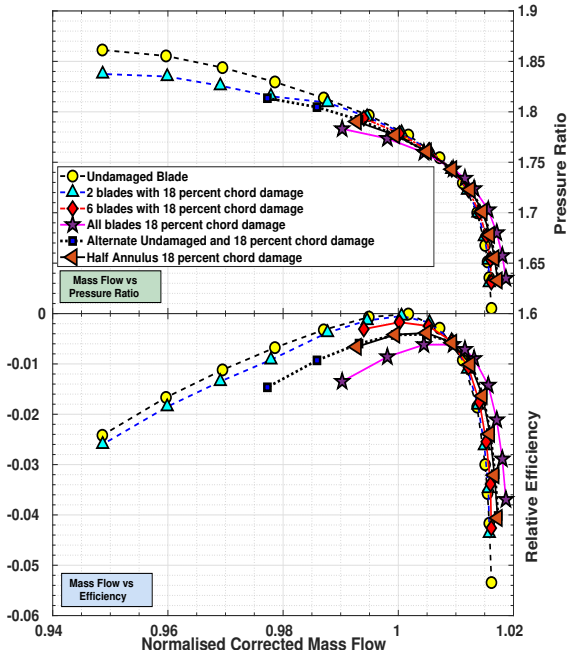


Figure 5.24: Effect Of Number Of Damaged Blades On Performance

that the pressure ratio, efficiency and stalling mass flow rate for an alternate arrangement of damaged blades and undamaged blades (zigzag arrangement) is better than the case with half of annulus consisting of damaged blades.

5.5 Future Work And Recent Advances

Fig. 5.25 shows a schematic of the mode shapes of blades and disk. As can be seen, the flap modes and torsional modes have been shown for the compressor blades (complex mode shapes having a combination of flap and torsional mode has not been shown). Also, shown in the schematic is the mode shape exhibited by the disk. As the disk can cause blade vibrations too, close attention must be paid to the position of blade failures on the disk *e.g.* failures at location 60° apart would indicate three nodal diameter mode of vibration (Cyrus and George, 1998). The damaged blade (and/or overhauled blade) will undergo a change in natural frequency as well as mode shape (severity of this will depend on the location of damage and amount of damage). Also, the aspect of rotor balancing has not been considered. Any imbalances in the rotor might lead to severe vibration problems. These factors have the potential to adversely

affect fatigue damage.

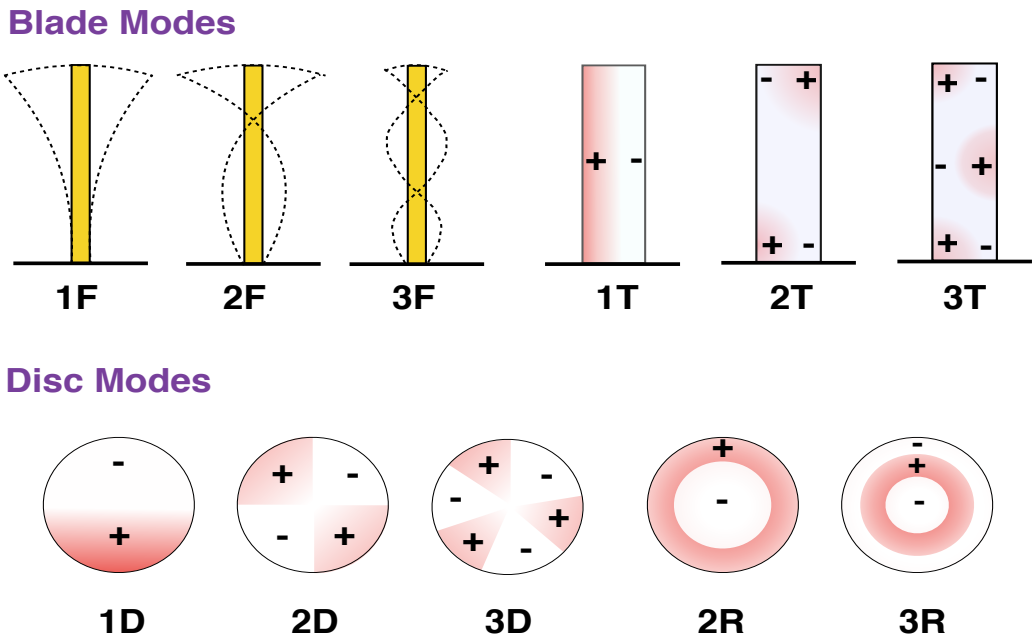


Figure 5.25: Schematic Of Basic Mode Shapes

Thus, apart from the aerodynamic performance, the acceptance or rejection of a damaged blade would also depend upon whether the change in mode shape and natural frequency is within the acceptable limits. Thus the damaged blades' (and/or overhauled blades') resonant frequencies have to be checked using Campbell diagram before they are assembled back in the compressor. The present study of optimal arrangement of damaged blades might still be applicable in such cases provided the resonant frequencies and mode shapes are within the acceptable limits determined by the OEM provider; however further study would need to be carried out to confirm this.

The work has assumed the blade repairs with only blending operations. A patch repair with the new metal welded at the damaged region has not been considered as it would involve more cost with respect to welding operation, post weld heat treatment procedure, machining operation and labour charges. Thus the cost of repairing the blade and reconstructing its profile would be as expensive as replacing the damaged blade with a new blade (in addition to the cost of shutting down the powerplant for a long duration). Moreover, the patch of new metal along with the filler material used in welding would create non-homogeneous material property in

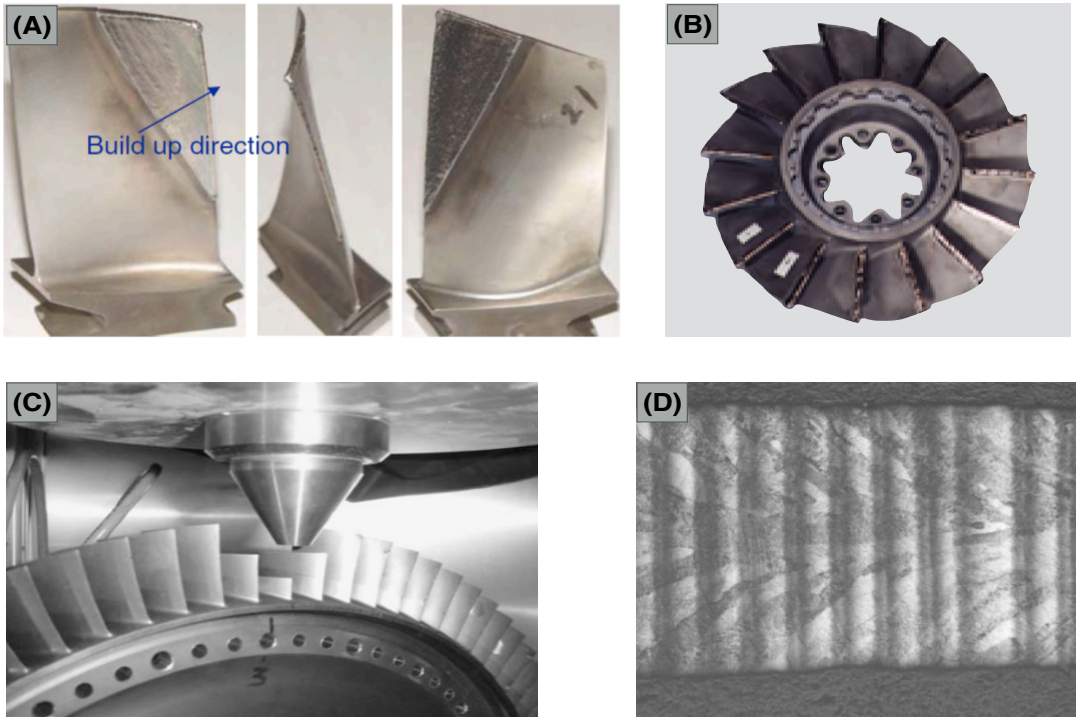


Figure 5.26: Laser Deposition With Adaptive Toolpath Method : (A) Used To Repair Blade (B) Used To Repair PT6 Blisk (C) Used To Repair Titanium Blisks (D) Microstructure Of The Laser Generated Compressor Blade - Figures Adapted From Guo and Brommesson (2018)

the overhauled blade. This might affect the mode shapes and natural frequency of the blade depending on the amount of material welded.

A major limitation of this work would be its applicability to the modern day "blisks". The blades in the "blisk" come as an integral part of the disk that cannot be detached and hence the optimal arrangement solution would not apply. Hence, the blisk has to be either repaired or discarded in such cases. New techniques like geometry-based adaptive toolpath laser powder deposition method developed by Qi et al. (2010) promises to address this issue. As shown in fig. 5.26(A), (B) and (C), the laser deposition technique has been used to successfully repair and reconstruct the profile of damaged compressor blades and blisks. Fig. 5.26(D) shows the fine crystalline microstructure of the laser generated compressor blade along with smooth transition between different welding layers. It is estimated that this method may reduce their repair costs by up to 92% (Guo and Brommesson, 2018).

Recent advances in coating technology by MDS Coating[3] shows promising results. The thin

[3] https://www.mdscoating.com/technology/

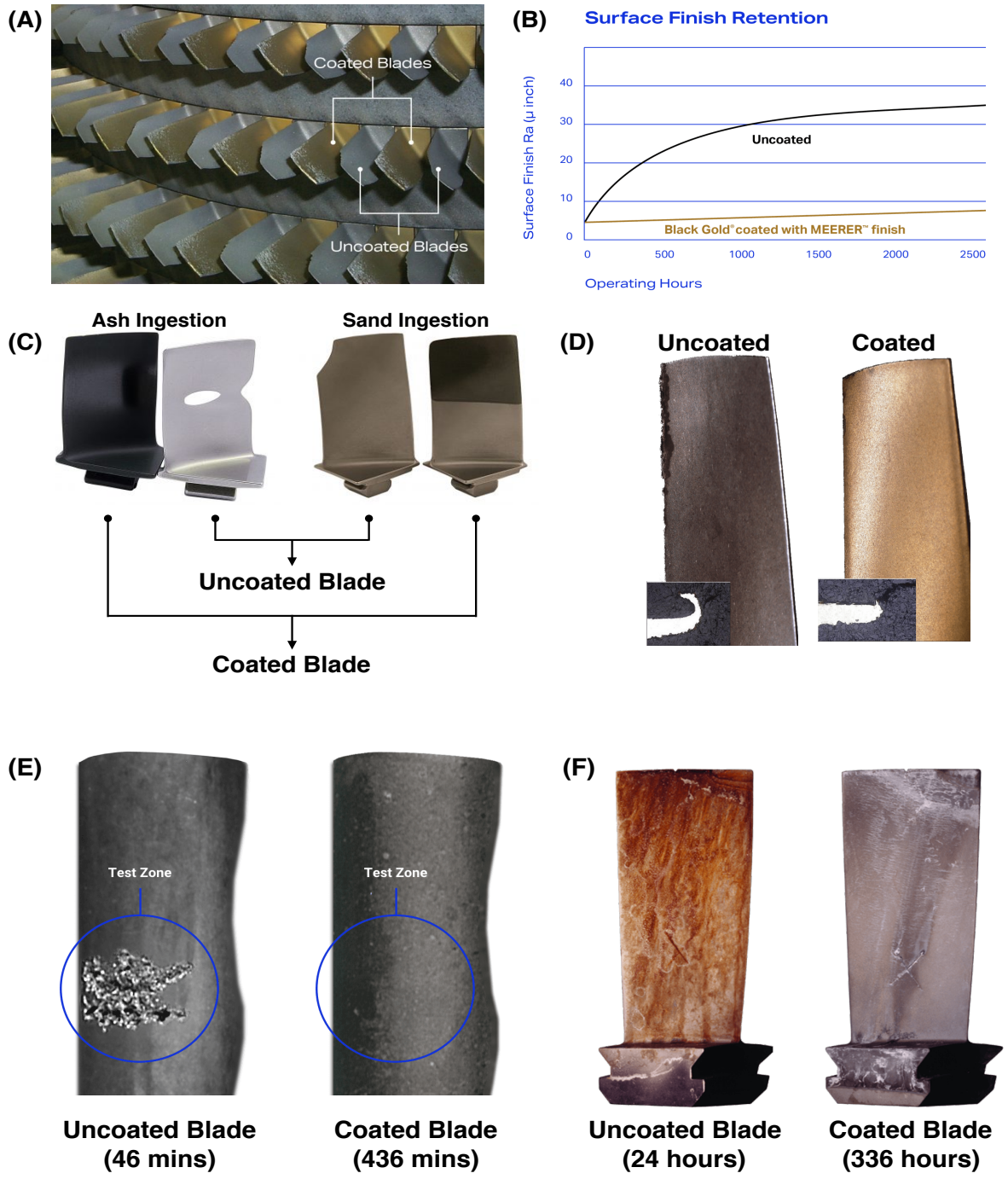


Figure 5.27: BlackGold® Coating Developed By MDS Coating Shows : (A) Difference In Erosion Levels Between Coated And Uncoated Blades (B) Impeccable Surface Finish Over An Extended Period Of Time (C) Coated Blade Outperforming The Uncoated Blades For Sand Ingestion And Ash Ingestion (D) Reduced Leading Edge Curling On T-58 Blades While Operating In Desert Environment (E) Resists Fluid Erosion Over A Longer Duration (F) Resists Corrosion Over An Extended Period

coating does not affect the weight of the compressor while improving its mechanical properties. This is a ceramic-metallic nano-composite coating that consists of alternate layers of hard substrate and soft phase which provides a combination of hardness and toughness to resist erosion (Kilchenstein, 2012; Alman and Duffles, 2013). The hard phase resists the impact while the soft phase keeps any initial crack from propagating further into the next layer of the substrate. The coating is applied using a proprietary method called physical vapour decomposition (PVD) process. A high purity solid coating material is evaporated under a high vacuum that subsequently attaches to the surface on a nano-level.

As shown in the fig. 5.27(A), the BlackGold® coated blades resists erosion while the uncoated blades undergo severe erosion. The surface finish of the coated blade gets maintained over an extended duration of time as shown in fig. 5.27(B). It can be seen from fig. 5.27(C), the BlackGold® coating minimises the abrasive effect of sand ingestion and ash ingestion in the compressor. The BlackGold® coating also mitigates the curling of the leading edge in T-58 blades while operating in dessert region as shown in fig. 5.27(D). The coated blades resist the fluid erosion and corrosion over an extended period as shown in fig. 5.27(E) and (F) respectively. While the coating thickness can vary according according to the engine type and compressor stage, as a general rule these coatings are at least 10 μm thick (Alman and Duffles, 2013).

5.6 Chapter Summary

A detailed background to the types of blade damages, its causes and the cost to industry has been given. 7 levels of leading edge damages have been considered which increases progressively both chord-wise as well as radially. The damage has been represented using a hyperbolic tangent function which represents the blended blades very well. The maximum damage considered is 18% chord-wise and from 65% span upwards radially. In addition to this, blades with increasing chord-wise damage at the same radial level and increasing radial level damage for the same chord have also been studied.

This one-stage IGT rotor is a highly tip loaded and the stall occurs due to excessive blockage

from tip clearance vortex. Thus, the chord-wise damage was observed to be more crucial parameter compared to radial level damage wherein it affects the stall margin more adversely. The behaviour of leading edge damaged blades has a few commonalities with differing tip gap study. It was seen that for random leading edge damage, a zigzag arrangement has the best performance and stability margin while sinusoidal arrangement has the worst performance and stability margin. The present study shows that the type of arrangement affects the performance of compressor while the earlier study with less damage showed no effect. This work quantifies the threshold at which the damage becomes influential.

It was also seen that the choked mass flow rate in case of damaged blade increases compared to undamaged blade. This was attributed to the larger throat area in case of damaged blades. Furthermore in case of sectoral damage for two rotors having same total damage, the rotor having more blades with smaller damage intensity fared better than the rotor with less blades with more damage intensity. Also, when increasing number of adjacent blades get damaged, an overall deterioration in the performance is observed. It was also seen that the alternate arrangement of undamaged blade and damaged blade provided better pressure ratio, efficiency and stability compared to the case where all the damaged blades were concentrated in one half of the annulus.

Finally recent advances in technology has been discussed which can help alleviate or postpone some of these problems. The BlackGold® coating minimises the abrasive effect of sand ingestion, ash ingestion and also the tip curl damage when operating in dessert region. This is a ceramic-metallic nano-composite coating that consists of alternate layers of hard substrate and soft phase which provides a combination of hardness and toughness to resist erosion. The technology was developed by MDS coating. Moreover new techniques like geometry-based adaptive toolpath laser powder deposition method promise to reduce the repair costs by up to 92%. Such techniques have been used successfully to repair and reconstruct the profile of damaged compressor blades and blisks.

Chapter 6

Development of Surrogate Model and Uncertainty Quantification

"All models are wrong, but some are more useful - George Box"

This chapter introduces the development of a novel surrogate model from the first principles along with the subsequent uncertainty quantification (UQ) of the compressor performance. It was seen in literature survey that techniques like Polynomial Chaos Expansion (PCE) suffer from 'curse of dimensionality' wherein the number collocation points become prohibitive as the random parameters increase. On the other hand, techniques like Monte Carlo Simulation (MCS) requires large sample size due to its slow convergence. Hence the repeated use of high fidelity deterministic CFD solver for performing UQ using both the above technique is impossible. Instead, the UQ has been carried out using a novel surrogate model based on an interpolation technique. This was summarised using the schematic shown in Fig. 6.1

The novel surrogate model has been developed specifically for predicting the performance of a compressor having blades of differing dimensions around the annulus. The surrogate model gives excellent prediction for tip loaded compressors like NASA Rotor 67 as well as the low speed, wide chord blade compressor and is found to be extremely robust at design and off-design speeds. In this study, two parameters *i.e.* stagger angle and tip gap, have been considered as a parameters of interest though other parameters could be studied as well in a similar way.

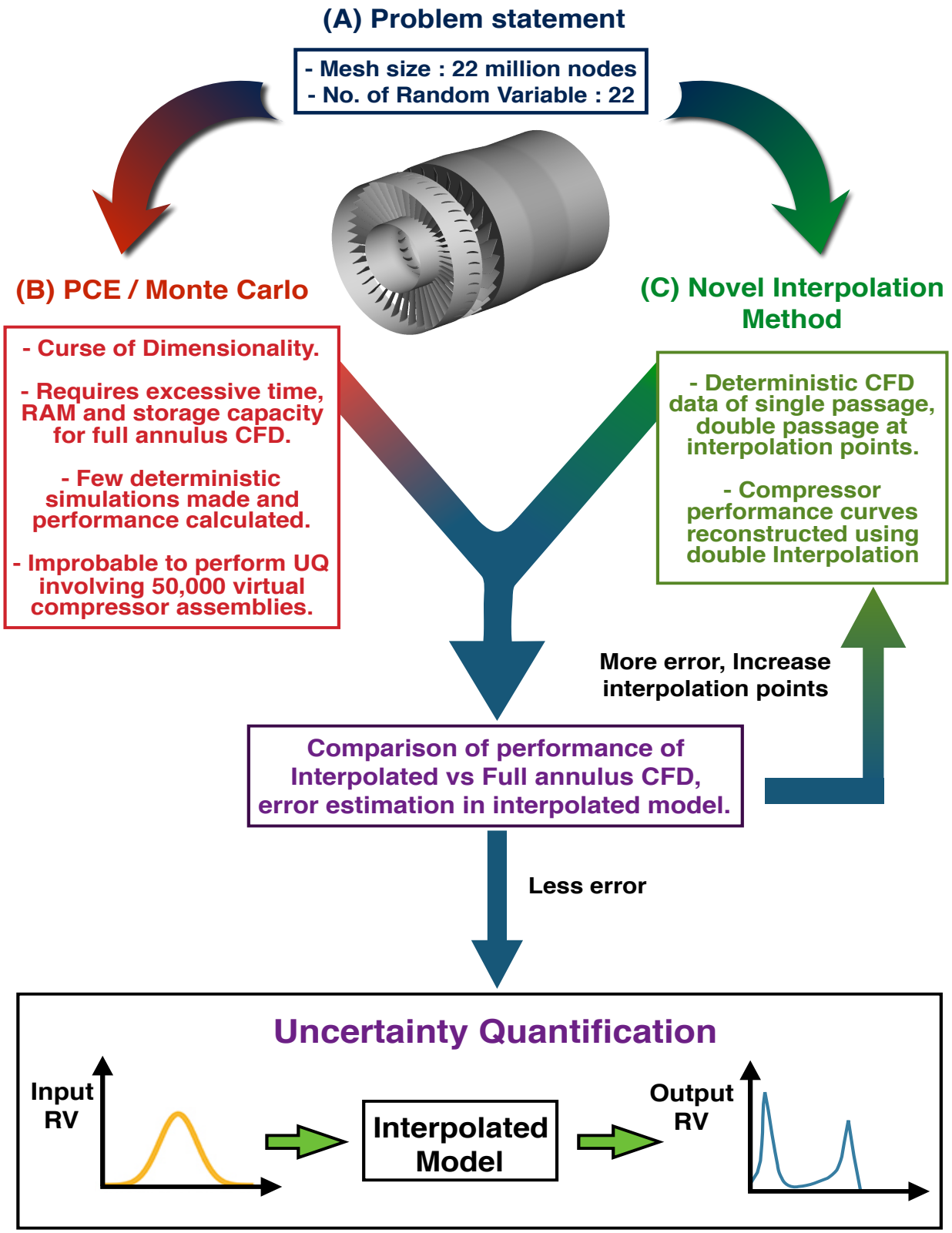


Figure 6.1: Uncertainty Quantification Using Novel Surrogate Model

6.1 First Principles To Build The Surrogate Model

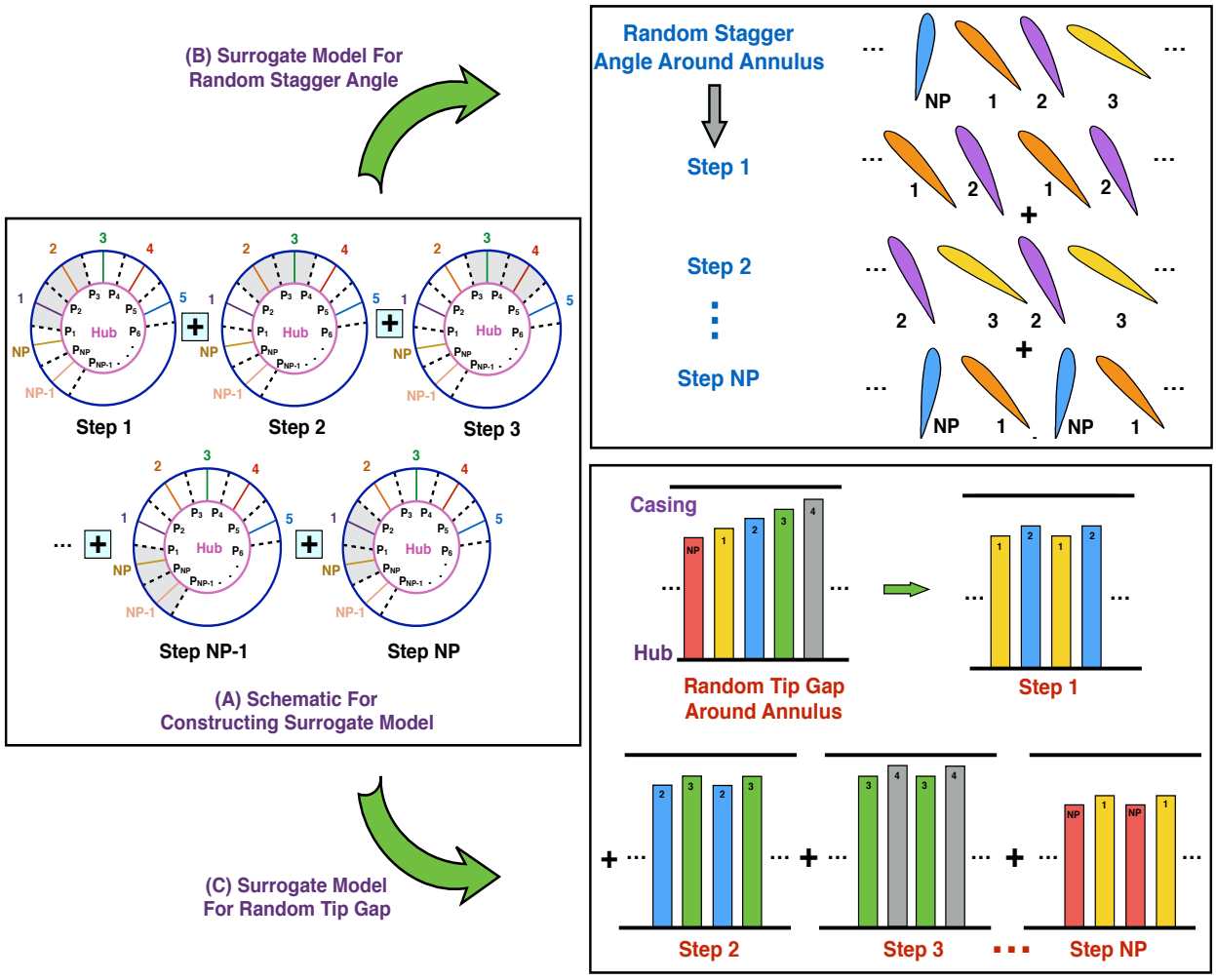


Figure 6.2: (A) General Schematic For Constructing Surrogate Model (B) Schematic Of Surrogate Model For Random Stagger Angle Around The Annulus (C) Schematic Of Surrogate Model For Tip Gap Around The Annulus

As discussed previously in chapter 3, an advantage of symmetry can be taken when all the blades in the compressor are of the same dimension. In such cases, instead of performing full annulus CFD simulation, a single blade can be considered along with the use of periodic flow condition at the passage boundaries. Such a sector is called single passage rotor domain. A double passage rotor domain is used when two different blades are arranged alternately.

Fig. 3.7(B) in Chapter 3 shows the schematic of single passage and double passage rotor domain used in a CFD simulation. As can be seen, the periodic surfaces P_1 and P_2 represents the passage boundaries for a single passage rotor domain. Similarly, the passage boundaries for a double passage rotor domain are represented using the periodic surfaces P_1 and P_3.

The imposition of periodic flow condition on the passage boundaries reduces the size of the computational domain compared to a full annulus CFD simulation. In general, the total number of blades 'N' has to be a multiple of the number of passage 'NP'. When there is no symmetry, a full annulus CFD simulation is carried out. A full annulus CFD simulation of compressor consisting of 22 blades would typically consume 22 units of more time compared to a single passage CFD simulation. If those 22 compressor blades are of differing geometric dimensions, a total of 21! unique arrangements are possible. Thus a full annulus CFD simulation using Monte Carlo technique is nigh impossible for predicting the performances of different possible arrangements of random staggered (and random tip gap) blades because of the sheer number of possible arrangements. Surrogate models become *sine qua non* for predicting the compressor performance under such circumstances. Such surrogate models are typically developed using the data from a few deterministic single passage and double passage CFD simulations and hence offer a quick turnaround time to engineers and researchers to perform UQ analysis. Data from different single passage and double passage CFD simulations are known *a priori*.

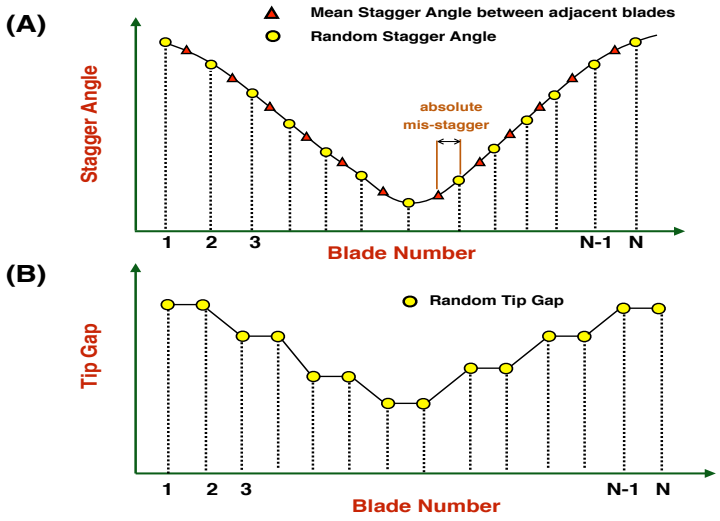


Figure 6.3: Schematic Of Sinusoidal Arrangement With Respect To Blade Number For (A) Stagger Angle Variation (B) Tip Gap Variation

In the present thesis, the surrogate model is built using a first order approximation similar to the one used by Palman et al. (2019), albeit with slight modifications. A line diagram schematic of a compressor shown in fig. 6.2(A) depicts the strategy used for the development of surrogate model. As seen, a full annulus geometry of blades with differing dimensions is divided into a number of passages and periodic surfaces. Passage 1 is bound by periodic surfaces P_1

and P_2, passage 2 by periodic surfaces P_2 and P_3 and so on till Passage NP which is bound by periodic surfaces P_{NP} and P_1. In fig. 6.2(A), the periodic surfaces are marked by black dashed lines. Fig. 6.2(B) and (C) shows the schematic of construction of surrogate model for random stagger angle and random tip gap respectively. These two figures make it very clear that the full annulus domain with random dimensions of blades is subdivided into smaller double passage domain. The pressure ratio and efficiency from these smaller double passage domains are mass averaged throughout the annulus using the following set of equations :

$$M_{ave} = \frac{\sum_{i=1}^{NP} (m_i)}{NP} \tag{6.1}$$

$$PR_{ave} = \frac{\sum_{i=1}^{NP} (m_i PR_i)}{\sum_{i=1}^{NP} (m_i)} \tag{6.2}$$

$$\eta_{ave} = \frac{\sum_{i=1}^{NP} (m_i \eta_i)}{\sum_{i=1}^{NP} (m_i)} \tag{6.3}$$

where M_{ave}, PR_{ave}, η_{ave} and NP are average mass flow rate, average pressure ratio, average efficiency and total number of passages respectively in the whole annulus. Similarly, the terms m_i, PR_i and η_i represents the data of mass flow rate, pressure ratio and isentropic efficiency from the two adjacent passages for each i as represented in fig. 6.2(A) as step 1, step 2 and so on. Fig. 6.2(A) depicts pictorially the mass averaging procedure shown in equations 6.1 - 6.3. In equations 6.1 - 6.3, the data from single passage simulation is used when the blades in the two adjacent passages (shown in fig. 6.2(B) and (C)) are same while data from the double passage simulation is used when the blades are different.

Fig. 6.3(A) and (B) shows the schematic of sinusoidal arrangement with respect to blade number for stagger angle variation and tip gap variation respectively. It can be seen that the distribution for stagger angle around the annulus is smooth (continuous random variable) while the tip gap distribution around the annulus is found to be discontinuous (discrete random variable). The

basic idea of surrogate model for stagger angle and tip gap as parameters of variation remains the same albeit with slight modification to account for the mis-stagger effects in stagger angle variation and the non-linear effects of tip gap variation. The predicted performance curves are then compared with full annulus CFD performance curve as a first step towards estimating the scatter of maximum efficiency, stall margin and their probability distribution function. All the single passage, double passage and full annulus simulations are carried out by throttling the rotor from choke to stall by incrementally closing the nozzle area in fixed steps. These fixed steps in which a nozzle is closed remains the same for a particular speed.

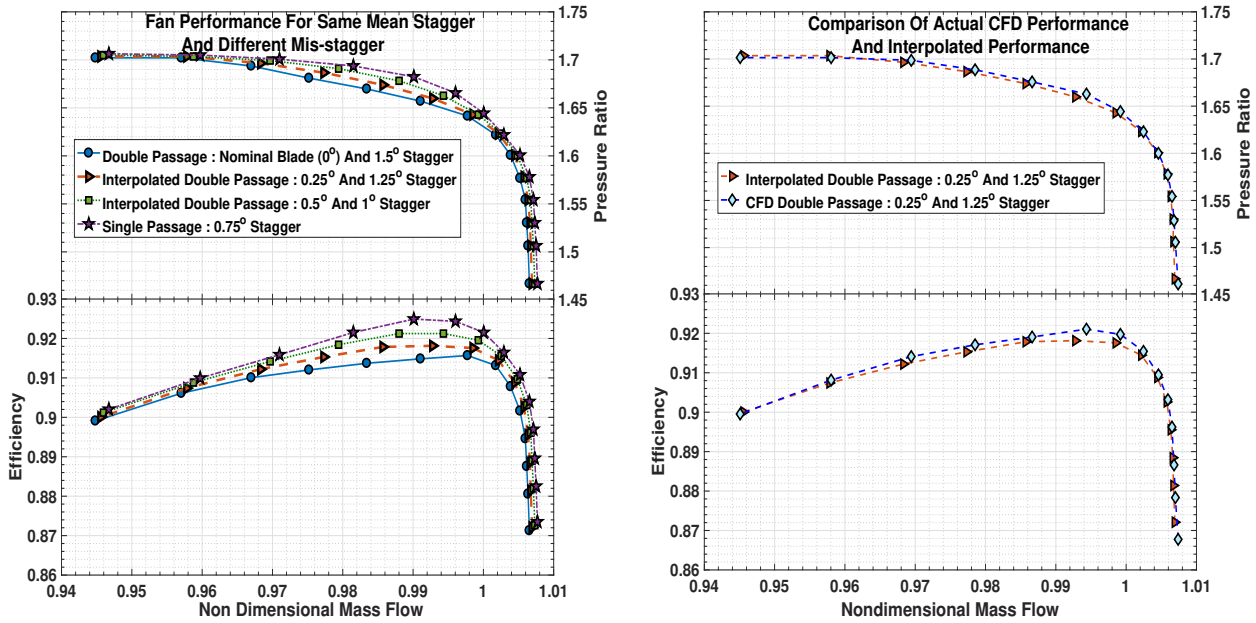
6.2 Surrogate Model For Stagger Angle

To begin with, the following two cases were simulated viz. (i) Single Passage : 0.75° stagger angle blade (ii) Double Passage : Nominal blade and 1.5° stagger angle blade. A cursory look at these two cases would show that both these cases have same mean stagger angle (0.75°) while differing in their mis-stagger levels. It can be seen that the mis-stagger between the blades of case (i) is zero while for case (ii) it is 0.75°. As shown in fig. 6.4(A), case (i) outperforms case (ii) due to zero mis-stagger between the blades of case (i). The area between the characteristic curves of case (i) and case (ii) can be thought of as the loss due to mis-stagger. It can thus be hypothesised that if the mis-stagger levels are reduced while keeping the same mean stagger angle, the characteristic curve would start approaching the single passage case (zero mis-stagger). Linear interpolation was carried out between case (i) and case (ii) such that they represented two cases having

(iii) mis-stagger of 0.5° (Double Passage : 0.25° and 1.25° stagger angle blade)
(iv) mis-stagger of 0.25° (Double Passage : 0.5° and 1° stagger angle blade).

Fig. 6.4(B) shows the comparison between characteristic curve of case (iii) obtained by linear interpolation and actual CFD simulation. It can be seen that a very good match is obtained between both these curves. Similar results obtained for case (iv) has not been shown for the sake brevity. At this stage, the author has made a simple assumption that the loss due to mis-

stagger remains the same irrespective of mean stagger angle. Thus, the characteristic curve for whole annulus case with differing stagger angles can be reconstructed provided the data for the mean stagger angle and loss due to mis-stagger is available *a priori*. Subsequent paragraphs would describe the surrogate model in detail.



(A) Fan Performance For Same Mean Stagger And Different Mis-stagger

(B) Comparison Of Actual CFD Performance And Interpolated Performance

Figure 6.4: CFD Performance Vs. Interpolation Performance (NASA Rotor 67) At 100% Speed For Different Mis-stagger Levels While Maintaining The Same Mean Stagger Angle

Two terms would be used in this section viz. absolute mis-stagger (S-abs. mist) and mean stagger angle (S-mean). Similar to the global parameters, $S_{ave.\ overall}$ and $C - MIST$ in equations 4.1 and 4.2, the terms absolute mis-stagger (S-abs. mist) and mean stagger angle (S-mean) are local parameters between two adjacent blades. These local parameters are used in the development of surrogate model. If there are **N** blades around the annulus and $\mathbf{S_i}$ is the stagger angle of individual blade, then

$$S - mean_i = \frac{S_i + S_{i+1}}{2} \tag{6.4}$$

$$S - \ abs.\ mist_i = \frac{|S_i - S_{i+1}|}{2} \tag{6.5}$$

As there are **N** blades in the compressor, the term $\mathbf{S_{N+1}}$ is the same as $\mathbf{S_1}$ in the equations 6.4

- 6.5. As seen from table 4.1 and fig. 4.12, the same set of varying dimension blades can give different cumulative mis-stagger for different arrangements though the overall average stagger angle remains the same for all the arrangements. It was seen in fig. 4.4(A) that the performance of a compressor deteriorates with increasing mis-stagger. A surrogate model described in equations 6.1 - 6.3 has been used to reconstruct the whole annulus performance curves for different arrangements of random stagger angle variation; with slight modification to account for the effects of mean stagger angle and absolute mis-stagger as shown in fig. 6.3(A). The schematic of sinusoidal arrangement in fig. 6.3(A) has been shown for the ease of visualising the development of surrogate though it can be equally applied on any kind of arrangement. As discussed earlier, the stagger angle variation is considered to be between $\pm 1.5^{\circ}$.

Fig. 6.5 shows the interpolation points used to build surrogate model for differing stagger angle. As can be seen, there are a series of single passage and double passage simulations that have been performed at these points. The double passage simulations are performed such that the mean stagger angle is 0° while the absolute mis-stagger between the blades gradually increase. The data of these (interpolation) cases would be used to interpolate (cubic spline) any intermediate single passage and double passage case. A convergence study was done to find the number of interpolation points required to predict the performance of compressor accurately compared to performance obtained using whole annulus CFD simulation. Each of the performance curve consists of 16 discrete points wherein each point corresponds to a change in nozzle area that is used to throttle the compressor from choke to stall. 3 cases for which convergence test has been done as shown in fig. 6.5 are : (**A**) Total interpolation cases : **7** (5 Single Passage and 2 Double Passage) and total points : **112** (= 7×16) (**B**) Total interpolation cases : **10** (7 Single Passage and 3 Double Passage) and total points : **160** (= 10×16) (**C**) Total interpolation cases : **19** (13 Single Passage and 6 Double Passage) and total points : **304** (= 19×16).

Fig. 6.6 shows the schematic of the double interpolation method used for predicting the performance of different arrangements of stagger angle. As can be seen, the performance curve of any arrangement is reconstructed in two parts. In the first part as shown in fig. 6.6(A), the performance of any mean stagger can be computed from the different single passage simulation carried out at interpolation points as described previously. For the second part as shown in

fig. 6.6(B), the performance curve of baseline case (0° stagger) is compared against a double passage case of blades having stagger angles 1.5° and -1.5°. It is important to note that double passage case is having mean stagger angle of 0° and hence the choke and stall mass flow rate would be comparable to the baseline case. Any change in the pressure ratio, efficiency and mass flow rate between the baseline case and double passage case would be because of the mis-stagger in the double passage case. This change in the mass flow rate, pressure ratio and efficiency between these two cases are assumed to be linearly varying (accuracy of the assumption can be increased by increasing the interpolation points of double passage simulations) and hence performance curve for intermediate level of mis-stagger can be computed using interpolation between these two cases.

As discussed previously, it is assumed that the losses due to absolute mis-stagger (change in mass flow rate, pressure ratio and efficiency) is independent of the mean stagger angle i.e. the same loss would be observed for all blades with different mean stagger angle but with same level of absolute mis-stagger. As can be seen in fig. 6.3(A), different blades have different stagger angles, hence the mean stagger angle ($S-mean_i$) and the absolute mis-stagger ($S-\ abs.\ mist_i$) between blades also vary throughout the annulus. For each nozzle angle, the losses (i.e. the change in mass flow rate, pressure ratio and efficiency) due to absolute mis-stagger ($S-\ abs.\ mist_i$) are mapped on from the fig. 6.6(B) to the value of corresponding mean stagger angle ($S-mean_i$) shown in fig. 6.6(A).

Once the effect of absolute mis-stagger ($S-\ abs.\ mist_i$) are mapped on corresponding mean stagger angle ($S-mean_i$) for each discrete nozzle area closure, a subsequent mass averaging of pressure ratio and efficiency is done using equations 6.1 - 6.3 to predict the performance of full annulus assembly of different staggered blades. The compressor characteristic curve shown in this section consists of average mass flow rate, average pressure ratio and average efficiency. Fig. 6.7(A) and (B) show the convergence of characteristic curve from surrogate model with respect to whole annulus CFD performance for sinusoidal arrangement and zigzag arrangement respectively (at 100% speed in case of NASA Rotor 67). It can be seen that with increase in interpolation points, the characteristic curve from surrogate model converges towards the whole annulus characteristic curve.

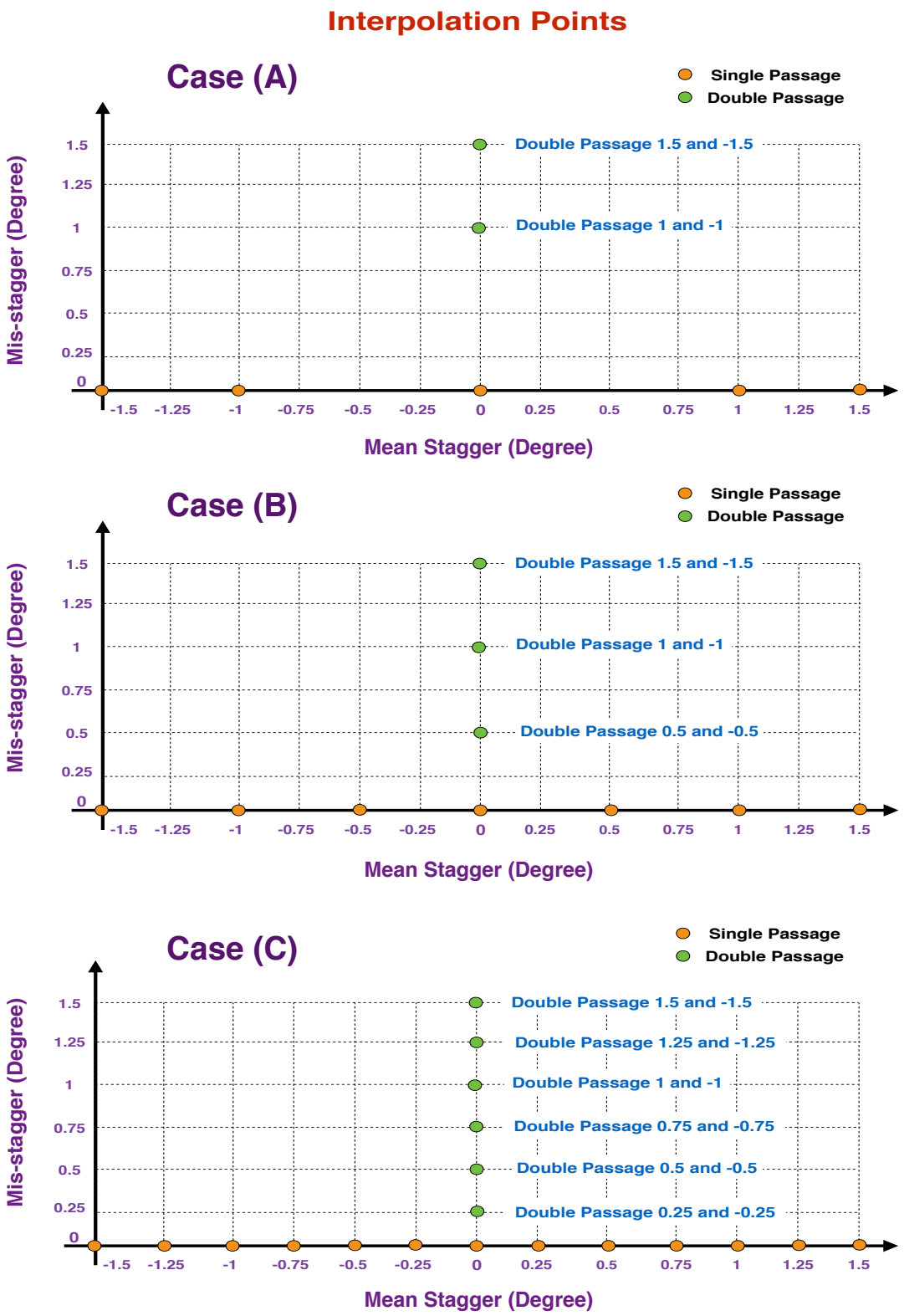


Figure 6.5: Schematic For Different Interpolation Cases For Building Surrogate Model Of Stagger Angle (A) Total 7 Interpolation Points *i.e.* 5 Single Passage and 2 Double Passage Cases (B) Total 10 Interpolation Points *i.e.* 7 Single Passage and 3 Double Passage Cases (C) Total 19 Interpolation Points *i.e.* 13 Single Passage and 6 Double Passage Cases

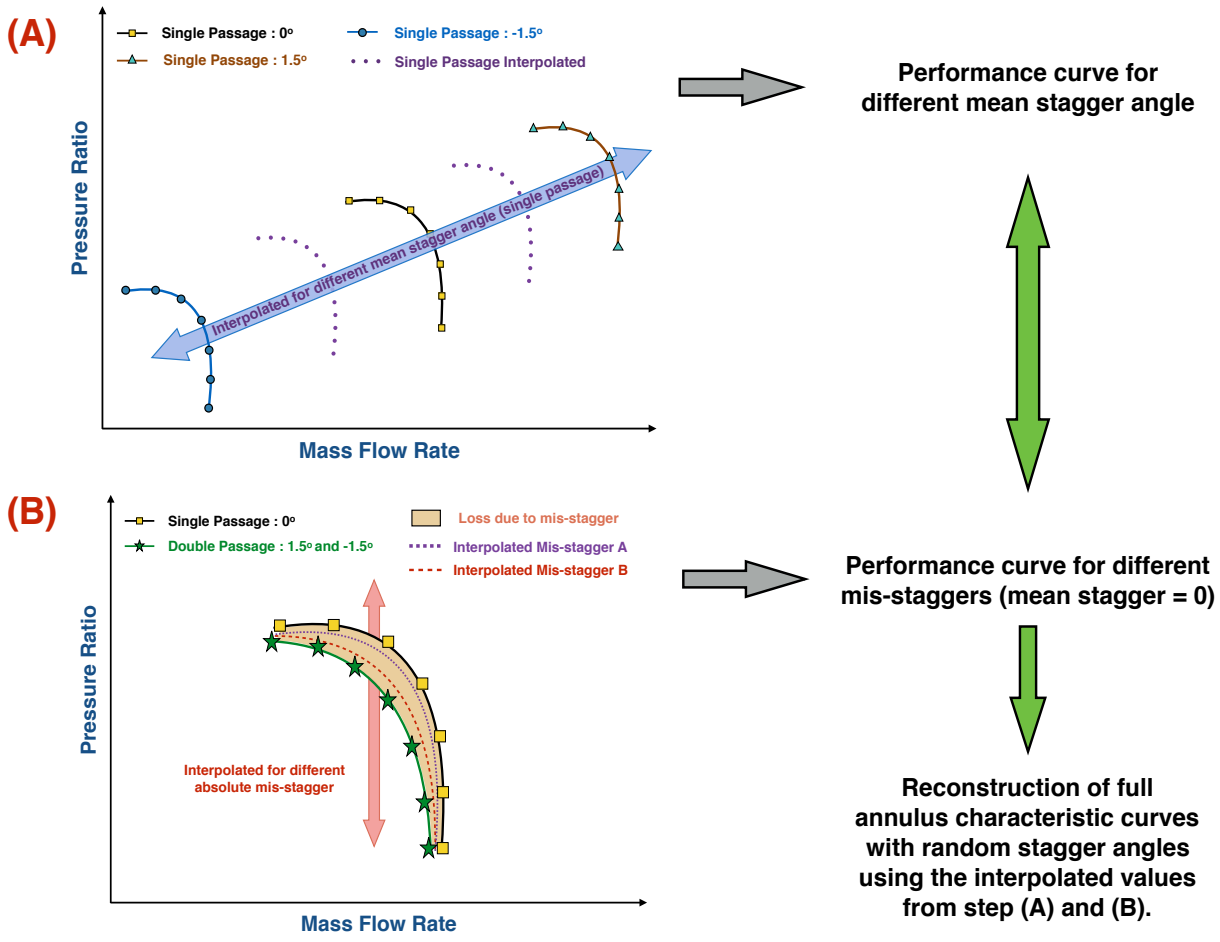
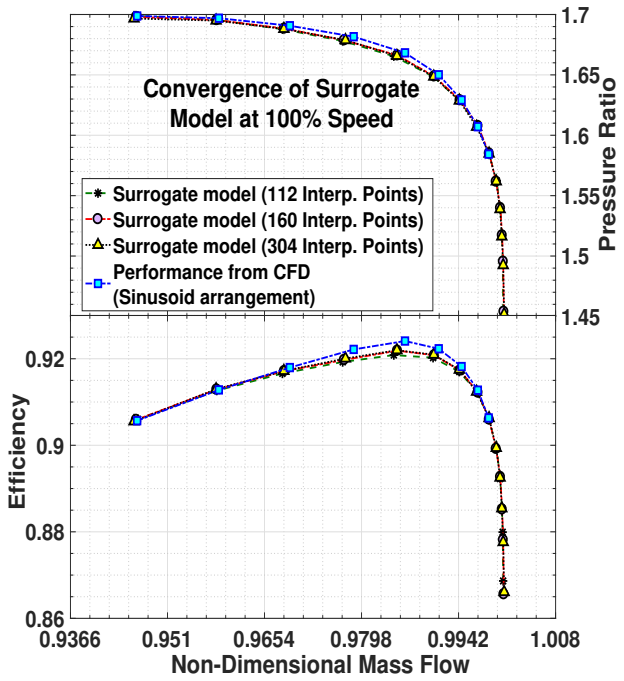
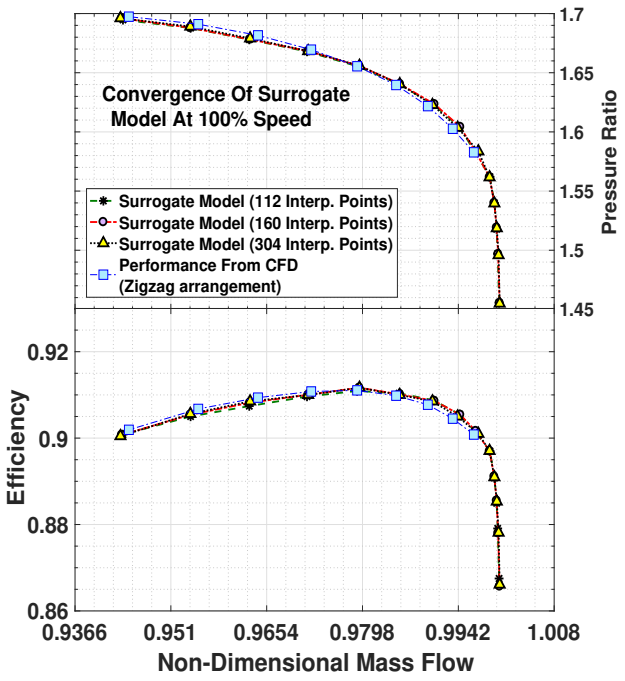


Figure 6.6: Schematic For Performance Prediction Of Different Arrangements Of Stagger Angle Using Double Interpolation Method (A) Interpolation For Different Single Passages (B) Interpolation For Different Mis-Staggers

Fig. 6.8 shows the mean absolute percentage error (MAPE) between the surrogate model (with 304 points) and whole annulus deterministic CFD simulation for pressure ratio, efficiency and mass flow rate respectively. It can be seen that the MAPE ranges from 0.08% for efficiency to 0.14% for mass flow rate. Thus the lower order surrogate model matches very well with the whole annulus deterministic CFD simulation. MAPE is computed by taking the average of absolute percentage error between the points represented by surrogate model and the corresponding points of whole annulus CFD simulation. The generality of this model is further established by plotting the characteristic curve for both NASA Rotor 67 at part speed condition (80% speed) and wide chord blade rotor at design speed in fig. 6.9(A) and (B) respectively. For these two cases, the surrogate model predicts the deterministic whole annulus CFD characteristic curve with just 112 points (thus the interpolation points were not increased any further).



(A) Convergence Of Characteristic Curve From Surrogate Model For Sinusoidal Arrangement



(B) Convergence Of Characteristic Curve From Surrogate Model For Zigzag Arrangement

Figure 6.7: Characteristic Curve From Surrogate Model For Stagger Angle Variation (NASA Rotor 67) At 100% Speed

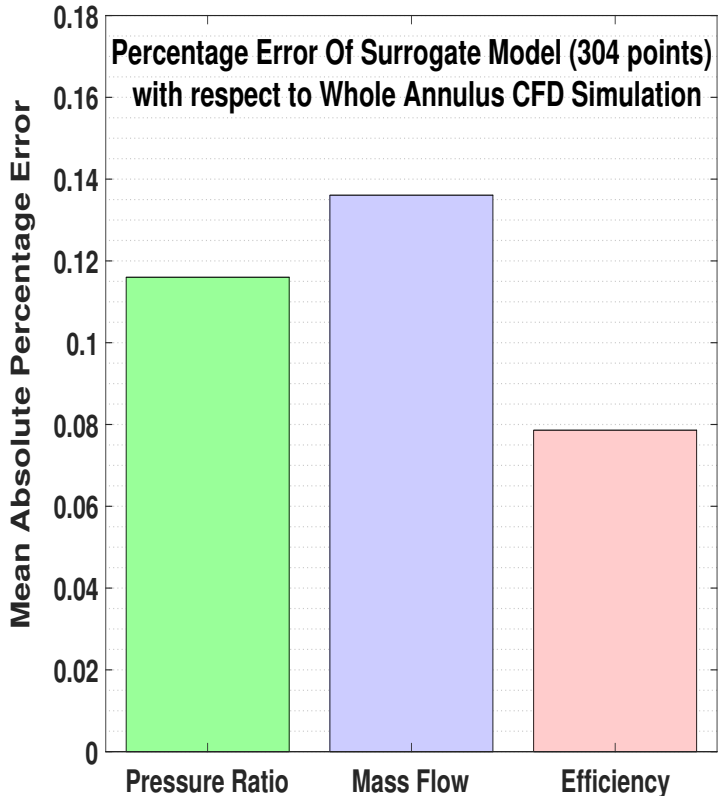
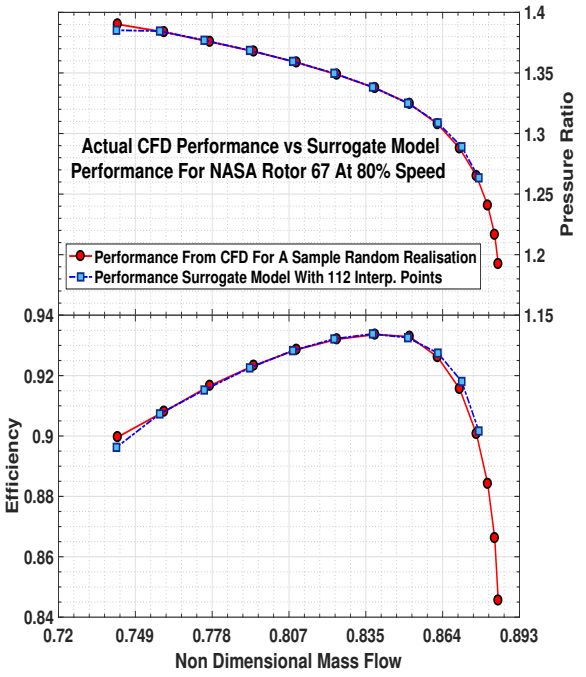
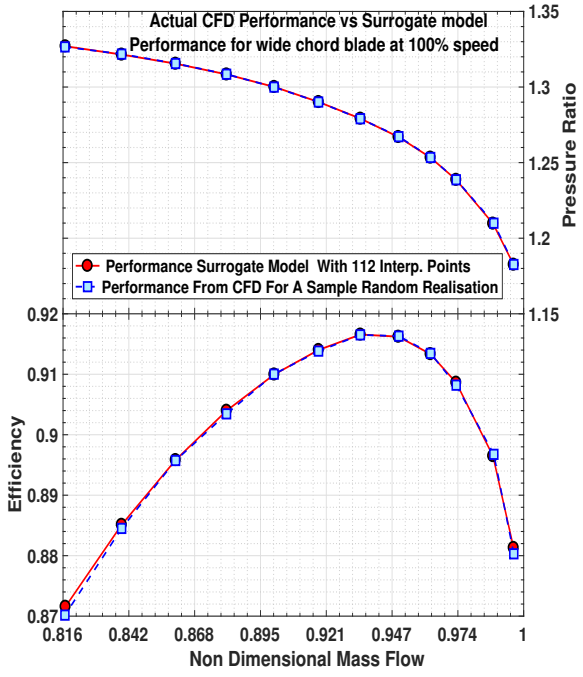


Figure 6.8: Mean Absolute Percentage Error Between The Surrogate Model And Full Annulus CFD Simulation



(A) Characteristic Curve For Nasa Rotor 67 At 80% Speed



(B) Characteristic Curve For Wide Chord Blade Rotor At 100% Speed

Figure 6.9: Comparison Of Characteristic Curve From Surrogate Model And Whole Annulus CFD Simulation For Stagger Angle Variation

6.3 Surrogate Model For Tip Gap

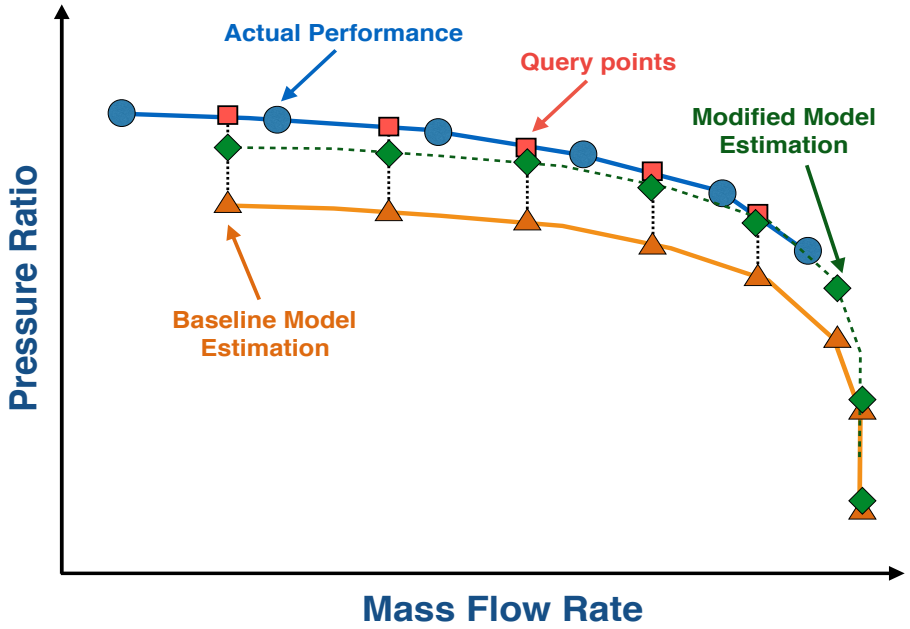


Figure 6.10: Schematic Of Performance Prediction For Baseline Surrogate Model And Modified Surrogate Model In Case Of Tip Gap

It was seen in Chapter 4 that the low speed, wide-chord blades (part-span loaded) are not so sensitive to variation in tip gap compared to tip-loaded blade like NASA Rotor 67. Discussion in this section will be focussed on development of surrogate model for tip gap as a parameter for NASA Rotor 67 at 100% speed. Fig. 6.3(B) shows the schematic of sinusoidal arrangement with respect to blade number for different tip gaps.

Unlike the stagger angle, the tip gap distribution around the annulus is found to be discontinuous (discrete random variable). Knapke et al. (2020) observed that the highest changes in aerodynamic loading in a 7-passage rotor was caused on the extreme blades compared to the adjacent blades. Hsu and Hoyniak (2011) have shown using influence coefficient method that a full annulus compressor of 24 blades can be replaced with a 5-blade model though the prediction accuracy starts to decrease with further reduction in the number of blades. Furthermore, for different arrangements of blades with differing tip gaps, different stalling mass flow rate was observed as seen in fig. 4.28 (the same is not true in case of different arrangements of blades with differing stagger angle as seen in fig. 4.13).

Thus the impact of differing tip gaps spans more adjacent blades compared to the case with differing mis-stagger. The surrogate model for differing tip gaps has been constructed using the data from single passage and double passage simulations and hence the limited accuracy. To account for the increased nonlinearity in tip gap as a parameter, slight modification has been made to the basic idea of surrogate model discussed in previous section.

The mass averaging of pressure ratio and efficiency as given in equations 6.1 - 6.3 implies that efficiency is independent of the pressure ratio. In case of tip gaps, this assumption is modified by introducing another variable called average temperature ratio (TR_{ave}) to those equations. Efficiency is treated as a dependent variable of average pressure ratio and average temperature ratio. The equations below show the building of surrogate model used for predicting the performance for whole annulus compressor with random tip gaps.

$$M_{ave} = \frac{\sum_{i=1}^{NP} (m_i)}{NP} \tag{6.6}$$

$$PR_{ave} = \frac{\sum_{i=1}^{NP} (\alpha \, m_i^{\beta} \, PR_i^{\kappa})}{\sum_{i=1}^{NP} (m_i^{\delta})} \tag{6.7}$$

$$TR_i = tr_i^{\frac{\gamma}{\gamma-1}} \tag{6.8}$$

$$TR_{sc} = \frac{\sum_{i=1}^{NP} (\alpha \, m_i^{\beta} \, TR_i^{\kappa})}{\sum_{i=1}^{NP} (m_i^{\delta})} \tag{6.9}$$

$$TR_{ave} = TR_{sc}^{\frac{\gamma-1}{\gamma}} \tag{6.10}$$

$$\eta_{ave} = \frac{PR_{ave}^{\frac{\gamma-1}{\gamma}} - 1}{TR_{ave} - 1} \tag{6.11}$$

$$\|F(x)\|_2^2 = min \left(\sum_{i=1}^{m} F_i^2(x) \right) \tag{6.12}$$

In eq. 6.12, $F(x) = \begin{bmatrix} F_1(x) \\ F_2(x) \\ F_3(x) \\ F_4(x) \\ F_5(x) \\ F_6(x) \end{bmatrix} = \begin{bmatrix} PR_{ave.\ (baseline\ surrogate\ model:\ zigzag)} - PR_{(CFD:\ zigzag)} \\ PR_{ave.\ (baseline\ surrogate\ model:\ linear)} - PR_{(CFD:\ linear)} \\ PR_{ave.\ (baseline\ surrogate\ model:\ HA)} - PR_{(CFD:\ HA)} \\ TR_{sc.\ (baseline\ surrogate\ model:\ zigzag)} - TR_{sc.\ (CFD:\ zigzag)} \\ TR_{sc.\ (baseline\ surrogate\ model:\ linear)} - TR_{sc.\ (CFD:\ linear)} \\ TR_{sc.\ (baseline\ surrogate\ model:\ HA)} - TR_{sc.\ (CFD:\ HA)} \end{bmatrix}$

For the baseline surrogate model, the values of $\alpha = \beta = \kappa = \delta = 1$ in equations 6.7 and 6.9. The value of γ (heat capacity ratio for air) is equal to 1.4 in the above equations. The terms m_i, tr_i and PR_i represents the data of mass flow rate, temperature ratio and pressure ratio

from single passage and double passage simulations for each i respectively. The performance predicted using baseline surrogate model is compared against deterministic whole annulus CFD performances and a nonlinear least square optimisation (functions available in MATLAB) is carried out as shown in equation 6.12. A pictorial depiction of the nonlinear least square optimisation is shown in fig. 6.10. The following three whole annulus CFD simulation (about 50 data points corresponding to pressure ratio and scaled temperature ratio) were used to calibrate the baseline surrogate model :

(i) Zigzag Arrangement (as in fig. 4.27)
(ii) Linear Arrangement (as in fig. 4.27)
(iii) Half annulus (HA) of blades with tip gaps 0.188% span and 0.94% span (as in fig. 4.25)

Once the optimal value of α, β, κ and δ are computed, the values of PR_{ave}, TR_{ave} and η_{ave} are recalculated using equations 6.7 to 6.11. This updated model is referred to as modified surrogate model in the present thesis. The rationale behind using scaled temperature ratio (TR_{sc}) over actual temperature ratio (tr) in equation 6.12 is explained below.

Fig. 6.11(A) shows a comparison between pressure ratio and the actual temperature ratio. As the scales of both the quantities are different, the y-axis of actual temperature ratio is shifted to coincide with that of pressure ratio as shown in fig. 6.11(B) for the ease of visualisation. It can be seen that the slopes of actual temperature ratio and pressure ratio are completely different and hence a direct application of nonlinear least square optimisation for these two curves would result in distortion of performance curves predicted by the modified model.

This drawback is overcome by taking advantage of the Pressure-Temperature relation in an adiabatic process wherein the pressure ratio is equal to temperature ratio raised to the exponent of $(\frac{\gamma}{\gamma-1})$. The data of temperature ratio from single passage and double passage simulation (tr_i) is thus raised to an exponent of $(\frac{\gamma}{\gamma-1})$ and the resulting value (TR_i) is used to calculate scaled temperature ratio (TR_{sc}) as shown in equations 6.8 and 6.9. A comparison between the scaled temperature ratio and pressure ratio has been shown in fig. 6.11(C). For the ease of visualisation, the y-axis of scaled temperature ratio is shifted to coincide with that of the pressure ratio as shown in fig. 6.11(D). The scaling of temperature ratio makes sure that slopes

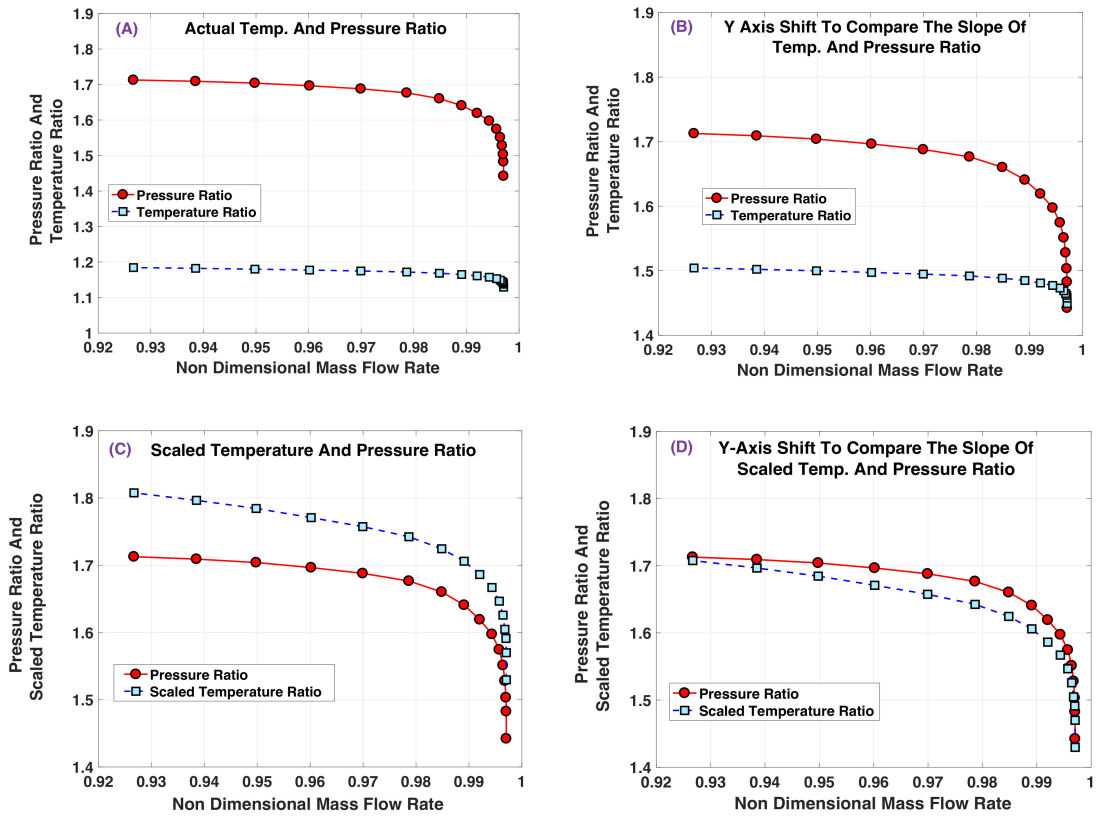
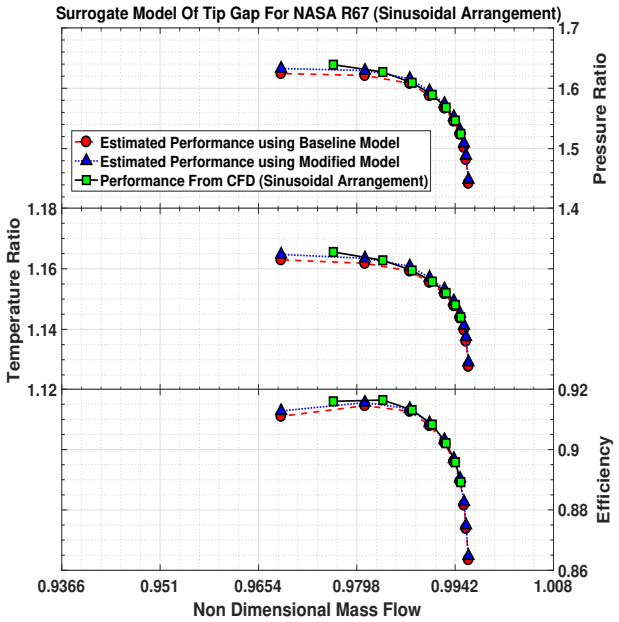


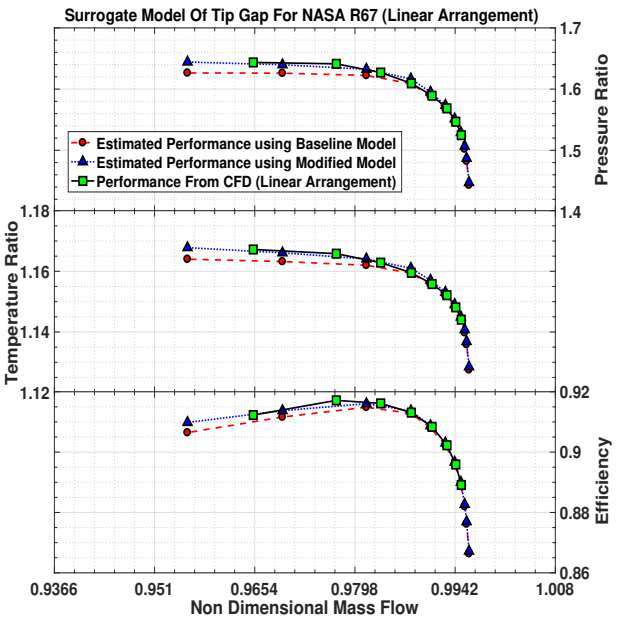
Figure 6.11: Comparison Of Slopes Of Actual Temperature Ratio And Scaled Temperature Ratio Vs. Pressure Ratio For A Sample Double Passage Case With Mixed Tip Gaps (A) Pressure Ratio And Actual Temperature Ratio Vs. Mass Flow Rate (B) Y Axis Of Actual Temperature Ratio Shifted To Coincide With Pressure Ratio (C) Pressure Ratio And Scaled Temperature Ratio Vs. Mass Flow Rate (D) Y Axis Of Scaled Temperature Ratio Shifted To Coincide With Pressure Ratio

of average pressure ratio and scaled temperature ratio are comparable while also ensuring availability of more data points for the correct estimation of parameters α, β, κ and δ. The average temperature ratio (TR_{ave}) is calculated by raising the TR_{sc} to an exponent of $(\frac{\gamma-1}{\gamma})$. The performance curve of the modified model can thus be predicted without any distortion.

The compressor performance curve shown in this section consists of average mass flow rate, average pressure ratio, average temperature ratio and average efficiency. The modified surrogate model, showed improved estimation of characteristic curve for not only the three data sets used to calibrate the baseline model (viz. zigzag arrangement, linear arrangement and half annulus arrangement) but also for the random arrangement and sinusoidal arrangement (which were used as validation cases). It should be noted that the value of α, β, κ and δ will be unique to operating speed and type of compressor.

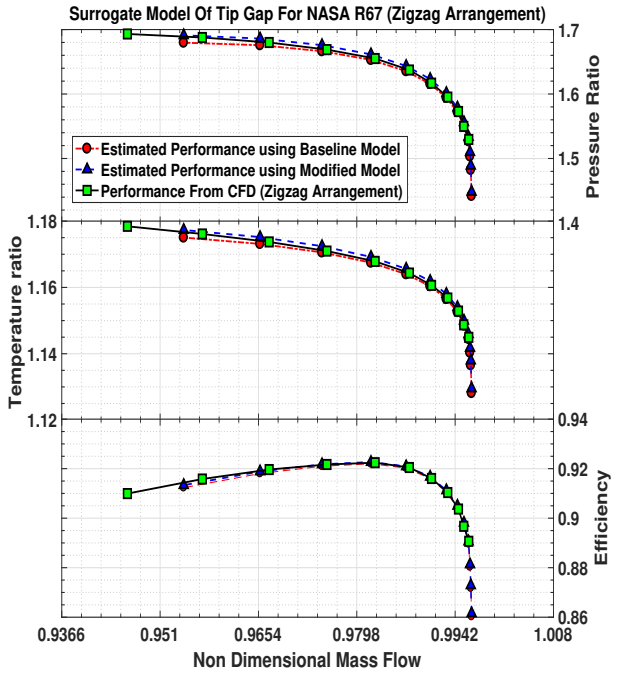


(A) Comparison Of Baseline Model, Modified Model And Full Annulus CFD Simulation For Sinusoidal Arrangement

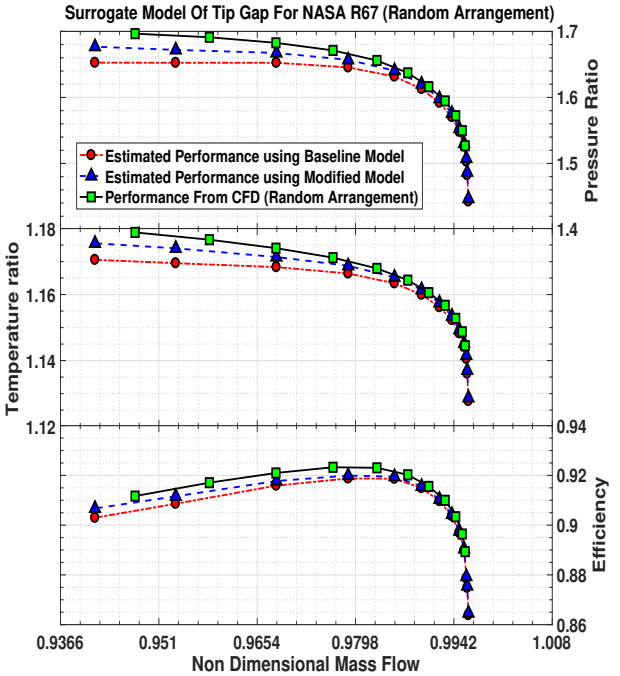


(B) Comparison Of Baseline Model, Modified Model And Full Annulus CFD Simulation For Linear Arrangement

Figure 6.12: Comparison Of Surrogate Models For Tip Gap Variation (NASA Rotor 67) At 100% Speed In Case Of Sinusoidal Arrangement And Linear Arrangement

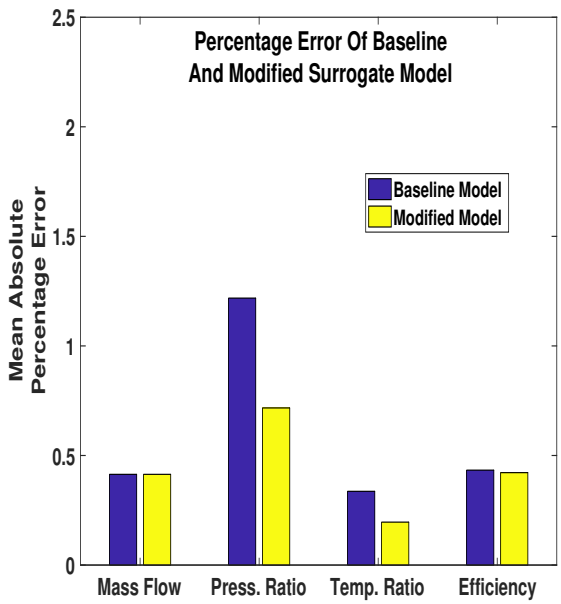


(A) Comparison Of Baseline Model, Modified Model And Full Annulus CFD Simulation For Zigzag Arrangement

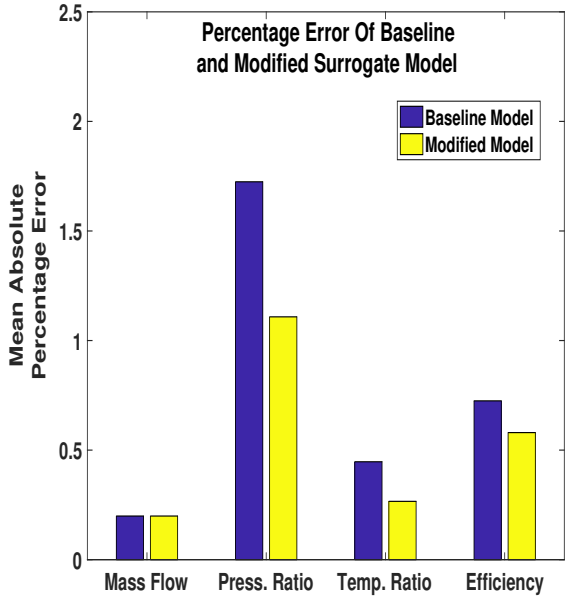


(B) Comparison Of Baseline Model, Modified Model And Full Annulus CFD Simulation For Random Arrangement

Figure 6.13: Surrogate Model For Tip Gap Variation (NASA Rotor 67) At 100% Speed In Case Of Zigzag Arrangement And Random Arrangement



(A) Mean Absolute Percentage Error Of Baseline Model And Modified Model For Zigzag Arrangement



(B) Mean Absolute Percentage Error Of Baseline Model And Modified Model For Random Arrangement

Figure 6.14: Mean Absolute Percentage Error (MAPE) Of Surrogate Models With Respect To Full Annulus CFD Simulation For Tip Gap Variation (NASA Rotor 67) (A) Zigzag Arrangement (B) Random Arrangement

Fig. 6.12(A) and (B) shows the characteristic curve obtained from baseline surrogate model, modified surrogate model and full annulus CFD simulation in case of sinusoidal arrangement and linear arrangement respectively. It can be seen that the performance prediction of the modified surrogate model is better compared to baseline surrogate model. Similar conclusion can be drawn from Fig. 6.13(A) and (B) that shows the characteristic curve obtained from baseline surrogate model, modified surrogate model and full annulus CFD simulation in case of zigzag arrangement and random arrangement respectively. Fig. 6.14(A) and (B) shows the mean absolute percentage error between the two surrogate models with respect to full annulus CFD simulation in case of zigzag arrangement and random arrangement. It can be seen that there is an overall reduction of error in case of modified surrogate model compared to baseline surrogate model for pressure ratio, temperature ratio and efficiency. It must be noted that this surrogate model has been calibrated only for Y axis quantities ($i.e.$ PR_{ave} and TR_{ave}) as shown in fig. 6.10. Thus no difference in percentage error for mass flow rate in the two models has been observed as seen in fig. 6.14(A) and (B). In future, this work can be extended to include

calibration of X axis quantity ($i.e.$ M_{ave}) and improve the overall prediction capability.

As discussed previously, the impact of differing tip gaps spans more adjacent blades compared to the case with differing mis-stagger. The accuracy of the surrogate model can be further increased by performing various triple passage simulations and using that data in the construction of surrogate model (a triple passage simulation would span more adjacent blades compared to double passage case). However, a correction factor for mass flow rate, pressure ratio, temperature ratio and efficiency would have to be introduced if the number of blades N is not a multiple of 3 (triple passage). Having proved the efficacy of surrogate models for both stagger angle and tip gaps, the next step entails performing uncertainty quantification before which we will discuss the limitations of the surrogate model.

6.4 Limitations Of Surrogate Model

As discussed previously, a CFD simulation of a compressor is useful when determining the flow physics along with the compressor characteristics and radial profiles of QoI. When dealing with combinatorial optimisation of compressor blade arrangement, there are a total of (N-1)! possible arrangements where 'N' is the number of blades in a compressor. Carrying out CFD simulation of all these combinations just to calculate the compressor performance would be a colossal waste of resources. Under such circumstances, it imperative that a surrogate model is used for further analysis. However, the prediction from the surrogate model would only be as good as the data being used to build it. In this section, we list the short comings of the present surrogate model.

As discussed in previous section, all the single passage and double passage rotor simulations are carried out by incrementally closing the nozzle area in fixed steps. These fixed steps in which a nozzle is closed, remains the same for all the simulations (including the full annulus CFD simulation) at a particular speed. Since the nozzle area is reduced (closed) in fixed discrete steps, the performance characteristics of the compressor is represented by a locus of points instead of a continuous curve. Any further reduction of the nozzle area after the stalling mass

flow rate results in drop of pressure ratio and the slope of performance curve turning positive thus depicting the stalling of the compressor.

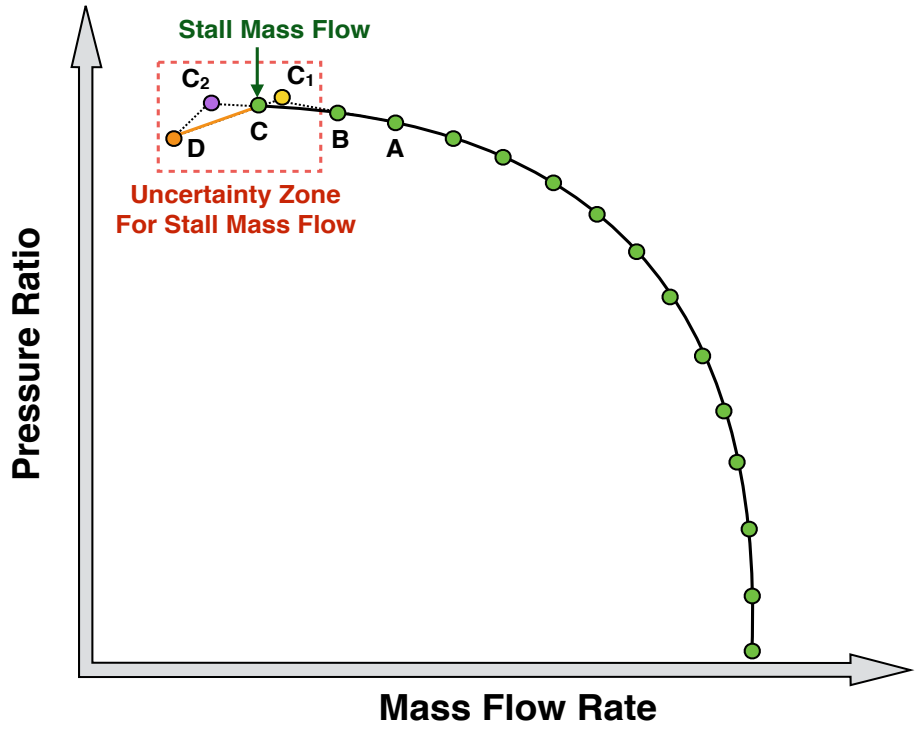
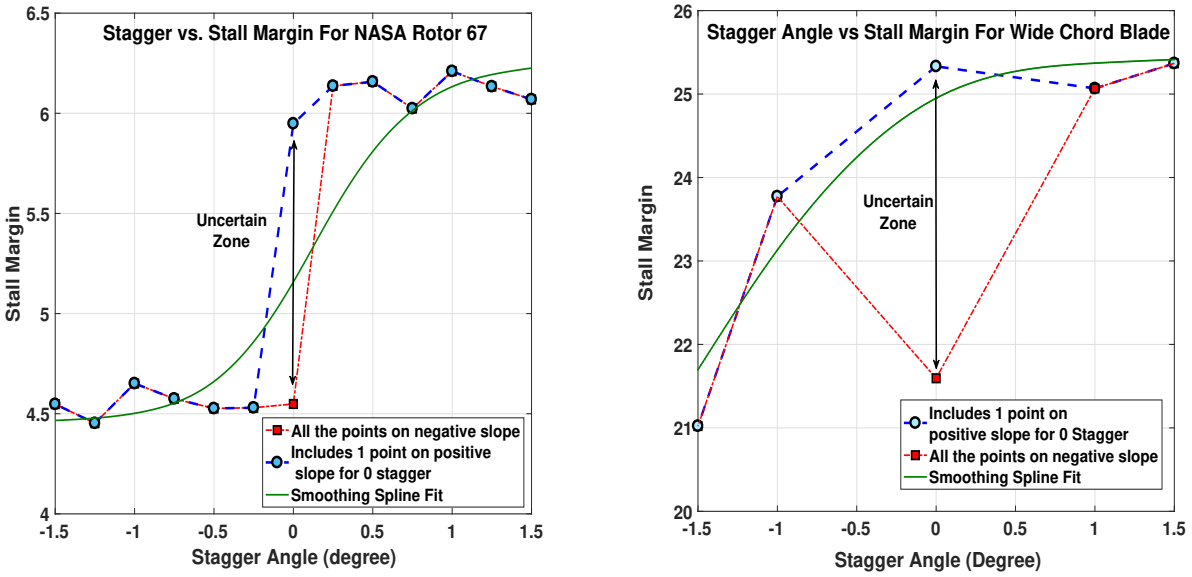


Figure 6.15: Schematic Depicting The Uncertainty In Stall Mass Flow Rate

As shown in fig. 6.15, let the last stable point be represented by C and the stall point by D. Also, let A and B represent the two preceding points before the last stable point C. As can be seen in fig. 6.15, there is a zone of uncertain stall mass flow rate. This arises due to the discrete nature of the nozzle area closure. It is quite possible that point C is already on the positive slope and the true stall mass flow rate is represented by point C_1 which follows the slope of line AB. Conversely, it is also possible that the true stall mass flow rate is represented by point C_2 which follow the slope of line BC.

In fig. 4.7 shown in Chapter 4, the last point in the performance curve of single passage 0% stagger change in wide chord blade is on the positive slope and hence ignored when computing the stability limits. Any further throttling of compressor beyond this point results in drastic loss of pressure ratio and mass flow rate (*i.e.* the compressor stalls). Including the last stable point (on the positive slope) in the characteristic curve would give a slightly higher stall margin (due to gain in mass flow rate). Similar behaviour is observed in case of NASA Rotor 67 where



(A) Stagger vs. SM For NASA Rotor 67 (B) Stagger vs. SM For Wide Chord Blade

Figure 6.16: Variation Of Stall Margin With Change In Stagger Angle For NASA Rotor 67 And Wide Chord Blade At Respective Design Speed

there is a gain of stall margin if the last stable point (on the positive slope) is included in the SM calculation. This is clearly seen in fig. 6.16(A) and (B) which shows the uncertain zone of SM as observed in case of NASA Rotor 67 and wide chord blade respectively.

The stall margin calculation as given in equation 4.3 requires selecting a reference pressure ratio and reference mass flow rate. In fig. 6.16(A) and (B), the reference pressure ratio and reference mass flow rate for the different staggered blades are taken at their respective maximum efficiency points. It can be seen that for the more open blades (positive staggered), the stall margin is higher and for the blades that are negatively staggered, the stall margin is lower. This uncertainty zone can be reduced by changing the nozzle area in very small steps; however this would lead to an increase in computational cost. In the present thesis, this uncertainty in stall margin is assumed to propagate equally for different arrangements (*i.e.* any extra gain or loss of SM would be the same for different arrangements) and hence neglected. The points on the positive slope have been neglected when plotting the performance curve (except in fig. 4.7 which was used as an example to show the zone of uncertainty in SM). This section is an important prelude to the discussion on uncertainty quantification of SM in the next section.

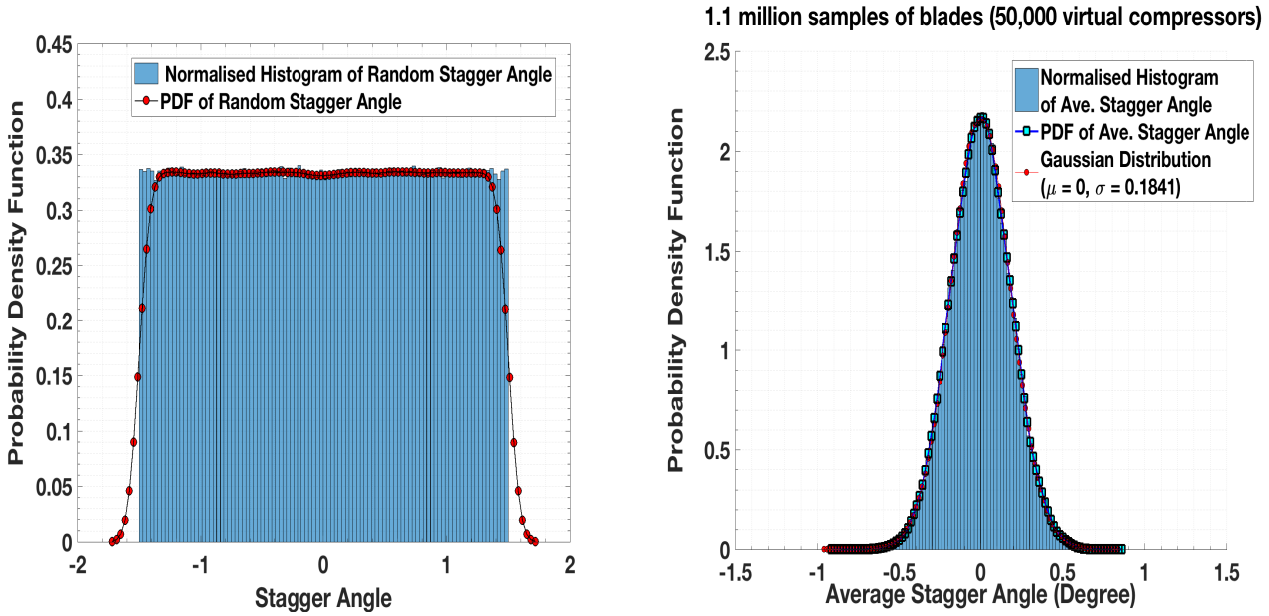
6.5 Uncertainty Quantification

Uncertainty Quantification (UQ) of the compressor performance is carried out by creating virtual samples of different possible arrangements and using surrogate models to create characteristic performance curves for each one of those virtual samples.

As was shown in fig. 4.9, the uniform distribution represents the design space much better compared to Gaussian distribution which is concentrated towards the mean within a closed interval [a,b]. Moreover, a uniform distribution is known to be the maximum entropy distribution (Park and Bera, 2009) for a closed interval [a,b] and hence chosen as a representative distribution of the manufacturing tolerance in the present study. The next sections would discuss the UQ being performed for stagger angle and tip gap respectively. 50,000 virtual compressor samples each consisting of 22 blades (total 1.1 million blades) were generated as a representative of manufacturing tolerance undergone by NASA rotor 67. Similarly, 50,000 virtual compressor samples each consisting of 18 blades (total of 900,000 blades) were generated as a representative of manufacturing tolerance undergone by wide chord blade.

6.5.1 UQ For Stagger Angle Variation

Fig. 6.17(A) shows the probability density function of stagger angle distribution in NASA Rotor 67. As discussed earlier, it can be seen that these blades are uniformly distributed. Furthermore, fig. 6.17(B) shows the probability density function of average stagger angle. It can be seen that the average stagger angle follows a Gaussian distribution (as a result of central limit theorem). The surrogate model was used to compute the performance curves for each of these 50,000 virtual compressor samples undergoing sinusoidal arrangement, linear arrangement, random arrangement and zigzag arrangement. Various statistical analysis can be subsequently performed from the resulting data.



(A) Probability Density Function Of Stagger Angle Distribution

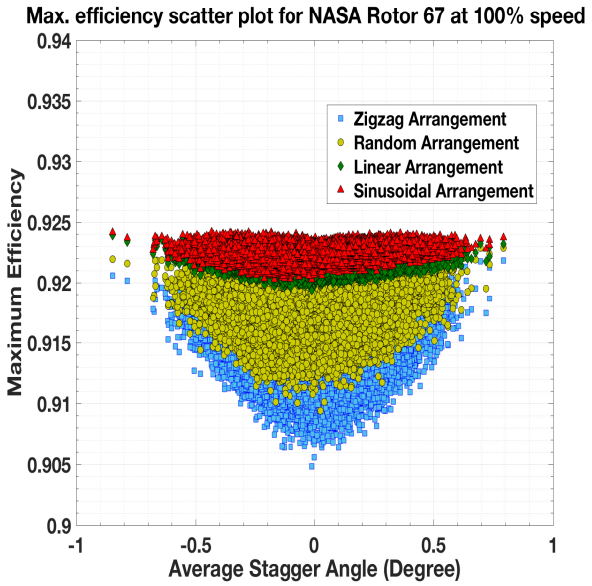
(B) Probability Density Function Of Average Stagger Angle Of Each Virtual Compressor

Figure 6.17: Manufacturing Tolerance Of Stagger Angle Variation For Nasa Rotor 67

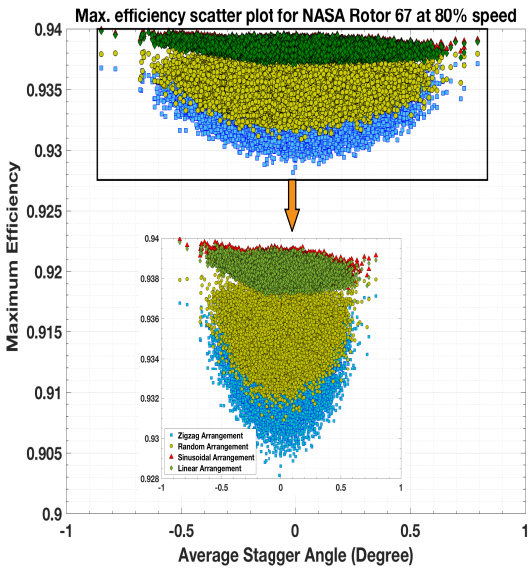
6.5.1.1 Uncertainty In Maximum Efficiency

Fig. 6.18 shows the effect of maximum efficiency for NASA Rotor 67 with respect to different arrangements and different speeds. Two main observations can be drawn from fig. 6.18(A) and (B) viz. (1) Sinusoidal and Linear arrangements give the 'highest' maximum efficiency while zigzag arrangement gives the 'lowest' maximum efficiency. This is because the cumulative mis-stagger is the least in sinusoidal and linear arrangement while it is the highest in zigzag arrangement. It can also be seen that the variation in maximum efficiency in case of sinusoidal and linear arrangement is almost negligible while the variation in random and zigzag arrangement is spread over a larger region. (2) As the speed reduces, the maximum efficiency increases for all the arrangements. This is expected as the shock losses decreases with reduction in speed proportional to $(M-1)^3$ and can be seen in the experimental data for different part speed conditions in fig. 6.19.

It is important to note that the maximum efficiency for part-speed condition being discussed here does not correspond to the maximum efficiency obtained on the working line of compressor; it is the actual maximum efficiency on the performance curve. From fig. 6.20 it can be seen



(A) Max. Efficiency vs. Ave. Stagger Angle At 100% Speed For NASA Rotor 67



(B) Max. Efficiency vs. Ave. Stagger Angle At 80% Speed For NASA Rotor 67

Figure 6.18: Variation Of Maximum Efficiency With Respect To Different Arrangements Of Stagger Angle At Different Speed For Nasa Rotor 67

that the experimental data for 80% speed does not cover all the points from choke to stall. The author has not conducted any CFD study related to differing tip gaps at part-speed condition and hence the uncertainty band for the CFD data was not plotted as was done in fig. 3.16 for design speed.

Fig. 6.21(A) shows the probability density function (PDF) of maximum efficiency for different arrangements at 100% speed. The peak of PDF represents the most probable value of maximum efficiency for each of the arrangement. It can be seen that for zigzag arrangement, the most probable value of maximum efficiency is around 91.45% while for sinusoidal arrangement, the most probable value of maximum efficiency is 92.2%. The standard deviation of maximum efficiency in case of zigzag arrangement is 0.2082% while in case of a sinusoidal arrangement it is 0.048%. This shows that the deviation of maximum efficiency for a sinusoidal arrangement is very less compared to a zigzag arrangement. Fig. 6.21(B) shows the reliability function of the maximum efficiency for different arrangements at 100% speed. From this figure, we can calculate the probability that a certain value would exceed a given number. It can be seen that there is 40% probability that the maximum efficiency will exceed 91.45% in a zigzag arrangement. For a sinusoidal arrangement, there is 40% probability that the maximum efficiency would

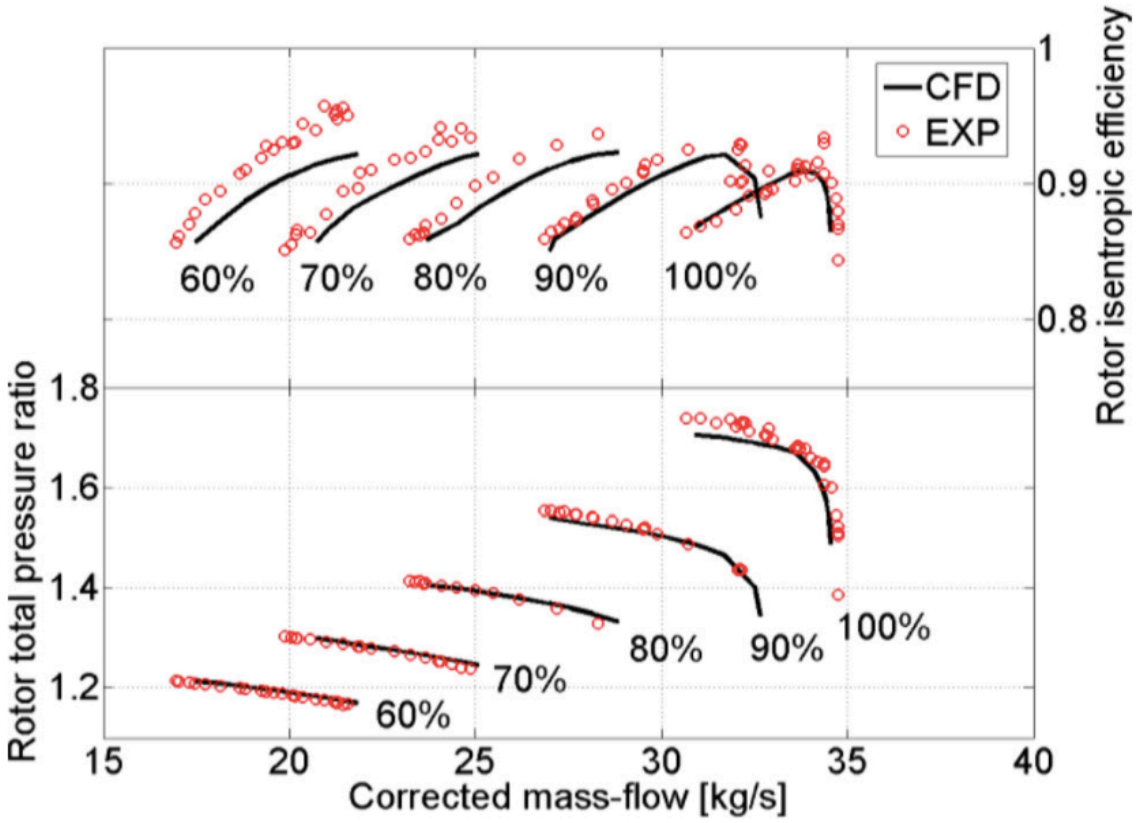


Figure 6.19: Operating Map For NASA Rotor 67 Adapted From Fidalgo et al. (2012)

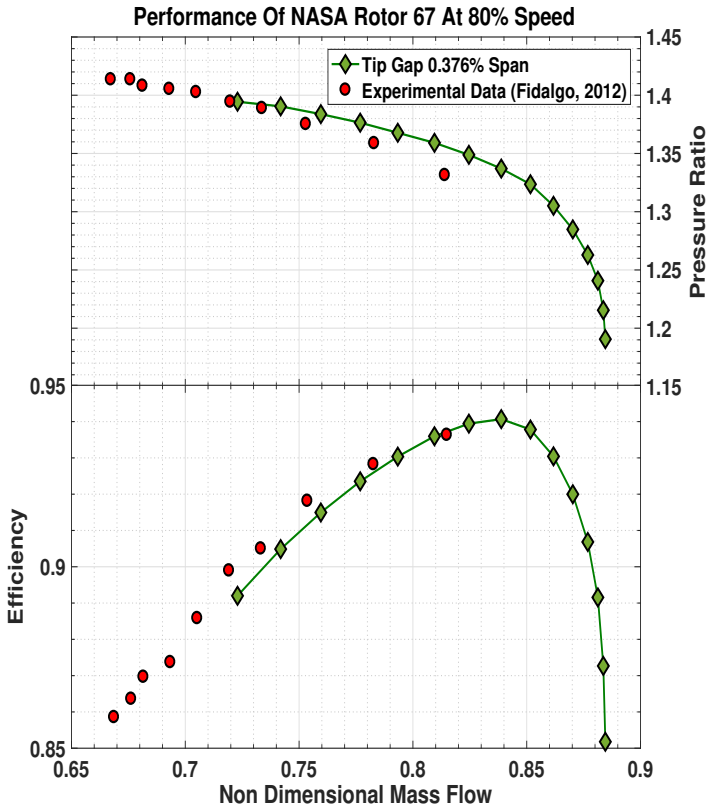
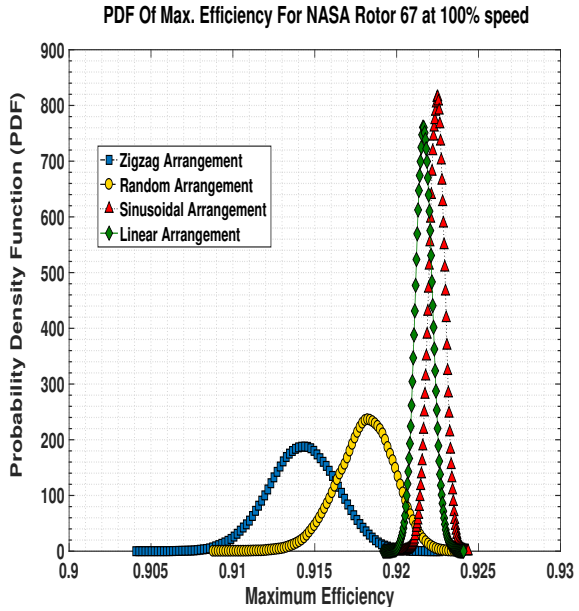
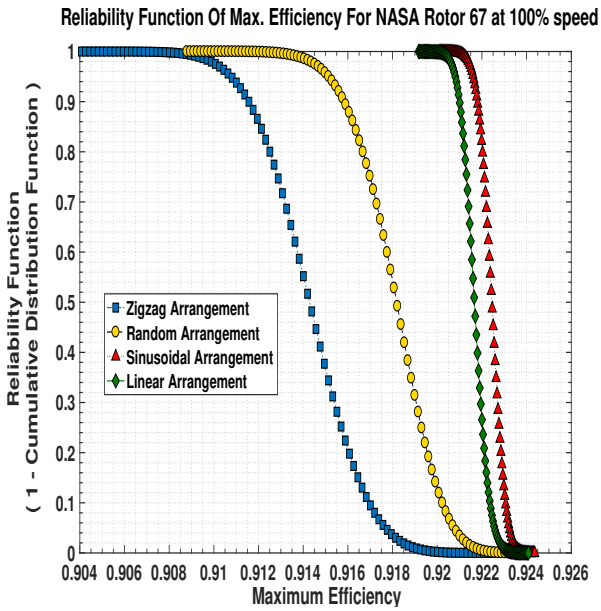


Figure 6.20: Experimental Validation At 80% Speed For NASA Rotor 67



(A) Probability Density Function Of Maximum Efficiency At 100% Speed For Nasa Rotor 67

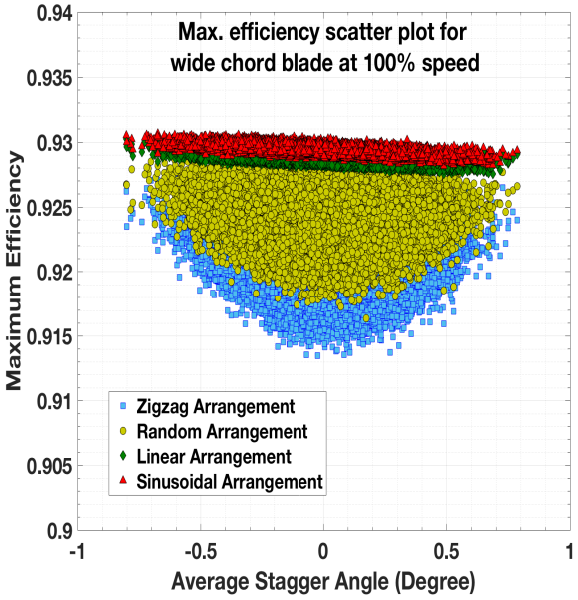


(B) Reliability Function Of Maximum Efficiency At 100% Speed For Nasa Rotor 67

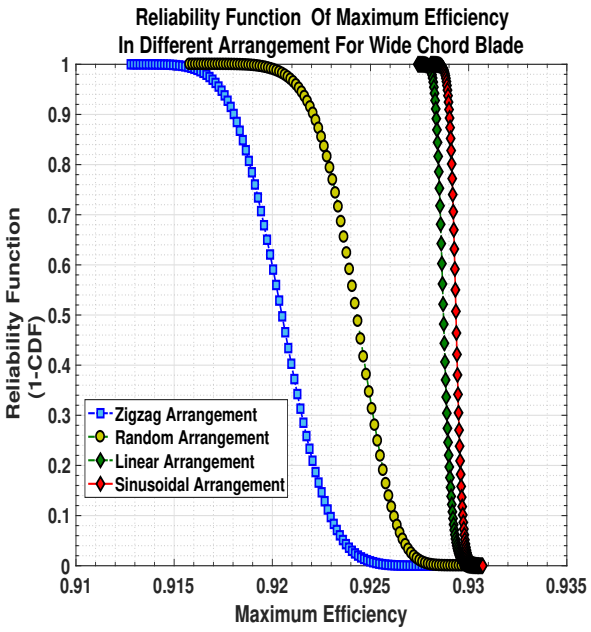
Figure 6.21: Probability Density Function And Reliability Function Of Maximum Efficiency With Respect To Different Arrangements Of Stagger Angle At 100% Speed For Nasa Rotor 67

exceed 92.25% (for the same probability, the difference between maximum efficiency predicted by sinusoidal arrangement and zigzag arrangement is almost 0.8%). Similar conclusions can be drawn for other parameters of interest.

Fig. 6.22(A) shows the scatter plot of maximum efficiency with respect to average stagger angle in case of wide chord blade undergoing different arrangements of random staggered blades. Similar to fig. 6.18 (A) and (B), it can be seen that sinusoidal arrangement performs the best while zigzag arrangement exhibits the worst performance. It can also be seen that at design speed, the wide chord blade has better efficiency compared to NASA Rotor 67 for all the arrangements. Similar to fig. 6.21(B), fig. 6.22(B) shows the reliability function of maximum efficiency for different arrangements at design speed for wide chord blade. Such a plot enables the engineers to calculate the probability that certain value would exceed a given number. As can be seen, there is 40% probability that the maximum efficiency would exceed 92.1% for zigzag arrangement. For sinusoidal arrangement, there is a 40% probability that the maximum efficiency would exceed 92.9% (there is a difference of 0.8% between the maximum efficiency for zigzag arrangement and sinusoidal arrangement at same probability level).



(A) Max. Efficiency vs. Ave. Stagger Angle At 100% Speed For Wide Chord Blade



(B) Reliability Function Of Maximum Efficiency At 100% Speed Wide Chord Blade

Figure 6.22: (A) Scatter Plot Of Maximum Efficiency With Respect To Angle Stagger Angle For Wide Chord Blade (B) Reliability Function Of Maximum Efficiency With Respect To Different Arrangements Of Stagger Angle At Design Speed For Wide Chord Blade

6.5.1.2 Uncertainty In Stability Margin

Fig. 6.23 shows a 3 dimensional joint probability distribution (joint PDF) of average stagger angle and stall margin in case of NASA Rotor 67 undergoing sinusoidal arrangement. This joint PDF in fig. 6.23 has been shown in 4 different views for the ease of visualising various peaks and identifying the hot-spot regions (most probable values of QoI). The 3 axes in the figure are (i) X : Average Stagger Angle (ii) Y : Stall Margin (iii) Z : Probability Density. The 4 views of joint PDF are : (A) XYZ Isometric view (B) YZ Plane (C) XY Plane (D) XZ Plane. It has to be noted that fig. 6.23(B) and (D) do not represent marginal PDF. Similarly, fig. 6.24 shows the joint probability distribution of average stagger angle and stall margin in case of NASA Rotor 67 undergoing zigzag arrangement in 4 different views : (A) XYZ Isometric view (B) YZ Plane (C) XY Plane (D) XZ Plane. It can be seen that both sinusoidal arrangement as well as zigzag arrangement exhibit the same kind of behaviour with 2 distinct peaks for stall margin at 4.5 and 6.1 respectively. This behaviour is similar to the behaviour exhibited by single passage stall margin vs. stagger angle plot for NASA Rotor 67 (at design speed) shown in fig. 6.16(A)

wherein a similar jump in the stall margin was observed at 0° stagger baseline case. This jump is due to insufficient refinement near the stall region while building the surrogate model as discussed in the section model limitation.

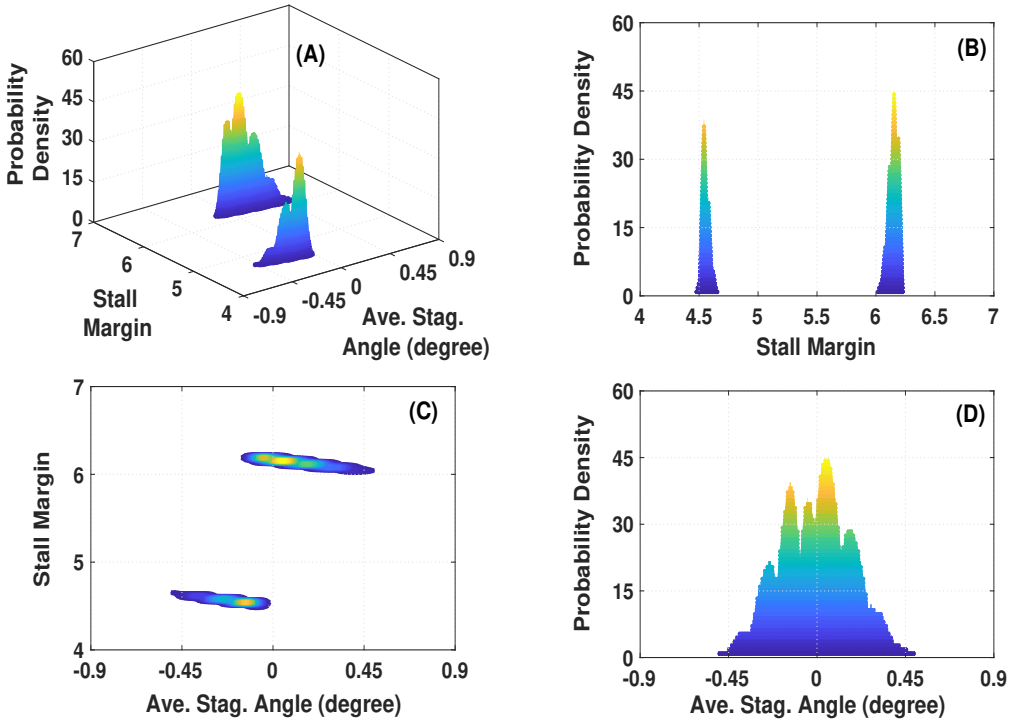


Figure 6.23: Joint PDF (Z Axis) For Average Stagger Angle (X Axis) And Stall Margin (Y Axis) : Sinusoidal Arrangement Of Blades With Differing Stagger Angle In Case Of NASA Rotor 67 At Design Speed Visualised In (A) XYZ Isometric view (B) YZ Plane (C) XY Plane (D) XZ Plane.

It has to be noted that higher value of the peak implies a higher probability of the particular value occurring. Thus it can be seen from fig. 6.23(B) and fig. 6.24(B) that the zigzag arrangement tends to have a slightly higher probability than sinusoidal arrangement in terms of having a higher SM. One reason for this could be a possible modelling error as the level of uncertainty is very small. Another reason could be a manifestation of the behaviour seen in case of blades with different tip gaps as well as damaged blades. It was seen that when blade with lowest SM is sandwiched between two blades of highest SM, the resulting arrangement gave a higher stability limit compared to sinusoidal arrangement. Hence, the zigzag arrangement of random staggered blades possibly give a slightly higher SM compared to a sinusoidal arrangement.

Similar figures have been plotted for wide chord blade at design speed. Fig. 6.25 shows the joint probability distribution of average stagger angle and stall margin in case of wide chord blade

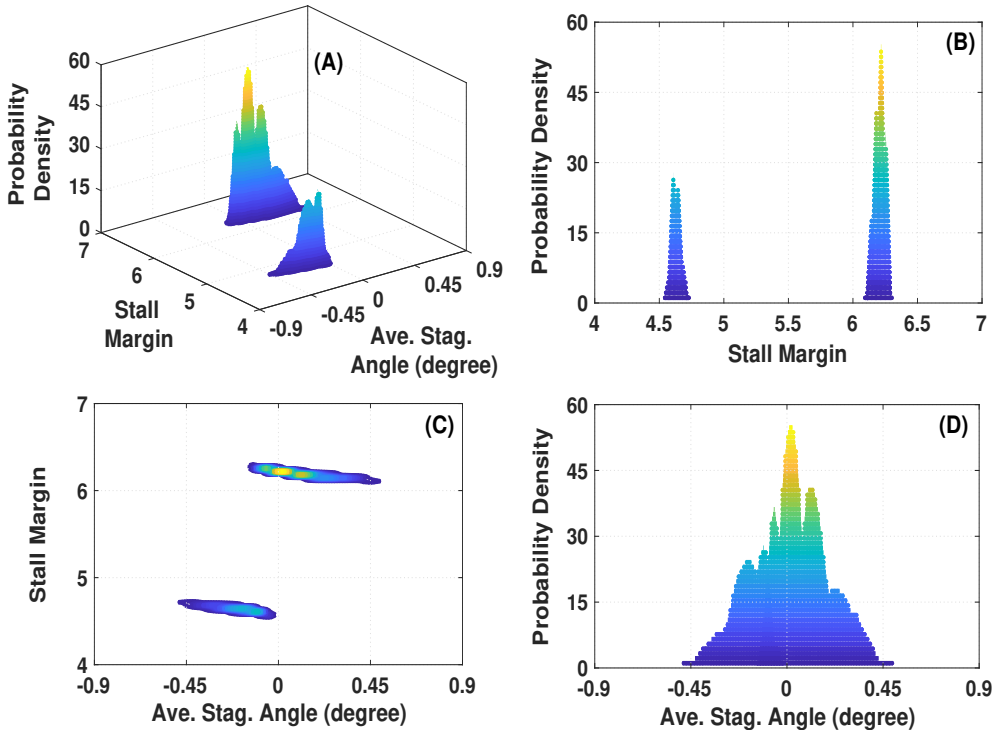


Figure 6.24: Joint PDF (Z Axis) For Average Stagger Angle (X Axis) And Stall Margin (Y Axis) : Zigzag Arrangement Of Blades With Differing Stagger Angle In Case Of NASA Rotor 67 At Design Speed Visualised In (A) XYZ Isometric view (B) YZ Plane (C) XY Plane (D) XZ Plane.

undergoing sinusoidal arrangement. Like the previous case, the joint PDF in fig. 6.25 has been shown in 4 different views for the ease of visualising various peaks and identifying the hot-spot regions (most probable values of QoI). The 3 axes in the figure are (i) X : Average Stagger Angle (ii) Y : Stall Margin (iii) Z : Probability Density. The 4 views of joint PDF are : (A) XYZ Isometric view (B) YZ Plane (C) XY Plane (D) XZ Plane. Similarly, fig. 6.26 shows the joint probability distribution of average stagger angle and stall margin in case of wide chord blade undergoing zigzag arrangement in 4 different views : (A) XYZ Isometric view (B) YZ Plane (C) XY Plane (D) XZ Plane. The behaviour is different compared to previous case of NASA Rotor 67. It can be seen that the probability density is high in case of sinusoidal arrangement compared to Zigzag arrangement as seen in fig. 6.25(A) and fig. 6.26(A) respectively. As the area under joint PDF is equal to 1, a higher spread of the data points will result in lower probability density. The spread of points for sinusoidal arrangement as shown in fig. 6.25(C) is narrower compared to zigzag arrangement shown in fig. 6.26(C) and hence a higher probability density.

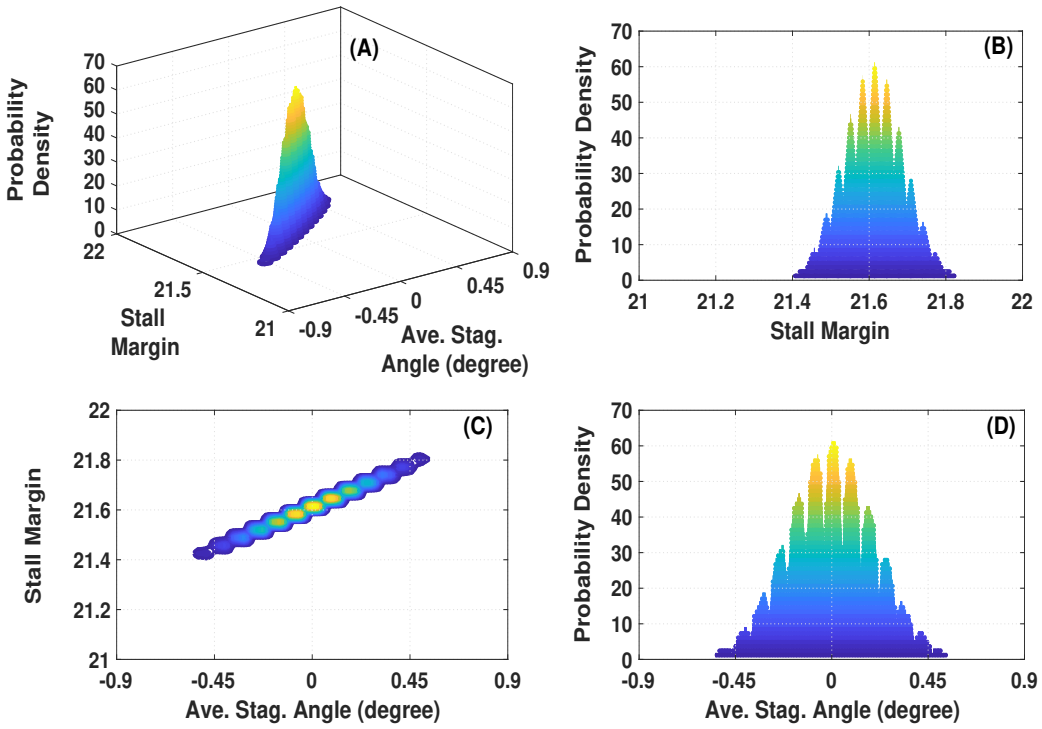


Figure 6.25: Joint PDF (Z Axis) For Average Stagger Angle (X Axis) And Stall Margin (Y Axis) : Sinusoidal Arrangement Of Blades With Differing Stagger Angle In Case Of Wide Chord Blade At Design Speed Visualised In (A) XYZ Isometric view (B) YZ Plane (C) XY Plane (D) XZ Plane.

Also, unlike the previous case of NASA Rotor 67 wherein a jump in SM was observed at 0° average stagger for sinusoidal arrangement (shown in fig. 6.23) and zigzag arrangement (shown in fig. 6.24), the variation of SM for wide chord blade is almost linear for both sinusoidal arrangement as well as zigzag arrangement as seen in fig. 6.25 and fig. 6.26 respectively.

A probable reason for this behaviour is that for NASA Rotor 67, a lot of interpolation points were considered in the nearby vicinity of 0° stagger baseline case as shown in fig. 6.16(A); whereas for a wide chord blade, the interpolation points were fewer and further away from the baseline case as seen in fig. 6.16(B). This resulted in SM of different arrangements in wide chord blade being dictated primarily by the SM of 0° stagger baseline case. In case of wide chord blade, the most likely value of SM for zigzag arrangement is 21.72 while for sinusoidal arrangement the most like value of SM is 21.62. This result is similar to the previous case of NASA Rotor 67 wherein zigzag arrangement showed a propensity for higher stall stall margin compared to sinusoidal arrangement.

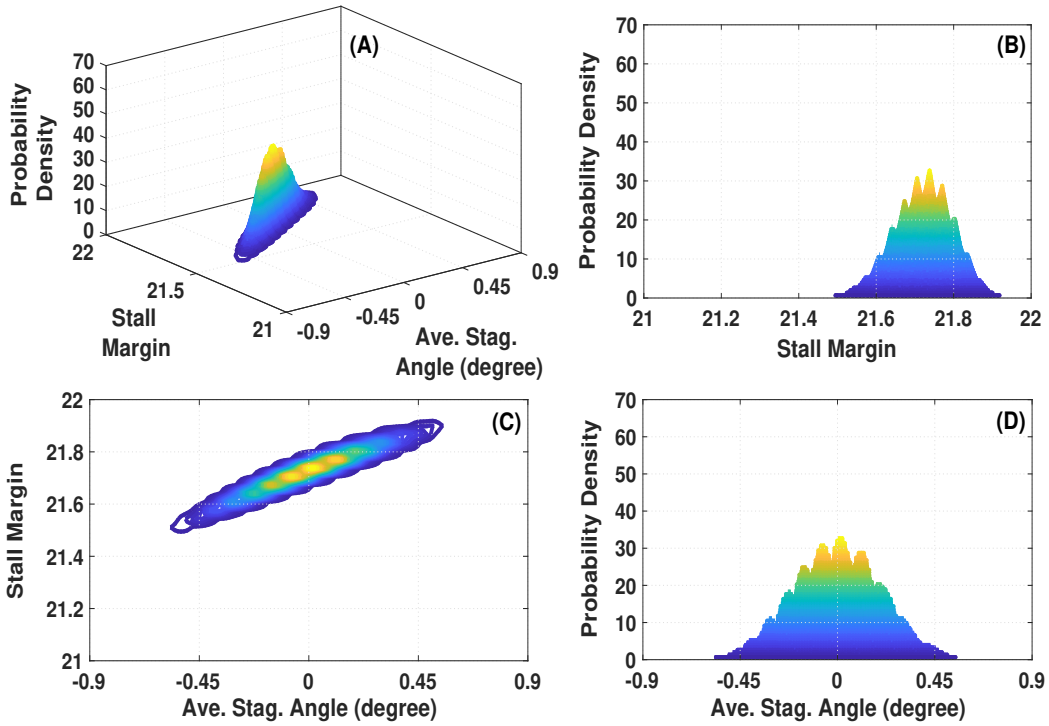


Figure 6.26: Joint PDF (Z Axis) For Average Stagger Angle (X Axis) And Stall Margin (Y Axis) : Zigzag Arrangement Of Blades With Differing Stagger Angle In Case Of Wide Chord Blade At Design Speed Visualised In (A) XYZ Isometric view (B) YZ Plane (C) XY Plane (D) XZ Plane.

The number of interpolation points were chosen based on the convergence with respect to deterministic CFD characteristic curve. It has to be noted NASA Rotor 67 having blades of differing stagger angle had an overall average stagger angle of 0.29° as shown in fig. 4.12. In case of wide chord blade, the overall average stagger angle was 0.11° as shown in fig. 4.14. Of the two rotor blades, the wide chord blade was more close to baseline case of 0° stagger angle and hence required lesser number of interpolation points to predict a deterministic CFD characteristic curve.

6.5.2 UQ for tip gap variation

Similar to previous section 50,000 virtual compressors samples each consisting of 22 blades of NASA rotor 67 are generated (total 1.1 million blades) having uniformly distributed random tip gaps. As said earlier, the tip gap variations are discrete random variables as opposed to stagger angle variations that are continuous random variables. Fig. 6.27 depicts the histogram

of average tip gap in the 50,000 virtual compressors that were generated. It can be seen that similar to stagger angle variation, the average tip gap also follows Gaussian distribution as a result of central limit theorem. Most of the realisations in fig. 6.27 are concentrated towards average tip gap of 0.9 mm (0.564% span) as this is the most probable value for a uniform random variable varying between the limits 0.3 mm and 1.5 mm.

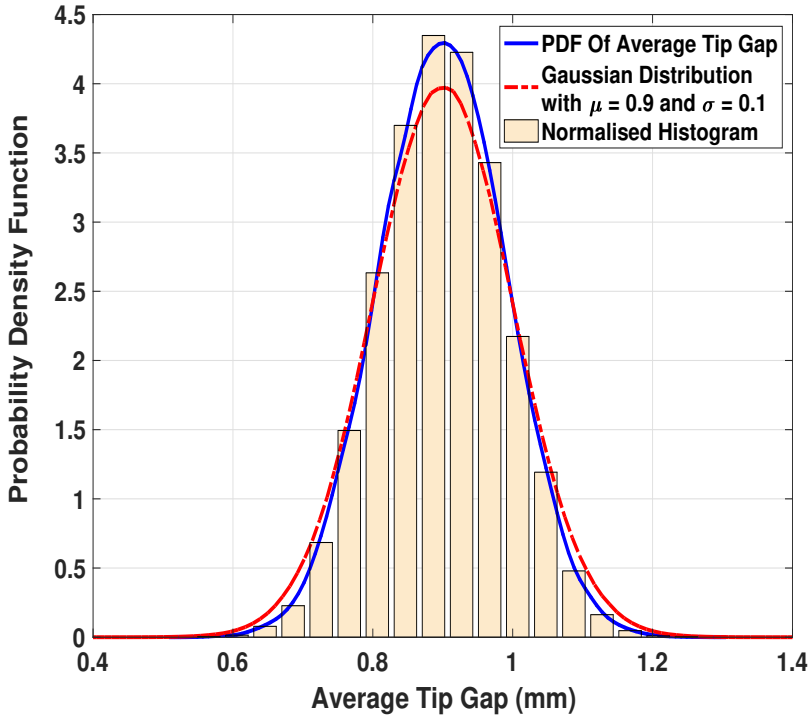


Figure 6.27: Normalised Histogram Of Random Tip Gaps

6.5.2.1 Uncertainty In Maximum Efficiency

The surrogate model was used to compute the performance curves for each of these 50,000 virtual compressor samples undergoing sinusoidal arrangement, linear arrangement, random arrangement and zigzag arrangement. Fig. 6.28 shows the scatter plot of maximum efficiency vs average tip gap for different arrangements at 100% speed for NASA Rotor 67. It can be seen that zigzag arrangement has the 'highest maximum' efficiency and sinusoidal arrangement has the 'lowest' maximum efficiency. There are very less number of realisations at the extremities due to the fact that average tip gap has a Gaussian distribution as seen in fig. 6.27. It can also be observed that as the average tip gap reduces, the maximum efficiency in all the arrangements starts increasing.

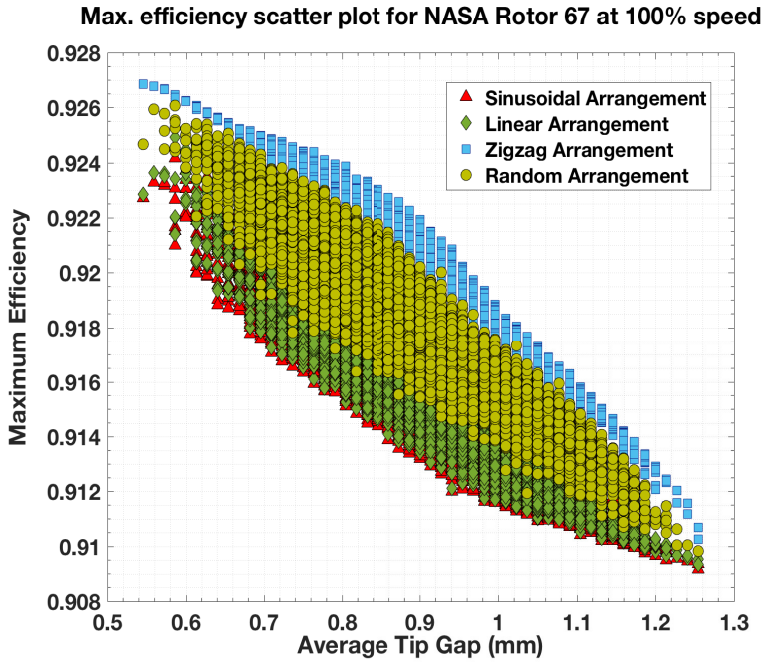
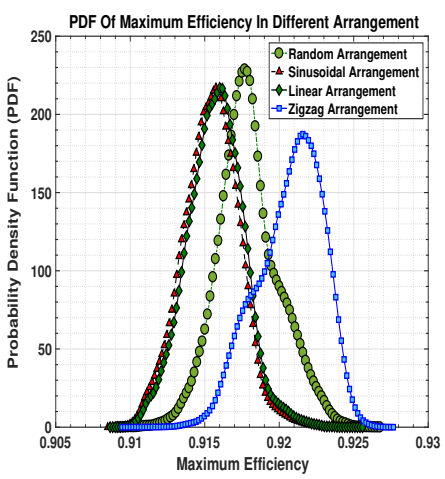
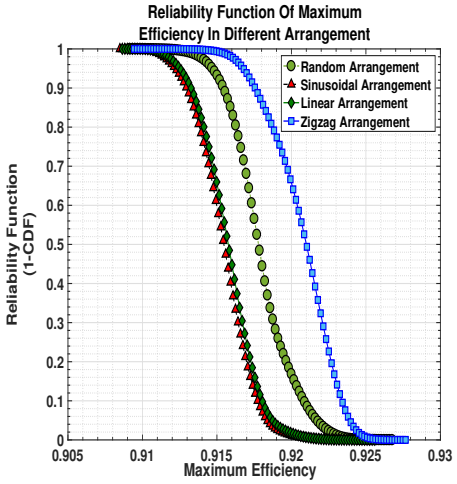


Figure 6.28: Scatter Plot Of Maximum Efficiency Vs Average Tip Gap For NASA Rotor 67 At 100% Speed



(A) Probability Density Function Of Maximum Efficiency At 100% Speed



(B) Reliability Function Of Maximum Efficiency At 100% Speed

Figure 6.29: Probability Density Function And Reliability Function Of Maximum Efficiency With Respect To Different Arrangements Of Tip Gaps At 100% Speed For NASA Rotor 67

Fig. 6.29(A) shows the PDF of maximum efficiency for different arrangements at 100% speed. It can be seen that for zigzag arrangement, the most probable value of maximum efficiency is 92.2% while for sinusoidal arrangement and linear arrangement, the most probable value of maximum efficiency is 91.6%. Fig. 6.29(B) shows the reliability function of the maximum efficiency for different arrangements at 100% speed. It can be seen that there is a 20% probability that

the maximum efficiency will exceed 91.7% in a sinusoidal arrangement while in case of zigzag arrangement, the probability that the maximum efficiency will exceed 91.7% is almost 92%. Such analyses will be able to give the researchers an insight into probable values of maximum efficiency, maximum pressure ratio, maximum temperature ratio, etc and thus help in robust predictive analysis.

6.5.2.2 Uncertainty In Stall Margin

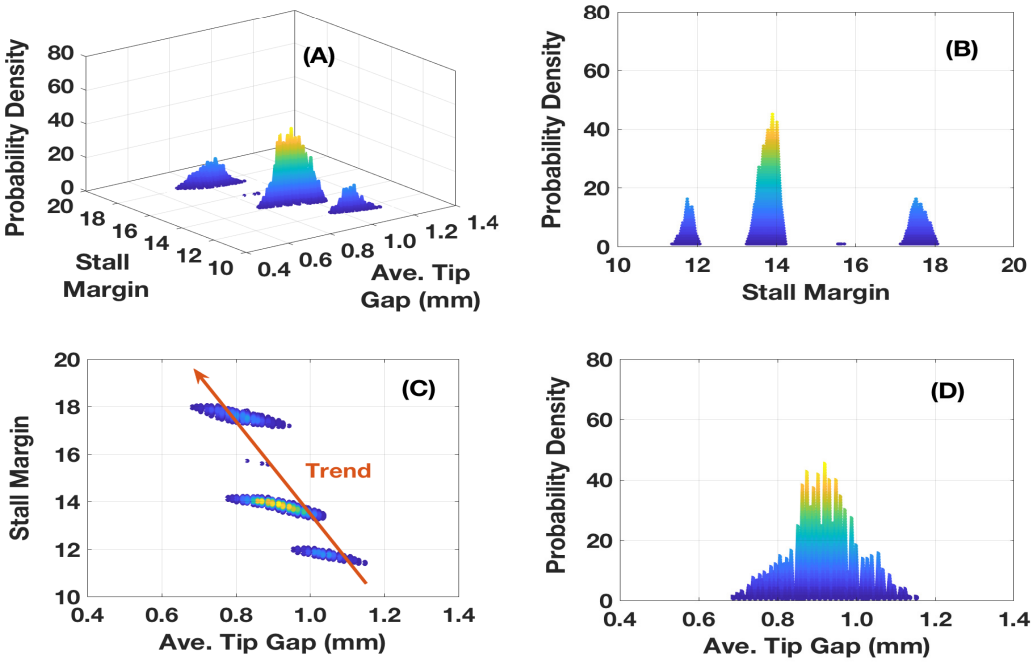


Figure 6.30: Joint PDF (Z Axis) For Average Tip Gap (X Axis) And Stall Margin (Y Axis) : Zigzag Arrangement Of Blades With Differing Stagger Angle In Case Of NASA Rotor 67 At Design Speed Visualised In (A) XYZ Isometric view (B) YZ Plane (C) XY Plane (D) XZ Plane.

It was seen in Chapter 4, that different arrangements of random tip gaps stall at different mass flow rate. It was observed that the first to stall was sinusoidal arrangement while the last to stall was zigzag arrangement. In this section we will discuss the stall margin for 50,000 virtual compressor samples having random tip gaps. Fig. 6.30 shows the joint probability density for average tip gap and stall margin in case of zigzag arrangement of random tip gap blades in 4 different views : (A) XYZ Isometric view (B) YZ Plane (C) XY Plane (D) XZ Plane. This allows easy ease of visualisation of various peaks and helps identify the hot-spot regions (most probable values of QoI). It is to be noted that fig. 6.30(B) and (D) do not represent marginal

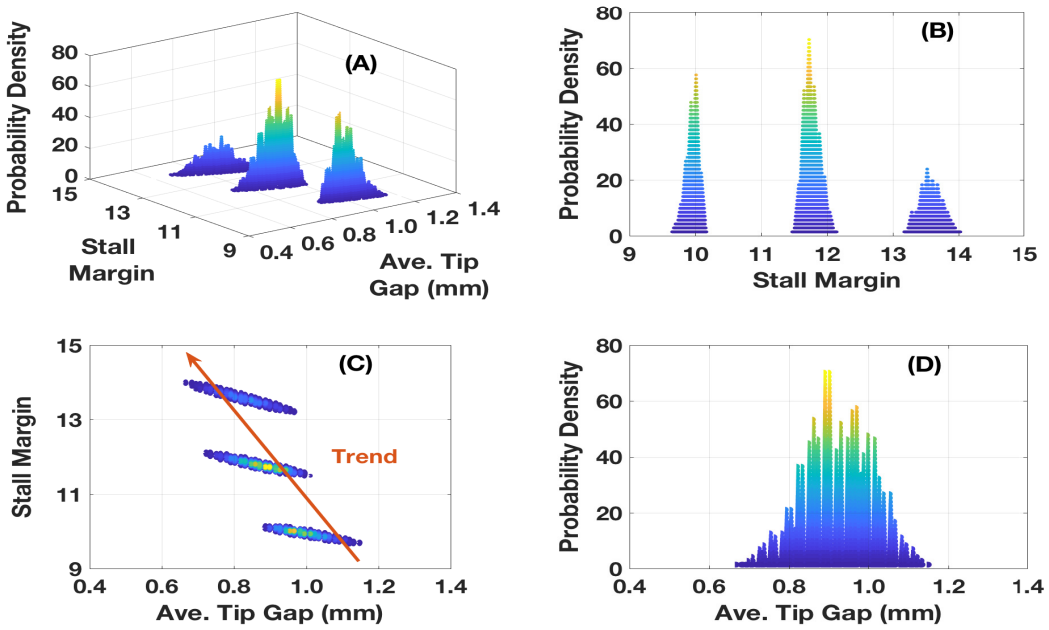


Figure 6.31: Joint PDF (Z Axis) For Average Tip Gap (X Axis) And Stall Margin (Y Axis) : Sinusoidal Arrangement Of Blades With Differing Stagger Angle In Case Of NASA Rotor 67 At Design Speed Visualised In (A) XYZ Isometric view (B) YZ Plane (C) XY Plane (D) XZ Plane.

PDF. Similarly, fig. 6.31 shows the joint PDF for tip gap and stall margin in case of sinusoidal arrangement of random tip gap blades in 4 different views : (A) XYZ Isometric view (B) YZ Plane (C) XY Plane (D) XZ Plane. Various concepts of joint PDF and marginal PDF has been explained lucidly by Vitt (2019)[1]. It can be seen that there are 3 distinct peaks in both fig. 6.30(A) as well as fig. 6.31(A). It can be clearly seen from fig. 6.30(B) that the zigzag arrangement exhibited stall margin with the 3 distinct peaks at 11.9, 14 and 17.5 respectively. In comparison, a sinusoidal arrangement had stall margin with the 3 distinct peaks at 10, 11.7 and 13.5 as shown in fig. 6.31(B). The general trend as shown in fig. 6.30(C) and fig. 6.31(C) is that with decreasing tip gap, the stall margin for both the arrangements increase.

Fig. 6.32 shows the reliability function of stall margin for NASA Rotor 67 having different arrangements of random tip gaps at design speed. It can be seen that there is 20% probability that the stall margin will exceed 17.5 in case of zigzag arrangement. For sinusoidal arrangement, there is 20% probability that the stall margin will exceed 13. Similarly, there is 80% probability that the stall margin will exceed 14 in case of zigzag arrangement while in case

[1] https://www.ed.ac.uk/files/atoms/files/lecture-2-probability-distributions-handout_0.pdf

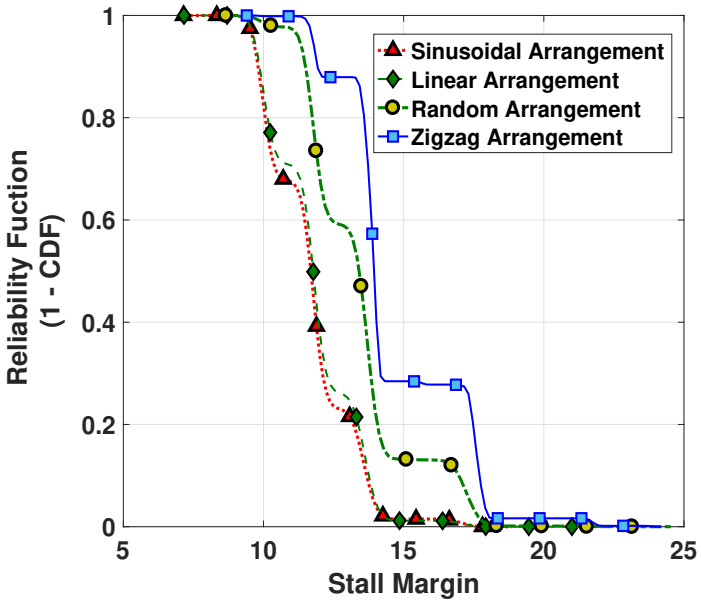


Figure 6.32: Reliability Function Of Stall Margin For NASA Rotor 67 Having Different Arrangements Of Blades With Differing Tip Gaps At 100% Speed

of sinusoidal arrangement there is 80% probability that the stall margin will exceed 10. Thus zigzag arrangement has the best SM compared to all arrangements while sinusoidal has the worst arrangement.

6.6 Chapter Summary

A compressor having 'N' blades of differing dimensions can undergo (N-1)! unique arrangements. Therefore an attempt has been made to predict (reconstruct) the characteristic curve of a compressor undergoing geometric uncertainty with a high degree of confidence using a surrogate model that can replace a full annulus CFD simulation. Stagger angle and tip gap have been chosen as parametric uncertainty. A lower order surrogate model has been built from the first principles wherein the data from the single passage and double passage simulation have been collated and given as an input to it.

In case of surrogate model for stagger angle, the losses due to mis-stagger has been assumed to be independent of the mean stagger angle. As the interpolation points increase, the performance prediction converges to deterministic full annulus CFD solution. The model is found to

be extremely robust as it can predict the performance curves at design speed, part speed as well as for different designs of compressor (NASA Rotor 67 and wide chord blade). For stagger angle variation of NASA Rotor 67, it is found that the maximum probable efficiency in case of sinusoidal arrangement (92.2%) is better than zigzag arrangement (91.45%). Moreover, the standard deviation of maximum efficiency in case of sinusoidal arrangement (0.048%) is almost 4 times lower than zigzag arrangement (0.2082%). This shows that sinusoidal arrangement is more robust in consistently achieving peak efficiency compared to zigzag arrangement. Moreover, NASA Rotor 67 has two distinct stall margin of 4.5 (for average stagger angle less than zero) and 6.2 (for average stagger angle greater than zero). In case of wide chord blade rotor, the stall margin variation was linear which was attributed to the number of interpolation points present in the surrogate model.

The surrogate model for tip gaps has been constructed for tip loaded blades like NASA Rotor 67 that are extremely sensitive to changes to tip gap. The baseline surrogate model for tip gaps does not predict the deterministic full annulus CFD performance curve very well. Hence, some of the parameters in the model is fine tuned by doing a non-linear least square optimisation from the deterministic full annulus CFD simulations. Three performance curves from the deterministic full annulus CFD simulations have been used for this purpose. It is seen that the most probable maximum efficiency in case of zigzag arrangement (92.2%) is much higher than that of sinusoidal arrangement (91.6%). In case of stall margin, there are three distinct peaks that are observed in case of both zigzag arrangement (11.9, 14 and 17.5) as well as sinusoidal arrangement (10,11.7 and 13.5). These three peaks represent the most probable values of stall margin for respective arrangement. It can be seen that zigzag arrangement exhibits an overall better stall margin compared to sinusoidal arrangement.

Chapter 7

Conclusions And Future Work

"Arise, awake, stop not till the goal is reached - Swami Vivekananda"

7.1 Conclusions

This present research discusses the effect of geometric uncertainty due to manufacturing tolerance as well as in-service degradation on the performance and stability boundaries of an axial compressor. This chapter summarises all the main conclusions that have been drawn in the present research. The findings are equally applicable to both aero-engines as well as industrial gas turbines.

(1) **Physical Understanding Of The Behaviour Of Geometric Uncertainties** :

Different geometric uncertainties considered in the present research are stagger angle variation (manufacturing tolerance), tip gap variation (manufacturing tolerance) and leading edge variation (in-service damage). Each of these parameters were randomly varied on all the blades of a compressor unlike majority of the previous researches wherein the effect of these parameters were considered by performing a single passage simulation (*i.e.* all the blades in the compressor undergo same variation).

A series of single passage and double passage CFD simulations have been performed to confirm

the underlying flow phenomenon. It was found that an increase in the mis-stagger between the blades of a compressor has a detrimental effect on the maximum efficiency of the compressor. This was due to one of the passage exhibiting choke condition while the other passage experiences maximum efficiency condition. This observation was valid for NASA Rotor 67 as well as the Wide Chord Rotor Blade. For tip gap variation, it was found that the performance and stability limit reduces as the size of tip gap increases in a single passage CFD simulation. Moreover, an alternate arrangement of blades with small tip gap and large tip gap had better stall margin compared to the half annulus arrangement of blades with small tip gap and large tip gap. In case of alternate arrangement, the blade with smaller tip gap unloads the blade with larger tip gap thereby delaying the onset of stall. This was more crucial for tip loaded rotors like NASA Rotor 67 and 1-Stage IGT than for a part-span loaded, wide chord blade rotor.

There were a few similarities in the behaviour of tip gap variation and leading edge variation (due to in-service damage). Similar to tip gap variation case, the alternate arrangement of undamaged blade and damaged blade had better performance and stability limits than the half annulus arrangement of undamaged blade and damaged blade. It was observed in case of leading edge damage on 1-Stage IGT, that the choked mass flow rate increases for increased levels of damage. This was attributed to the increased throat area of the damaged blades from 65% span (from hub) upwards. Furthermore, it was observed that chord-wise damage is more critical than radial damage. This is because in the 1-stager IGT, majority part of the pressure rise is obtained at the tip of the compressor as seen in fig. 3.6. Thus, the changes in the chord at the tip impacts the Stall Margin more than the changes in radial extent of the damage.

In addition, NASA Rotor 67 was also subject to simultaneous variation of stagger angle and tip gaps. For such cases, it was found that the baseline double passage case of mixed tip gaps exhibited two possibilities :

(A) Large Tip gap Open and Small Tip gap Closed (LTO-STC)
(B) Small Tip gap Open and Large Tip gap Closed (STO-LTC)

For small mis-stagger between the blades having differing tip gap, it was observed that case

(A) performed better than baseline double passage case of mixed tip gaps. This is because the mis-staggering causes the asymmetrical shock waves in the adjacent passage of non-uniform tip gaps to become symmetrical. As the mis-stagger starts to increase, the performance of case (A) starts worsening compared to baseline double passage case. At this stage, the effect of mis-stagger was more dominating and the shock waves in the adjacent passage of non-uniform tips gaps become asymmetrical again. For case (B) it was observed that the mis-staggering causes the stalled passage in the baseline case to be even more stalled while the choked passage in the baseline case becomes even more choked and hence an overall loss of performance.

(**2**) **Suggestion Of Optimal Arrangement For Geometric Uncertainty** :

It was hypothesised that smoother re-distribution of blades with differing stagger angle around the annulus would give better performance. On the other hand, a zigzag kind of arrangement would increase the blade-to-blade mis-stagger and hence result in lower efficiency. Using a heuristic method for different arrangements, it was found that sinusoidal arrangement and linear arrangement exhibited lowest cumulative mis-stagger while a zigzag arrangement had the largest cumulative mis-stagger. The results from heuristic arrangement was further backed up using genetic algorithm (GA) based TSP solver. A full annulus simulation at design speed and off-design speed for NASA Rotor 67 confirmed that sinusoidal arrangement and linear arrangement gave best performance while zigzag arrangement gave the worst performance. Similar results are obtained for a full annulus simulation of a wide chord blade undergoing different arrangements. It was thus concluded that the change in passage area (as a result of change in stagger angle between various blades) causes a drop in efficiency for different arrangements.

Similarly, in case of differing tip gaps and differing leading edge damaged blades, it was hypothesised that a zigzag arrangement wherein the blade with least stall margin is sandwiched between the two blades having best stall margin would improve the overall stability limit and performance. This was further confirmed using deterministic full annulus CFD simulations. It was seen that the zigzag arrangement undergoes a uniform stall inception whereas in sinusoidal arrangement, one half of the annulus stalls causing overall deterioration of performance

and stability limit. This study was valid for NASA Rotor 67 as well as 1-stage IGT. Furthermore, using TSP analogy it was successfully shown for a compressor undergoing simultaneous variation of stagger angle and tip gap, a zigzag arrangement of tip gap followed by smooth variation of stagger angle gives the best performance. This required a slight modification in the calculation of euclidean distance compared to traditional definition.

(**3**) **Uncertainty Quantification Under Parametric Variation** :

This work represents an important milestone insofar as the development of surrogate model for predicting the performance of compressor undergoing combinatorial optimisation is concerned. A quick, reliable and easy to use tool has been developed from the first principles which uses data from single and double passage simulations. The time required to solve single passage computation is $T \times N^{-1}$ where 'T' is the time required to solve full annulus computation having 'N' number of blades in a compressor. It requires approximately 4 hrs of CPU time on a MacBook Air having 1.6 GHz Intel Core i5 Processor with 8 GB RAM to reconstruct the performance curves of all 4 arrangements of 50,000 virtual samples.

It was seen that the surrogate model for stagger angle is extremely robust and accurate. It predicted the performance curves of NASA Rotor 67 at design speed and part speed conditions very well. The generality of the surrogate model was established as it successfully predicted the performance of wide chord blade rotor for different arrangements of stagger angle. The baseline surrogate model in case of tip gap as a parameter of variation, was improved by using nonlinear least square method to correct for the pressure ratio, temperature ratio and efficiency. It was observed that for stagger angle as a parameter of variation, different arrangements did not exhibit appreciable change in stability limit though the maximum efficiency for sinusoidal and linear arrangement was the highest. In case of tip gap as a parameter of variation, different arrangements exhibited differing maximum efficiency as well as the stability limits. It was found that zigzag arrangement produced the best performance and stability limits while sinusoidal arrangement exhibited the worst performance and stability limits. Also seen was an increased efficiency and stability limit irrespective of the type of arrangement for decreasing mean tip gap value.

7.2 Importance From Industrial Perspective

This is the first time an attempt has been made to develop a surrogate model for predicting the compressor performance of different arrangements. A rule of thumb has been developed for not only giving the best possible arrangement but also for predicting its performance without resorting to expensive full annulus CFD simulation. Using this tool, UQ has been performed on 50,000 virtual samples of compressors which can give the engineers an excellent estimate of the expected performance and stability margins which was previously impossible.

Roberts et al. (2013) have shown that an increase of 0.5% of efficiency across fan and compressor can result in fuel savings worth tens of thousands of pounds per engine per year. As of 2017, there were almost 25,000[1] aircrafts in operation and this number is projected to increase up to 60,000[2] aircrafts by 2037. In the present thesis, it was seen that at Sea-Level-Static (SLS) condition an efficiency gain of almost 1-1.5% can be made along with better stability margin by redistributing the blades around the annulus in a controlled manner. This becomes even more crucial when considering a drop in efficiency, pressure ratio and stall mass flow rate reported at high altitude cruise condition (low Reynolds number) compared to SLS condition (Choi et al., 2010). Thus a potential fuel savings of billions of pounds per year to the aircraft industry can be accrued while also saving a few million of tonnes of carbon emissions.

The MRO sector contributes upwards of 50% revenue for Original Equipment Manufacturers (OEM). A cost savings in the MRO sector will potentially increase revenue for the industry. Usually, the blades would be scrapped off when the manufacturing tolerance and/or damage exceeds certain preset value as determined by the OEM. Through this study, a controlled circumferential re-arrangement of blades (having differing dimension) can be done due to its positive impact on performance and stability margin of a compressor. The industry could therefore potentially reuse the blades having defects instead of scrapping it off. This novel research enables the engineers and researchers to perform sensitivity analysis of QoI in case of compressors undergoing manufacturing tolerance.

[1] https://www.telegraph.co.uk/travel/travel-truths/how-many-planes-are-there-in-the-world/
[2] http://www.travelweek.ca/news/exactly-many-planes-world-today/

7.3 Future Work

The author has listed the potential areas for future research work based on the computational resource. These are divided into steady simulation and unsteady simulation :

7.3.1 Steady Simulation

(**1**) **Blade Count Sensitivity** :

A wake from the rotor blade row having 'N' blades and rotating at 'F' Hz excites the downstream stator vane at 'NF' Hz. When the excitation frequency coincides with one of the natural frequency of the blade, vibration levels can grow and potentially cause fatigue failure. It is thus conceivable that the designers would play around with number of rotor blades (potentially impacting the solidity). It is also possible to reduce the number of blades with an intention of reducing the weight. Future research can be carried out to gauge the sensitivity of the surrogate model to the increased/decreased number of rotor blades. Suitable correction factors can be introduced to the original data used to build a surrogate model such that it can be used to predict the performance of the compressor with different solidity.

(**2**) **N − Parameter Variation Case** :

An optimal arrangement for a two parameter variation case has been arrived at by using CFD simulation and TSP analogy. However, the construction of a surrogate model for a two parameter case is an onerous task. For NASA Rotor 67 with 22 blades with each blade having 2 degree of freedom (stagger angle and tip gap variation simultaneously), it would involve a total of 44 random variables. It is estimated that for a step size of 0.5° and 0.3 mm, there would be a total of 105 interpolation cases and 1680 points at which single passage and double passage CFD simulation would need to be done. Humongous computational resources would be required to build a surrogate model. Expanding this problem to a N-Parameter variation case, would further complicate the problem. Future research could concentrate on building a more efficient surrogate model by reducing the number of interpolation cases and also use of machine

learning techniques (Taylor et al., 2019) to predict the compressor performance accurately.

7.3.2 Unsteady Simulation

(**1**) **Effect Of Inlet Distortion** :

All the computations in the present thesis have been carried out at Sea-Level-Static (SLS) condition with uniform total pressure and total temperature at the inlet. However, the fans and compressors can also be subjected to non-uniform inflow conditions - more commonly called as inlet distortion. Though the inlet distortion is usually detrimental for both mass flow range as well as pressure ratio, Zhang (2019) showed that there is an increase in the pressure ratio for a distortion strength of 2% compared to the clean flow case with a slight change in stalling mass flow rate. It would be interesting to study the effect of inlet distortion on a compressor subject to geometric uncertainty.

(**2**) **Rotor Stator Interaction** :

The present research considers geometric uncertainty on rotors only. This work could be further extended by considering manufacturing tolerance and/or inservice degradation on rotor as well as stator simultaneously to see the effect of different arrangements on the performance and stability boundaries of a compressor. Four potential cases of rotor-stator arrangements could be studied (i) Zigzag-Zigzag (ii) Sinusoidal-Sinusoidal (iii) Zigzag-Sinusoidal (iv) Sinusoidal-Zigzag. This study is of engineering relevance as the engine manufacturers would be advised whether controlled assembly of blades around the annulus needs to be carried out for rotor only or for both rotor as well as stator.

(**3**) **Flutter Computation For Damage Blade** :

A zigzag arrangement of damaged blades has been predicted to give the best compressor performance and stability margin. The maximum chord-wise damage is considered to be 18% while the maximum radial damage starts from 66% of span (from hub) up to the tip of the compressor. The damage can change the natural frequency and mode shape of the compressor

blade; thereby detrimentally affecting the fatigue life of the component by causing the blade to undergo flutter oscillations. It would thus be an extremely important study to perform flutter calculations on such damaged blades. It would also be of engineering relevance to see if the type of arrangement has any effect on the flutter oscillations.

(**4**) **Running Geometry Prediction And Estimating Of Performance** :

The present research does not consider the running geometry changes due to aeroelastic coupling. A surrogate model has been built based on the simulation data of cold geometry from choke to stall. Lu (2020) has shown using an aeroelastic coupling that the geometry of a typical compressor changes from choke to stall. The effect of manufacturing tolerance and/or in-service degradation on such geometry changes needs to be studied. Furthermore, using the machine learning techniques, a running geometry of a compressor could be predicted *a priori* and this can be combined with the present surrogate model to estimate the actual expected performance. This would require a large number of training data sets to help train the model and testing data sets used to test and validate the trained model (hence increased computational resources).

(**5**) **Buzz Saw Noise** :

It would be interesting to study the effect of parametric variation on the buzz saw noise. International Civil Aviation Organisation (ICAO) recommends technical standards to limit the noise from the aircrafts. In addition, bodies like Department for Transport (DfT) and Civil Aviation Authority (CAA) retains direct responsibility for regulating aviation noise and has final say on where the aircrafts are allowed to fly in UK. With the modern aircrafts subject to stringent regulations over noise production, it would be of engineering relevance to find an optimised arrangement that reduces the amount of noise being produced without compromising on performance and stability limits. However, a very fine mesh of the order of 200 million points for full annulus domain would be required for the accurate prediction buzz saw noise (Sureshkumar et al., 2017). A computation of this size would require humongous resource especially from the point of view of parametric variation.

Bibliography

E. H. Abed, P. K. Houpt, and W.M. Hosny. "Bifurcation Analysis Of Surge And Rotating Stall In Axial Flow Compressors". *ASME J. Turbomach.*, 115(4):817–824, October 1993.

J. J. Adamczyk, M. L. Celestina, and E. M. Greizer. "The Role of Tip Clearance in High-Speed Fan Stall". *ASME J. Turbomach.*, 115(1):28–38, January 1993.

Agilent Technologies. "Practical Strain Gage Measurements". See The URL :"`https://www.omega.co.uk/techref/pdf/StrainGage_Measurement.pdf`", 1999.

D. Alman and M. Duffles. "Erosion-Resistant Nanocoatings For Improved Energy Efficiency In Gas Turbines". Technical Report 09NT77707, U.S. Department Of Energy, NETL - Office Of Research And Development, 2013.

J. Alqallaf, N. Ali, J. A. Teixeira, and A. Addali. "Solid Particle Erosion Behaviour and Protective Coatings for Gas Turbine Compressor Blades—A Review". *Processes*, 8(984): 1–42, August 2020.

T. Arima, T. Sonoda, M. Shirotori, A. Tamura, and K. Kikuchi. "A Numerical Investigation of Transonic Axial Compressor Using a Low-Reynolds-Number κ-ϵ Turbulence Model". *ASME J. Turbomach.*, 121(1):44–58, January 1999.

D. Arzina. "Vibration Analysis Of Compressor Blade Tip-Rubbing". Master's thesis, Cranfield University, UK, 2011.

ATSB. "Engine Failure Involving Airbus A330, 9M-XXE". Technical Report AO-2017-066, Australian Transport Safety Bureau, Australian Government, June 2020.

J. Aust and D. Pons. "Taxonomy Of Gas Turbine Blade Defects". *Aerospace*, 6(58):1–35, April 2019.

A. Awad, I. Von Poser, and M. T. Aboul-Ella. *"Real Genetic Algorithm for Traveling Salesman Problem Optimisation"*, volume 28. Proceedings of the European Computing Conference, Springer, USA, 2009.

J. Axerio-Cilies. *"Predicting Formula 1 Tire Aerodynamics: Sensitivities, Uncertainties & Optimization"*. PhD thesis, Stanford University, USA, June 2012.

I. Babuska, R. Tempone, and G. E. Zouraris. "Galerkin Finite Element Approximations Of Stochastic Elliptical Differential Equations". *SIAM Journal on Numerical Analysis*, 42(2): 800–825, 2004.

C. Balan and W. Tabakoff. "Axial Flow Compressor Performance Deterioration". In *20th Joint Propulsion Conference*, page p. 1208, 1984.

B. H. Beheshti, B. Farhanieh, J. A. Teixeira, P. C. Ivey, and K. Ghorbanian. "Parametric Study of Tip Clearance-Casing Treatment on Performance and Stability of a Transonic Axial Compressor". *ASME J. Turbomach.*, 126(4):527–535, December 2004.

S. Bell. "A Beginner's Guide To Uncertainty Of Measurement". "`https://www.npl.co.uk/special-pages/guides/gpg11_uncertainty.pdf`", The National Physical Laboratory, UK, March 2001.

J. R. Bergner, S. Kablitz, D. K. Hennecke, H. Passrucker, and E. Steinhardt. "Influence Of Sweep On The 3D Shock Structure In An Axial Transonic Compressor". In *Proceedings of ASME Turbo Expo 2005*, volume 6: Turbo Expo 2005, Parts A and B of *Turbo Expo: Power for Land, Sea, and Air*, pages 343–352, 2005. Paper Number : GT2005-68835.

A. Bhosekar and M. Ierapetritou. "Advances In Surrogate Based Modeling, Feasibility Analysis, And Optimization: A Review". *Computers & Chemical Engineering*, 108:250–267, January 4 2018.

N. Birks, F. Pettit, and D. Rishel. "Erosion-Corrosion And Wear". *Journal de Physique IV Colloque*, 03(C9):C9–667–C9–678, 10.1051/jp4:1993970.jpa–00252411, 1993. https://hal.archives-ouvertes.fr/jpa-00252411.

M. A. Bouhlel, N. Bartoli, A. Otsmane, and J. Morlier. "Improving Kriging Surrogates Of High-Dimensional Design Models By Partial Least Squares Dimension Reduction". *Structural And Multidisciplinary Optimization*, 53(5):935–952, 2016.

G. Britton. "Notes On Tolerance Planning And Control". Lecture Notes, Tampere University Of Technology, 2000.

R. W. Bunton and C. M. Denegi. "Limit Cycle Oscillation Characteristics Of Fighter Aircraft". *Journal Of Aircraft*, 37(5):916–918, 2000.

D. E. Caguiat. "Rolls Royce/Allison 501-K Gas Turbine Antifouling Compressor Coatings Evaluation". *ASME J. Turbomach.*, 125(3):482–488, 2003.

P. Chaganti. "Development Of A Software Tool To Estimate Airfoil Feature Variations ". Master's thesis, West Virginia University, December 2012.

M. Choi, J. H. Baek, J. Y. Park, S. H. Oh, and H. Y. Ko. "Effects of Low Reynolds Number on Loss Characteristics in Transonic Axial Compressor". *Trans. Japan Soc. Aero. Space Sci.*, 53(181):162–170, June 2010.

M. Choi, M. Vahdati, and M. Imregun. "Effects Of Fan Speed On Rotating Stall Inception And Recovery". *ASME J. Turbomach.*, 133(4):1–8, April 2011. 031030.

G. R. Cogorno. *"Geometric Dimensioning And Tolerancing For Mechanical Design"*. McGraw-Hill Companies Inc, 2006.

P. G. Constantine. *"Active Subspaces Emerging Ideas For Dimension Reduction In Parameter Studies"*. Society for Industrial and Applied Mathematics, 2015.

P. G. Constantine, Q. Wang, A. Doostan, and G. Iaccarino. "A Surrogate- Accelerated Bayesian Inverse Analysis Of The HyShot II Flight Data". In *52nd AIAA/ASME/ASCE Structures, Structural Dynamics and Materials Conference*, Denver, USA, 2011. Paper Number : AIAA-2011-2037.

W. W. Copenhaver, E. R. Mayhew, C. Hah, and A. R. Wadia. "The Effect of Tip Clearance on a Swept Transonic Compressor Rotor". *ASME J. Turbomach.*, 118(2):230–239, April 1996.

N. A. Cumpsty. *"Compressor Aerodynamics"*. Krieger Publishing Company, 2^{nd} Revised edition, July 2004.

N. A. Cumpsty and J. A. Horlock. "Averaging Uniform Flow For A Purpose". *Journal of Turbomachinery*, 128(1):120–129, 2006.

B. P. Curlett. "The Aerodynamic Effect Of Fillet Radius In A Low Speed Compressor Cascade". NASA Technical Memorandum 105347, Lewis Research Center, NASA, November 1991.

B. M-H. Cyrus and G. George. "Gas Turbine Blade Failures - Causes, Avoidance, And Troubleshooting". In *Proceedings Of The 27th Turbomachinery Symposium*, pages 129–180. Texas A& M University, Turbomachinery Laboratory, 1998.

C. R. Davison and T. A. Rutke. "Assessment And Characterization Of Volcanic Ash Threat To Gas Turbine Engine Performance". *Journal of Engineering for Gas Turbines and Power*, 136(8):081201(1–10), August 2014.

J. D. Denton. "Calculation Of 3D Viscous Flow Through Multi-Stage Turbomachines". *Journal of Turbomachinery*, 114(1):18–26, 1992.

J. D. Denton. "The Effects Of Lean And Sweep On Transonic Fan Performance: A Computational Study". *Task Quarterly*, 6(1):7–23, 2002.

J. D. Denton. "Multall - An Open Source, Computational Fluid Dynamics Based, Turbomachinery Design System". *ASME J. Turbomach.*, 139(12):121001, September 2017.

A. Desai. "Analysis Of A Nonlinear Aeroelastic System With Parametric Uncertainties Using Polynomial Chaos Expansion". Thesis, Indian Institute of Technology Madras, Chennai, India, March 2011.

A. Desai and S. Sarkar. "Analysis Of A Nonlinear Aeroelastic System With Parametric Uncertainties Using Polynomial Chaos Expansion". *Mathematical Problems In Engineering*, 2010, July 2010.

J. Dodds. *"Rotating Stall In Variable Geometry Compressors"*. PhD thesis, Imperial College London, UK, September 2016.

J. Dodds and M. Vahdati. "Rotating Stall Observations in a High Speed Compressor-Part 2: Numerical Study". *ASME J. Turbomach.*, 137(5):051003, May 2015.

T. J. Drzewiecki. *"Adjoint Based Uncertainty Quantification And Sensitivity Analysis For Nuclear Thermal-Fluids Codes"*. PhD thesis, University of Michigan, USA, 2013.

K. Duraisamy, G. Iaccarino, and H. Xiao. "Turbulence Modeling In The Age Of Data". *Annual Review of Fluid Mechanics*, 51:357–77, January 2019.

Y. Dvirnyk, D. Pavlenko, and R. Przysowa. "Determination Of Serviceability Limits Of A Turboshaft Engine By The Criterion Of Blade Natural Frequency And Stall Margin". *Aerospace*, 6(12):132, 2019.

F. Eger, D. Coupek, D. Caputo, M. Colledani, M. Penalva, J. A. Ortiz, H. Freiberger, and G. Kolleger. "Zero Defect Manufacturing Strategies For Reduction Of Scrap And Inspection Effort In Multi-Stage Production Systems". *Procedia CIRP*, 67:368–373, 2018.

M. E. Elmstrom, K. T. Millsaps, G. V. Hobson, and J. S. Patterson. "Impact Of Nonuniform Leading Edge Coatings On The Aerodynamic Performance Of Compressor Airfoils". *ASME J. Turbomach.*, 133(4):041004, April 2011.

Federal Aviation Administration. "Aviation Maintenance Technician Handbook – Powerplant, Volume 2". Technical Report FAA-H-8083-32, U.S. Department of Transportation, 2018.

V. J. Fidalgo, C. A. Hall, and Y. Colin. "A Study Of Fan-Distortion Interaction Within the NASA Rotor 67 Transonic Stage". *ASME J. Turbomach.*, 134(5):051011, September 2012.

G. Fritsch and M. B. Giles. "An Asympototic Analysis Of Mixing Loss". *Journal of Turbomachinery*, 117(3):367–374, 1995.

X. Gao, H. Du, and M. Han, editors. *"Combinatorial Optimisation And Applications : 11^{th} International Conference, COCOA 2017"*. Theoretical Computer Science And General Issues. Springer International Publishing, Shanghai, China, 1 edition, December 16-18 2017.

R. G. Ghanem and P. D. Spanos. "Polynomial Chaos In Stochastic Finite Elements". *Journal of Applied Mechanics*, 57:197–202, 1990.

R. G. Ghanem and P. D. Spanos. *"Stochastic Finite Elements: A Spectral Approach"*. Springer, New York, 1991.

R. G. Ghanem and P. D. Spanos. "A Stochastic Galerkin Expansion For Nonlinear Random Vibration Analysis". *Probabilistic Engineering Mechanics*, 8(3-4):255–264, 1993.

A. Ghenaiet, S. C. Tan, and R. L. Elder. "Prediction Of An Axial Turbomachine Performance Degradation Due To Sand Ingestion". *Proceedings of the Institution of Mechanical Engineers, Part A: Journal of Power and Energy*, 219(4):273–287, 2005.

T. Ghisu, G. T. Parks, P. M. Jarrett, and P. J. Clarkson. "Adaptive Polynomial Chaos For Gas Turbine Compression Systems Performance Analysis". *AIAA J*, 48(6):1156–1170, 2010.

L. Gibson, L. Galloway, S. I. Kim, and S. Spence. "Assessment Of Turbulence Model Predictions For A Centrifugal Compressor Simulation". *Journal of Global Power And Propulsion Society*, 1:142–156, July 2017.

A. Giebmanns, J. Backhaus, C. Frey, and R. Schnell. "Compressor Leading Edge Sensitivities And Analysis With An Adjoint Flow Solver". In *Proceedings of ASME Turbo Expo 2013*, volume 6A: Turbomachinery of *Turbine Technical Conference and Exposition*, San Antonio, USA, June 3-7 2013. Paper Number : GT2013-94427.

A. A. Giunta, J. M. McFarland, L. P. Swiler, and M. S. Eldred. "The Promise And Peril Of Uncertainty Quantification Using Response Surface Approximations". *Structure And Infrastructure Engineering*, 2(3-4):175–189, October 2006.

G. H. Golub and J. H. Welsch. "Calculation Of Gauss Quadrature Rules". *Mathematics of Computation*, 23(106):221–230, 1969.

N. Gourdain. "Prediction Of The Unsteady Turbulent Flow In An Axial Compressor Stage. Part 1: Comparison Of Unsteady Rans And Les With Experiments.". *Comput Fluids*, 106: 119–129, 2015.

M. B. Graf, T. S. Wong, E. M. Greizer, F. E. Marble, C. S. Tan, H. W. Shin, and D. C. Wisler. "Effects of Nonaxisymmetric Tip Clearance on Axial Compressor Performance and Stability". *ASME J. Turbomach.*, 120(4):648–661, October 1998.

W. Guo and R. Brommesson. "Business Case For Repair Via Ded Processes And Best Practice For Classification And Qualification Of Component Damage". Technical Report AMOS GA690608, Additive Manufacturing Optimisation And Simulation : Joint EU-Canadian Collaboration, January 31 2018.

C. Hah. "Large Eddy Simulation Of Transonic Flow Field In NASA Rotor 37". Technical Report NASA/TM - 2009-215627, Glenn Research Center, NASA, Ohio, USA, September 2009.

C. Hah, S. L. Puterbaugh, and A. R. Wadia. "Control Of Shock Structure And Secondary Flow Field Inside A Transonic Compressor Rotor Through Aerodynamic Sweep". In *ASME 1998 International Gas Turbine and Aeroengine Congress and Exhibition*, volume 1: Turbomachinery, 1998. Paper number : 98-GT-561.

M. H. Hamilton. "Sandy Environment And/Or Combat Operations For T700 Series Engines". Technical Bulletin TB 55-2840-248-20-17, Department Of The Army, Washington, D.C., November 30th 1992.

J. M. Hammersley and D. C. Handscomb. *"Monte Carlo Methods"*. Fletcher & Son Ltd, Norwich, 1964.

J. Hesthaven. "Uncertainty Quantification in Computational Science". Lecture Notes-DTU 2010, Lecture 1, Brown University, August 2010. See URL `https://www.yumpu.com/en/document/read/29955208/lecture-1-brown-university`.

P. Hill and C. Peterson. *"Mechanics And Thermodynamics Of Propulsion"*. Pearson Education Inc., 2nd edition, 1992.

I. M. Hongsik, X. Chen, and G. Zha. "Simulation of 3D Multistage Axial Compressor Using a Fully Conservative Sliding Boundary Condition". In *Proceedings of ASME-IMECE 2011*, volume 6: Fluids and Thermal Systems; Advances for Process Industries, Parts A and B, pages 1321–1330, Colorado, USA, November 11-17 2011. Paper number : IMECE2011-62049.

K. Hsu and D. Hoyniak. "A Fast Influence Coefficient Method for Linearized Flutter and Forced-Response Analysis". In 49^{th} *AIAA Aerospace Sciences Meeting Including the New Horizons Forum and Aerospace Exposition*, Orlando, Florida, January 4-7 2011. Paper number : AIAA 2011-229.

M. Inoue and M. Kuroumaru. "Structure Of Tip Clearance Flow In An Isolated Axial Compressor Rotor". *ASME J. Turbomach.*, 111(3):250–256, July 1989.

K. Isomura. *"A Numerical Investigation Of A Flutter In A Transonic Fan"*. PhD Thesis, Massachusetts Institute Of Technology, USA, June 1996.

A. Jameson and S. Kim. "Reduction Of The Adjoint Gradient Formula In The Continuous Limit ". In *41st Aerospace Science Meeting And Exhibit*, Reno, USA, January 6-9 2003. Paper Number : AIAA 2003-0040.

M. Jasiczek, D. Szczesniak, J. Kaczorowski, and M. Innocenti. "Investigation Of Fatigue Failures Of Titanium Alloy Blades Used In Compressor Modules Of Aeroderivative Industrial Gas Turbines". *J Fail. Anal. and Preven.*, 13:689–696, 2013.

I. K. Jennions and M. G. Turner. "Three-Dimensional Navier-Stokes Computations of Transonic Fan Flow Using an Explicit Flow Solver and an Implicit κ-ϵ Solver". *ASME J. Turbomach.*, 115(2):261–272, April 1993.

V. B. John. *"Introduction To Engineering Materials"*. Palgrave Macmillan, London, 3rd edition, 1992.

J. O. Jongsik. "The Effects Of Blade Fillets On Aerodynamic Performance Of A High Pressure Ratio Centrifugal Compressor". In *23rd International Compressor Engineering Conference*, pages 1–9, Purdue, USA, July 11-14 2016.

D. Kartofelev. "Classification Of Bifurcations in 2-D Sysytems". Lecture notes YFX1520, TalTech University, February 2020.

S. A. Khalid, A. S. Khalsa, I. A. Waitz, C. S. Tan, E. M. Greizer, N. A. Cumpsty, J. J. Adamczyk, and F. E. Marble. "Endwall Blockage In Axial Compressors". *ASME J. Turbomach.*, 121(3):499–509, 1999.

G. Kilchenstein. "Erosion / Corrosion Resistant Coatings for Compressor Airfoils". "`https://apps.dtic.mil/dtic/tr/fulltext/u2/a601448.pdf`", August 29th 2012.

J. Kirk. "Genetic Algorithm Based Traveling Salesman Problem." Retrieved On December 12, 2018 From MATLAB Central File Exchange. For More Information, See The URL :"`https://www.mathworks.com/matlabcentral/fileexchange/13680-traveling-salesman-problem-genetic-algorithm`", May 2014.

A. D. Kiureghian and O. Ditlevsen. "Aleatory or epistemic? Does it matter?". *Struct. Saf.*, 31 (2):105–112, 2009. Risk Acceptance and Risk Communication.

J. Klinner, A. Hergt, and C. Willert. "Experimental Investigation Of The Transonic Flow Around The Leading Edge Of An Eroded Fan Airfoil". *Experiments In Fluids*, 55(9):1800, 2014.

C. Knapke, M. Wolff, and D. A Johnston. "Blended Fan Blade Effects On Unsteady Aerodynamics". In *Proceedings Of AIAA Scitech 2020 Forum*, January 6-10 2020. Paper number : AIAA 2020-0130.

B. Korte and J. Vygen. *"Combinatorial Optimisation : Theory And Algorithm"*. Algorithms and Combinatorics. Springer-Verlag Berlin Heidelberg, 5^{th} edition, 2011.

R. Kundu. *"Impact Of Engine Icing On Jet Engine Compressor Flow Dynamics"*. PhD Thesis, Georgia Institute Of Technology, USA, July 2015.

J. Kurzke. "Correlations Hidden In Compressor Maps". In *Proceedings of ASME Turbo Expo 2011*, volume 1: Aircraft Engine; Ceramics; Coal, Biomass and Alternative Fuels; Wind Turbine Technology of *Turbo Expo: Power for Land, Sea, and Air*, pages 161–170, British Columbia, Canada, June 6-10 2011. Paper number : GT2011-45519.

A. Lange, M. Voigt, K. Vogeler, H. Schrapp, E. Johann, and V. Gummer. "Probabilistic CFD Simulation Of A High-Pressure Compressor Stage Taking Manufacturing Variability Into Account". In *Proceedings of ASME Turbo Expo 2010*, volume 6: Structures and Dynamics, Parts A and B of *Turbo Expo: Power for Land, Sea, and Air*, pages 617–628, Glasgow, UK, June 14-18 2010. Paper number : GT2010-22484.

K. B. Lee, M. J. Wilson, and M. Vahdati. "Numerical Study on Aeroelastic Instability for a Low Speed Fan". *ASME J. Turbomach.*, 139(7):1–8, February 2017. 071004.

K. B. Lee, M. J. Wilson, and M. Vahdati. "Validation of a Numerical Model for Predicting Stalled Flows in a Low Speed Fan - Part 1: Modification of Spalart-Allmaras Turbulence Model". *ASME J. Turbomach.*, 140(5):051008, April 2018.

H. D. Li and L. He. "Blade Aerodynamic Damping Variation With Rotor-Stator Gap : A Computational Study Using Single Passage Approach". *ASME J. Turbomach.*, 127(3):573–579, March 2005.

Y. L. Li and A. I. Sayma. "CFD Simulation Of Blade Damage Effect On The Performance Of A Transonic Axial Compressor Near Stall". *Proceedings of the Institution of Mechanical Engineers, Part C: Journal of Mechanical Engineering Science*, 229(12):2242–2260, 2015.

D. C. Liaw, R. A. Adomaitis, and E.H. Abed. "Two-Parameter Bifurcation Analysis Of Axial Flow Compressor Dynamics". In *1991 American Control Conference*, pages 2955–2960, Boston, USA, June 26-28 1991. IEEE.

A. Liefke, V. Marciniak, U. Janoske, and H. Gottschalk. "Using Adjoint Cfd To Quantify The Impact Of Manufacturing Variations On A Heavy Duty Turbine Vane". In 6^{th} *European Conference On Computational Mechanics And* 7^{th} *European Conference on Computational Fluid Dynamics*, pages 1–14, Glasgow, UK, June 11-15 2019.

P. Lin, C. Wang, and M. Wang. "Bifurcation Predication In Axial Compressors With Nonuniform Inflow Via Deterministic Learning". *International Journal of Bifurcation and Chaos*, 27(10):1750159(1–10), 2017.

J. L. Lions, L. Lubeck, J. L. Fauquembergue, G. Kahn, W. Kubbat, S. Levedag, L. Mazzini, L. Merle, and C. O'Halloran. "ARIANE 5 Flight Failure Report". Technical report, The Inquiry Board, July 19^{th} 1996.

M. S. Liou and W. Yao. "Flutter Analysis For Turbomachinery Using Volterra Series". In *Proceedings of the ASME Turbo Expo 2014*, volume 7B: Structures and Dynamics of *Turbine Technical Conference and Exposition*, pages 1–13, Dusseldorf, Germany, June 16–20 2014. Paper Number : GT2014-25474.

G. J. A. Loeven. *"Efficient Uncertainty Quantification In Computational Fluid Dynamics"*. PhD Thesis, Technische Universiteit Delft, Netherlands, June 2010.

G. J. A. Loeven, J. A. S. Witteveen, and H. Bijl. "Probabilistic Collocation: An Efficient Non-Intrusive Approach For Arbitrarily Distributed Parametric Uncertainties". In *45th AIAA Aerospace Sciences Meeting and Exhibit*, Reno, Nevada, USA, January 8-11 2007. Paper Number : AIAA-2007-317.

R. L. Loud and A. A. Slaterpryce. "Gas Turbine Inlet Air Treatment". Technical Report GER-3419A, GE Power Generation, GE Company, Schenectady, 1991.

Y. Lu. *"Alternate Passage Divergence Of Wide Chord Transonic Fan Blades"*. PhD Thesis, Imperial College London, London, UK, March 2020.

Y. Lu, J. Green, M. Vahdati, and S. C. Stapelfeldt. "Effect of Geometry Variability on Fan Performance and Aeromechanical Characteristics". In *Proceedings of* 15^{th} *International Symposium on Unsteady Aerodynamics, Aeroacoustics and Aeroelasticity of Turbomachines*, pages 1–9, University of Oxford, UK, September 24-27 2018. Paper number : ISUAAAT15-095.

Y. Ma, N. R. Vadlamani, J. Cui, and P. Tucker. "Comparative Studies Of RANS Versus Large Eddy Simulation For Fan–Intake Interaction". *ASME. J. Fluids Eng.*, 141(3):031106(1–13), March 2019.

O. P. L. Maître and O. M Knio. *"Spectral Methods For Uncertainty Quantification: With Applications To Computational Fluid Dynamics"*. Springer Science and Business Media, 2010.

O. P. L. Maître, M. T. Reagan, H. N. Najm, R. G. Ghanem, and O. M. Knio. "A Stochastic Projection Method For Fluid Flow: 2. Random Process". *Journal of Computational Physics*, 181(1):9–44, September 2002.

J. Marshall, H. Cull, and H. Broad. "Engine Compressor Surges". Technical Report Aviation inquiry 11-005, Transport Accident Investigation Commission, July 2013.

J. Marx, J. Stading, G. Reitz, and J. Friedrichs. "Investigation And Analysis Of Deterioration In High Pressure Compressors Due To Operation". *CEAS Aeronautical Journal*, 5(4):515–525, July 2014.

F. E. McCaughan. "Bifurcation Analysis Of Axial Flow Compressor Stability". *SIAM Journal On Applied Mathematics*, 50(5):1232–1253, October 1990.

Major General Lee McFann. "United States Air Force Flying Safety Magazine - Year In Review". See url : "`https://www.safety.af.mil/Portals/71/documents/Magazines/FSM/fsmjanfeb05.pdf?ver=2017-03-28-101134-187`", 2005.

A. Mehdi. *"Effect of Swirl Distortion on Gas Turbine Operability"*. PhD Thesis, Cranfield University, UK, May 2014.

U. B. Mehta, D. R. Eklund, V. J. Romero, J. A. Pearce, and N. S. Keim. "Simulation Credibility : Advances in Verification, Validation and Uncertainty Quantification". Technical Publication NASA-TP-2016-219422, Lewis Research Center, NASA, November 2016.

F. Montomoli, M. Carnevale, A. D'Ammaro, M. Massini, and S. Salvadori. *"Uncertainty Quantification in Computational Fluid Dynamics and Aircraft Engines"*. SpringerBriefs in Applied Sciences and Technology. Springer International Publishing, 2nd edition, 2015.

R. D. Moore. "Rotor Tip Clearance Effects on Overall and Blade-Element Performance of Axial-Flow Transonic Fan Stage". Technical Publication NASA-TP-2049, Lewis Research Center, NASA, Cleveland, OH, September 1982.

Navy Training Publications Centre. *"Aviation Machinist's Mate J 3 & 2"*. Bureau Of Naval Personnel, Millington, Tennese, 1971.

W. L. Oberkamph and T. G. Trucano. "Verification and Validation in Computational Fluid Dyncamics". *Progress in Aerospace Sciences*, 38(3):209–272, 2002.

N. Odier, F. Duchaine, L. Y. M. Gicquel, G. Dufour, and N. Garcia-Rosa. "Comparison Of Les And Rans Predictions With Experimental Results Of The Fan Of A Turbofan". In *Proceedings of* 12^{th} *European Conference on Turbomachinery Fluid dynamics & Thermodynamics*, pages 1–14, April 2017. Paper number : ETC2017-126.

M. M. J. Opgenoord. *"Transonic Flutter Prediction And Aeroelastic Tailoring For Next-Generation Transport Aircraft"*. PhD thesis, Massachusetts Institute Of Technology, USA, August 2018.

M. Palman, B. Leizeronok, and B. Cukurel. "Mission Analysis and Operational Optimisation of Adaptive Cycle Microturbofan Engine In Surveillance and Firefighting Scenarios". *J. Eng. Gas Turbines Power*, 141(1):011010, January 2019.

S. Y. Park and A. K. Bera. "Maximum Entropy Autoregressive Conditional Heteroskedasticity Model". *J. Econom.*, 150(2):219–230, January 2009.

A. T. Patera and M. Yano. "Monte Carlo Integration...In A Nutshell". Published By MIT OpenCourseWare : "`https://ocw.mit.edu/courses/mechanical-engineering/2-086-numerical-computation-for-mechanical-engineers-fall-2014/nutshells-guis/MIT2_086F14_Monte_Carlo.pdf`", 2014.

D. B. Pengra and L. T. Dillman. "Notes on Data Analysis and Experimental Uncertainty". Published By University Of Washington : "`https://courses.washington.edu/phys431/uncertainty_notes.pdf`", January 2009.

B. Perot and P. Moin. "A New Approach To Turbulence Modeling". In *Proceedings Of The Summer Program 1996*, pages 35–46, Stanford University, USA, 1996. Center For Turbulence Research.

J. Peter and M. Marcelet. "Comparison Of Surrogate Models For Turbomachinery Design". *Wseas Transactions on Fluid Mechanics*, 3(1):10–17, 2008.

D. Poirel and S. J. Price. "Bifurcation Characteristics Of A Two-Dimensional Structurally Non-Linear Airfoil In Turbulent Flow". *Nonlinear Dynamics*, 48(4):423–435, 2007.

H. Qi, M. Azer, and P. Singh. "Adaptive Toolpath Deposition Method For Laser Net Shape Manufacturing And Repair Of Turbine Compressor Airfoils". *The International Journal of Advanced Manufacturing Technology*, 48(1):121–131, 2010.

P. V. Ramakrishna and M. Govardhan. "Numerical Study Of The Stagger Angle Effects In Forward Swept Axial Compressor Rotor Passages". In *Proceedings of ASME Turbo Expo 2010*, volume 7: Turbomachinery, Parts A, B, and C of *Turbo Expo: Power for Land, Sea, and Air*, pages 443–453, Glasgow, UK, June 14-18 2010. Paper number : GT2010-23160.

R. Rasmussen, C. Wade, F. Hage, S. Landolt, M. Tryhane, J. Cole, A. Ramsay, D. Fleming, R. K. Moore, A. Davis, T. Lisi, M Kjolleberg, and K. M. Rosenlund. "New Ground Deicing Hazard Associated with Freezing Drizzle Ingestion by Jet Engines". *Journal Of Aircraft*, 43 (5):1148–1457, September 2006.

W. B. Roberts, A. Armin, G. Kassaseya, K. L. Suder, S. A. Thorp, and A. J. Strazisar. "The Effect of Variable Chord Length on Transonic Axial Rotor Performance". *ASME J. Turbomach.*, 124(3):351–357, July 2002. 011001.

W. B. Roberts, S. A. Thorp, P. S. Prahst, and A. J. Strazisar. "The Effect of Ultrapolish On a Transonic Axial Rotor". *ASME J. Turbomach.*, 135:011001 (1–6), January 2013.

W. P. Rogers, N. A. Armstrong, D. C. Acheson, E. E. Covert, R. P. Feynman, R. B. Hotz, D. J. Kutyna, S. K. Ride, R. W. Rummel, J. F. Sutter, A. B. C. Walker, A. D. Wheelon, and C. E. Yeager. "Report To The President : On The Space Shuttle Challenger Accident". Technical report, Presidential Commission, June 6^{th} 1986.

T. M. Russi. *"Uncertainty Quantification With Experimental Data And Complex System Models"*. PhD thesis, UC Berkeley, USA, 2010.

S. Sakulkaew, C. S. Tan, E. Donahoo, C. Cornelius, and M. Montgomery. "Compressor Efficiency Variation With Rotor Tip Gap From Vanishing to Large Clearance". *ASME J. Turbomach.*, 135(3):1–10, May 2013. 031030.

A. Samad, K. Y. Kim, T. Goel, R. T. Haftka, and W. Shyy. "Multiple Surrogate Modeling For Axial Compressor Blade Shape Optimization". *Journal of Propulsion and Power*, 24(2): 301–310, March 2008.

M. Sammak. "Anti Icing In The Gas Turbine". Master's thesis, Lund University, Sweden, February 2006.

S. Sarkar, J. A. S. Witteveen, G. J. A. Loeven, and H. Bijl. "Effect Of Uncertainty On The Bifurcation Behavior Of Pitching Airfoil Stall Flutter". *Journal of Fluids and Structures*, 25 (2):304–320, February 2009.

A. I. Sayma, M. Vahdati, and M. Imregun. "An Integrated Nonlinear Approach For Turbomachinery Forced Response Prediction. Part I: Formulation". *Journal of Fluids and Structures*, 14(1):87–101, 2000a.

A. I. Sayma, M. Vahdati, L. Sbardella, and M. Imregun. "Modeling of Three-Dimensional Viscous Compressible Turbomachinery Flows Using Unstructured Hybrid Grids". *AIAA J*, 38(6):945–954, 2000b.

P. Seshadri, G. T. Parks, J. Jarrett, and S. Shahpar. "Towards Robust Design Of Axial Compressors With Uncertainty Quantification". In *54th AIAA/ASME/ASCE/AHS/ASC Structures, Structural Dynamics and Materials Conference*, Boston, MA, USA, April 2013.

P. Seshadri, S. Shahpar, and G. T. Parks. "Robust Compressor Blades For Desensitizing Operational Tip Clearance Variations". In *Proceedings of ASME Turbo Expo 2014*, volume 2A: Turbomachinery of *Turbine Technical Conference and Exposition*, pages 1–12, Dusseldorf, Germany, June 16-20 2014. Paper Number : GT2014-26624.

P. Seshadri, S. Shahpar, P. Constantine, G. T. Parks, and M. Adams. "Turbomachinery Active Subspace Performance Maps". In *Proceedings of ASME Turbo Expo 2017*, volume 2A: Turbomachinery of *Turbomachinery Technical Conference and Exposition*, pages 1–14, Charlotte, North Carolina, USA, June 26-30 2017. Paper Number : GT2017-64528.

C. V. Sidwell. *"On The Impact Of Variability And Assembly On Turbine Blade Cooling Flow And Oxidation Life"*. PhD thesis, Massachusetts Institute Of Technology, USA, July 2004.

I. Sladojevic, A. I. Sayma, and M. Imregun. "Influence of Stagger Angle Variation on Aerodynamic Damping and Frequency Shifts". In *Proceedings of GT2007*, volume 5: Turbo Expo 2007 of *Turbo Expo: Power for Land, Sea, and Air*, pages 683–700, Montreal, Canada, May 14-17 2007. Paper number : GT2007-28166.

R. K. Souter and J. B. Emerson. "Summary Of Available Hail Literature And The Effect Of Hail On Aircraft In Flight". Technical Report NACA-TN-2734, National Advisory Committee For Aeronautics, Langley Aeronautical Laboratory, September 1952.

P. Spalart and S. Allmaras. "A One-Equation Turbulence Model For Aerodynamic Flows". *AIAA J*, 439, 01 1992.

S. C. Stapelfeldt. *"Advanced Methods for Multi-Row Forced Response and Flutter Computation"*. PhD Thesis, Imperial College London, London, UK, January 2014.

W. E. Stewart. "Condensation and Icing in Gas Turbine Systems: Inlet Air Temperature and Humidity Limits". Technical Report AT-01-15-3, ASHRAE, February 2001.

B. Stratford and D. Newby. "A New Look At The Generation Of Buzz-Saw Noise". In *4th Aeroacoustics Conference*, page 1343, October 1977.

A. J. Strazisar, J. R. Wood, M. D. Hathaway, and K. L. Suder. "Laser Anemometer Measurements in a Transonic Axial-Flow Fan Rotor". Technical Publication NASA-TP-2879, Lewis Research Center, NASA, Cleveland, OH, November 1989.

K. L. Suder and M. L. Celestina. "Experimental and Computational Investigation of the Tip Clearance Flow in a Transonic Axial Compressor Rotor". *ASME J. Turbomach.*, 118(2): 218–229, April 1996.

P. Sureshkumar, M. Vahdati, A. Parry, S. Bianchi, and M. Doherty. "Towards A Holistic Prediction Of Fan Stage Tone Noise Mechanism". In *Proceedings of* 12^{th} *European Conference on Turbomachinery Fluid Dynamics & Thermodynamics*, pages 1–13, April 2017. Paper number : ETC2017-279.

K. Suzuki, Y. Matsumura, K. Takata, S. Hada, M. Yuri, and J. Masada. "Evolution Of MHPS Large Frame Gas Turbines : J To Air Cooled JAC". In *Proceedings of ASME Turbo Expo 2018*, volume 3: Coal, Biomass, and Alternative Fuels; Cycle Innovations; Electric Power; Industrial and Cogeneration; Organic Rankine Cycle Power Systems of *Turbo Expo: Power for Land, Sea, and Air*, Oslo, Norway, June 11-15 2018. Paper number : GT2018-77273.

K. Suzuki, F. Zhao, and M. Vahdati. "Numerical Analysis Of Flutter In Variable Geometry Compressors". In *Proceedings of ASME Turbo Expo 2020*, Turbo Expo: Power for Land, Sea, and Air, pages 1–13, London, UK, June 22-26 2020. Paper number : GT2020-15127.

D. Tang and E. H. Dowell. "Experimental And Theoretical Study On Aeroelastic Response Of High Aspect Ratio Wings". *AIAA J*, 39(8):1430–1441, 2001.

N. C. Tang and A. Chilkoti. "Combinatorial codon scrambling enables scalable gene synthesis and amplification of Repetitive Proteins". *Nature Materials*, 15:419–424, April 2016.

J. V. Taylor, B. Conduit, A. Dickens, C. Hall, M. Hillel, and R. J. Miller. "Predicting the operability of damaged compressors using machine learning". In *Proceedings of ASME Turbo Expo 2019*, Turbo Expo: Power for Land, Sea, and Air, Arizona, USA, June 17-21 2019. Paper number : GT2019-91339.

A. Thensen and A. Jantayavichit. "Design And Evaluation Of A Selective Assembly Station For High-Precision Scroll Compressor Shells". In *Proceedings Of The 1999 Winter Simulation Conference*, pages 694–700, Phoenix, AZ, USA, December 5-8 1999. IEEE.

D. W. Thompson, P. I. King, and D. C. Rabe. "Experimental Investigation Of Stepped Tip Gap Effects On The Performance of a Transonic Axial-Flow Compressor Rotor". *ASME J. Turbomach.*, 120(3):477–486, July 1998.

P. Tucker, S. Eastwood, C. Klostermeier, H. Xia, P. Ray, J. Tyacke, and W. Dawes. "Hybrid LES Approach for Practical Turbomachinery Flows—Part II: Further Applications". *ASME J. Turbomach.*, 134(2):021024, March 2012.

P. G. Tucker. *"Unsteady Computational Fluid Dynamics In Aeronautics"*, volume 104 of *Fluid Mechanics And Its Applications*. Springer Netherlands, 1st edition, 2014.

M. Vahdati and M. Imregun. "A Non-Linear Aeroelasticity Analysis of a Fan Blade Using Unstructured Dynamic Meshes". *Proceedings of the IMechE, Part C - J. Mech. Eng. Sci.*, 210(6):549–564, 1996.

M. Vahdati, A. I. Sayma, C. Freeman, and M. Imregun. "On the Use of Atmospheric Boundary Conditions for Axial-Flow Compressor Stall Simulations". *ASME J. Turbomach.*, 127(2): 349–351, April 2005.

S. Venkatesh, S. Sarkar, and I. Rychlik. "Uncertainties In Blade Flutter Damage Prediction Under Random Gust". *Probabilistic Engineering Mechanics*, 36(4):44–55, 2014.

S. Venkatesh, Q. Rendu, M. Vahdati, and L. Salles. "Effect of Manufacturing Uncertainties in Flow Past A Compressor Blade". In *Proceedings of 13th European Conference on Turbomachinery Fluid Dynamics and Thermodynamics*, April 8-12 2019. Paper number : ETC2019-178.

S. Venkatesh, K. Suzuki, M. Vahdati, L. Salles, and Q. Rendu. "Effect Of Geometric Uncertainty On A One Stage Transonic Compressor Of An Industrial Gas Turbine ". In *Proceedings of ASME Turbo Expo 2020*, Turbo Expo: Power for Land, Sea, and Air, London, UK, June 22-26 2020. Paper number : GT2020-16315.

L. S. L. Wang and T. P. Hong. *"Intelligent Soft Computation and Evolving Data Mining : Integrating Advanced Technologies"*. IGI Global, USA, 2010.

Z. Wang, C. Zhu, and N. Zhao. "Experimental Study On The Effect Of Different Parameters On Rotor Blade Icing In A Cold Chamber". *Applied Sciences*, 10(5884):1–14, August 2020.

Z. N. Wang and X. Yuan. "Unsteady Mechanisms Of Compressor Corner Separation Over A Range Of Incidences Based On Hybrid LES/RANS". In *Proceedings of the ASME Turbo Expo 2013*, volume 6A: Turbomachinery of *Turbine Technical Conference and Exposition*, pages 1–11, San Antonio, Texas, USA, June 3-7 2013. Paper number : GT2013-95300.

A. J. Wennerstrom. "Experimental Study of a High-Throughflow Transonic Axial Compressor Stage". *ASME J. Eng. Gas Turb. Power*, 106(3):552–560, July 1984.

N. Wiener. "The Homogeneous Chaos". *American Journal of Mathematics*, 60(4):897–936, October 1938.

M. J. Wilson, M. Imregun, and A. I. Sayma. "The Effect of Stagger Variability in Gas Turbine Fan Assemblies". In *Proceedings of GT2006*, volume 5: Marine; Microturbines and Small Turbomachinery; Oil and Gas Applications; Structures and Dynamics, Parts A and B of *Turbo Expo: Power for Land, Sea, and Air*, pages 1059–1069, Barcelona, Spain, May 8-11 2006. Paper number : GT2006-90434.

H Xiao, F. Zhao, and M. Vahdati. "Uncertainty Quantification of Spalart–Allmaras Turbulence Model Coefficients for Simplified Compressor Flow Features". *ASME. J. Fluids Eng.*, 142 (9):091501, September 2020a.

H Xiao, F. Zhao, and M. Vahdati. "Uncertainty Quantification Of Spalart-Allmaras Turbulence Model Coefficients For Compressor Stall". In *Proceedings of GT2020*, Turbo Expo: Power for Land, Sea, and Air, London, UK, June 22-26 2020b. Paper number : GT2020-15014.

D. Xiu and G. E. Karniadakis. "Modeling Uncertainty In Flow Simulations Via Generalized Polynomial Chaos". *Journal of Computational Physics*, 187(1):137–167, May 2003.

Y. S. Yoon, S. J. Song, and H. Shin. "Influence Of Flow Coefficient, Stagger Angle, and Tip Clearance On Tip Vortex In Axial Compressors". *ASME. J. Fluids Eng.*, 128(6):1274–1280, 2006.

T. A. Zaki, J. G. Wissink, W. Rodi, and P. A. Durbin. "Direct Numerical Simulations Of Transition In A Compressor Cascade: The Influence Of Free-Stream Turbulence". *J. Fluid Mech.*, 665:55–98, October 2010.

W. Zhang. *"Influence of Inlet Distortion on Fan Aerodynamic Performance"*. PhD Thesis, Imperial College London, London, UK, July 2019.

F. Zhao. *"Embedded Blade Row Flutter"*. PhD Thesis, Imperial College London, London, UK, October 2016.

F. Zhao, J. Dodds, and M. Vahdati. "Poststall Behaviour Of A Multistage High Speed Compressor At Off-Design Conditions". *ASME J. Turbomach.*, 140(2):121002, October 2018.

S. Zheng, L. Fan, J. Teng, and X Qiang. "The Impact of Uncertain Stagger Angle Variation on High-Pressure Compressor Rotor Performance". In *Proceedings of Shanghai 2017 Global Power and Propulsion Forum*, pages 1–7, Shanghai, China, 30^{th} October - 1^{st} November 2017. Paper number GPPS-2017-0045.

X. Zheng and H. Yang. "Influence Of Tip Clearance On The Performance And Matching Of Multistage Axial Compressors". In *Proceedings of ASME Turbo Expo 2016*, volume 2A: Turbomachinery of *Turbomachinery Technical Conference And Exposition*, pages 1–12, Seoul, South Korea, June 13-17 2016. Paper number : GT2016-56232.

Appendix : Copy Rights Permission

(**A**) Permission To Use Figures In Thesis From Federal Aviation Administration (USA)

(**B**) Permission To Use Figures In Thesis From Prof. Montomoli And Prof. Pinelli

(**C**) Permission To Use Figures In Thesis From Computers And Fluids (Elsevier)

(**D**) Permission To Use Figures In Thesis From Journal Of Failure Analysis And Prevention (Springer)

(**E**) Permission To Use Figures In Thesis From Metallurgical Transactions, A, Physical Metallurgy And Material Science (Springer)

(**F**) Permission From ASME To Re-Use My Publications In The Thesis

(**G**) Permission From ASME To Use Figures Of Other Researchers

(**H**) Permission To Use Proprietary Figures In The Thesis From Rolls-Royce, PLC

(**I**) Permission To Use Proprietary Image In The Thesis From ISRO (India)

From: Hyde, Barry (FAA) <Barry.Hyde@faa.gov>
Sent: 29 November 2021 19:58
To: Suriyanarayanan, Venkatesh <v.suriyanarayanan16@imperial.ac.uk>
Cc: 9-AMC-AFS630-Comments (FAA) <AFS630Comments@faa.gov>
Subject: FAA Aviation Maintenance Technician Handbooks are available without copyright concern

This email from Barry.Hyde@faa.gov originates from outside Imperial. Do not click on links and attachments unless you recognise the sender. If you trust the sender, add them to your safe senders list to disable email stamping for this address.

Happy blue skies, Suriyanarayanan Venkatesh!

Thank you for your great question in reference to using the FAA's Aviation Maintenance Technician Handbooks. It is our understanding that anything placed in the public domain, such as our handbooks, which are available without any copyright concerns or further authorizations. Hope this answers your questions about them being available! Smiles!

Good luck with your doctoral degree, thanks again, and safe flying!

Dr. Barry Hyde
Aviation Safety Analyst
Airman Testing Standards Branch, AFS-630
Barry.Hyde@faa.gov

From: Suriyanarayanan, Venkatesh <v.suriyanarayanan16@imperial.ac.uk>
Sent: Sunday, November 21, 2021 4:54 PM
To: 9-AMC-AFS630-Comments (FAA) <AFS630Comments@faa.gov>
Subject: Fw: Permission to use figure in PhD thesis

Dear Sir/Madam,

As a follow-up to my previous two emails, I would like to kindly request the speedier addressal for my following request as I am due for my PhD thesis submission.

I, S. Venkatesh, a PhD student at Imperial College London would like to use figure 10.57 on page number 10-46 from "Aviation Maintenance Technician Handbook – Powerplant, Volume 2" in my PhD thesis titled "Uncertainty Quantification Of Performance And Stability Of High-Speed Axial Compressors" to be submitted to the university by December 2021

(https://www.faa.gov/regulations_policies/handbooks_manuals/aviation/media/FAA-H-8083-32-AMT-Powerplant-Vol-2.pdf)

I would be extremely grateful if you could please allow me to use the figure as it would add value to the future readers of the thesis. Hoping for a positive response from you.

Regards,
Venkatesh

From: Suriyanarayanan, Venkatesh <v.suriyanarayanan16@imperial.ac.uk>
Sent: 14 September 2020 10:47
To: Pinelli Michele <michele.pinelli@unife.it>; Montomoli, Francesco <f.montomoli@imperial.ac.uk>
Subject: Re: Permission to use figures in PhD thesis from your book UQ in CFD and Aircraft Engines

Dear Sirs,

Thanks a lot for letting me use the figures in my thesis. I will cite the figure and work at appropriate places. Have a good day.

Kind Regards,
Venkatesh

From: Pinelli Michele <michele.pinelli@unife.it>
Sent: 14 September 2020 07:53
To: Montomoli, Francesco <f.montomoli@imperial.ac.uk>
Cc: Suriyanarayanan, Venkatesh <v.suriyanarayanan16@imperial.ac.uk>
Subject: Re: Permission to use figures in PhD thesis from your book UQ in CFD and Aircraft Engines

This email from michele.pinelli@unife.it originates from outside Imperial. Do not click on links and attachments unless you recognise the sender. If you trust the sender, add them to your safe senders list to disable email stamping for this address.

Francesco,
no problem also for me.
Regards
Michele

Michele Pinelli, PhD
Professore Associato di Macchine a Fluido (ING-IND/08)
Dipartimento di Ingegneria
Università degli Studi di Ferrara
via Saragat 1, 44121 Ferrara
Tel. +39-0532-974889
Cell. +39-328-8606259
e-mail: michele.pinelli@unife.it

Il giorno lun 14 set 2020 alle ore 07:33 Montomoli, Francesco <f.montomoli@imperial.ac.uk> ha scritto:

> Dear Venkatesh
> I am fine with that
> But the pictures belong to University of Ferrara
> Dear Michele
> Is it OK for you?
> Yours
>
> Francesco

From: no-reply@copyright.com <no-reply@copyright.com>
Sent: 21 October 2021 01:52
To: Suriyanarayanan, Venkatesh <v.suriyanarayanan16@imperial.ac.uk>
Subject: Thank you for your order with RightsLink / Elsevier

This email from no-reply@copyright.com originates from outside Imperial. Do not click on links and attachments unless you recognise the sender. If you trust the sender, add them to your safe senders list to disable email stamping for this address.



Thank you for your order!

Dear Mr. Venkatesh Suriyanarayanan,

Thank you for placing your order through Copyright Clearance Center's RightsLink® service.

Order Summary

Licensee:	Mr. Venkatesh Suriyanarayanan
Order Date:	Oct 20, 2021
Order Number:	5173350626218
Publication:	Computers & Fluids
Title:	Prediction of the unsteady turbulent flow in an axial compressor stage. Part 1: Comparison of unsteady RANS and LES with experiments
Type of Use:	reuse in a thesis/dissertation
Order Total:	0.00 USD

View or print complete details of your order and the publisher's terms and conditions.

Sincerely,

Copyright Clearance Center

Tel: +1-855-239-3415 / +1-978-646-2777
customercare@copyright.com
https://myaccount.copyright.com

CCC RightsLink®

From: no-reply@copyright.com <no-reply@copyright.com>
Sent: 21 October 2021 00:20
To: Suriyanarayanan, Venkatesh <v.suriyanarayanan16@imperial.ac.uk>
Subject: Thank you for your order with RightsLink / Springer Nature

This email from no-reply@copyright.com originates from outside Imperial. Do not click on links and attachments unless you recognise the sender. If you trust the sender, add them to your safe senders list to disable email stamping for this address.

SPRINGER NATURE

Thank you for your order!

Dear Mr. Venkatesh Suriyanarayanan,

Thank you for placing your order through Copyright Clearance Center's RightsLink® service.

Order Summary

Licensee:	Mr. Venkatesh Suriyanarayanan
Order Date:	Oct 20, 2021
Order Number:	5173311161706
Publication:	Journal of Failure Analysis and Prevention
Title:	Investigation of Fatigue Failures of Titanium Alloy Blades Used in Compressor Modules of Aeroderivative Industrial Gas Turbines
Type of Use:	Thesis/Dissertation
Order Total:	0.00 GBP

View or print complete details of your order and the publisher's terms and conditions.

Sincerely,

Copyright Clearance Center

Tel: +1-855-239-3415 / +1-978-646-2777
customercare@copyright.com
https://myaccount.copyright.com

CCC RightsLink®

From: no-reply@copyright.com <no-reply@copyright.com>
Sent: 21 October 2021 01:22
To: Suriyanarayanan, Venkatesh <v.suriyanarayanan16@imperial.ac.uk>
Subject: Thank you for your order with RightsLink / Springer Nature

This email from no-reply@copyright.com originates from outside Imperial. Do not click on links and attachments unless you recognise the sender. If you trust the sender, add them to your safe senders list to disable email stamping for this address.

SPRINGER NATURE

Thank you for your order!

Dear Mr. Venkatesh Suriyanarayanan,

Thank you for placing your order through Copyright Clearance Center's RightsLink® service.

Order Summary

Licensee:	Mr. Venkatesh Suriyanarayanan
Order Date:	Oct 20, 2021
Order Number:	5173340315486
Publication:	Metallurgical transactions, A, Physical metallurgy and materials science
Title:	Mechanisms in the simultaneous erosion-oxidation attack of nickel and cobalt at high temperature
Type of Use:	Thesis/Dissertation
Order Total:	0.00 USD

View or print complete details of your order and the publisher's terms and conditions.

Sincerely,

Copyright Clearance Center

Tel: +1-855-239-3415 / +1-978-646-2777
customercare@copyright.com
https://myaccount.copyright.com

CCC RightsLink®

From: Beth Darchi <DarchiB@asme.org>
Sent: 01 December 2021 15:53
To: Suriyanarayanan, Venkatesh <v.suriyanarayanan16@imperial.ac.uk>
Subject: RE: Publication of papers in thesis

This email from DarchiB@asme.org originates from outside Imperial. Do not click on links and attachments unless you recognise the sender. If you trust the sender, add them to your safe senders list to disable email stamping for this address.

Dear Mr. Suriyanarayanan,
It is our pleasure to grant you permission to use **all or any part of** the following ASME papers:

- Effect of Manufacturing Tolerance in Flow Past a Compressor Blade, by Venkatesh Suriyanarayanan, Quentin Rendu, Mehdi Vahdati, Loic Salles, J. Turbomach. Apr 2022, 144(4)
- Effect of Geometric Uncertainty on a One Stage Transonic Compressor of an Industrial Gas Turbine, by S. Venkatesh, K. Suzuki, M. Vahdati, L. Salles, Q. Rendu, Paper No: GT2020-16315

cited in your letter for inclusion in a PhD thesis entitled Uncertainty Quantification Of Performance And Stability Of High-Speed Axial Compressors to be published by Imperial College London.

Permission is granted for the specific use as stated herein and does not permit further use of the materials without proper authorization. Proper attribution must be made to the author(s) of the materials. **Please note**: if any or all of the figures and/or Tables are of another source, permission should be granted from that outside source or include the reference of the original source. ASME does not grant permission for outside source material that may be referenced in the ASME works.

As is customary, we request that you ensure full acknowledgment of this material, the author(s), source and ASME as original publisher.

Many thanks for your interest in ASME publications.

Sincerely,

Beth Darchi
Publishing Administrator
ASME
2 Park Avenue
New York, NY 10016-5990

From: Beth Darchi <DarchiB@asme.org>
Sent: 26 October 2021 18:23
To: Suriyanarayanan, Venkatesh <v.suriyanarayanan16@imperial.ac.uk>
Subject: RE: Permission to include figures in PhD thesis

Dear Mr. Suriyanarayanan,
It is our pleasure to grant you permission to use the ASME materials:

- **Figure 1 only** from “Structure Of Tip Clearance Flow In An Isolated Axial Compressor Rotor”, Inoue and Kuroumaru, ASME J. Turbomach., 111(3):250–256,
- **Figure 2 only** from "Probabilistic CFD Simulation Of A High-Pressure Compressor Stage Taking Manufacturing Variability Into Account", Proceedings of ASME Turbo Expo 2010, Paper number : GT2010-22484
- **Figures 2,10,15 only** from “Turbomachinery Active Subspace Performance Maps”, Proceedings of ASME Turbo Expo 2017, Paper Number : GT2017-64528
- **Figures4,8 only** from "Assessment and Characterization of Volcanic Ash Threat to Gas Turbine Engine Performance", C. R. Davison and T. A. Rutke, Journal of Engineering for Gas Turbines and Power, 136(8)
- **Figures 8,9 only** from K. B. Lee, M. J. Wilson, and M. Vahdati. “Validation of a Numerical Model for Predicting Stalled Flows in a Low Speed Fan - Part 1: Modification of Spalart-Allmaras Turbulence Model”. ASME J. Turbomach., 140(5)

cited in your letter for inclusion in a thesis entitled Uncertainty Quantification Of Performance And Stability Of High-Speed Axial Compressors to be published by Imperial College London.

Permission is granted for the specific use as stated herein and does not permit further use of the materials without proper authorization. As is customary, we request that you ensure full acknowledgment of this material, the author(s), source and ASME as original publisher.

Many thanks for your interest in ASME publications.

Sincerely,

Beth Darchi
Publishing Administrator
ASME
2 Park Avenue, 6th Floor
New York, NY 10016-5990
darchib@asme.org

From: GBS Service Portal <rollsroycegbs@service-now.com>
Sent: 18 February 2022 13:45
To: Suriyanarayanan, Venkatesh <v.suriyanarayanan16@imperial.ac.uk>
Subject: GBS0009727 - We've completed your service request

This email from rollsroycegbs@service-now.com originates from outside Imperial. Do not click on links and attachments unless you recognise the sender. If you trust the sender, add them to your safe senders list to disable email stamping for this address.

GBS Service Portal

Hi Customer,

We've completed your service request.

Ticket reference ID:	GBS0009727
Service requested:	Permision to use Rolls Royce Images in my PhD thesis

The final comments are:
Fulfillment completed

If you are happy with our response please **accept the resolution**. If you need us to take another look you can **reopen the service request ticket** within the **next five days**.

If we don't hear back from you, this ticket will be closed and you will be unable to log any further comments.

Thank you for using Group Business Services.

How did we do?

Your feedback is really important to us and helps us to keep improving our services. Please tell us about your experience by completing our **short survey.**

Group Business Services

From: isropr@isro.gov.in <isropr@isro.gov.in>
Sent: 12 October 2020 12:48
To: Suriyanarayanan, Venkatesh <v.suriyanarayanan16@imperial.ac.uk>
Subject: Re: Permission for including the Image of GSLV-F05 in thesis

This email from isropr@isro.gov.in originates from outside Imperial. Do not click on links and attachments unless you recognise the sender. If you trust the sender, add them to your safe senders list to disable email stamping for this address.

Dear Shri Venkatesh,

Greetings from ISRO!!!

With reference to your mail, you are granted the permission to use the said image in your thesis.

Nevertheless, the material has to be reproduced accurately and not to be used in a derogatory manner or in a misleading context. You are also requested to acknowledge appropriately for the material used. Further, it should not be used for commercial purpose.

With Warm Regards,
Office of Media and Public Relations
ISRO HQ
Bengaluru